APPLIED COMPUTATIONAL ELECTROMAGNETICS SOCIETY JOURNAL

March 2022
Vol. 37 No. 3
ISSN 1054-4887

The ACES Journal is abstracted in INSPEC, in Engineering Index, DTIC, Science Citation Index Expanded, the Research Alert, and to Current Contents/Engineering, Computing & Technology.

The illustrations on the front cover have been obtained from the ARC research group at the Department of Electrical Engineering, Colorado School of Mines

Published, sold and distributed by: River Publishers, Alsbjergvej 10, 9260 Gistrup, Denmark

MARCH 2022 REVIEWERS

Giulio Antonini
Manuel Arrebola
Alireza Baghai-Wadji
Thomas Bauernfeind
Billel Bentouhami
Giuseppe Chitarin
Arkaprovo Das
Alessandro Formisano
Guan-Long Huang
Robert Ilgner
Tianqi Jiao
Poom Kumam
Jinghe Li
Yingsong Li
Fabrizio Loreto
Shengyuan Luo
Andrea Michel
Mahdi Oliaei
Andrew Peterson
Kenedy Santos
Yufa Sun
Wanchun Tang
Grzegorz Tytko
Marsellas Waller
Zhonggen Wang
Steven Weiss
Gaobiao Xiao
Yuancheng Xu
Huanhuan Yang
Shihyuan Yeh
Qiwei Zhan
Xiaoyan Zhang
Yuanguo Zhou

THE APPLIED COMPUTATIONAL ELECTROMAGNETICS SOCIETY JOURNAL

Vol. 37 No. 3 March 2022

TABLE OF CONTENTS

Women's History Month Special Article: Interview with "Professor Ozlem Kilic"

Sima Noghanian

CommScope Ruckus Wireless
Sunnyvale, CA, USA
Sima_noghanian@ieee.org

***Abstract* –** The month of March is Women's History Month. We all have heard and know that only a small percentage of electrical engineers are female. This percentage is even smaller for those that are experts in the field of applied computational electromagnetics. In this article, we are focusing on Dr. Ozlem Kilic, one of the well-known and established intellectuals in the field of computational electromagnetics. Dr. Kilic not only has been a role model for young students as an excellent researcher, a technical leader, and a prolific writer in this field, but also she has extensive experience in teaching and has taken many academic administration roles.

***Keywords* –** Women in STEM, women in applied computational electromagnetics.

I. INTRODUCTION

By the year 2021, the Applied Computational Electromagnetics Society (ACES) has elected 42 fellows from its members, and only one of them is female. Professor **Ozlem Kilic** was promoted to a fellow member in 2016. Additionally, she took leading roles at ACES. She was a member of the ACES Board of Directors between 2009 and 2012 and the Founding Editor-in-Chief for *ACES Express Journal*. She received the ACES Recognition Award in 2018 for her contributions. She is a remarkable researcher and educator. I got a chance to communicate with her and ask her a few questions. This article summarizes our conversation. I am sure it will be inspiring for our society members.

II. BIOGRAPHY

Professor Ozlem Kilic is currently the Associate Dean for Academic and Student Affairs with the Tickle College of Engineering, University of Tennessee Knoxville (UTK), Knoxville, TN, USA (Figure 1). In this role, she oversees a variety of the college's programs, including undergraduate and graduate curricula, diversity, study abroad, advising, student recruitment, scholarship and fellowships, and the Heath Integrated Business and Engineering program.

Before joining UTK, Professor Kilic served as the Associate Dean of the College of Engineering at the Catholic University of America in Washington, DC, USA. Before that, she was the Chair of the Electrical Engineering and Computer Science Department at the same university for two consecutive terms. Professor Kilic is a fellow of the Applied Computational Electromagnetic Society and an elected council member for the Maryland Clean Energy Center. She has served as Chair and Vice-Chair of the International Union of Radio Scientists (URSI) Commission A, and as an advisory committee member of IEEE Antennas and Propagation Society. She has authored more than 135 peer-reviewed articles.

Dr. Kilic earned the bachelor's degree from Istanbul's Bogazici University in 1989, and the master's and doctorate degrees from George Washington University in 1991, and 1996, respectively, all in electrical engineering.

Fig. 1. Professor Kilic in Tickle College of Engineering, the University of Tennessee Knoxville.

III. Questions and Answers (Q & A)

Q: Tell me about your career path. Why did you get interested in electromagnetics?

A: I love math (having a mathematician dad may have something to do with it). I love the ability that math pro-

Submitted On: April 6, 2022
Accepted On: April 6, 2022

https://doi.org/10.13052/2022.ACES.J.370301

vides to model, understand, and explain complex concepts in physics in short and elegant ways. Something that may take more than two pages of writing using words can be explained with just one short equation. So, when I saw the four elegant equations of Maxwell, you can imagine, it was in love at first sight! Volumes of books are continuously being written to capture what they mean.

Q: How did you become involved in the ACES?

A: I remember my first ACES meeting in Niagara Falls. I had started my academic career a few years prior. My research was heavily focused on hardware-accelerated electromagnetics modeling of electrically large problems. The ACES conference's relatively small size was very attractive as it enabled close interactions.

Q: Why do you think Applied Computational Electromagnetics is an important area of research and development?

A: The ability to model a scenario requires an in-depth understanding of the concept. Once that is achieved, one can apply the concept to many different scenarios without having to be in the scene, opening up tremendous opportunities for investigation and learning at the tips of a "return" button. Electromagnetic modeling is fascinating as our devices and scenarios get more intricate, our dimensions shrink, and the complexity of our problems increases. We can compute things faster and faster, enabling "real-time" investigation and understanding of such complex scenarios.

Q: How do you see yourself as a role model for the young girls who are interested in STEM, engineering, and electromagnetics?

A: It is always helpful to see people you can relate to in positions you aspire to. It is even more helpful to have people you relate to in positions you would not even consider. If a young girl can see in me a potential for her future and a glimmer of motivation to pursue STEM, I consider myself lucky. Engineering remains a career that is not accessible by the female population. But we need to be aware that it is not just women who can be role models to aspiring young women to pursue STEM careers. After all, it was men who were doing inspiring work that motivated me, starting with my father. Later in my career, it was my male colleagues and role models that supported me to get where I am today. I see myself as a role model to our male students in the field so that, in the future, they support women as colleagues and leaders.

Q: Tell me about the type of challenges you had to face and how you overcame them.

A: I guess my challenges relate to being a minority in most of the settings my career took me. It was from my first day in college onward that I was almost always either the only or one of the few women in the room. It inadvertently brings pressure that mistakes can easily be attributed to the gender that is likely seen as one the most defining features of oneself in such settings. There could also be a tendency that by being different, one may not always receive the benefit of social interactions that can enhance collegial relationships at work. These drive one to be a perfectionist and strive for the best to ensure success. I see this trait in all my female colleagues. However, challenges do not necessarily determine a negative outcome, and everybody deals with them. We all just need to focus on what matters most and not lose sight of our ultimate goals. The path does not always have to be, and never is, the same for everyone. Also, at each turning point, I like to look back and make sure I am helping others to avoid or overcome the challenges I have had to face.

Q: What are the topics you are working on now and why do you see them challenging and worth attention.

A: I am in an administrative role now, and one of my highest priorities is making engineering education accessible and attainable. Being at a land-grant institution has been wonderful as it has allowed me to look back and help others to avoid or overcome the challenges I faced. I oversee UTK Tickle College of Engineering's student success programs as part of my role as the Associate Dean. My office serves as a hub to connect our faculty and their research to support healthy pathways to an engineering degree at UTK (Figure 2).

Fig. 2. Professor Kilic giving a talk to young students.

Q: Any word of advice to the young researchers that are in the early stages of their careers?

A: Have fun and make time to build relationships on your campus and in your professional societies as you work very hard on your research. Step out of your comfort zones at every chance. Do not forget to engage "unlikely" research partners from other disciplines either as the bigger problems we need to solve involve us all.

IV. CONCLUSION

It is always inspiring for me to hear from leaders in the field, especially from a fellow female engineer and professor. Finally, I invite you to watch the video by Professor Kilic that was created for NIMBioS and is available on YouTube [1].

REFERENCES

[1] O. Kilic, One girl's journey in engineering – Pave your own path!, available online: https://www.youtube.com/watch?v=2FzYlLJT_pk&ab_channel=NIMBioS.

Sima Noghanian received the B.Sc. degree in electrical engineering from the Sharif University of Technology, Tehran, Iran, and the M.Sc. and Ph.D. degrees, both in electrical engineering, from the University of Manitoba, Winnipeg, Canada. She is the chair of ACES Communication and Membership Committee and serves as an Associate Editor for *ACES Journal*. She received a Postdoctoral Fellowship from the Natural Sciences and Engineering Research Council of Canada in 2002, which she took at the University of Waterloo. She was a researcher with YottaYotta Corporation, Edmonton, AB, Canada. She was an Assistant Professor with the Department of Electrical Engineering, Sharif University of Technology, from 2002 to 2003. From 2003 to 2008, she was an Assistant Professor with the Department of Electrical and Computer Engineering, University of Manitoba, Winnipeg, MB, Canada. She was an Assistant/Associate Professor and the Director of the Applied Electromagnetic and Antenna Engineering Laboratory in the Department of Electrical Engineering, University of North Dakota, Grand Forks, ND, USA, from 2008 to 2018. She also served as the Electrical Engineering Department Chair from 2014 to 2016 at the University of North Dakota. From 2018 to 2019, she was a visiting Professor with the Department of Electrical and Computer Engineering, San Diego State University, San Diego, CA, USA. She was an Electromagnetic Application Engineer with Phoenix Analysis and Design Technologies Inc. (PADT) (2019-2020), and a Principal Antenna Design Engineering with Wafer LLC (2020-2021). She is currently a Principal Antenna Design Engineer with CommScope, Sunnyvale, CA, USA. Her research interests include MIMO antennas for wireless communications, wearable and implanted antennas, 3D printed antennas, wireless power transfer, microwave imaging, and wireless channel modeling.

Generalized Finite Difference Method for Solving Waveguide Eigenvalue Problems

Hui Xu[1] **and Yang Bao**[1,2]

[1]Department of Electronic and Optics Engineering,
Nanjing University of Posts and Telecommunications, Nanjing 210000, China
1090760655@qq.com

[2]State Key Laboratory of Millimeter Waves,
Southeast University, Nanjing 210096, China
brianbao@njupt.edu.cn

Abstract **–** The generalized finite difference method (GFDM) is a meshless method that has become popular in recent years. The basic theory underlying GFDM is to expand the point cluster function value at the center node by Taylor's formula and then obtain the best linear combinations of these function values to represent the derivative at the central node by the least square fitting technique. Subsequently, the minimized weighted error between the approximated value and the accurate value is obtained. This paper establishes the general steps for solving waveguide eigenvalue problems with GFDM. Excellent performance is shown by comparing the proposed method and other common solutions. The robustness of the proposed method is verified by calculating the cutoff wavenumbers of typical waveguides and the eccentric circular waveguide in different modes.

Index Terms **–** Cutoff wavenumber, generalized finite difference method, meshless method, waveguide eigenvalue problem.

I. INTRODUCTION

The waveguide eigenvalue problem can be described as the electromagnetic wave propagation problem in closed or open structures under different boundary shapes and conditions. For regular-shaped waveguides, analytical expressions can be obtained by the variable separation method, and the cutoff wavelength of the main mode of the ridge waveguide can be obtained by the transverse resonance method [1]. However, most waveguides with complex cross-sectional geometries must be solved numerically. The finite difference method (FDM) is one of the common methods to solve waveguide problems. Thereby, the basic idea is to approximate the derivative of the target node with the difference quotient of function values. The compact two-dimensional (2D) frequency-domain finite difference method (FDFD) is derived from Maxwell's curl equations and uses compact 2D Yee cells to mesh the waveguide cross section [2]. This method only involves four transverse field components, which can greatly reduce the CPU time compared to the 3D finite-difference time-domain method (FDTD) [3]. The finite element method (FEM) transforms the eigen-problem into an equivalent variational equation, constructs the divisional basis functions on the grid elements of the waveguide cross section, and uses the Ritz method or Galerkin method to construct the algebraic finite element equation [4]. When dealing with complex structures or discontinuous boundaries, these grid-based methods suffer from the problem of complex meshing and low accuracy. The radial basis function (RBF) interpolation method is a meshless method, and its main idea is to use basis functions to approximate the function to be sought over the entire simulation domain [5]. By requiring that the approximate value and actual value are strictly equal, a matrix equation with weight coefficients as variables is constructed, and the derivative at the center node is transformed into a linear combination of the function values of the surrounding nodes. Recently, RBF and the variational principle have been combined to analyze the propagation characteristics of inhomogeneous waveguides, which further expands the application of this method [6]. Although meshless methods have been successfully applied to many scientific and engineering fields, their employment in the field of computational electromagnetics is still relatively slow [7].

The generalized finite difference method (GFDM) is a relatively new domain-style meshless method that uses the weighted sum of surrounding function values to represent the derivative at center node. Benito gave the basic concepts of the GFDM, including node distribution, local approximation, and the construction of point clusters [8–10]. The influence of factors such as the size of the point cluster, the shape of the point cluster, and

Submitted On: October 24, 2021
Accepted On: April 4, 2022

https://doi.org/10.13052/2022.ACES.J.370302

the selection of the weight function on the accuracy of the GFDM is also analyzed [11]. Kamyabi proposed an improved version of the GFDM, which makes it no longer dependent on the least square method and can handle the Neumann boundary conditions in a sophisticated way [12]. At present, the GFDM has been effectively applied in many fields. For example, Li and Fan applied this method to solve the shallow water wave equation [13], Gu solved the inverse heat source problem [14], and Zhang analyzed the sloshing phenomenon [15]. In the field of electromagnetism, Chen verified the effectiveness of the GFDM in calculating static electromagnetic field problems and analyzing 3D transient electromagnetic problems [16]. The results show that the GFDM is more accurate and faster than the FEM.

In our previous work [17], GFDM was effectively used to analyze the propagation characteristics of the waveguide. However, when solving the TE mode problem, it relied on the second set of node distribution schemes, that is, an additional layer of discrete points needs to be arranged outside the boundary. In this paper, the general steps to solve eigenvalue problem of waveguides are given based on the meshless features of GFDM, and the calculation result of an eccentric circular waveguide is added. This paper also proposes a new version of GFDM, which can directly use Neumann boundary conditions for the calculation of derivatives. The improved GFDM compares the Taylor expansion of adjacent nodes with the expression of the governing equation to construct the matrix equation. Consequently, the solution process is more convenient and faster than the traditional GFDM. In addition, we compare the GFDM against other common methods to demonstrate the unique merits of this method in solving the waveguide problem.

II. FORMULATION OF GFDM

A. Basic theory of GFDM

Without loss of generality, consider solving the second-order partial differential equation

$$\lambda_{10}\frac{\partial\varphi}{\partial x}+\lambda_{01}\frac{\partial\varphi}{\partial y}+\lambda_{20}\frac{\partial^2\varphi}{\partial x^2}+\lambda_{02}\frac{\partial^2\varphi}{\partial y^2}+\lambda_{11}\frac{\partial^2\varphi}{\partial x\partial y}=f(x,y). \tag{1}$$

In order to obtain the generalized finite difference equivalence of eqn (1), the computational node $\boldsymbol{X}=[x,y]$ of the function $\varphi(\boldsymbol{X})$ is arranged inside and on the boundary of the simulation domain. The distribution of the discrete nodes may or may not be uniform.

The GFDM puts forward the concept of point clusters, which amounts to finding m nearest adjacent nodes around the center node $\boldsymbol{X_0}$ according to the shortest distance criterion. The set of $m+1$ nodes including the center node is referred to as the point cluster of $\boldsymbol{X_0}$ (as shown in Figure 1) and its shape is determined by the distribution of adjacent nodes. Assume that φ_0 and φ_i represent the function values at the center node and adjacent nodes, respectively. In order to establish the relationship between the differential at $\boldsymbol{X_0}$ and its point cluster, φ_i is expanded at φ_0 by Taylor's series expansion formula and truncated at the second derivate,

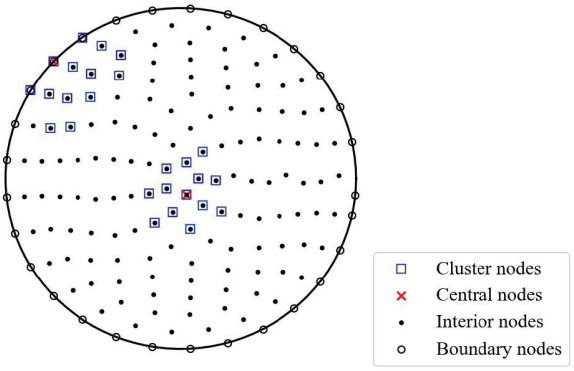

Fig. 1. Schematic diagram of GFDM. Irrespectively of the position of the central node, being an interior or a boundary node, 12 suitably- chosen adjacent nodes constitute a point cluster.

$$\varphi_i=\varphi_0+h_i\left(\frac{\partial\varphi}{\partial x}\right)_0+k_i\left(\frac{\partial\varphi}{\partial y}\right)_0+\frac{h_i^2}{2}\left(\frac{\partial^2\varphi}{\partial x^2}\right)_0+\frac{k_i^2}{2}\left(\frac{\partial^2\varphi}{\partial y^2}\right)_0+h_ik_i\left(\frac{\partial^2\varphi}{\partial x\partial y}\right)_0, i=1,2,\ldots,m. \tag{2}$$

where $h_i{=}x_i{-}x_0$ and $k_i{=}y_i{-}y_0$, respectively, represent the vertical and horizontal distances between $\boldsymbol{X_i}$ and $\boldsymbol{X_0}$.

The error between the expanded and actual values, the residual function, can be expressed as

$$B(\varphi)=\sum_{i=1}^{m}\left[\left(\varphi_0-\varphi_i+h_i\left(\frac{\partial\varphi}{\partial x}\right)_0+k_i\left(\frac{\partial\varphi}{\partial y}\right)_0+\frac{h_i^2}{2}\left(\frac{\partial^2\varphi}{\partial x^2}\right)_0+\frac{k_i^2}{2}\left(\frac{\partial^2\varphi}{\partial y^2}\right)_0+h_ik_i\left(\frac{\partial^2\varphi}{\partial x\partial y}\right)_0\right)\omega(\boldsymbol{X}_i)\right]^2, \tag{3}$$

where $\omega(\boldsymbol{X_i})$ is the error weighting function. The expression of weighting function is not unique, but they all have a common feature, that is, the closer they are to center node, the greater the weight given, and the greater the contribution to the final calculation result. In this paper, the expression of $\omega(\boldsymbol{X_i})$ is defined as

$$\omega(\boldsymbol{X_i})=1-6\left(\frac{d_i}{d_{\max}}\right)^2+8\left(\frac{d_i}{d_{\max}}\right)^3-3\left(\frac{d_i}{d_{\max}}\right)^4, \tag{4}$$

where d_i represents the distance from $\boldsymbol{X_i}$ to $\boldsymbol{X_0}$, and $d_{\max}$ is the maximum value among all d_i. The coefficient in $\omega(\boldsymbol{X_i})$ adds up to 0, which changes the function range from 0 to 1. In addition, the function $\omega(\boldsymbol{X_i})$ is monotonically decreasing and has a pole when $d_i/d_{\max}$ equals 0 or 1, which makes the function smooth. This construction also implies that $\omega(\boldsymbol{X_i})$ decreases rapidly when d_i increases, which explicitly gives the weight distribution of each point in the cluster.

For brevity, define

$$\mathbf{D}_\varphi = \left[\frac{\partial\varphi}{\partial x}, \frac{\partial\varphi}{\partial y}, \frac{\partial^2\varphi}{\partial x^2}, \frac{\partial^2\varphi}{\partial y^2}, \frac{\partial^2\varphi}{\partial x\partial y}\right]^T, \tag{5}$$

$$p_i = \left\{h_i, k_i, \frac{h_i^2}{2}, \frac{k_i^2}{2}, h_i k_i\right\}, \tag{6}$$

$$\mathbf{P} = \begin{bmatrix} p_1 \\ p_2 \\ \vdots \\ p_m \end{bmatrix} = \begin{bmatrix} h_1 & k_1 & \cdots & h_1k_1 \\ h_2 & k_2 & \cdots & h_2k_2 \\ \vdots & \vdots & \ddots & \vdots \\ h_m & k_m & \cdots & h_mk_m \end{bmatrix}. \tag{7}$$

Then the residual function $B(\varphi)$ in eqn (3) can be expressed in the form of the matrix as

$$\mathrm{B}(\varphi) = \left(\mathbf{P}\mathbf{D}_\varphi + \mathbf{\Phi}_0 - \mathbf{\Phi}\right)^T \mathbf{W}\left(\mathbf{P}\mathbf{D}_\varphi + \mathbf{\Phi}_0 - \mathbf{\Phi}\right), \tag{8}$$

where $\mathbf{\Phi} = [\varphi_1, \ldots, \varphi_m]^T$ and $\mathbf{\Phi}_0 = [\varphi_0, \ldots, \varphi_0]^T$ are the vectors of function values sampled at $\boldsymbol{X_i}$ and $\boldsymbol{X_0}$, respectively. Furthermore, $\mathbf{W} = \mathrm{diag}(\omega_1^2, \ldots, \omega_m^2)$ is a diagonal matrix.

The residual function can be regarded as a cost function in an optimization algorithm with the elements in D_φ as independent variables. The optimal solution is obtained by minimizing the norm $B(\varphi)$

$$\frac{\partial B}{\partial\{\boldsymbol{D}_\varphi\}} = 0, \tag{9}$$

resulting in the linear equation

$$\mathbf{A}\mathbf{D}_\varphi = \mathbf{b}, \tag{10}$$

with $\mathbf{A} = \mathbf{P}^T\mathbf{W}\mathbf{P}$ and $\mathbf{b} = \mathbf{P}^T\mathbf{W}(\mathbf{\Phi} - \mathbf{\Phi}_0)$. The matrix $\mathbf{A}$ is symmetric, and, thus, the Cholesky decomposition method can be used to solve eqn (10). The expression of $\mathbf{A}$ indicates that at least five adjacent nodes should be found to construct the difference scheme; otherwise, the matrix $\mathbf{A}$ is not invertible because its rank must satisfy the condition: $\mathrm{rank}(\mathbf{A}) = \min\{\mathrm{rank}(\mathbf{P}), \mathrm{rank}(\mathbf{W})\}$.

By solving eqn (10), $\mathbf{D}_\varphi$ can be expressed as

$$\mathbf{D}_\varphi = \mathbf{A}^{-1}\left(-\sum_{i=1}^{m}\omega_i^2 p_i^T, \omega_1^2 p_1^T, \ldots, \omega_m^2 p_m^T\right)\begin{pmatrix}\phi_0 \\ \phi_1 \\ \vdots \\ \phi_m\end{pmatrix}. \tag{11}$$

Eqn (11) shows that all second-order derivatives at center node $\boldsymbol{X_0}$ can be represented by a linear combination of function values at the nodes in point cluster. Each row element of the coefficient matrix in front of the vector $[\varphi_0, \varphi_1, \ldots, \varphi_0]^{\mathrm{T}}$ corresponds to the difference result of each element in $\mathbf{D}_\varphi$.

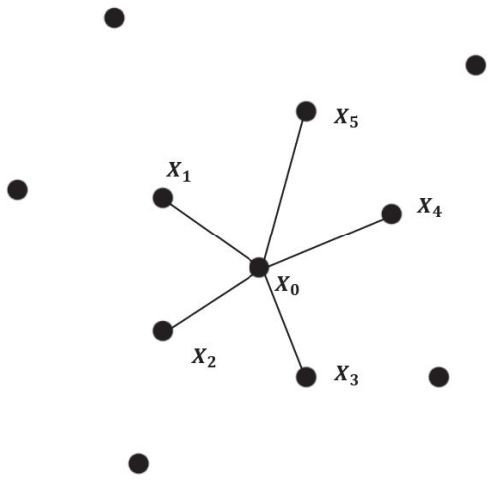

Fig. 2. Schematic diagram of improved version of GFDM. Only five adjacent nodes around the central node need to be found to construct a point cluster.

B. Improved version of GFDM

From the above difference scheme, it can be seen that at least five adjacent nodes need to be found to represent the derivative at center node, which provides an idea for the improved version of GFDM. The second derivative of $\varphi(\boldsymbol{X})$ with respect to each variable of x and y at the node $\boldsymbol{X_0}$ is approximated as linear combinations of the neighbor nodes

$$L\varphi(\boldsymbol{X_0}) = \sum_{i=0}^{5} c_i\varphi_i, \tag{12}$$

where L represents the derivative operator of the governing equation that φ satisfies, and $c_i, i = 0, \ldots, 5$ are weight coefficients to be determined. First, expand these five nodes according to eqn (2) and then group similar terms. According to the coefficient in front of the similar term and the corresponding coefficient in L are strictly equal, the following matrix equation can be obtained:

$$\begin{bmatrix} 1 & 1 & 1 & 1 & 1 & 1 \\ 0 & h_1 & h_2 & h_3 & h_4 & h_5 \\ 0 & k_1 & k_2 & k_3 & k_4 & k_5 \\ 0 & h_1^2/2 & h_2^2/2 & h_3^2/2 & h_4^2/2 & h_5^2/2 \\ 0 & k_1^2/2 & k_2^2/2 & k_3^2/2 & k_4^2/2 & k_5^2/2 \\ 0 & h_1k_1 & h_2k_2 & h_3k_3 & h_4k_4 & h_5k_5 \end{bmatrix}\begin{bmatrix} c_0 \\ c_1 \\ c_2 \\ c_3 \\ c_4 \\ c_5 \end{bmatrix} = \begin{bmatrix} b_0 \\ b_1 \\ b_2 \\ b_3 \\ b_4 \\ b_5 \end{bmatrix}, \tag{13}$$

where b_0 is the coefficient in front of φ_0, $b_i, i = 1, \ldots, 5$ are the coefficients in front of each element in $\mathbf{D}_\varphi$. The value of b_i is determined by the governing equation. For example, when solving eqn (1), b_i is the corresponding value in the set $\{0, \lambda_{10}, \lambda_{01}, \lambda_{20}, \lambda_{02}, \lambda_{11}\}$.

The weight coefficient c_i can be obtained by solving the matrix equation $\mathbf{Ac} = \mathbf{b}$ given by eqn (13).

When constructing a cluster of nodes around the boundary, several nodes on the boundary are also included. Assume that $\boldsymbol{X_5}$ is the boundary node and $\varphi(\boldsymbol{X}_5)$ satisfies the Neumann boundary condition. Express the derivative at $\boldsymbol{X_0}$ as

$$L\varphi(\boldsymbol{X}_0) = \sum_{i=0}^{4} c_i\varphi_i + c_5\bar{r}\left(\frac{\partial\varphi}{\partial n}\right)_5. \tag{14}$$

Here, $\bar{r}$ is the average distance between adjacent nodes and the center nodes. The purpose of adding this item is to ensure that all coefficients are in the same order of magnitude. Expand the last term in eqn (14) according to Taylor's series formula

$$\begin{aligned}\left(\frac{\partial\varphi}{\partial n}\right)_0 =& \left(\frac{\partial\varphi}{\partial x}\right)_0 n_x + \left(\frac{\partial\varphi}{\partial y}\right)_0 n_y \\ &+ \left(\left(\frac{\partial^2\varphi}{\partial x^2}\right)_0 n_x + \left(\frac{\partial^2\varphi}{\partial x\partial y}\right)_0 n_y\right) h_5 \\ &+ \left(\left(\frac{\partial^2\varphi}{\partial x\partial y}\right)_0 n_x + \left(\frac{\partial^2\varphi}{\partial y^2}\right)_0 n_y\right) k_5, \end{aligned} \tag{15}$$

where n_x and n_y correspond to the axial component of the unit normal vector at node $\boldsymbol{X_5}$, respectively.

For each adjacent node, if it is located on the boundary, expand according to eqn (15); otherwise, it is expanded by eqn (2). Grouping terms of similar kind, the following matrix equation can be obtained:

$$\begin{bmatrix} 1 & 1 & 1 & 1 & 1 & 0 \\ 0 & h_1 & h_2 & h_3 & h_4 & \bar{r}n_x \\ 0 & k_1 & k_2 & k_3 & k_4 & \bar{r}n_y \\ 0 & h_1^2/2 & h_2^2/2 & h_3^2/2 & h_4^2/2 & \bar{r}n_x h_5 \\ 0 & k_1^2/2 & k_2^2/2 & k_3^2/2 & k_4^2/2 & \bar{r}n_y k_5 \\ 0 & h_1k_1 & h_2k_2 & h_3k_3 & h_4k_4 & \bar{r}(n_y h_5 + n_x k_5) \end{bmatrix} \begin{bmatrix} c_0 \\ c_1 \\ c_2 \\ c_3 \\ c_4 \\ c_5 \end{bmatrix} = \begin{bmatrix} b_0 \\ b_1 \\ b_2 \\ b_3 \\ b_4 \\ b_5 \end{bmatrix}. \tag{16}$$

The matrix $\boldsymbol{A}$ in eqn (13) or eqn (16) must be automatically scaled by "1", "$\bar{r}$", and "$\bar{r}^2$" because of the appearance of the first and second derivatives. Vector $\boldsymbol{b}$ has to make the same change to ensure the equation is correct. In addition, taking $\bar{r}$ as a normalized factor can effectively avoid the singularity of matrix due to uneven distribution of adjacent points.

C. General steps for analyzing waveguides

When electromagnetic waves propagate in a uniform metal waveguide with the axis along the z-direction, the governing equations and boundary conditions that the electromagnetic field satisfies are

$$L\varphi + k_c^2\varphi = 0 \tag{17}$$

$$L_B\varphi = 0, \tag{18}$$

where φ is the electromagnetic field component, k_c is the cutoff wavenumber, $L{=}\nabla_t^2$ is the transverse Laplacian operator, and L_B is the boundary operator. When propagating TM wave, $\varphi{=}E_z$, L_B refers to the Dirichlet boundary $E_z{=}0$. When propagating TE wave, $\varphi{=}H_z$, L_B refers to the Neumann boundary $\partial H_z/\partial n{=}0$.

As the generalized finite difference scheme given by eqn (11), GFDM simultaneously gives the numerical discrete results of all derivatives of $\varphi(\boldsymbol{X})$ at a certain node; so the coefficient matrix obtained by GFDM should be combined according to the governing equation. The difference result of the internal node is multiplied by the vector $[0,0,1,1,0]$ because it satisfies the Laplace equation. For nodes on the boundary, when solving the TM wave problem, the differential processing is not required because the boundary value $\varphi{=}0$ is known, and when solving the TE wave problem, the result should be multiplied by the vector $[n_x, n_y, 0, 0, 0]$ because the Neumann boundary condition is satisfied.

First, we arrange N_I discrete points inside the cross section and N_B discrete points on the boundary, with $N = N_I + N_B$. According to the difference scheme for solving the waveguide problem given above, the internal node repeats this process N_I times to obtain the matrix A, and eqn (17) can be written as

$$\begin{bmatrix} \boldsymbol{A_I} & \boldsymbol{A_B} \end{bmatrix} \begin{bmatrix} \boldsymbol{\varphi_I} \\ \boldsymbol{\varphi_B} \end{bmatrix} = -\boldsymbol{k_c^2\varphi_I}, \tag{19}$$

where $\boldsymbol{\varphi_I}{=}[\varphi_1,\ldots,\varphi_{N_I}]^{\mathrm{T}}$ and $\boldsymbol{\varphi_B}{=}[\varphi_{N_I+1},\ldots,\varphi_N]^{\mathrm{T}}$. For nodes on the boundary, when Neumann BCs have to be satisfied, matrix B can be obtained similarly

$$\begin{bmatrix} \boldsymbol{B_I} & \boldsymbol{B_B} \end{bmatrix} \begin{bmatrix} \boldsymbol{\varphi_I} \\ \boldsymbol{\varphi_B} \end{bmatrix} = \boldsymbol{0}. \tag{20}$$

Combining eqn (19) and (20), the eigenvalue equation describing the waveguide problem can be discretized and written in the matrix form

$$\begin{bmatrix} \boldsymbol{A_I} & -\boldsymbol{A_B}\left(\boldsymbol{B_B^{-1}B_I}\right) \end{bmatrix} \boldsymbol{\varphi_I} = -k_c^2\boldsymbol{\varphi_I}. \tag{21}$$

The Dirichlet boundary condition can be directly substituted into the matrix because $\boldsymbol{\varphi_B}{=}\boldsymbol{0}$ means that the weight coefficients of the boundary nodes in the generalized finite difference schema can be ignored, that is, the matrix $\boldsymbol{A_B}$ can be omitted.

When using the improved version of GFDM to solve the waveguide problem, the value of vector b is $[0,0,0,1,1,0]$. Compared with traditional GFDM, the coefficient matrix can be constructed more conveniently by eqn (13) and (16). Especially when solving the TE wave problem, the boundary node avoids additional differencing because the Neumann boundary can be directly used as shown in eqn (14).

III. NUMERICAL RESULTS

To validate the GFDM in analyzing the waveguide eigenvalue problems, we analyzed the dispersion characteristics of TE modes and TM modes in different waveguides. The size of the point cluster in GFDM is set to be 10. The GFDM solution is compared with the FDM, FDFD, and RBF solutions, and the reasons for the differences in the result are also given.

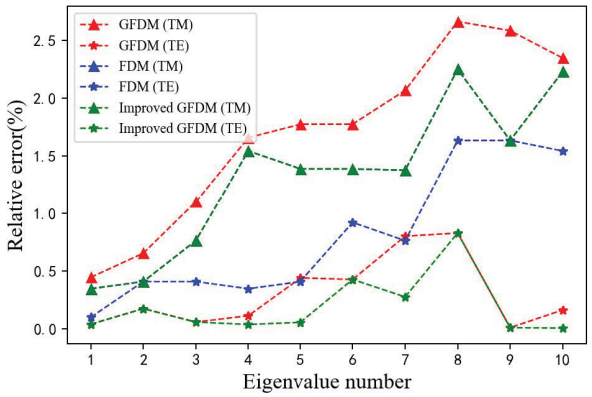

Fig. 3. Error comparison of GFDM solution, FDM solution, and improved GFDM solution for cutoff wavenumbers of the TM wave and TE wave in the rectangular waveguide. The "improved GFDM (TM)" line and the "FDM (TM)" line coincide.

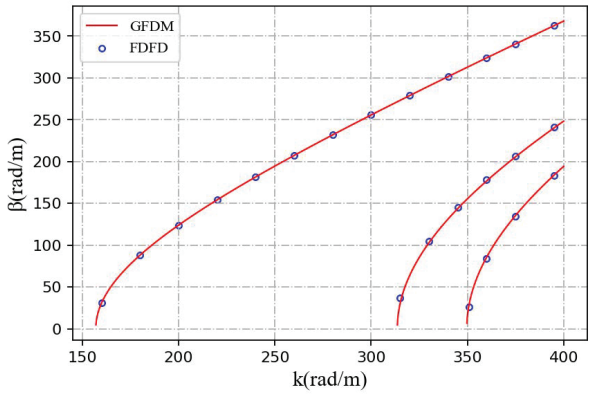

Fig. 4. Dispersion characteristics of TE_{10}, TE_{01}, and TM_{11} modes in rectangular waveguide. Results are calculated using GFDM and FDFD.

First, we consider a rectangular waveguide with a size of 20 mm $\times$ 10 mm and divide the calculation domain uniformly at intervals of 1 mm. Figure 3 shows the error comparison of GFDM solution, FDM solution, and improved GFDM solution for cutoff wavenumbers of the TM wave and TE wave in the rectangular waveguide. When solving TM wave problems, the improved GFDM solution is equal to the FDM solution because the equally spaced and uniform distribution of the sampling points leads to the same weight coefficient obtained by eqn (13) as the FDM. When solving TE wave problems, the improved GFDM and GFDM have obvious advantages over FDM by virtue of the handing of Neumann boundary conditions. This is because FDM needs an extra layer of grid outside the boundary in order to deal with the Neumann BCs, and the value of these grids is equal to the function value of the nodes symmetrical to it in the boundary. This means that the nodes on the boundary must also be differentiated according to the governing equation, and this process produces additional errors. In addition, FDM needs to modify the difference formula to satisfy the boundary conditions, while the solution process of GFDM is more versatile.

Figure 4 shows the dispersion characteristics of TE_{10}, TE_{01}, and TM_{11} modes in rectangular waveguide by using GFDM and FDFD, respectively. The improved GFDM is not included in Figure 4 because it is almost equal to the GFDM solution, which can be seen from Figure 1. The eigenvalue equation of FDFD is derived from Maxwell's curl equations, where the eigenvalue and eigenvector expressions are β/k_0 and $[E_x, E_y, H_x, H_y]^{\mathrm{T}}$, respectively. This method cannot directly yield k_c for each mode, nor can it determine the wave transmission mode; so the results are given as scatter points. Since the eigenvector involves four field components, the correction of the FDFD difference formula at the boundary is more complicated than that of FDM, and it is necessary to consider both the Dirichlet BCs and the Neumann BCs. In addition, each discrete point of FDFD will produce two variables. Consequently, the size of the coefficient matrix obtained by FDFD is about $2N_I \times 2N_I$, and the size of GFDM is about $N_I \times N_I$. This means that using the same subdivision, GFDM saves memory space when compared against FDFD.

RBF is similar to GFDM, and both express the derivative at the center node by the weighted sum of the function values of each node in the point cluster. The size of the point cluster N_s in RBF needs to satisfy $N_s \gtrsim 2N_p$, where N_p is the number of polynomials included in the interpolation function, and the value of N_p is related to the highest degree d of the polynomial. For example, when d= 2, all polynomials are $\{1, x, y, x^2, y^2, xy\}$, the number of polynomials is $N_p = 6$, and RBF requires that the cluster size must satisfy $N_s \gtrsim 12$.

Take a circular waveguide with a radius of 1 mm as an example to compare the stability and accuracy of GFDM and RBF. The numbers of computational points inside the cross section and on the boundary are N_I= 305 and N_B= 50, and the cluster size is set to be 12. Figure 5 shows the relative error of the GFDM solution and RBF solution of the TE main mode and TM main mode in circular waveguide at different cluster sizes. If the relative error in the figure is on the dotted line, it means that the result is wrong. The improved GFDM result was not used for comparison because its cluster size was fixed to be 6. As the point cluster size changes, GFDM is significantly more stable and accurate than RBF. It is worth mentioning that although increasing the number of polynomials in RBF is beneficial to improving the performance of the method, it means that more

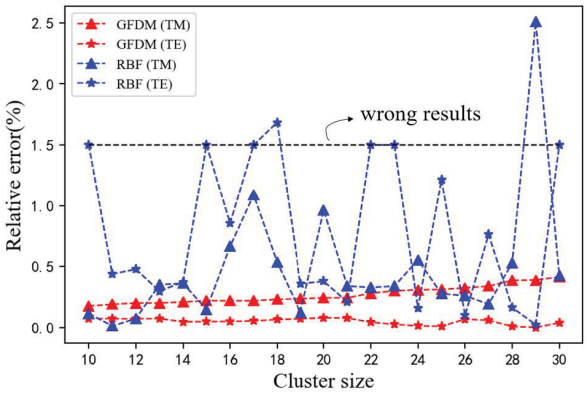

Fig. 5. Error comparison between the GFDM solution and the RBF solution of the cutoff wavenumbers of the TE main mode and TM main mode in the circular waveguide.

Table 1: Comparison of computer execution time in GFDM and RBF

Point cluster size	GFDM	RBF
12	0.3886 s	0.7555 s
20	0.4080 s	1.5053 s
30	0.4333 s	2.8191 s

adjacent nodes need to be found to represent the derivative, which will lead to a sharp increase in the amount of calculation. Table 1 gives the comparison of computer execution time between GFDM and RBF under the same sampling point and cluster size. As the number of adjacent points increases, that is, the size of the point cluster increases, the advantages of GFDM are more obvious. The main reason is that RBF needs to calculate the distance between each node in the point cluster and all remaining nodes, when calculating the weight coefficient, while GFDM only requires the distance between the central node and the adjacent nodes.

Finally, GFDM and an improved version of GFDM are used to solve the cutoff wavenumbers of an eccentric circular waveguide. Since the cross section of the waveguide is symmetrical about the x-axis, the odd and even modes can be solved separately. Figure 6 shows the distribution of computational nodes on the cross section of the eccentric circular waveguide when solving even TM modes. As shown in Table 2, the results of traditional GFDM and improved GFDM agree with the results given in [5].

Table 2: Normalized cutoff wavenumber for the first six even TM modes

Traditional GFDM	Improved GFDM	Method in [5]
4.8001	4.8016	4.8106
6.1505	6.1530	6.1724
7.3591	7.3646	7.3945
8.4473	8.4591	8.4974
9.2701	9.2776	9.3409
9.4048	9.4198	9.4739

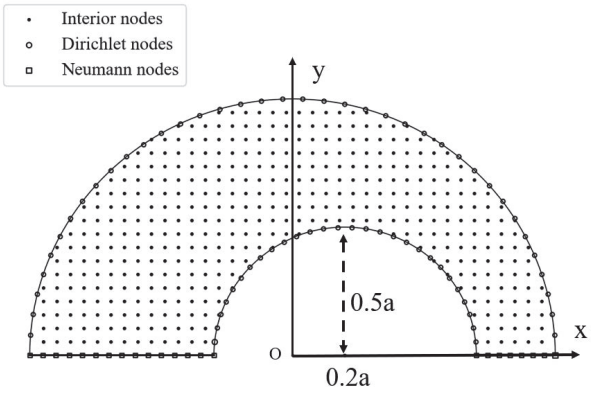

Fig. 6. The distribution of computational nodes on the cross-section of the eccentric circular waveguide when solving even TM modes. The outer and inner radii of the waveguide are a and 0.5a, respectively. The distance between the two circle centers is 0.2a.

IV. CONCLUSION

In this paper, the effectiveness of GFDM to solve the eigenvalue problem for the waveguide is verified. Compared with FDM and FDFD, GFDM avoids the complicated meshing process, and the difference formula is more versatile. What is more, GFDM owns the meshless feature to better handle Neumann boundary conditions. Compared with RBF, which is one of the meshless methods, GFDM has higher efficiency and better stability. GFDM provides a new idea and contributes significantly to solving the eigenvalue problems associated with waveguides.

V. ACKNOWLEDGMENT

This work was supported in part by the NUPTSF under Grant NY220074, by the National Nature Science Foundation of China for Youth under Grant 62001245, by the Natural Science Foundation of Jiangsu Province for Youth under Grant BK20200757, and by the State Key Laboratory of Millimeter Waves under Grant K202108. The authors are grateful to Prof. Ming Zhang for the useful discussions.

REFERENCES

[1] J. R. Pyle, "The cutoff wavelength of the TE_{10} mode in ridged rectangular waveguide of any aspect ratio," *IEEE Trans. Microw. Theory and Techn.*, vol. 14, no. 4, pp. 175-183, Apr. 1966.

[2] Y. J. Zhao, K. L. Wu, and K. Cheng, "A compact 2-D full-wave finite-difference frequency-domain method for general guided wave structures," *IEEE Trans. Microw. Theory and Techn*., vol. 50, no. 7, pp. 1844-1848, Jul. 2002.

[3] D. H. Chai, Harrington, and W. Hoefer, "The Finite-Difference-Time-Domain method and its application to eigenvalue problems," *IEEE Trans. Microw. Theory and Techn.*, vo. 34, no. 12, pp. 1464-1470, Dec. 1986.

[4] J. Svedin, "Propagation analysis of chirowaveguides using the finite-element method," *IEEE Trans. Microw. Theory and Techn*., vol. 38, no. 10, pp. 1488-1496, Oct. 1990.

[5] J. A. Pereda and A. Grande, "Analysis of homogeneous waveguides via the meshless radial basis Function-Generated-Finite-Difference method," *IEEE Micro. and Wirel. Compon. Lett*., vol. 30, no. 3, pp. 229-232, Mar. 2020.

[6] V. Lombardi, M. Bozzi, and L. Perregrini, "Evaluation of the dispersion diagram of inhomogeneous waveguides by the variational meshless method," *IEEE Trans. Microw. Theory and Techn*., vol. 67, no. 6, pp. 2105-2113, Jun. 2019.

[7] S. Yang, Z. Chen, and Y. Yu, "A Divergence-Free meshless method based on the vector basis function for transient electromagnetic analysis," *IEEE Trans. Microw. Theory and Techn*., vol. 62, no. 7, pp. 1409-1416, Jul. 2014.

[8] L. Gavete, M. L. Gavete, and J. J. Benito, "Improvements of generalized finite difference method and comparison with other meshless method," *Appl. Math. Model.*, vol. 27, no. 10, pp. 831-847, Oct. 2003.

[9] L. Gavete, F. Urena, and J. J. Benito, "Solving second order non-linear elliptic partial differential equations using generalized finite difference method," *J. Comput. Appl. Math*., vol. 318, pp. 378-387, Jul. 2017.

[10] J. J. Benito, and F. Urea, "An h-adaptive method in the generalized finite differences," *Comput. Meth. Appl. Mech. Eng*., vol. 192, no. 5-6, pp. 735-759, Jan. 2003.

[11] J. J. Benito, F. Urena, and L. Gavete, "Influence of several factors in the generalized finite difference method," *Appl. Math. Model*., vol. 25, no. 12, pp. 1039-1053, Dec. 2001.

[12] A. Kamyabi, V. Kermani, and M. Kamyabi, "Improvements to the meshless generalized finite difference method," *Eng. Anal. Bound. Elem*., vol. 99, pp. 233-243, Feb. 2019.

[13] P. W. Li and C. M. Fan, "Generalized finite difference method for two-dimensional shallow water equations," *Eng. Anal. Bound. Elem*., vol. 80, pp. 58-71, Jul. 2017.

[14] Y. Gu and L. Wang, "Application of the meshless generalized finite difference method to inverse heat source problems," *Int. J. Heat Mass Transf*., vol. 108, pp. 721-729, May 2017.

[15] T. Zhang, Y. F. Ren, C. M. Fan, and P. W. Li, "Simulation of two-dimensional sloshing phenomenon by generalized finite difference method," *Eng. Anal. Bound. Elem*., vol. 63, pp. 82-91, Feb. 2016.

[16] C. Jian, G. Yan, and M. Wang, "Application of the generalized finite difference method to three-dimensional transient electromagnetic problems," *Eng. Anal. Bound. Elem*., vol. 92, pp. 257-266, Jul. 2017.

[17] H. Xu, Y. C. Mei, and Y. Bao, "Application of generalized finite difference method in analysis of transmission characteristics of waveguide," *2020 APMC*., Hong Kong., China, pp. 785-787, 2020.

Hui Xu was born in Wuxi, Jiangsu, China. He received the B.Eng. degree from the Nanjing University of Posts and Telecommunications, Nanjing, China. He is currently working toward the M.S. degree with the School of Electronic and Optical Engineering, Nanjing University of Posts and Telecommunications.

His research interests include the electromagnetic field theory, electromagnetic engineering, and computer aided analysis and design.

Yang Bao was born in Nanjing, Jiangsu, China. He received the B.Eng. and M.S. degrees from the Nanjing University of Posts and Telecommunications, Nanjing, China, in 2011 and 2014, respectively, and the Ph.D. degree in electrical engineering from Iowa State University, Ames, IA, USA, in 2019.

In December 2019, he joined the Nanjing University of Posts and Telecommunications as an Assistant Professor with the School of Electronic and Optical Engineering. His research interests focus on modeling and simulations of composite material, electromagnetic wave scattering using fast algorithms, and eddy current nondestructive evaluation.

Pattern Reconstruction for Antennas with Characteristic Mode Analysis and Surrogate Model

Adem Yilmaz[1,2], Hulusi Acikgoz[1], and Alaa E. El-Rouby[2]

[1]Department of Electrical and Electronics Engineering,
KTO Karatay University, Konya, Turkey
adem.yilmaz@karatay.edu.tr, hulusi.acikgoz@karatay.edu.tr

[2]Department of Electrical and Electronics Engineering,
Ankara Yildirim Beyazit University, Ankara, Turkey
alaa.elrouby@ybu.edu.tr

Abstract **–** A novel approach is applied to obtain a desired pattern for a perfect electric plate with two ports. The location of ports is decided with the help of characteristic mode analysis. Two capacitive coupling elements are chosen to be used as excitation. The magnitude and phase of each excitation are obtained by the Bayesian inference method. In order to avoid complexity of computational design, a surrogate model, which is based on polynomial chaos expansion, is built. The surrogate model is ensured to mimic the computational model over 90%. Then, the desired pattern is compared with the synthesized one, and it is seen that the two patterns fit very well to each other and the correlation between the two patterns is above 0.9.

Index Terms **–** Bayesian inference, characteristic mode analysis, pattern synthesis, polynomial chaos expansion.

I. INTRODUCTION

Pattern synthesis has been applied extensively in antenna designs lately since it enhances the performance of the overall antenna system. Traditionally, phased array antennas have been used for this purpose by varying the phase and magnitude of each antenna element [1–3]. However, if one wants to obtain a pattern synthesis within a single antenna, it is challenging since there is only one radiator. However, some literature succeeded to obtain pattern synthesis with an electrically large single antenna, such as reflector antennas [4], leaky wave antennas [5], and horn antennas [6]. On the other hand, there are few studies that synthesize a pattern within a single antenna, namely a conducting plate.

Characteristic mode analysis (CMA) is one of the useful methods to synthesize a desired pattern for a single antenna. In CMA, unique features of scattering and radiation properties can be revealed for any conductive body of arbitrary shape without any excitation [7–10]. Characteristic modes (CMs) are the real current modes that can be numerically computed. Since CMs form a set of orthogonal functions, the total current on the surface of the body is a linear superposition of the CMs. In CMA, the far-field of each mode is also orthogonal to each other. Hence, the desired pattern is the selective excitation of each CM [12]. In order to properly excite the desired CM, capacitive coupling elements (CCEs) and inductive coupling elements (ICEs) can take place in antenna design without any alteration of CMs [13, 14]. Moreover, the desired pattern construction does not only depend on the selection of the coupling element's type and location, but it also depends on the excitation scheme, i.e., magnitude and phase of each coupling element. Thus, there are some literature papers that investigate to obtain the proper excitation scheme to excite the desired modes and, hence, to obtain the desired pattern. In [15], a multiobjective optimization method is applied to electrically small unmanned aerial vehicle (UAV) and high frequency band antennas for shipboard structures to obtain the desired pattern. In [16], a desired up-tilted beam is achieved by using random search optimization of phases. In [17], the asymmetric CM excitation is observed to obtain a null of an antenna pattern for two ports, and in [18], a linear equation solution is given considering the phase and magnitude of excitation. In [19], a compress sensing algorithm is provided for the desired pattern.

This paper proposes a novel approach to obtain the proper excitation scheme for a desired pattern within a single antenna. The approach is based on the Bayesian inversion that provides the statistical inference of unknown input parameters. The Bayesian inference has already been applied to linear antenna array [20, 21]. However, this paper considers a single antenna, where the main aim is to prove the applicability of the proposed method. The Bayesian framework offers

Submitted On: September 20, 2021
Accepted On: March 17, 2022

https://doi.org/10.13052/2022.ACES.J.370303

an input parameter quantification based on the measured/computed data in the manner of an inverse problem solving [22]. Indeed, the Bayesian inference method gives a posterior probability distribution over the input with repeated solutions of the forward model. For this purpose, the sampling approach, such as Markov chain Monte Carlo (MCMC) [23], of the input parameters have to be applied at every repeated step during the inverse solution. However, this cannot be affordable when the forward model is computationally expensive. In order to apply Bayesian inference to such a computational design, a surrogate model can be built as a forward model. A surrogate model [24], which is also called metamodel, is a replacement of the high-fidelity computational model with a more efficient surrogate one to avoid the computational burden while studying prediction, optimization, sensitivity analysis, and uncertainty analysis. There are different types of technique that builds surrogate model, such as polynomial chaos expansion (PCE) [25–28], artificial neural networks [29], Gaussian process (Kriging modeling) [30], support vector machines [31], etc. Among them, PCE is chosen in this work due to its advantages such as interpretation and versatility [32]. It has been applied in computational electromagnetic in various areas [33–37]. The PCE depends on three main processes: a random sampling of each input parameter, propagation of such random inputs through the computational model, and then obtention of the random outputs. With input and output data at hand, a model based on the polynomial series can be built. Within a surrogate model, the Bayesian inference can be applicable to complex computational models; hence, one can obtain the values of the excitation scheme for the desired pattern in a single antenna. The organization of this paper is as follows: a brief overview of CMA is given in Section II, and Bayesian inference and PCE are introduced in Section III. The application of the proposed method and the results are given in Section IV. Final conclusions are given in Section V.

II. CHARACTERISTIC MODE ANALYSIS

CMA provides the inherent current modes without any excitation and the total current distribution (J_{tot}) is calculated by the sum of orthogonal current modes (J_n)

$$J_{\text{tot}} = \sum_n \alpha_n J_n \,, \tag{1}$$

where α_n are called modal weighting coefficients (MWC), and they are related to the current modes J_n. J_n are natural current distributions that do not depend on the excitation. On the contrary, MWCs are strongly dependent on the excitation; thus, the desired current distribution on the structure under consideration is dependent on the selective excitation of the modes. In order to excite the desired modes properly, the locations of the external excitation source (port) should be carefully investigated.

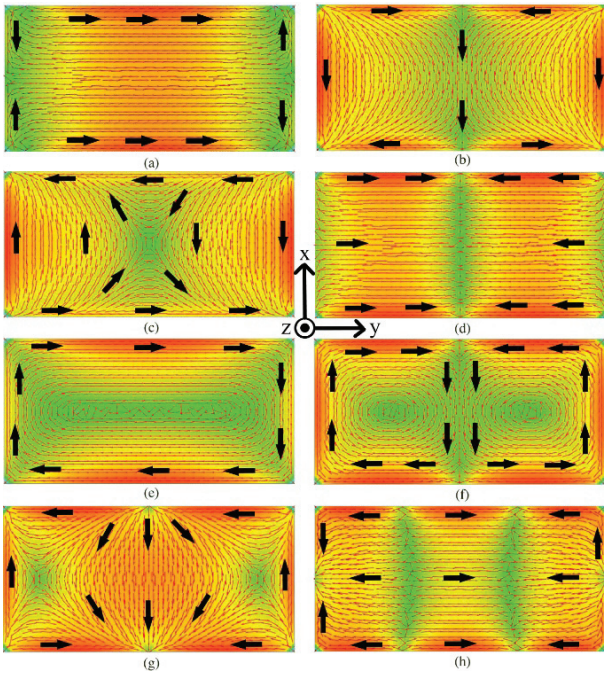

Fig. 1. Current distribution on the conducting plate related to the number of modes (a) 1, (b) 2, (c) 3, (d) 4, (e) 5, (f) 6, (g) 7, and (h) 8 (arrows indicate the direction of current).

In this paper, a conducting plate with dimensions of 150×75 mm^2 is considered to obtain a desired pattern. One of the possible patterns that can be obtained by a PEC plate is a null pattern on the upper half of the plate, which has been successfully achieved in [17], where asymmetric excitation of the phase of the ports are considered and null patterns are obtained between -30° and 30°. In order to determine the location of the ports for a desired null pattern, the current distribution of the first eight modes is investigated with CMA and the results are illustrated in Figure 1. The location of ports can be determined with the current or electric field maxima of each mode. A desired mode can be excited by placing a CCE at a current minimum or placing an ICE at a current maximum [14]. One can see from Figure 1 that mode 1, mode 4, and mode 8 can be properly excited by locating the CCE in the middle of the short edges, where the current is minimum, i.e., the maximum of E-field. Similarly, CCE can be placed in the middle of the long edges to excite mode 2, mode 4, and mode 7. Since the current distributions of mode 4 and mode 8 are mostly along the y-direction, it is possible to obtain a null pattern on the upper half of plate. For that reason, these two modes are desired to be excited by placing CCE at the minimum current distribution, i.e., at the middle of the short edges. The overall structure with

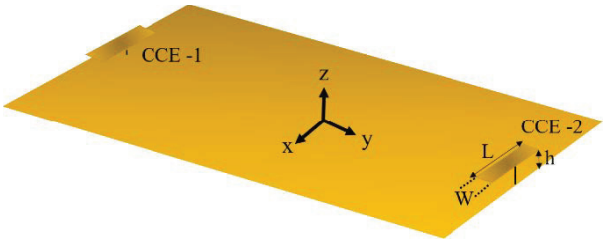

Fig. 2. Overall structure with two CCE ports (L = 25.5 mm, W = 9.5 mm, and h = 4 mm).

two CCE ports is illustrated in Figure 2. Once the locations of the excitation (two CCE ports) are determined with the help of CMA, the phase and magnitude of ports should be specified for a desired pattern. In this work, this is achieved with a surrogate model and Bayesian inversion.

III. POLYNOMIAL CHAOS EXPANSION AND BAYESIAN INFERENCE

A. Polynomial chaos expansion

PCE can be used to build a surrogate model which substitutes the computationally expensive models with an easy to work surrogate model. In PCE, the response of the system (Y) is computed by the independent input parameters of (X) and the polynomial expansion for building the surrogate model is given by

$$Y = \sum_{\alpha \in N^m} y_\alpha \, \psi_\alpha(X), \tag{2}$$

where the $\psi_\alpha(X)$ are the multivariate polynomials, α are the multi-indices that identify the components of $\psi_\alpha(X)$, and y_α are the expansion coefficients to be determined. There are two main approaches to compute the expansion coefficients: intrusive and non-intrusive methods. The former indicates the modification of the underlying code of the computational model, while the latter one considers the computational model as a black box; thus, one does not need to modify the code to build the model. The least-squares minimization is one of the strategies that compute the expansion coefficients non-intrusively. In practice, the infinite sum in eqn (2) needs to be truncated to a finite sum for the computational purpose. In PCE, the number of polynomial basis P is calculated as

$$P = \begin{pmatrix} M+p \\ p \end{pmatrix}, \tag{3}$$

where M is the number of input variables and p is the degree of the polynomial. One can understand from eqn (3) that if the input parameters are high and/or the degree of the polynomial are set to a high degree to ensure the accuracy of the surrogate model, then a large number of polynomials have to be taken into account. To avoid working with the high-dimensional polynomial basis, the least angle regression selection (LARS) algorithm can be applied to reduce the number of polynomial bases. There are two main ways to estimate the error between the computational model and the surrogate model. The normalized empirical error is a generalization error based on the accuracy with which the surrogate model reproduces the computational model evaluations. However, it is also well-known that if the polynomial model is too complex, an overfitting problem may occur. In order to overcome this problem, the leave-one-out cross-validation (error_{LOO}) technique is usually performed as an alternative way.

B. Bayesian inference

Bayesian inference is one of the statistical inference methods that are based on the Bayes' rule. In this method, the unknown parameters of the prior probability density function (PDF) are inferenced by integrating prior information and the observations through the inference of the posterior as

$$p(\boldsymbol{x} \mid \boldsymbol{y}) = \frac{p(\boldsymbol{y} \mid \boldsymbol{x}) \; p(\boldsymbol{x})}{p(\boldsymbol{y})}, \tag{4}$$

where $\boldsymbol{x}$ is the parameter vector to be inferenced, $\boldsymbol{y}$ is the observation, $p(\boldsymbol{x})$ is the prior probability, $p(\boldsymbol{y})$ is the marginal distribution and usually a normalized constant, and $p(\boldsymbol{y} \mid \boldsymbol{x})$ is the likelihood function, which measure the fitness between predictions and observations. Once the posterior distribution is obtained, then one can select a point from this distribution to identify the unknown parameter. One of the choices is the posterior mean which is the mean value of the posterior distribution. Another choice is the posterior mode which is also known as the maximum *a posteriori* (MAP) and given as $\text{MAP}(x) = \text{argmax}_x p(\boldsymbol{x} \mid \boldsymbol{y})$. In this inverse procedure, however, there is no closed-form solution to obtain posterior distribution. One of the well-known methods to compute the inverse solution is based on MCMC sampling technique. The basic idea of MCMC technique is to construct Markov chains that are guaranteed to produce samples distributed according to the posterior distribution. The theoretical background of the PCE and Bayesian inference are far beyond the scope of this paper. For more information on these topics, one can see the reports [38, 39] and the references therein.

IV. APPLICATION AND RESULTS

A. Pattern synthesis with two CCE ports

In order to obtain a proper excitation scheme for the desired pattern, a general framework in this study is given in Figure 3 and summarized as following steps:

1) CMA is applied to the structure under consideration. The current distribution of each mode is investigated. The locations of ports are identified. Then, the computational model, including ports, is constructed.

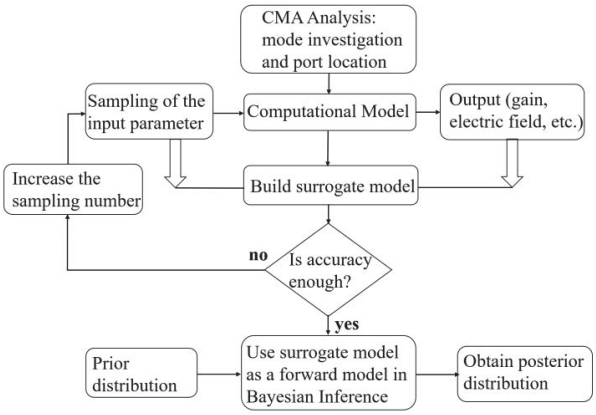

Fig. 3. Proposed procedure for obtaining desired pattern.

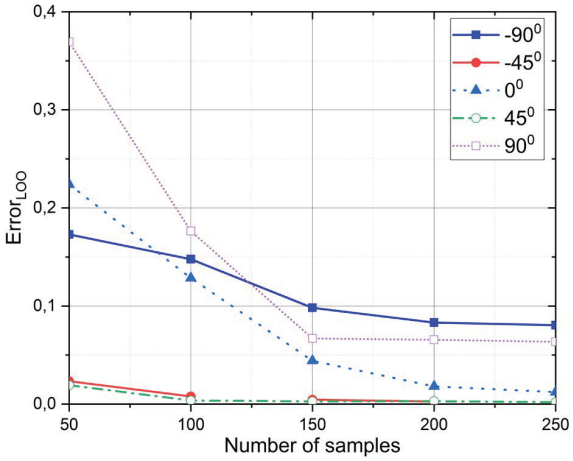

Fig. 4. Error variation while increasing sample number.

2) Random sampling of input parameters (phase and magnitude of each port) is performed. Then, the random samples are propagated through the computational model. The output values of the overall structure, such as gain, total electric field, etc., are obtained for each random input.
3) The inputs/outputs set given by the computational model is presented to the PCE to build a surrogate model. The accuracy of the surrogate model is investigated to ensure that the surrogate model mimics the computational model successfully.
4) The surrogate model is given to the Bayesian scheme a forward model. Prior distribution is chosen to be consistent with the random sampling range. Posterior distribution is obtained for the desired pattern.
5) Post-processing on the results of Bayesian inference is performed. The MAP is applied to choose the best candidate for input parameters.

As discussed in Section II, the main aim in this work is to obtain a null pattern at the upper hemisphere of the plate, and to achieve that purpose, the first step stated in Figure 3 is accomplished in Section II. In the next step, the phase and magnitude of each CCE ports are randomly and independently sampled between allowable regions, i.e., $[-180^\circ, 180^\circ]$ and [0, 1 V], respectively, to build a surrogate model. The sampled input is given to the computational model and the output, namely total normalized electric field, of each sample is obtained by method of moments. The number of samples is increased step by step to ensure that the sample number is adequate for an accurate model. As mentioned in Section III, the error_{LOO} is the quantification of how well the surrogate model mimics the computational model. So, at each increased step, a surrogate model is built and the error_{LOO} is examined. In Figure 4, five elevation angles are chosen to explore the effect of increased sample number on error_{LOO}. One can say that the 150 samples are sufficient to build relatively accurate model since the error_{LOO} does not decrease further. This finding is also observed for all elevation angles. Moreover, the total error_{LOO} for all elevation angles is illustrated in Figure 5 for chosen 150 sample numbers. One can keep in mind that increasing the number of samples will bring a computational burden; hence, the number of samples is kept as 150 in this work.

Once the surrogate model is built and the accuracy of the model is ensured, it is conveyed to the Bayesian framework as a forward model. Since the input parameters do not follow any specific distribution, the prior distributions in Bayesian inference are given as a uniform distribution between the $[-180^\circ, 180^\circ]$ for phases and [0, 1 V] for magnitudes. The posterior distribution in Bayesian inference is obtained for the

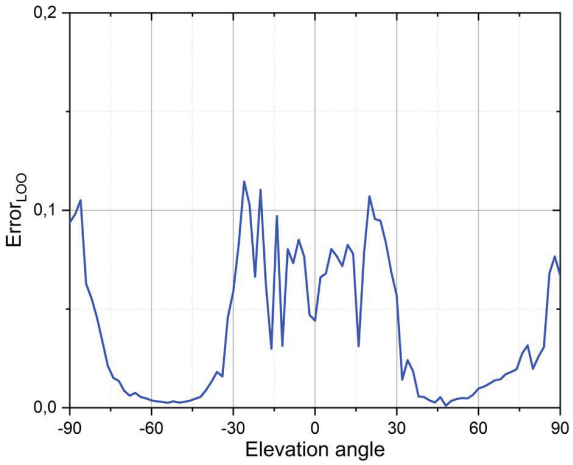

Fig. 5. Error for all elevation angles with 150 sample numbers.

Table 1: The excitation scheme for two cases

		Phase (degree)		Magnitude (volts)	
		Case 1	Case 2	Case 1	Case 2
Des.	Port 1	45	−90	0.5	0.75
	Port 2	45	90	0.5	0.75
Syn.	Port 1	−93	−98	0.51	0.69
	Port 2	−78	93	0.53	0.69

desired pattern. In this work, the null patterns at various elevation angles between $[-30^\circ,\ 30^\circ]$ are considered as the desired pattern. For illustration purpose, two cases are taken into consideration: case 1 is a desired pattern with a null at 0° and case 2 is a desired pattern with two nulls at around $-30^\circ,\ 30^\circ$. Then, the Bayesian framework is conducted, and the results are examined. The mode of each output distribution is chosen as the best candidate for phases and magnitudes. As a final step, the results obtained from Bayesian inference are given to the computational model to compare the desired pattern with the synthesized one given by the forward computational model. The excitation scheme of ports for two cases is given in Table 1. One can keep in mind that the structure under consideration exhibits repetitive pattern that depends on the phase differences between two ports. For that reason, the desired phase difference is achieved with different phase values in case 1. In Figure 6, one can say that the Bayesian framework works well to identify the magnitude and phase of ports in a single antenna for obtaining a desired pattern. Moreover, the correlations between desired and synthesized patterns are 0.9389 for case 1 and 0.9717 case 2, which indicates that the two patterns fit very well [12, 14].

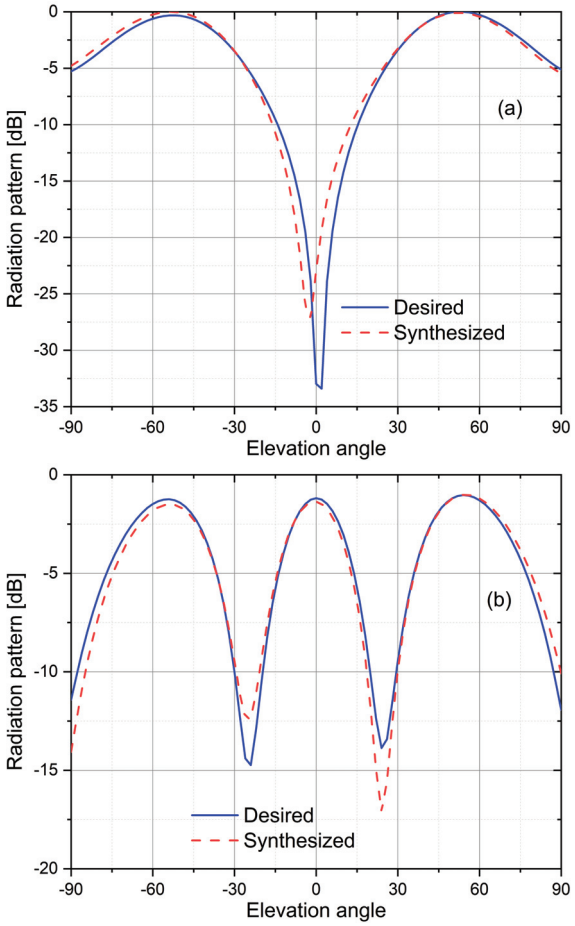

Fig. 6. Desired and synthesized patterns. (a) Case 1. (b) Case 2.

B. CCE port design

The dimensions of CCE ports are selected to have an input impedance to have only real part of impedance at the operating frequency. For this purpose, the procedure for obtaining a desired pattern given in Figure 3 is also applied to choose the dimension of the CCE ports. In this case, the input parameters for Bayesian framework are the dimensions of the CCE ports. The varied dimensions of CCE ports are length, width, and the height of the CCE from the PEC plate (see Figure 2).

Each input parameter is randomly sampled between the ranges given in Table 2. The limits of ranges are deliberately chosen to be comparable with practical application purposes. A surrogate model is built with 100 random samples of each input parameter, and it is conveyed to Bayesian framework as a forward model. A desired distribution, which mimics a real input impedance value, is given in Bayesian inference. The MAP is applied on the results of the Bayesian inference, and it is obtained that the length $L = 25.5$ mm, the width $W = 9.5$ mm, and the height $h = 4$ mm are the best candidates for a nearly zero imaginary part of the impedance. The CCE ports are designed with obtained values, and both real and imaginary parts of port impedances are illustrated in Figure 7. One can say that the imaginary

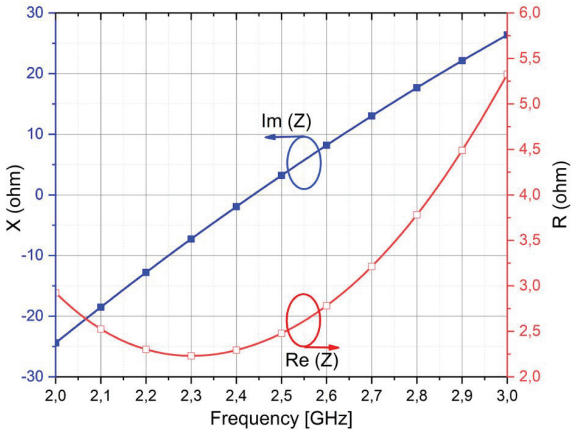

Fig. 7. Real and imaginary impedances.

Table 2: CCE port dimensions (in mm)

Length	Width	Height
[5–65]	[2–15]	[4–10]

part of the impedance is nearly zero at operating frequency while real part is at around 2.5 Ω. For practical application purposes, this real impedance can be easily matched to 50Ω by an impedance matching circuit.

V. CONCLUSION

A procedure for pattern synthesis for an antenna is proposed. The procedure is based on two main theories: CMA and Bayesian inference. The CMA has been applied to identify the locations of ports. Two CCE ports are properly placed on conducting plate. To avoid the computational complexity, a surrogate model is built with PCE. The surrogate model is used as a forward model in Bayesian inference to efficiently obtain the unknown input parameters for a desired pattern. Two desired patterns that exhibit nulls at upper hemisphere of the plate are achieved by the proposed procedure with good agreement. The proposed procedure can be applied to more complex computational models, which remain as future works.

REFERENCES

[1] D. W. Boeringer and D. H. Werner, "Particle swarm optimization versus genetic algorithms for phased array synthesis," *IEEE Trans. Antennas Propag.*, vol. 52, no. 3, 2004.

[2] K. K. Yan and Y. Lu, "Sidelobe reduction in array-pattern synthesis using genetic algorithm," *IEEE IEEE Trans. Antennas Propag.*, vol. 45, no. 7, 1997.

[3] H. Lebret and S. Boyd, "Antenna array pattern synthesis via convex optimization," *IEEE Trans. Signal Process.*, vol. 45, no. 3, 1997.

[4] A. Foudazi and A. R. Mallahzadeh, "Pattern synthesis for multi-feed reflector antennas using invasive weed optimisation," *IET Microw. Antennas Propag.*, vol. 6, no. 14, 2012.

[5] J. L. Gomez-Tornero, A. J. Martinez-Ros, and R. Verdu-Monedero, "FFT synthesis of radiation patterns with wide nulls using tapered leaky-wave antennas," *IEEE Antennas Wirel. Propag. Lett.*, vol. 9, 2010.

[6] M. A. Moharram and A. A. Kishk, "Optimum feeds for reflectarray antenna: synthesis and design," *IEEE Trans. Antennas Propag.*, vol. 64, no. 2, 2016.

[7] R. Garbacz and R. Turpin, "A generalized expansion for radiated and scattered fields," *IEEE Trans. Antennas Propag.*, vol. 19, no. 3, pp. 348-358, 1971.

[8] R. F. Harrington and J. R. Mautz, "Theory of characteristic modes for conducting bodies," *IEEE Trans. Antennas Propag.*, vol. 19, no. 5, pp. 622-628, 1971.

[9] R. Harrington and J. Mautz, "Computation of characteristic modes for conducting bodies," *IEEE Trans. Antennas Propag.*, vol. 19, no. 5, pp. 629-639, 1971.

[10] A. Araghi and G. Dadashzadeh, "Detail-oriented design of a dual-mode antenna with orthogonal radiation patterns utilizing theory of characteristic modes," *Applied Computational Electromagnetics Society (ACES) Journal*, vol. 28, no. 10, pp. 952-959, 2013.

[11] N. Michishita and H. Morishita, "Helmet antenna design using characteristic mode analysis," *Applied Computational Electromagnetics Society (ACES) Journal*, vol. 35, no. 2, pp. 161-166, 2020.

[12] E. Safin and D. Manteuffel, "Reconstruction of the characteristic modes on an antenna based on the radiated far field," *IEEE Trans. Antennas Propag.*, vol. 61, no. 6, pp. 2964-2971, 2013.

[13] R. Valkonen, A. Lehtovuori, and D. Manteuffel, "Capacitive coupling elements - Changing the way of designing antennas," in *The 8th European Conference on Antennas and Propagation (EuCAP 2014)*, no. EuCAP, pp. 229-233, Apr. 2014.

[14] D. Manteuffel and R. Martens, "Systematic design method of a mobile multiple antenna system using the theory of characteristic modes," *IET Microw., Antennas Propag.*, vol. 8, no. 12, pp. 887-893, 2014.

[15] Y. Chen and C.-F. Wang, "HF band shipboard antenna design using characteristic modes," *IEEE Trans. Antennas Propag.*, vol. 63, no. 3, pp. 1004-1013, 2015.

[16] Z. Liang, J. Ouyang, F. Yang, and L. Zhou, "Design of license plate rfid tag antenna using characteristic mode pattern synthesis," *IEEE Trans. Antennas Propag.*, vol. 65, no. 10, pp. 4964-4970, 2017.

[17] F. A. Dicandia, S. Genovesi, and A. Monorchio, "Null-steering antenna design using phase-shifted characteristic modes," *IEEE Trans. Antennas Propag.*, vol. 64, no. 7, pp. 2698-2706, 2016.

[18] F. A. Dicandia, S. Genovesi, and A. Monorchio, "Advantageous exploitation of characteristic modes analysis for the design of 3-D null-scanning antennas," *IEEE Trans. Antennas Propag.*, vol. 65, no. 8, pp. 3924-3934, 2017.

[19] H. Li, S. Sun, W. Li, M. Wu, and C. Zhou, "Systematic pattern synthesis for single antennas using characteristic mode analysis," *IEEE Trans. Antennas Propag.*, vol. 68, no. 7, pp. 5199-5208, 2020.

[20] C. Y. Chan and P. M. Goggans, "Using Bayesian inference for linear antenna array design," *IEEE Trans. Antennas Propag.*, vol. 59, no. 9, 2011.

[21] C. Y. Chan and P. M. Goggans, "Multiobjective design of linear antenna arrays using bayesian inference framework," *IEEE Trans. Antennas Propag.*, vol. 62, no. 11, 2014.
[22] A. Gelman, J. B. Carlin, H. S. Stern, D. B. Dunson, A. Vehtari, and D. B. Rubin, *Bayesian Data Analysis, Third Edition*, 2013.
[23] G. C. Christian P. Robert, *Monte Carlo Statistical Methods - 2nd Edition*, vol. 109, no. 1, 2004.
[24] R. W. Blanning, "The construction and implementation of metamodels," *SIMULATION*, vol. 24, no. 6, pp. 177-184, 1975.
[25] B. Sudret, "Uncertainty propagation and sensitivity analysis in mechanical models – Contributions to structural reliability and stochastic spectral methods," Habilitation à diriger des recherches, Université Blaise Pascal, Clermont-Ferrand, France , 2007.
[26] B. Sudret, "Global sensitivity analysis using polynomial chaos expansions," *Reliab. Eng. Sys. Safety*, vol. 93, no. 7, pp. 946-979, 2008.
[27] K. Sepahvand, S. Marburg, and H. J. Hardtke, "Uncertainty quantification in stochastic systems using polynomial chaos expansion," *Int. J. Appl. Mech.*, vol. 2, no. 2, 2010.
[28] P. Kersaudy, S. Mostarshedi, B. Sudret, O. Picon, and J. Wiart, "Stochastic analysis of scattered field by building facades using polynomial chaos," *IEEE Trans. Antennas Propag.*, vol. 62, no. 12, 2014.
[29] D. J. C. MacKay, "Bayesian methods for adaptive models," Computation and Neural Systems, California Institute of Technology, Pasadena, CA, 1991.
[30] J. P. C. Kleijnen, "Kriging metamodeling in simulation: A review," *Eur. J. Oper. Res.*, vol. 192, no. 3. 2009.
[31] X. Zhang, R. Srinivasan, and M. van Liew, "Approximating SWAT model using artificial neural network and support vector machine," *J. Am. Water Resour. Assoc.*, vol. 45, no. 2, 2009.
[32] Z. Liu, D. Lesselier, B. Sudret, and J. Wiart, "Surrogate modeling based on resampled polynomial chaos expansions," *Reliab. Eng. Sys. Safety,* vol. 202, p. 107008, Oct. 2020.
[33] F. Boeykens, H. Rogier, and L. Vallozzi, "An efficient technique based on polynomial chaos to model the uncertainty in the resonance frequency of textile antennas due to bending," *IEEE Trans. Antennas Propag.*, vol. 62, no. 3, 2014.
[34] H. Acikgoz and R. Mittra, "Stochastic polynomial chaos expansion analysis of a split-ring resonator at terahertz frequencies," *IEEE Trans. Antennas Propag.*, vol. 66, no. 4, 2018.
[35] C. Chauvière, J. S. Hesthaven, and L. Lurati, "Computational modeling of uncertainty in time-domain electromagnetics," *SIAM J. Sci. Comput.*, vol. 28, no. 2, 2006.
[36] H. Acikgoz, R. K. Arya, and R. Mittra, "Statistical analysis of 3D-printed flat GRIN lenses," in *2016 IEEE International Symposium on Antennas and Propagation (APSURSI)*, pp. 473-474, Jun. 2016.
[37] H. Acikgoz, R. K. Arya, J. Wiart, and R. Mittra, "Statistical electromagnetics for antennas," in *Developments in Antenna Analysis and Design: Volume 2*, Institution of Engineering and Technology, pp. 259-286, 2018.
[38] S. Marelli and B. Sudret, "UQLab user manual – Polynomial chaos expansions," 2019.
[39] P.-R. Wagner, J. Nagel, S. Marelli, and B. Sudret, "UQLab user manual – Bayesian inversion for model calibration and validation," ETH Zurich, 2021.

Adem Yilmaz received the B.S. and M.S. degrees in electrical and electronics engineering from the University of Gaziantep and Ankara Yildirim Beyazit University, respectively. He is currently working toward the Ph.D. degree with Ankara Yildirim Beyazit University, Turkey.

From 2010 to 2011, he was a Researcher with Goethe Frankfurt University, Germany. Since 2011, he has been a Research Assistant with KTO Karatay University. His research interests include computational electromagnetics, the theory of characteristic modes, and design and characterization of periodic structures.

Hulusi Acikgoz received the B.S. and master's degrees in applied physics from Marne-La-Vallée University, France, and the Ph.D. degree in electrical engineering from Pierre and Marie Curie University, Paris, France, in 2008.

He has been a Teaching Assistant with UPMC-Paris IV from 2009 to 2010. After a year of post-doctoral research at L2E (Laboratoire d'Electronique et d'Electromagn Supétisme) in computational electromagnetic dosimetry, he joined KTO Karatay University, Konya, Turkey, in 2011, as an Associate Professor. His research interests include microwave characterization of dielectric materials, electromagnetic dosimetry, homogenization, antennas for microwave cancer ablation, high impedance surfaces, graphene applications in EM, and statistical analysis of EM structures.

Alaa E. El-Rouby received the B.Sc. and M.Sc. degrees from Cairo University, Egypt, in 1993 and 1996, respectively, and the Ph.D. degree from the University of Michigan, Ann Arbor, MI, USA, in 2000, all in electrical engineering.

He started his academic career as an Assistant Professor, and he was then an Associate Professor with Cairo University till 2014. He then moved to Yildirim Beyazit University, where he is currently a Professor. Dr. Elrouby had a strong connection with semiconductor industry through working for Intel Corp. and then for Mentor Graphics for over 14 years. Since 2015, he has been working as a consultant for RF/MW, antenna, GNSS, PCB, and signal and power integrity, which are his current research interests as well.

Gain-Enhanced Wideband Circularly Polarized Antenna with a Non-Uniform Metamaterial Reflector

Bosong Qiu[1], Yinfeng Xia[1], and Yingsong Li[2]

[1]Department of Information and Communication Engineering,
Harbin Engineering University, Harbin 150009, China

[2]Key Laboratory of Intelligent Computing and Signal Processing Ministry of Education,
Anhui University, Hefei 230601, China
liyingsong@ieee.org

***Abstract* –** In this paper, a gain-enhanced wideband circularly polarized (CP) antenna with a non-uniform metamaterial (NUM) reflector is presented, which is composed of a modified wide S-shaped slot antenna and a NUM reflector. To achieve a wideband CP operation, a modified S-shaped slot is fed by an L-shaped microstrip feedline that ends with a triangular patch to improve axial ratio (AR) bandwidth and impedance bandwidth. A NUM reflector composed of rectangular metal units with different sizes is employed and its units are unevenly distributed. The proposed CP antenna is designed, fabricated, and measured. The measured results show that the impedance bandwidth covers 3.0-6.0 GHz (66.7%) and a 3-dB AR bandwidth covers 3.1-5.6 GHz (57.4%). A peak gain of 6.0 dBi is obtained at 3.8 GHz by using the reflector. The advantages of the proposed antenna are the simple structure, high gain, and broad CP bandwidth.

***Index Terms* –** Circular polarization, gain enhancement, broadband antenna, non-uniform metamaterial reflector

I. INTRODUCTION

With the rapid development of wireless communication, circularly polarized (CP) antennas play important roles in creating high-performance communication systems due to the superiorities of overcoming polarization mismatch, immunity to the Faraday rotation, and suppressing multipath [1–11]. To enhance the capacity of wireless communication systems, wideband CP antennas are good candidate for transmitting and receiving signal, which becomes an attractive option. However, wide axial ratio (AR) bandwidth and high gain are quite challenging directions for CP antenna designs.

To realize wideband CP operation, a variety of structures and methods have been proposed in the past few years. In [12-14], wide slots fed by L-shaped microstrip and co-planar waveguide (CPW) are utilized to realize wide AR bandwidth. The complementary split ring resonator (CSRR) structure is loaded on the L-shaped feeding structure to further expand the AR bandwidth [15]. Furthermore, modified trapezoid and inverted L-shaped strip structures are introduced to the antenna [16, 17] to achieve 92% and 56.4% AR bandwidths, respectively. L-shaped structure expands AR bandwidth at the expense of the radiation pattern stability, which leads to the radiation pattern tilted with frequency increment. Antennas [18, 19] expend the AR bandwidth by using defective square rings, which provide an additional CP operation band. However, the antennas mentioned above suffer from low gain caused by bidirectional radiation patterns, limiting their application such as long-distance communication. Additionally, feeding network with power divider and phase shifter to provide constant phase difference is also employed in antennas [20–23] to achieve wideband CP operation. The feeding network significantly increases the size of the antenna compared to a single-fed antenna. Moreover, cross-dipole antennas fed by a quarter of microstrip ring are proposed in [24] and [25], and parasitic elements are introduced to expand AR bandwidth. Recently, metamaterial technique is also a good choice to improve CP bandwidth. For antennas [26–29], electromagnetic bandgap (EBG), high-impedance surface (HIS) [27], and artificial magnetic conductor (AMC) [28, 29] are utilized to enhance gain over the operating band. Besides, the metal cavity is placed under the aperture antenna [30, 31] to alleviate the undesirable back radiation, which also improves the gain of the antenna. However, all of these antennas have the disadvantage of being difficult to install and complex in geometry.

In this paper, a wideband CP antenna with a non-uniform metamaterial (NUM) reflector is proposed. To achieve wide AR bandwidth, a modified S-shaped slot is etched on the ground and an L-shaped microstrip line is used to feed the developed CP antenna. Diagonally distributed cutting corners are also employed in the

Submitted On: September 30, 2021
Accepted On: March 14, 2022

https://doi.org/10.13052/2022.ACES.J.370304

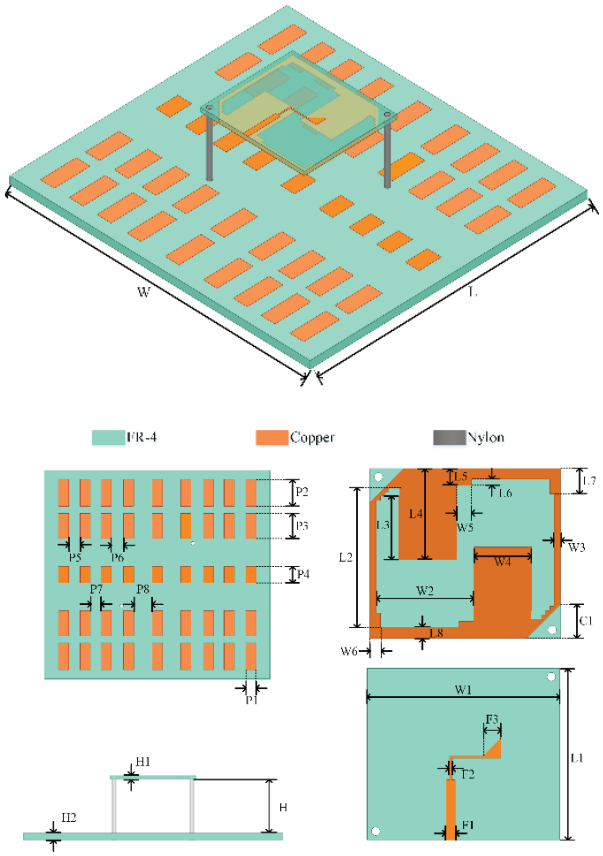

Fig. 1. Configuration of the proposed antenna.

developed antenna. A NUM reflector is placed under the slot antenna to enhance the gain in the boresight direction while maintaining wide AR bandwidth. The proposed broadband CP antenna is simulated, optimized, fabricated, and measured, and the results show that the NUM reflector-backed S-shaped slot antenna achieves an impedance bandwidth of 66.7% (3.0-6.0 GHz), a wide CP bandwidth of 57.4% (3.1-5.6 GHz), and more than 3 dBi gain enhancement is obtained over the operating band.

II. ANTENNA DESIGN

A. Wideband CP S-shaped slot antenna design

As shown in Figure 1, the proposed CP antenna is designed on FR-4 substrate (ε_r = 4.4; tanδ = 0.02) with substrate thicknesses of H1. The modified S-shaped slot and inverse L-shaped feeding stub are utilized in the upper of the antenna to generate CP characteristics. Stepped structures on the edge of the wide slot extend the path of the current, improving impedance matching and achieving CP operation at lower frequencies. By cutting two corners symmetrically on the diagonal, the antenna radiates CP waves at a higher frequency. The S-shaped slot structure is symmetrical about the center

Table 1: Parameters of the proposed antenna (unit: mm)

Param.	Size	Param.	Size	Param.	Size
W	130	L	120	H	23.8
H1	1.6	P1	6	P2	15.5
P3	14.5	P4	9.5	P5	6.5
P6	7	P7	6	P8	10.5
F1	2.1	F2	0.5	F3	4
W1	45	W2	23	W3	1.5
W4	13.7	W5	3.5	W6	2.5
L1	40	L2	32.9	L3	14.9
L4	21.5	L5	4	L6	1.5
L7	6	L8	2.5	C1	8

of the antenna, effectively overcoming the drawbacks of the beam tilted with frequency increments. Moreover, an inverted L-shaped strip is employed to connect with the end of the 50-Ω feedline and the modified triangle patch to obtain broadband property. The triangular patch is designed to excite two mutually orthogonal modes with equal magnitude.

B. Non-uniform metamaterial reflector

Although the S-shaped slot antenna has obtained good CP performance, the gain of right-hand circular polarization (RHCP) in broadside direction is low due to bidirectional radiation pattern, which limits its application. To increase the gain of the antenna, a NUM reflector is placed underneath the slot antenna with a distance of H. The upper and lower substrates are supported by nylon cylinder. The reflector is also designed on FR-4 with substrate thicknesses of H2. The reflector consists of 9 × 5 metal cells of different sizes, and the spacing of the metal cells and their dimensions are shown in Figure 1 and Table 1. With unevenly distributed metal cells, the NUM reflector acts as a perfect magnetic conductor and reflects the backward wave effectively. The reflected and forward waves interfere with each other, achieving high gain in the operating band.

C. Comparison of different reflector surface

To further demonstrate the function of the NUM reflector in improving antenna performance, three different antennas are simulated and compared, including the S-shaped slot antenna without reflector, with perfect electric conductor (PEC) surface, and with NUM reflector. As shown in Figure 2 (a), there is a slight deterioration of S11 from 3 to 4.25 GHz due to the introduction of the reflector. Simulated AR bandwidths of three antennas are illustrated in Figure 2 (b), and the S-shaped slot antenna obtains the widest 3-dB AR bandwidth of 60.1% (3.2-5.95 GHz). AR bandwidth of the slot antenna with NUM reflector is slightly reduced, which is 54.9% (3.3-5.8 GHz). Due to the mirror image current generated on the PEC radiated waves of opposite polarization,

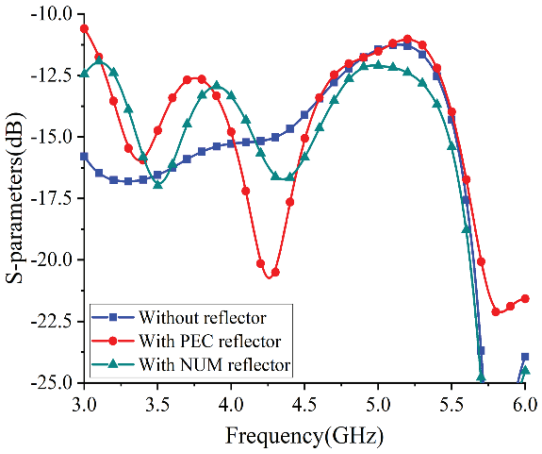

(a)

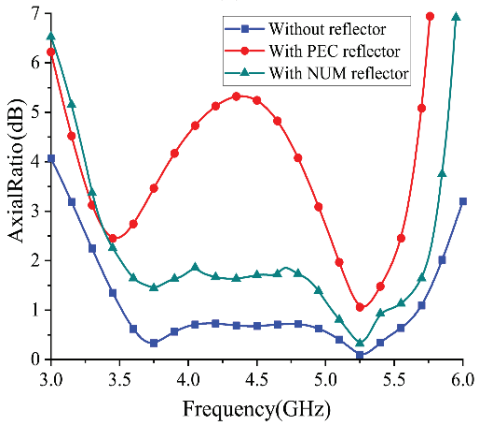

(b)

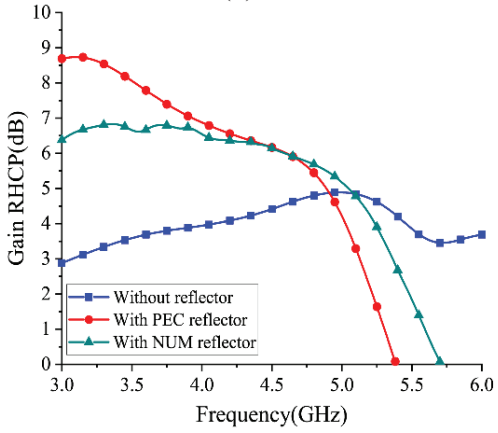

(c)

Fig. 2. Comparisons of different antennas' performances. (a) S11 of the antenna. (b) AR of the antenna. (c) Gain of the antenna.

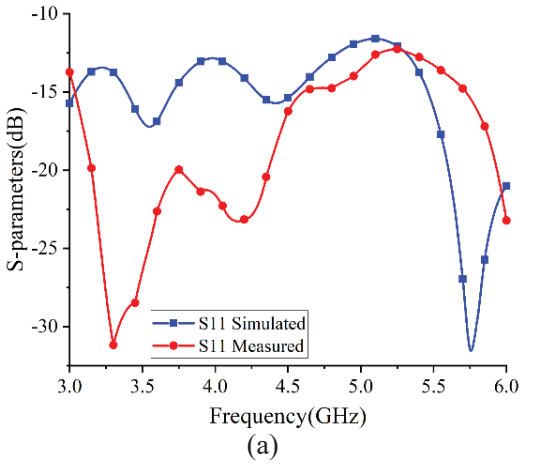

(a)

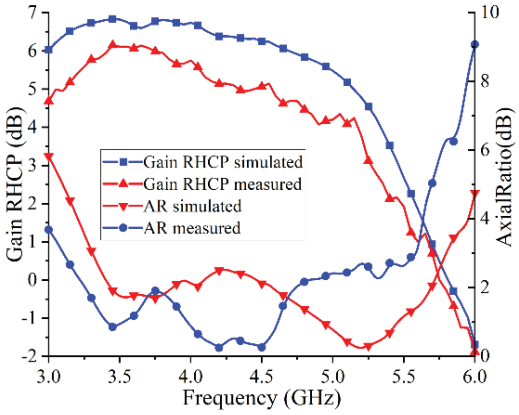

(b)

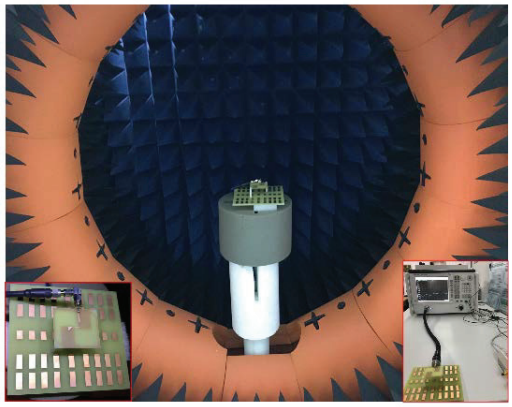

(c)

Fig. 3. Simulated and measured results of the proposed antenna.

the PEC reflector severely deteriorates the AR performance of the antenna. For Figure 2 (c), it can be concluded that the gain of the S-slot antenna can be improved by the reflector, where the NUM reflector provides a lower gain improvement than the PEC reflector since the incident wave is only partially reflected. From the comparison of the three antennas, the antenna with NUM reflector achieves a gain improvement of more than 3 dBi over the CP operating band, whereas the S-shaped slot antenna maintains its wideband CP properties.

III. EXPERIMENTAL VERIFICATION

As shown in Figure 3 (c), an assembled prototype for the designed CP antenna is fabricated and measured to verify simulated results. According to the simulated and measured reflection coefficients illustrated in Figure 3 (a), the impedance matching is enhanced at lower frequencies with a −10 dB bandwidth of 66.7% (3.0-6.0 GHz) and completely covers the AR bandwidth of 57.4% (3.1-5.6 GHz). Figure 3 (b) shows that the 6.0 dBi measured gain of RHCP is obtained at 3.8 GHz in boresight. The major performance metrics of the proposed antennas are compared with other reported CP antenna of similar structures, as shown in Table 2. In comparison, the proposed antenna has demonstrated the advantages of wider AR bandwidth. Furthermore, stable radiation patterns are achieved over the CP operation band, as illustrated in Figure 4. The difference between measurement and simulation is caused by alignment problems and the experimental environment in the Lab.

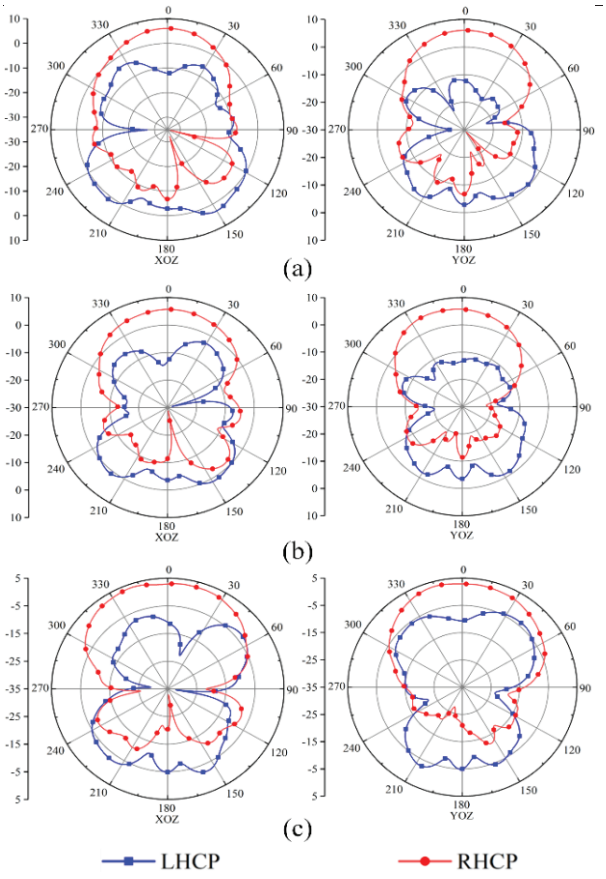

Fig. 4. Measured radiation patterns in XOZ and YOZ planes. (a) 3.5 GHz. (b) 4.0 GHz. (c) 4.5 GHz.

Table 2: Performance comparison between the proposed antenna and previous CP antenna with similar structure

Ref.	Antenna structure	Dimension (λo/GHz)	Peak gain (dBic)	IMBW (%)	ARBW (%)
Proposed	Single-layer NUM	1.88 × 1.74 × 0.35/4.35	6.0	66.7	57.4
[21]	Single-layer AMC	1.14 × 1.14 × 0.22/4.50	4.9	86.2	44.1
[22]	Single-layer AMC	0.83 × 0.69 × 0.35/8.27	5.6	137.1	56.6
[23]	Single-layer FSS	1.35 × 1.40 × 0.33/6.25	10	84.8	56.0
[24]	Single-layer AMC	0.81 × 0.53 × 0.20/6.25	7.5	38.3	31.6
[25]	Three-layer AMC	0.72 × 0.60 × 0.19/6.0	7.0	33.2	36.2

IV. CONCLUSION

A wideband circular polarized antenna with a NUM reflector for achieving wide CP operation bandwidth and high gain is presented. The optimized antenna is fabricated and measured. The antenna achieves 57.4% (3.1-5.6 GHz) AR bandwidth in practice and 54.9% (3.3-5.8 GHz) in simulation. Moreover, 66.7% (3.0-6.0 GHz) of the relative impedance bandwidth is obtained in both simulation and measurement. With the NUM reflector, the gain of the S-shaped slot antenna is enhanced by up to 3 dBi during the CP operating bandwidth, and steady radiation patterns are achieved. The proposed wide CP antenna with high gain property is suitable for high-capacity long-distance communications in 5G applications.

REFERENCES

[1] K. L. Chung, X. Yan, and Y. Li, "Circularly-polarized linear antenna array of non-identical radiating patch elements for WiFi/WLAN applications," AEÜ - *International Journal of Electronics and Communications*, vol. 129, ID: 153526, 2021.

[2] K. L. Chung, X. Yan, and Y. Li, "Circularly-polarized linear antenna array of non-identical radiating patch elements for WiFi/WLAN applications," AEÜ - *International Journal of Electronics and Communications*, vol. 129, ID: 153526, 2021.

[3] X. Yan, K. L. Chung, Y. Li, and Y. Li, "A Jia-shaped artistic patch antenna for dual-band circular polarization," AEÜ - *International Journal*

of Electronics and Communications, vol. 120, ID: 153207, 2020.

[4] J. Li, J. Shi, L. Li, T. A. Khan, J. Chen, Y. Li, and A. Zhang, "Dual-band annular slot antenna loaded by reactive components for dual-sense circular polarization with flexible frequency ratio," *IEEE Access* vol. 6, no. 1, pp. 64063-64070, 2018.

[5] Y. Li and R. Mittra, "A three-dimensional circularly polarized antenna with a low profile and a wide 3-dB beamwidth," *Journal of Electromagnetic Waves and Applications*, vol. 30, no. 1, pp. 89-97, 2016.

[6] W. Zhou, Y. Li, and Y. Xia, "A 5G Hybrid Circular Polarization MIMO Antenna," *IEEE 4th International Conference on Electronic Information and Communication Technology (ICEICT 2021)*, 18-20th, August, Xi'an, China, 2021.

[7] W. Zhou, C. Yue, Y. Li, Y. Xia, B. Qiu, and K. L. Chung, "A High Gain Si-shaped Circularly Polarized Patch Antenna for 5G Application," *IEEE 4th International Conference on Electronic Information and Communication Technology (ICEICT 2021)*, 18-20th, August, China, 2021.

[8] J. Jiang, C. Yue, Y. Xia, B. Qiu, and Y. Li, "A Circularly-Polarized Zhong-Shaped MIMO Antenna with Meta-Materials for WLAN Application," *International Applied Computational Electromagnetics Society (ACES-China) Symposium*, 28-30th, July, Chengdu, China, 2021.

[9] B. Qiu, Y. Xia, Y. Li, C. Yue, and T. Jiang, "A Compact Wideband Circularly Polarized Antenna for Sub-6 GHz Application," *IEEE 4th International Conference on Electronic Information and Communication Technology (ICEICT 2021)*, 18-20th, August, Xi'an, China, 2021.

[10] Y. Li, Y. Wang, and K. Yu, "A single-band and dual-band circular polarized antenna by using asymmetric-circular shaped slots," *IEEE 5th Asia-Pacific Conference on Antennas and Propagation (APCAP)*, 26th-29th, July, Kaohsiung, Taiwan, 2016.

[11] J. Jiang and Y. Li, A Wideband Kanji Patch Antenna for 5G Sub-6-GHz Applications, 2020 UK-Europe-China Workshop on Millimeter Waves and Terahertz Technologies, Tianjin, China, 29th Aug.-1st Sep. 2020.

[12] Z. Li, X. Zhu, and C. Yin, "CPW-fed ultra-wideband slot antenna with broadband dual circular polarization," *AEU - International Journal of Electronics and Communications*, vol. 98, pp. 191-198, Nov. 2019.

[13] S. Zhou, P. Li, Y. Wang, W. Feng, and Z. Liu, "A CPW-fed broadband circularly polarized regular-hexagonal slot antenna with L-shape monopole," in *IEEE Antennas and Wireless Propagation Letters*, vol. 10, pp. 1182-1185, Oct. 2011.

[14] J. Pourahmadazar, C. Ghobadi, J. Nourinia, N. Felegari, and H. Shirzad, "Broadband CPW-fed circularly polarized square slot antenna with inverted-L strips for UWB applications," in *IEEE Antennas and Wireless Propagation Letters*, vol. 10, pp. 369-372, Apr. 2011.

[15] M. S. Ghaffarian, G. Moradi, and P. Mousavi, "Wide-band circularly polarized slot antenna by using novel feeding structure," *11th European Conference on Antennas and Propagation (EUCAP)*, pp. 2172-2175, Mar. 2017.

[16] B. Qiu and Y. Li, "Asymmetric CPW-fed wideband circularly polarized antenna for sub-6 GHz application," *2020 IEEE 3rd International Conference on Electronic Information and Communication Technology (ICEICT)*, pp. 626-628, Apr. 2020.

[17] P. Chaudhary and A. Kumar, "Compact ultra-wideband circularly polarized CPW-fed monopole antenna," *AEU - International Journal of Electronics and Communications*, vol. 107, pp. 137-145, May 2019.

[18] K. Ding, C. Gao, T. Yu, and D. Qu, "Broadband C-Shaped Circularly Polarized Monopole Antenna," in *IEEE Transactions on Antennas and Propagation*, vol. 63, no. 2, pp. 785-790, Feb. 2015.

[19] K. Ding, Y. Guo, and C. Gao, "CPW-fed wideband circularly polarized printed monopole antenna with open loop and asymmetric ground plane," in *IEEE Antennas and Wireless Propagation Letters*, vol. 16, pp. 833-836, Sep. 2017.

[20] R. Xu, "Analysis and design of ultrawideband circularly polarized antenna and array," in *IEEE Transactions on Antennas and Propagation*, vol. 68, no. 12, pp. 7842-7853, Dec. 2020.

[21] V. Rafii, J. Nourinia, C. Ghobadi, J. Pourahmadazar, and B. S. Virdee, "Broadband circularly polarized slot antenna array using sequentially rotated technique for C-band applications," in *IEEE Antennas and Wireless Propagation Letters*, vol. 12, pp. 128-131, Jan. 2013.

[22] W. Tan, X. Shan, and Z. Shen, "Ultra-wideband circularly polarized antenna with shared semi-circular patches," in *IEEE Transactions on Antennas and Propagation* pp. 1-1, Nov. 2020.

[23] R. Xu, J. Li, and K. Wei, "Wideband circular polarized antenna and its array," 2016 *IEEE 5th Asia-Pacific Conference on Antennas and Propagation (APCAP)*, pp. 73-74, Jul. 2016.

[24] G. Feng, L. Chen, X. Xue, and X. Shi, "Broadband circularly polarized crossed-dipole antenna with a single asymmetrical cross-loop," in *IEEE Antennas and Wireless Propagation Letters*, vol. 16, pp. 3184-3187, Oct. 2017.

[25] G. Feng, L. Chen, X. Wang, X. Xue, and X. Shi, "Broadband circularly polarized crossed bowtie dipole antenna loaded with parasitic elements," in *IEEE Antennas and Wireless Propagation Letters*, vol. 17, no. 1, pp. 114-117, Jan. 2018.

[26] Li, H., Xu, K. W., Wang, X. B, "Low-profile circularly polarized loop antenna assisted with an effective PMC bandwidth," *Electron. Lett*, vol. 49, no. 16, pp. 978–979, Aug. 2013.
[27] Y. M. Cai, K. Li, Y. Z. Yin, "Dual-band circularly polarized antenna combining slot and microstrip modes for GPS with HIS ground plane," *IEEE Antennas Wirel. Propag. Lett*, vol. 14, pp. 1129–1132, Jan. 2015.
[28] K. Agarwal, Nasimuddin and A. Alphones, "Wideband circularly polarized AMC reflector backed aperture antenna," in *IEEE Transactions on Antennas and Propagation*, vol. 61, no. 3, pp. 1456-1461, Mar. 2013.
[29] Z. Wang, Y. Jiao, Y. Zhang, J. Wen, and G. Zhao, "Wideband AMC surface and applications to low profile circularly polarized slot antennas," 2019 *International Conference on Microwave and Millimeter Wave Technology (ICMMT)*, pp. 1-3, May 2019.
[30] W. Yang and J. Zhou, "Wideband circularly polarized cavity-backed aperture antenna with a parasitic square patch," in *IEEE Antennas and Wireless Propagation Letters*, vol. 13, pp. 197-200, Jan. 2014.
[31] Y. Zhang, Y. Jiao, Z. Zhang, and S. Feng, "Wideband accurate-out-of-phase-fed circularly polarized array based on penta-mode aperture antenna element with irregular cavity," in *IEEE Transactions on Antennas and Propagation*, vol. 67, no. 1, pp. 638-642, Jan. 2019.

Bosong Qiu was born in Panjin, Liaoning. He received the B.S. and M.S. degrees from Harbin Engineering University, Harbin, China, in 2019 and 2022, respectively.

His research interest mainly focuses on circular polarized antenna designs.

Yinfeng Xia was born in Huanggang Hubei. He received the B.S. degree in communication engineering from Harbin Engineering University, Harbin, China, in 2017. He is currently working toward the Ph.D. degree in information and communication engineering with Harbin Engineering University.

His research interest mainly focuses on low-frequency antenna design, circular polarization antenna design, and microwave circuits.

Yingsong Li received the B.S. degree in electrical and information engineering and the M.S. degree in electromagnetic field and microwave technology from Harbin Engineering University (HEU), Harbin, China, in 2006 and 2011, respectively. He received the Ph.D. degree from both the Kochi University of Technology (KUT), Kami, Japan and HEU in 2014.

He has been a Full Professor with the School of Electronic and Information Engineering, Anhui University, Hefei, China, since March 2022. He was a Professor with HEU from 2014 to 2022, a visiting Scholar with the University of California, Davis, Davis, CA, USA, from March 2016 to March 2017, a visiting Professor with the University of York, York, U.K., in 2018, and a visiting Professor with Far Eastern Federal University (FEFU), Vladivostok, Russia and KUT. He has been holding the Visiting Professor position of School of Information, KUT since 2018. He is a Postdoc with the Key Laboratory of Microwave Remote Sensing, Chinese Academy of Sciences, Beijing, China, from 2016 to 2020. He is currently a Fellow of Applied computational Electromagnetics Society (ACES Fellow), and he is also a Senior Member of Chinese Institute of Electronics (CIE) and a Senior Member of IEEE. He has authored and coauthored about 300 journal and conference papers in various areas of electrical engineering. His current research interests include remote sensing, underwater communications, signal processing, adaptive filters, metasurface designs, and microwave antennas.

Dr. Li serves as an Area Editor for AE*Ü-International Journal of Electronics and Communications* from 2017 to 2020, and he is an Associate Editor for *IEEE Access*, *Applied Computational Electromagnetics Society Journal* (ACES Journal), and *Alexandria Engineering Journal*. He is the TPC Co-Chair of the *2019 IEEE International Workshop on Electromagnetics (iWEM 2019-2020)*, *2019 IEEE 2nd International Conference on Electronic Information and Communication Technology (ICEICT 2019)*, *2019 International Applied Computational Electromagnetics Society (ACES) Symposium-China*, and *2019 Cross Strait Quad-regional Radio Science and Wireless Technology Conference (2019 CSQRWC)* and the TPC Chair of *ICEICT 2021-2022*. He is also a General Co-Chair of *ICEICT 2020* and a General Chair of *IEEE 9th International Conference on Computer Science and Network Technology (ICCSNT 2021)* and *ICCSNT 2022*. He also serves as a Session Chair or Organizer for many international and domestic conferences, including the *WCNC*, *AP-S*, *ACES*, etc. He acts as a Reviewer for numerous IEEE, IET, Elsevier, and other international journals.

Cavity-Backed Slot V2X Antenna for Automotive Applications

Mohamed O. Khalifa, Ahmad M. Yacoub, and Daniel N. Aloi

Department of Electrical Engineering
Oakland University, Rochester, MI 48309, USA
MKhalifa@Oakland.edu, Ahmadyacoub@Oakland.edu, Aloi@Oakland.edu

Abstract – In this work, a cavity-backed slot antenna has been designed to cover vehicle-to-everything (V2X) frequencies ($5.85 - 5.925$ GHz). The antenna is made to be easily integrated in a vehicle windshield or rear mirror. The cavity-backed slot antenna does not require a ground plane to sit on which makes it an ideal model for below horizon performance. Antenna simulation has been done using high-frequency structure simulator (HFSS) and then on-foam and on vehicle's windshield measurements have been carried out inside an anechoic chamber. The proposed antenna achieved a linear average gain (LAG) above 2.5 dBi in the targeted V2X elevation and azimuth angles with better than 15 dB return loss. The antenna performance has been reported in terms of reflection coefficient, surface current density, radiation pattern, LAG, and efficiency.

Index Terms – Automotive antennas, V2X, 5G, V2I, V2P, V2N, V2V, cavity-backed slot antenna.

I. INTRODUCTION

In the recent years, the automobiles industry has been drastically affected by the new technology advancements. The vehicle is no longer made of primitive mechanical components; only, however, it is loaded with many sensors for various applications. Long road trip hours increased the possibility of car accidents and other serious socioeconomic problems. Vehicle-to-everything (V2X) communication technology includes vehicle-to-vehicle (V2V), vehicle-to-infrastructure (V2I), vehicle-to-network (V2N), and vehicle-to-pedestrian (V2P), and it allows the vehicle's system to exchange information with infrastructure, pedestrians, and vehicles to smoothen traffic flow and improve humans' safety. There are two implementable schemes for V2X: dedicated short-range communication (DSRC) and 5G network. Both schemes can operate with each other to result in a complete solution for V2X communication. The 5G cellular communication can be considered as a backup to the DSRC while supporting high data rates that can lengthen the communication path beyond the short range of the DSRC technology [1].

Vehicular V2X antennas are required to communicate with vehicles, infrastructure, network, and pedestrians that are located at various elevations with respect to the vehicle's antenna. Thus, good coverage in Theta angles range $75^\circ < \theta < 95^\circ$ is important to make sure that good reception performance is achieved for electromagnetic waves originating from antennas mounted in high locations like base station towers as well as to cover waves incident from below-horizon angles [2].

In [3], two V2X antennas are designed to fit in an automotive shark-fin; however, low average gain of -2.3 dBi was reported at 5.9 GHz. A tri-polarized antenna was designed to cover 5G and V2X frequencies in [4] with an H-plane gain of $2.05 - 2.88$ dBi in the V2X band; however, it comes with an increased antenna volume with dimensions of $76 \times 76 \times 17\text{mm}^3$. Similar drawbacks of large volumes can also be seen in [5–9] with less than zero gain in [7] and [8], whereas a gain of 0.97 dBi was reported in [9]. A mean realized gain of 0.043 dBi was achieved in [10] with a multiband antenna that covers long-term evolution (LTE) and V2X with a big volume of $120 \times 70 \times 0.1\text{mm}^3$. In addition to those similar large volumes, multiband designs that cover both LTE and V2X with maximum realized gain values of -0.5 and 2 dBi are reported in [11] and [12], respectively. In [13], a quarter-wave balun fed Vivaldi antenna with dimensions of $190 \times 187.5 \times 187.3\text{mm}^3$ was designed and an average gain of -5 dBi was reported around 5.9 GHz. The work in [2] shows a peak gain of 8 dBi at 5.9 GHz; however, it does not show average gain values and it does not tell at which elevation angles this peak gain is achieved. Unlike the above designs, the proposed cavity-backed slot antenna is made to be attached to the vehicle windshield instead of the roof which allows improved radiation pattern for elevation angles $> 90^\circ$ and consequently improve the V2X communication scheme.

The work in this paper is organized in two sections: Section II details the antenna element layout and the design goals; Section III presents the cavity-backed slot antenna simulation and measurements results and compares it to the available work in literature.

Submitted On: October 25, 2021
Accepted On: February 4, 2022

https://doi.org/10.13052/2022.ACES.J.370305

II. ANTENNA ELEMENT LAYOUT

The cavity-backed slot antenna is constructed of metal sheet with volume of 40.5 mm height × 38.7 mm length × 16.8 mm width. A coaxial cable is used to feed the antenna where its center pin is used as a monopole to excite the cavity-backed slot antenna. Figures 1 and 2 show the proposed antenna with geometrical dimensions highlighted. The feeding monopole is made of two parts, the lower part which is coaxial cable center pin with a length (LFL) of 1.74 mm and diameter of 0.2 mm, whereas the top part has a length (FL) of 10.97 mm and a wider diameter (FD) of 1.7 mm to help in having wider overall bandwidth for the monopole.

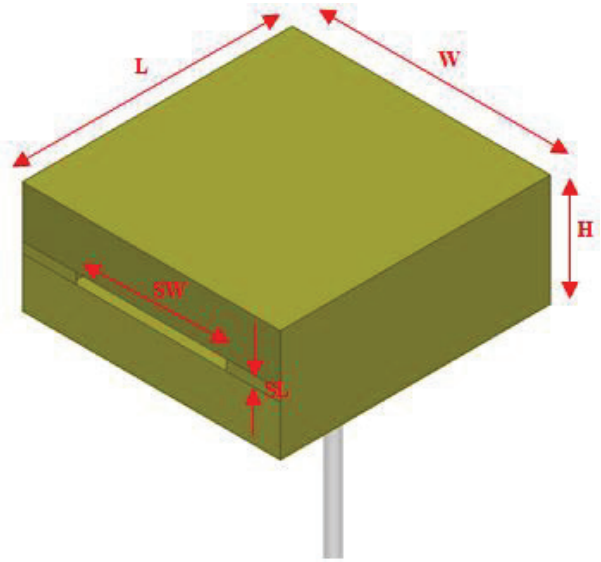

Fig. 1. Cavity-backed slot antenna dimensions.

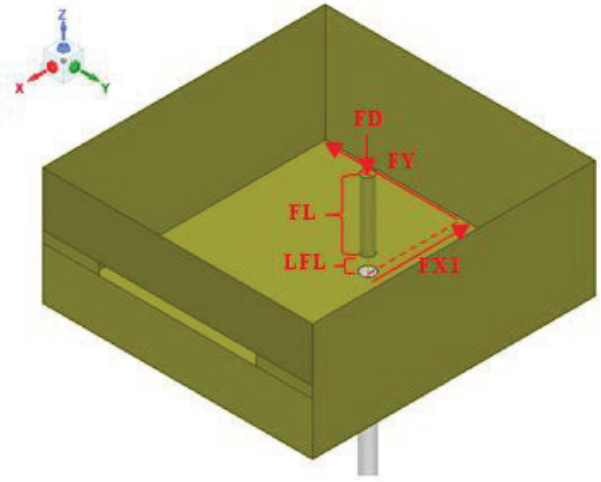

Fig. 2. Cavity-backed slot antenna dimensions with the top side removed.

Table 1: Values of the cavity-backed slot antenna geometrical parameters

Parameter	Value (mm)	Parameter	Value (mm)
H	16.8	FL	11
L	40.5	LFL	1.74
W	38.7	FD	1.7
SW	22.5	FX1	13.3
SL	1.6	FY	19.35

Table 2: Design guidelines

Parameter	Value
Polarization	Vertical linear polarization (VLP)
Reflection coefficient	−10 dB (2:1 VSWR)
Avg. total efficiency	45%
LAG for solid angle: $-60^\circ < \Phi < 60^\circ$ $88^\circ < \theta < 91^\circ$	Minimum of 2 dB

The total length of the monopole is set to be 12.71 mm which is a quarter-wavelength at 5.9 GHz and can be calculated as follows:

$$\text{Monopole length} = \frac{c}{4 * f},$$

where c is the speed of light ($c = \lambda f = 3 \times 10^8$ m/s) and f = 5.9 GHz. The feeding monopole is located at approximately FX $= \frac{\lambda_{\text{center-freq}}}{4}$ from the back side (opposite to the slot side) of the cavity to allow for an in-phase reflection of energy from the back of the cavity to the slot side. It is assumed that the cavity is filled with air and experimental trials are used to determine the geometrical dimensions of the cavity with the assumption that TE_{101} mode will be excited in the antenna. Table 1 shows the values of various antenna parameters with their final values.

Table 2 lists the targeted design goals for the proposed V2X antenna in terms of polarization, reflection coefficient, efficiency, and linear average gain (LAG). The design goals are generated based on the anticipated coverage and performance of V2X antenna based on the requirements of some of the original equipment's manufacturer (OEMs) in the automotive industry.

The antenna simulation is done using high-frequency structure simulator (HFSS), measured on-foam inside an anechoic chamber as in Figure 3, and, finally, vehicle level measurement has been performed with the antenna mounted on the vehicle's windshield as can be seen in Figure 4.

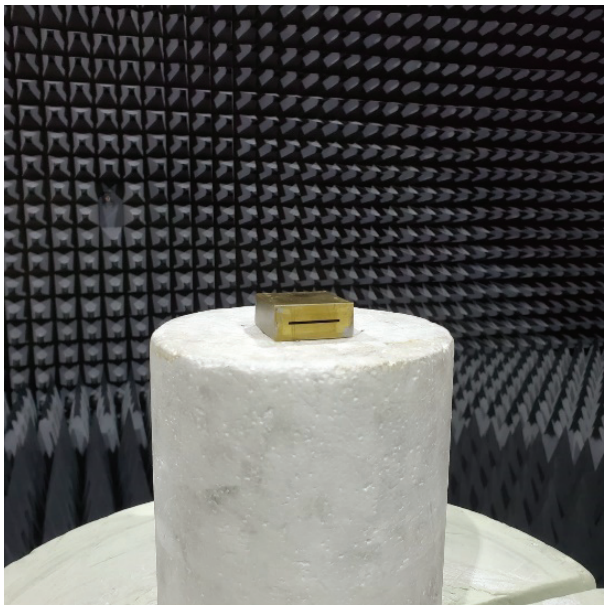

Fig. 3. On-foam measurement setup.

Fig. 4. Antenna placement on vehicle windshield.

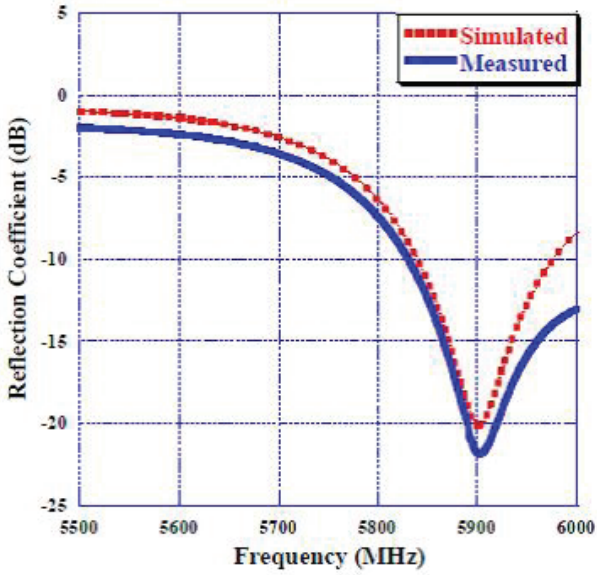

Fig. 5. Comparison of reflection coefficient (dB) between simulation and measurement.

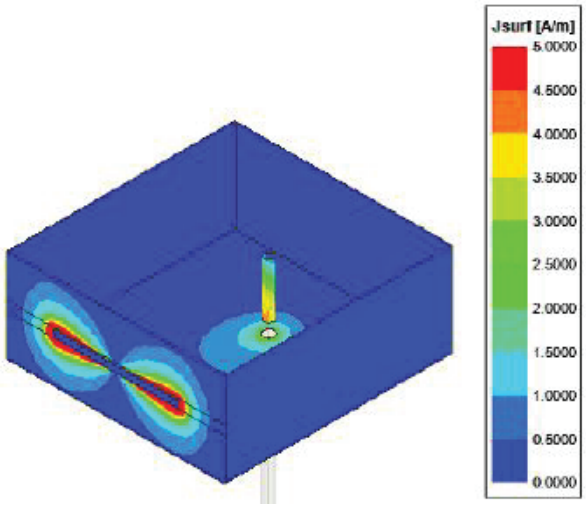

Fig. 6. Simulated surface current density (A/m) at 5.9 GHz.

III. PROPOSED ANTENNA SIMULATION AND MEASUREMENT RESULTS

The proposed antenna's reflection coefficient is depicted in Figure 5. Similar matching characteristics between the simulation and measurements can be observed with mid-band return losses of 20 and 22 dB in simulation and measurements, respectively. In order to further study the antenna, the surface current density is reported in Figure 6. The high values of surface current density at 5.9 GHz near the cavity slot indicates that most of the energy radiated by the feeding monopole is exiting the cavity through the slot either directly or after it bounces from the back of the cavity.

Next, a parametric study has been conducted to study the effect of various cavity parameters on the V2X antenna performance and to check the possibility of miniaturizing the antenna without impacting the performance. The study started by changing the front side slot width (SW) and length (SL) by 1 mm around the optimized value listed in Table 1. Increasing slot length or width by 1 mm moves the resonance fre-

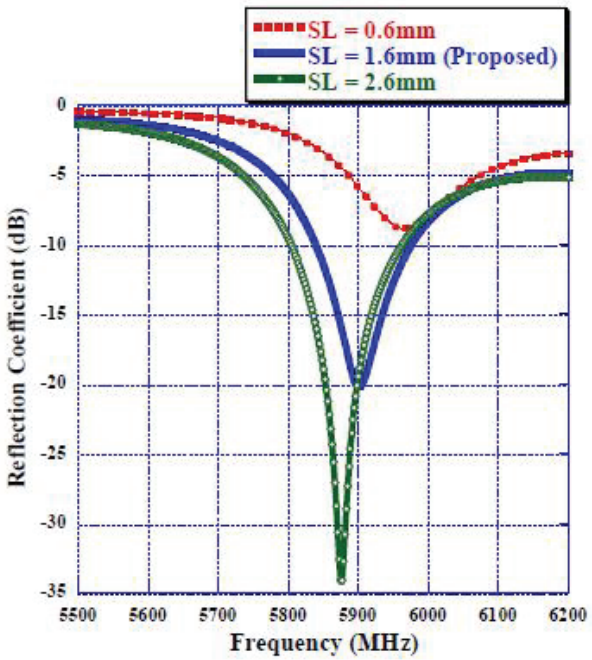

Fig. 7. Effect of changing SL on reflection coefficient.

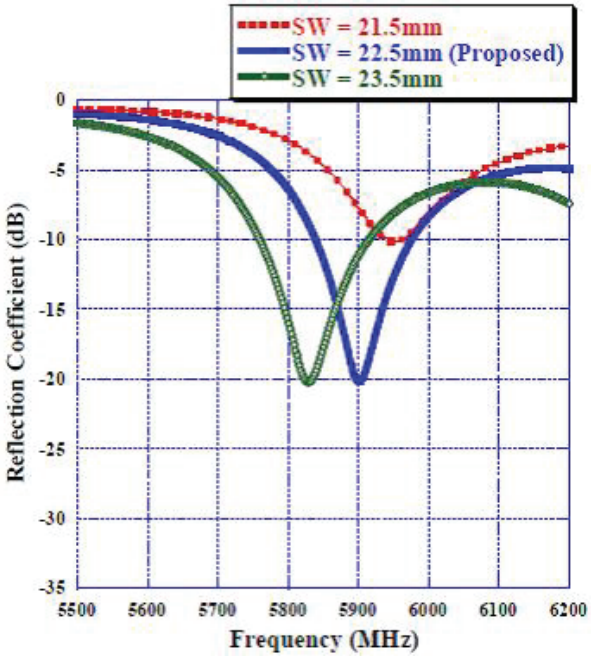

Fig. 8. Effect of changing SW on reflection coefficient.

quency toward lower frequencies while reducing them shifts the resonance frequency higher as Figures 7 and 8 suggest. In fact, increasing SL or SW increases resistance and inductance the input impedance antenna input impedance, while the opposite happens when SL and SW lengths are reduced. The impact of changing slot dimensions can easily be understood by invoking the Babinet's principle where the horizontal slot can be replaced by the corresponding vertical half-wave dipole. Since increasing the slot dimensions is equivalent to increasing dipole dimension, previous argument is proved to be valid. Furthermore, the cavity with the slot (or equivalent dipole) acts like a parasitic director to help make the antenna more directive to the front. Since the director length is typically slightly less than half of the wavelength at 5.9 GHz, SW optimized value was found to be 22.5 mm which corresponds to 0.45λ at 5.9 GHz.

Fine-tuning of the resonance frequency can be achieved by adjusting the *y*-axis sides of the cavity, where increasing distance between monopole and cavity sides along the *y*-axis (FY) allows better radiation characteristics for bigger wavelength while the opposite happens when monopole to side distance is reduced as depicted in Figure 9. In order to find the minimum dimensions that result in a satisfactory performance of the V2X antenna, the relative distances between the monopole and *x*-axis sides of the cavity have been studied. Figure 10 shows the effect of changing monopole

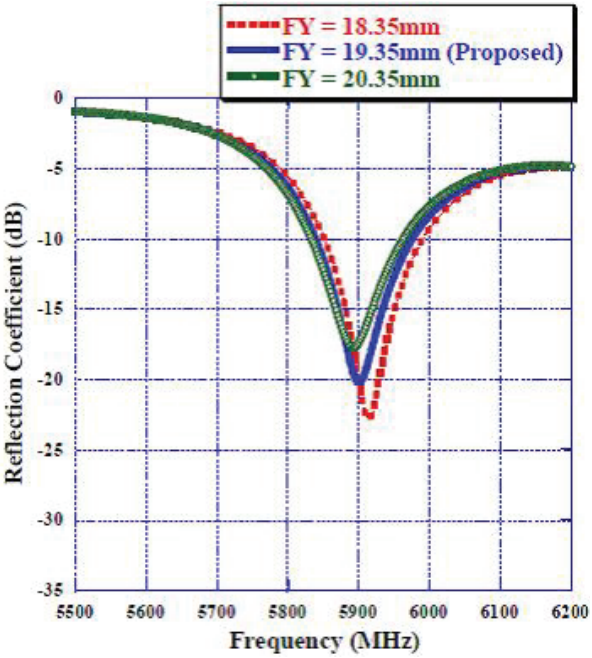

Fig. 9. Effect of changing FY on reflection coefficient.

to cavity backside distance (FX1). It can be noticed that reducing FX1 length by only 1 mm entirely sabotages the antenna reflection coefficient and, consequently, the overall antenna performance, whereas the change in reflection coefficient due to 1 or 2 mm FX1 increase is almost insignificant. As a result, the optimized value

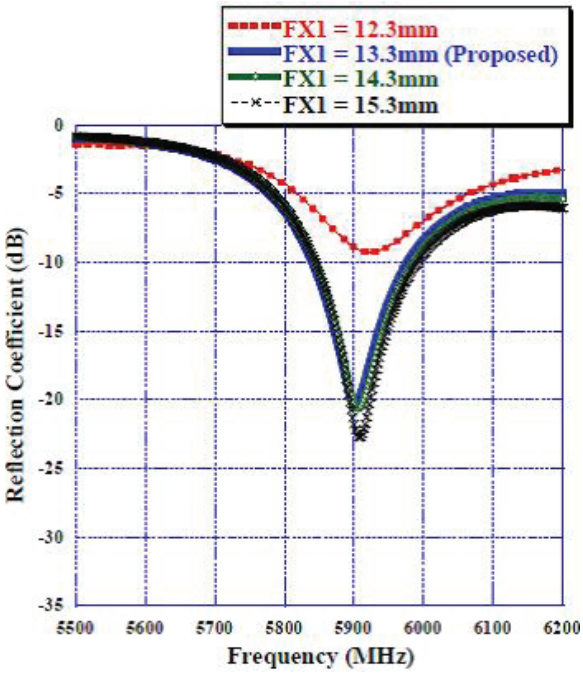

Fig. 10. Effect of changing FX1 on reflection coefficient.

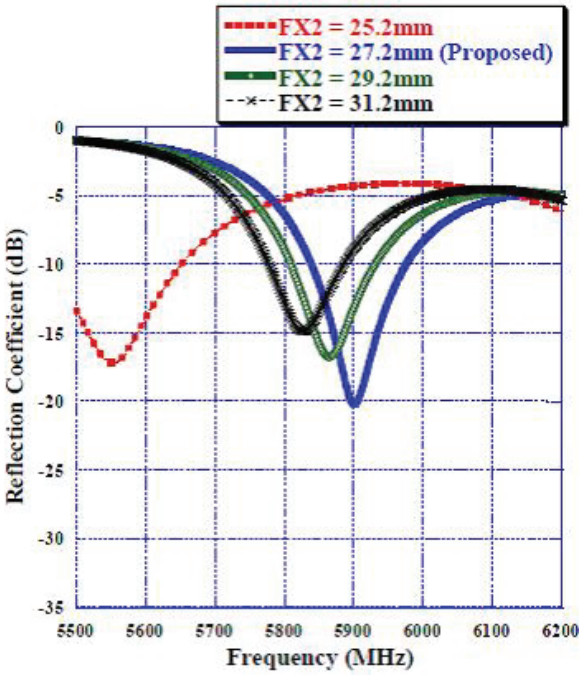

Fig. 11. Effect of changing FX2 on reflection coefficient.

of FX1 = 13.5 mm represents the smallest monopole to cavity back-side distance that allows for satisfactory V2X antenna performance according to the requirements listed in Table 2. Similar analysis can be shown for monopole to cavity front-side distance (FX2 = L-FX1 = 27.2 mm) as illustrated in Figure 11. For this parameter, the variation step has been set to 2 mm to allow for noticeable change in the reflection coefficient response. As it can be seen in Figure 11, as FX2 value decreases from 31.2 mm, antenna resonance frequency is shifted toward higher frequencies and a perfect matching is obtained around FX2 = 27.2 mm. Reducing FX2 value beyond 27.2 mm results in a complete mismatch of the antenna at 5.9 GHz, indicating that the antenna size cannot get any smaller in that direction. To shed some light on the nature of change the cavity-backed slot antenna exhibits when the front side of cavity is pushed toward the monopole, the antenna input impedance is analyzed at different FX2 distances. As shown in Figure 12, the antenna input impedance at FX2 = 27.2 mm is 41.5 + j2.6 Ω at 5.9 GHz. increasing FX2 by 2 and 4 mm results in increased input reactance (inductive effect) of j20 and j39, respectively, while having insignificant effect on the input resistance (around 5 Ω) across the whole V2X band. However, when FX2 is reduced to 25.2 mm, the antenna sees a huge input impedance of 191+j51 Ω at 5.9 GHz with a significant increase in antenna input resistance. FX1 and FX2 distances of the cavity-backed slot antenna were found to have a great impact on the antenna performance, and they were optimally set to be slightly greater than quarter and half of the wavelength at 5.9 GHz, respectively. In summary, by optimizing the values of FX1, FX2, FY, SW, and SL, the smallest cavity-backed slot antenna that satisfies V2X design requirements listed in Table 2 can be found.

To meet the V2X wide azimuth front beam ($-60 < \Phi < 60$) and various elevation angle requirements, the cavity SW and length must be carefully optimized. In Figures [13–15], the antenna radiation patterns have been reported at different elevation angles and at sample frequencies across the V2X band. The elevation angles are selected in a way that will reflect various V2X communication scenarios. For example, vertical gain radiation pattern at Theta = 80° will mimic electromagnetic waves incident from base station towers or traffic light signals, whereas Theta = 90° and Theta = 93° will represent waves originating from other cars at or below the horizon, respectively. The on-vehicle's windshield average vertical gain in between azimuth angles range $-60° < \Phi < 60°$ at 5.9 GHz was found to be 2, 2.8, and 2.2 dB at Theta angles 80°, 90°, and 93°, respectively.

Since the proposed antenna does not sit on a ground plane by design, the antenna demonstrates a good performance below horizon and that can be seen by looking at average vertical realized gain at Theta = 93° which was found to be 2.4, 2, and 2.3 dB at 5.85, 5.9, and 5.925 GHz, respectively.

A practical way to measure automotive V2X antenna performance is by calculating the LAG across theta angles from 88° to 91° as in Table 2. The theta

Table 3: Literature review summary

Ref.	Type	Antenna dimension ($L \times W \times H$) (mm_3)	Avg./Peak gain (dBi)	Below horizon performance
Proposed	Cavity-backed slot	$40.5 \times 38.7 \times 16.8$	2.75/6.5	Yes
[2]	Disc shape	$\pi \times 80^2 \times 20$	NA/8	NA
[3]	Printed monopoles	$14 \times 0.8 \times 28$ $14 \times 1.6 \times 50$	-2.3/NA -2.9/NA	NA
[4]	Tri-polarized	$76 \times 76 \times 17$	2.4/2.88	NA
[7]	V-shaped slot	$\pi \times 32^2 \times 3$	NA	NA
[8]	Stacked microstrip monopolar patch	$\pi \times 85^2 \times 4$	<0/7.5	NA
[9]	Patch antenna	$\pi \times 42^2 \times 1.6$	NA/0.97	NA
[10]	Printed flexible	$120 \times 70 \times 0.1$	0.043/4.6	NA
[11]	Three-port multiband antenna	$60 \times 87 \times 1.6$	NA/-0.5	NA
[12]	Combined LTE and V2X antenna	$290 \times 40 \times 7.6$	NA/2	NA
[13]	Vivaldi antenna	$190 \times 187.5 \times 187.3$	-4/NA	NA

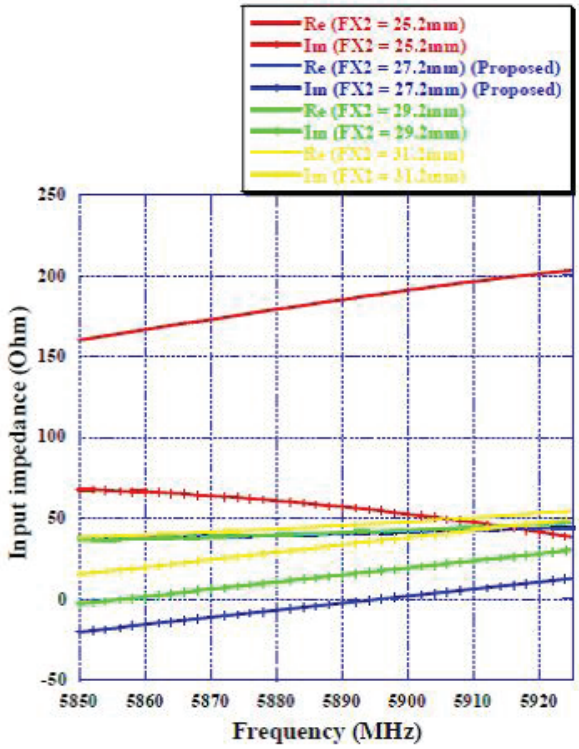

Fig. 12. Effect of changing FX2 on antenna input impedance.

angles simulate the electromagnetic waves exchanged between vehicles. LAG measured in dB for a frequency (f) and polarization (γ) is given by

$$\mathrm{LAG}_{\mathrm{dB}}(f,\gamma) = 10\log_{10}\left[\frac{\sum_{i=1}^{M}\sum_{j=1}^{N}\sin(\theta_i)\,G_{\mathrm{linear}}\left(f,\theta_i,\varphi_j,\gamma\right)}{MN}\right],$$

where θ_i is the spherical coordinate theta angle in degrees referenced by the index i; M is the total number of theta angles (four angles for theta from 88 to 91°); φ_j is the spherical coordinate phi angle in degrees referenced by the index j; N is the total number of phi angles (360 angles for phi from 0 to 359°); and $G_{\mathrm{linear}}\left(\theta_i,\varphi_j\right)$ in the gain in linear units for a discrete point on the spherical surface for a given frequency (f) and polarization (γ).

Figure 16 depicts the LAG against frequency for simulated, measured on-foam, and measured on a vehicle's windshield. In all three cases, the LAG has stayed above 2.5 dBi across V2X frequencies, satisfying the design goals listed in Table 2. Finally, the total efficiency of the antenna measured on-foam and on vehicle's windshield is reported across V2X frequencies in Figure 17. The on-foam measurements show a 56% average total efficiency, whereas the on-vehicle measurements exhibit reduced average efficiency of 45.5% indicating that antenna performance is compromised at other elevation and azimuth angles apart from the targeted ones due to reflections within the vehicle.

Table 3 compares the cavity-backed slot antenna to other V2X antennas in the literature. The proposed antenna demonstrates a good performance in terms of LAG and peak gain as well as below-horizon performance as it can be seen in the Figures 13–15. The proposed antenna with the demonstrated performance in terms of radiation pattern, reflection coefficient, LAG, and efficiency represent an ideal model for V2X antenna element that could be used to construct a complete V2X antenna solution for modern vehicle communication.

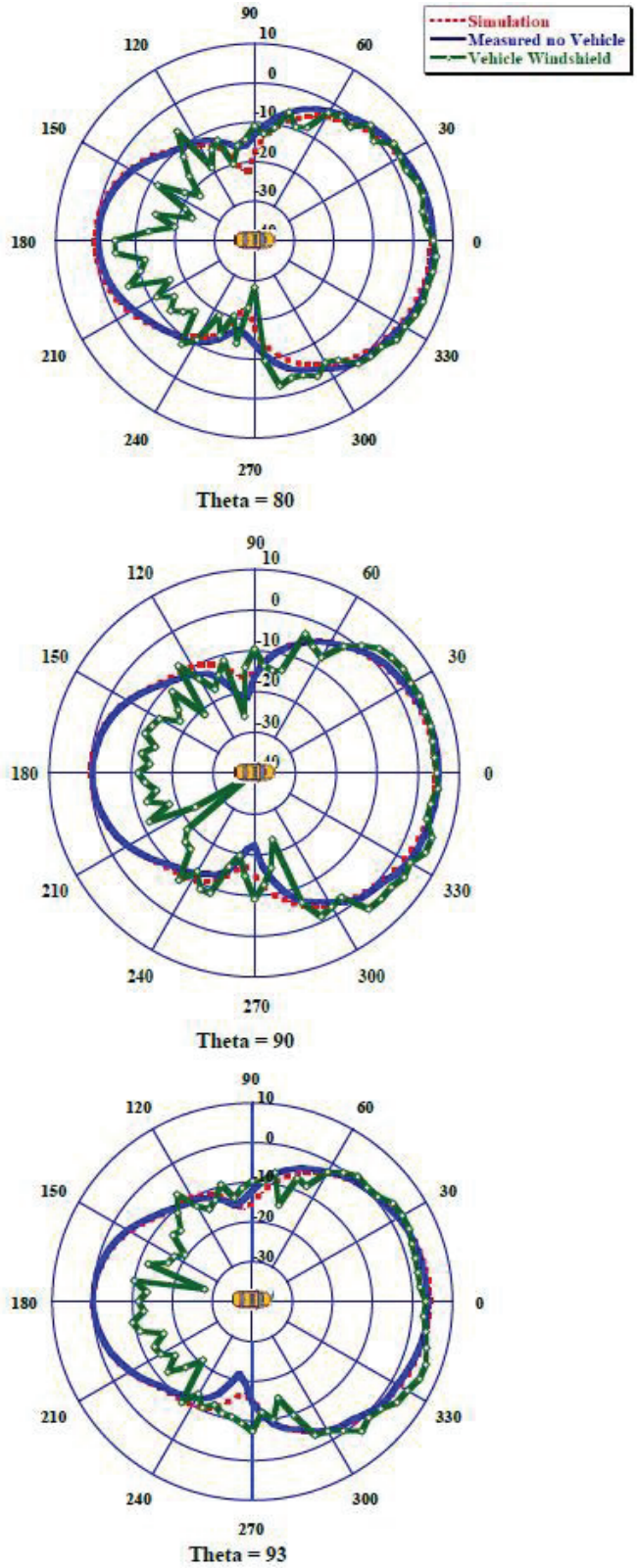

Fig. 13. Realized vertical gain at 5.85 GHz for simulated, measured, and on vehicle windshield at Theta = 80°, Theta = 90°, and Theta = 93°.

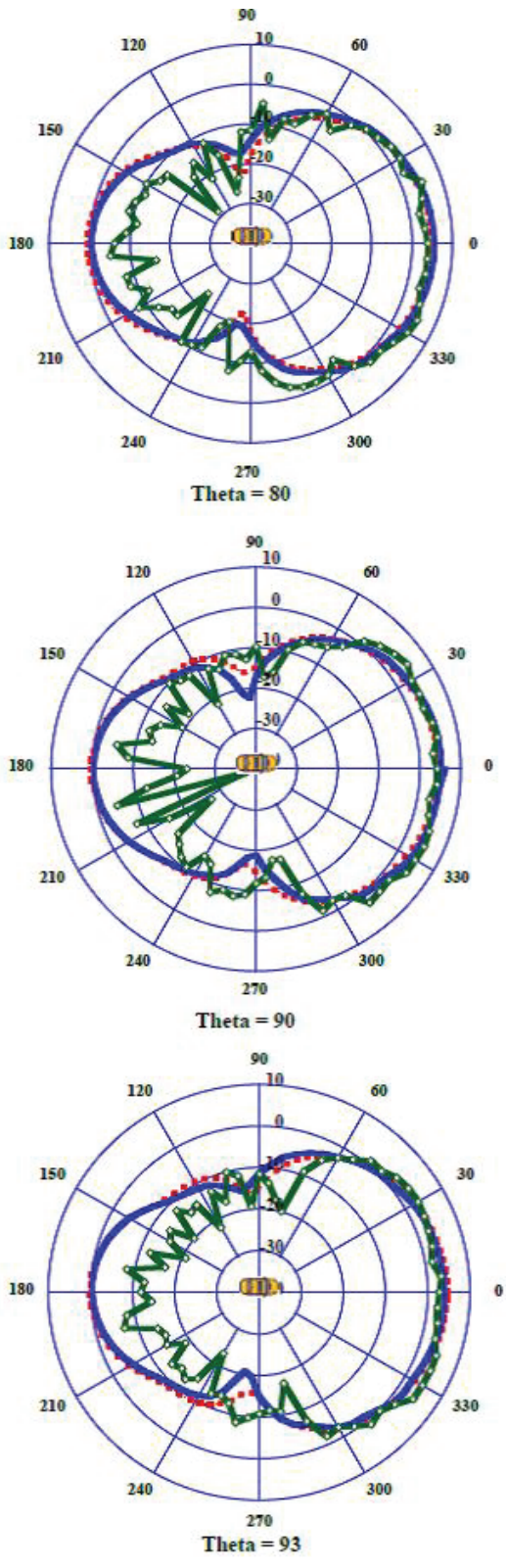

Fig. 14. Realized vertical gain at 5.9 GHz for simulated, measured, and on vehicle windshield at Theta = 80°, Theta = 90°, and Theta = 93°.

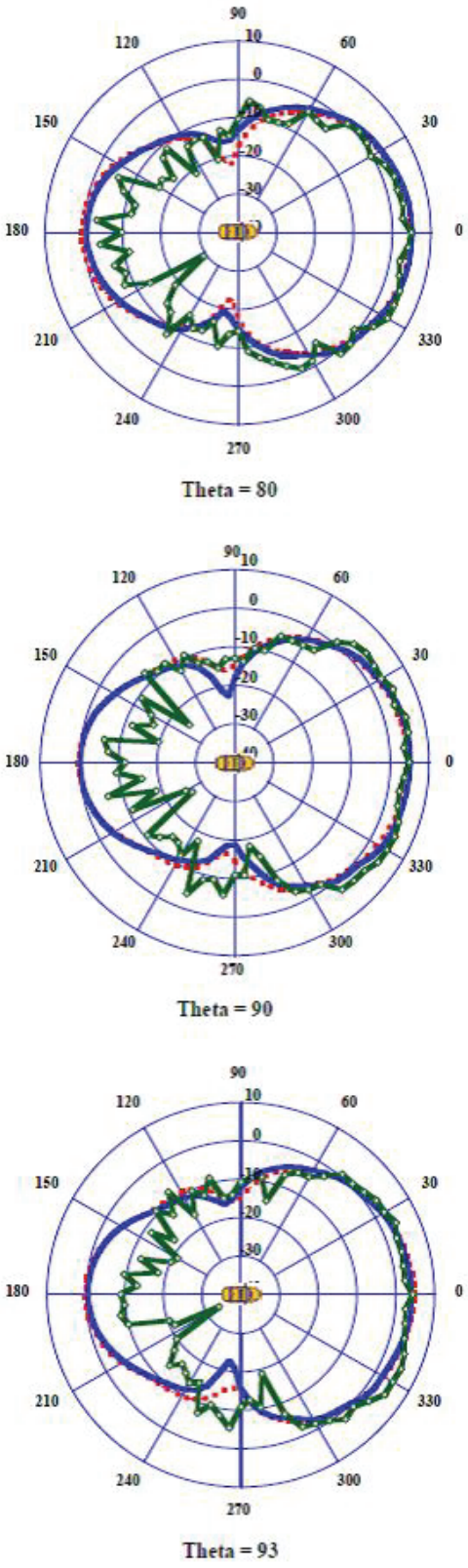

Fig. 15. Realized vertical gain at 5.925 GHz for simulated, measured, and on vehicle windshield at Theta = 80°, Theta = 90°, and Theta = 93°.

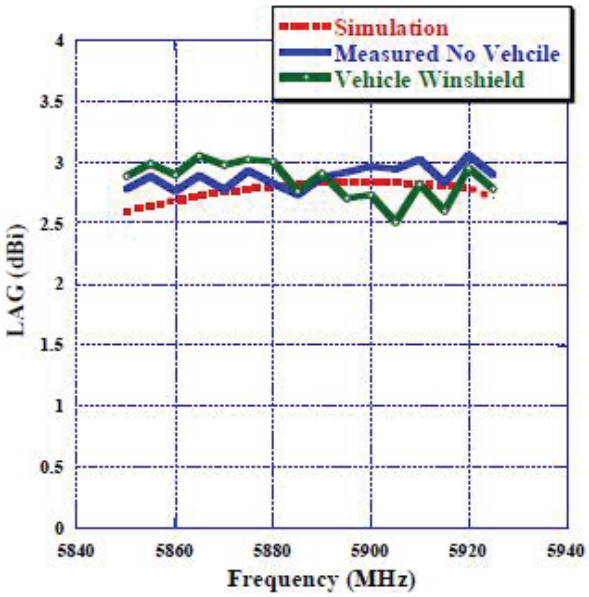

Fig. 16. LAG against frequency compassion between simulation, measured on-foam, and measured on vehicle's windshield.

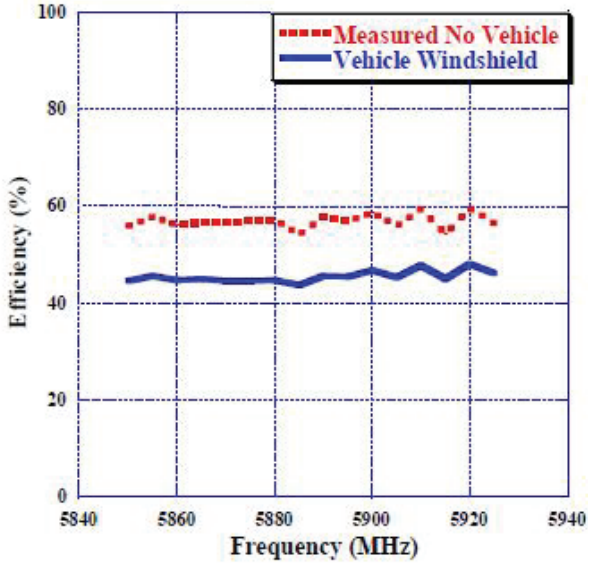

Fig. 17. Efficiency against frequency compassion between measured on-foam and measured on vehicle's windshield.

IV. CONCLUSION

In this work, a cavity-backed slot antenna has been developed to work at V2X frequencies and to allow for below horizon communication by eliminating the need for ground plane commonly used by other automotive antennas for performance enhancement. The proposed antenna is small in size, i.e., $40.5 \times 38.7 \times 16.8\text{mm}^3$,

and can easily be integrated in a vehicle's windshield or rear mirror without the need for protruding parts at the vehicles' exterior. Good matching characteristics of better than 15-dB return loss at V2X frequencies were observed. The realized vertical gain stayed almost above 0 dBi for the azimuth beam $-60^\circ < \Phi < 60^\circ$ for all elevations between $75^\circ < \theta < 95^\circ$. The antenna demonstrated good performance for the solid angle $-60^\circ < \Phi < 60^\circ$ and $88^\circ < \theta < 91^\circ$ with more than 2.5-dBi LAG across the V2X band with comparable results for simulation, on-foam, and on-vehicle's windshield measurements. Finally, average total efficiencies of 56% for on-foam measurements and of 45.5% for vehicle's windshield measurements were reported for the proposed antenna. In general, the proposed antenna has a satisfactory performance and can easily be used for V2X automotive applications upon the desired requirement, styling, and dimension.

ACKNOWLEDGMENT

The authors would like to thank Oakland University for supporting this research with measurements tools and simulation software.

REFERENCES

[1] K. Abboud, H. A. Omar, and W. Zhuang, "Interworking of DSRC and Cellular Network Technologies for V2X communications: A Survey," *In IEEE Transactions on Vehicular Technology*, vol. 65, no. 12, pp. 9457-9470, Dec. 2016.

[2] J. Chen, C. Chen, J. F. Locke, "A compact 4-channel MIMO 5G Sub-6 GHz/LTE/WLAN/V2X antenna design for modern vehicles," *IEEE Transactions on Antennas and Propagation,* vol. 69, no. 11, pp. 7290-7297, Nov. 2021.

[3] B. Seungbok, K. Sangpil, K. Choulhee, K. Heeyoung, and K. Yoongi, "Design of a V2X vehicle antenna," *2018 International Symposium on Antennas and Propagation (ISAP)*, Busan, South Korea, pp. 1-2, Jan. 2019.

[4] B. Feng, J. Chen, S. Yin, C. Sim, and Z. Zhao, "A Tri-Polarized antenna with diverse radiation characteristics for 5G and V2X communications," *IEEE Transactions on Vehicular Technology*, vol. 69, no. 9, pp. 10115–10126, Sep. 2020.

[5] M. O. Khalifa, A. M. Yacoub, D. N. Aloi, "A Multi-wideband compact antenna design for vehicular Sub-6 GHz5G wireless systems," *IEEE Transactions on Antennas and Propagation,* vol. 69, no. 12, pp. 8136-8142, Dec. 2021.

[6] A. M. Yacoub, M. O. Khalifa, and D. N. Aloi, "Wide bandwidth Low profile PIFA for vehicular Sub-6GHz 5G and V2X wireless systems," *Progress in Electromagnetics Research C,* vol. 109, pp. 257-273, 2021.

[7] H. Wong, K. K. So, and X. Gao, "Bandwidth enhancement of a monopolar patch antenna with V-shaped slot for car-to-car and WLAN communications," *IEEE Transactions on Vehicular Technology,* vol. 65, no. 3, pp. 1130-1136, Mar. 2016.

[8] S. Gao, L. Ge, D. Zhang, and W. Qin, "Low-Profile Dual-Band Stacked Microstrip Monopolar Patch Antenna for WLAN and Car-to-Car Communications," *IEEE Access*, vol. 6, pp. 69575-69581, Oct. 2018.

[9] A. Liu, Y. Lu, and L. Huang, "Low-profile patch antennas with enhanced horizontal omnidirectional gain for DSRC applications," *IET Microwaves, Antennas and Propagation*, vol. 12, no. 2, pp. 246-253, Jan. 2018.

[10] A. Chletsou, Y. He, J. F. Locke, and J. Papapolymerou, "Multi-band, Flexible, Lightweight Antenna on LCP for Automotive Applications," 2020 *IEEE International Symposium on Antennas and Propagation and North American Radio Science Meeting,* Montreal, Canada, pp. 1507-1508, Feb. 2021.

[11] Y. Hua, L. Huang, and Y. Lu, "A compact 3-port multiband antenna for v2x communication," *2017 IEEE International Symposium on Antennas and Propagation & USNC/URSI National Radio Science Meeting*, San Diego, USA, pp. 639-640, Oct. 2017.

[12] E. Neira, J. Carlsson, K. Karlsson, and E. G. Strom, "Combined LTE and IEEE 802.11p antenna for vehicular applications," 9th European Conference on Antennas and Propagation (EuCAP), Lisbon, Portugal, pp. 1-5, Aug. 2015.

[13] P. A. Dzagbletey, J. Shim and J. Chung, "Quarter-Wave Balun Fed Vivaldi Antenna Pair for V2X Communication Measurement," *IEEE Transactions on Antennas and Propagation*, vol. 67, no. 3, pp. 1957-1962, Mar. 2019.

Mohamed O. Khalifa received the B.S. degree in electrical and electronic engineering from the University of Khartoum, Khartoum, Sudan, in 2010 and the M.S. degree in electrical engineering from the King Fahd University of Petroleum and Minerals, Dhahran, KSA, in 2015. He is currently working toward the Ph.D. degree in electrical and computer engineering with Oakland University, Rochester, MI, USA.

He served as a Research Assistant with the King Fahd University of Petroleum and Minerals; as a Visiting Graduate Intern with I-Radio Lab within the School of Engineering, University of Calgary, Calgary, AB, Canada; and a Research Assistant with Applied EMAG

and Wireless Lab at Oakland University from 2012 to 2018. He has been employed with Ficosa North America, Madison Heights, MI, USA, from 2018 to 2019 and then with Molex LLC, Grand Blanc, MI, USA, from 2019 until present. His research interests reside in the areas of power amplifier design and linearization techniques and applied electromagnetics with emphasis on antenna measurements, antenna modeling/analysis, and antenna design. He has authored/co-authored around 13 technical papers and is an inventor on 3 patents.

Ahmad M. Yacoub received the B.S. degree in electrical engineering from the Princess Sumaya University for Technology, Amman, Jordan, in 2014 and the M.S. degree in electrical and computer engineering from Oakland University, Rochester, MI, USA, in 2018. He is currently working toward the Ph.D. degree in electrical and computer engineering with Oakland University.

He served as a Research Assistant with Applied EMAG and Wireless lab at Oakland University from 2016 to 2018. He has been employed with Molex LLC, Grand Blanc, MI, USA, from 2018 until present. His research interests reside in the area of applied electromagnetics with emphasis on antenna measurements, antenna modeling/analysis, and antenna design. He is an inventor/co-inventor of 2 patents.

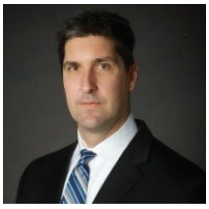

Daniel N. Aloi received the B.S., M.S., and Ph.D. degrees in electrical engineering from Ohio University, Athens, OH, USA, in 1992, 1996, and 1999, respectively.

He served as a Research Assistant from 1995 to 1999 with the Avionics Engineering Center within the School of Engineering and Computer Science, Ohio University; Summer Intern with Rockwell International, Cedar Rapids, IA, USA; and Senior Project Engineer with OnStar, Incorporated, a subsidiary of General Motors, from 2000 to 2002. He has been employed with the Electrical and Computer Engineering Department, Oakland University, Rochester, MI, USA, from 2002 until present. He is the Founder and Director of the Applied EMAG and Wireless lab at Oakland University. His research interests reside in area of applied electromagnetics with emphasis on antenna measurements, antenna modeling/analysis and antenna design. He has authored/co-authored more than 100 technical papers and is an inventor on 5 patents.

Dr. Aloi is a member of the Institute of Navigation and is a senior member of the Institute of Electrical and Electronics Engineers (IEEE). He has received in excess of $4M in research funding from a variety of federal and private entities including the Federal Aviation Administration, Defense Advanced Research Program Agency (DARPA), and the National Science Foundation (NSF).

A Wrench-Shaped UWB Antenna Yielding Dual Notched Bands for WLAN Application

Tongyu Ding, Mengyu Wang, Jie Guo, Liang Zhang*, and Jun Xiao*

School of Ocean Information Engineering
Jimei University, Xiamen 361021, China
*Corresponding author: liangzhang@jmu.edu.cn, xiaojun@jmu.edu.cn

***Abstract* –** A wrench-shaped ultrawideband (UWB) antenna with dual notched bands is proposed and investigated. The antenna has a wrench-shaped patch and two T-shaped slots on the ground, realizing the required UWB band. To achieve the dual notched band characteristics in upper and lower wireless local area network (WLAN) bands, an Omega-shaped slot is etched on the feedline and a novel composite right/left-handed electromagnetic bandgap (CRLH-EBG) structure is built on the ground. Measured results present an operating frequency band from 3.04 to 11.4 GHz, with two notched bands of 5.1–5.4 GHz (uplink of WLAN band) and $5.7-5.98$ GHz (downlink of WLAN band), respectively. Both measured and simulated results of the proposed antenna are exhibited, promising that the antenna applies to UWB applications and can precisely overcome WLAN interference.

***Index Terms* –** UWB antenna, dual notch band, WLAN.

I. INTRODUCTION

The growing demand for wideband devices with anti-interference performance toward the fifth generation (5G) framework and radio frequency (RF) region has prompted a wide and continuous interest in notch band ultrawideband (UWB) antennas [1, 2]. On one hand, numerous antennas have been designed to pursue a wider operating bandwidth, satisfying the needs for higher data rates in 5G deployment [3]. On the other hand, they are also required to possess band-notch function, which is necessarily indispensable for anti-interference in various 5G communication scenarios [4].

Since microstrip patch antennas provide several advantages such as low profile and low expenses, they have rapidly become a good choice for UWB applications [5, 6]. Originally, microstrip UWB antennas mostly adopted straightforward geometric shapes using half-cutting and folding technologies, etc. [7, 8]. More recently, novel structures as well as patch shapes have been derived such as axe-shaped, tree-shaped, and polygon-shaped patches [9–11]; novel designs such as exponential-curve-edged log-periodic slot antenna have also been reported in UWB applications [12], all of which testified the feasibility of planar microstrip designs in pursuit of superior UWB characteristics.

As for band notching techniques, etching different curved slots, such as U-shaped and double C-shaped slots on the radiating patch or feedline [11, 12], placing stubs in a suitable position on the patch to impose certain limitation to electromagnetic signal, etc., have been well reported [12, 13]. For instance, in [12], a double band-notched effect has been produced by using two *L*-shaped stubs of different lengths. More recently, band notching techniques of using parasite elements or implanting the electromagnetic bandgap (EBG) and split ring resonator (SRR) structures have also been reported [13–26], such as [19]; it uses mushroom-shaped EBGs with open meander slits to realize notched frequency bands around 3.5 and 5.5 GHz. To highlight, the natural isolation performance of notch structures has been widely used for multi-input multi-output (MIMO) systems [20, 21, 23].

Nevertheless, it is still a non-trivial task to realize two or more narrowed rejected bands that are quite adjacent to each other, meanwhile maintaining the UWB characteristics over the entire frequency band. As we know, structures operating at adjacent frequencies in limited space are subject to serious interference, thus bringing about degradation or even malfunction of the antenna and hindering its use in wireless scenarios with such needs. It is, therefore, of paramount significance to develop band-notch designs that not only achieve excellent notching effects but also create a compatible companion network.

This paper proposed a microstrip UWB antenna with a wrench-shaped radiating patch and T-shape-grooved ground, which realized good impedance match and, therefore, UWB property from 3.04 to 11.4 GHz. It then combined the strength of etching and loading techniques and realized one narrow rejected band at 5.725–5.875 GHz by etching a bent slot design on the feedline and another at 5.15–5.35 GHz by constructing an EBG strip design on the ground plane. It is worth noting that

Submitted On: December 23, 2021
Accepted On: January 31, 2022

https://doi.org/10.13052/2022.ACES.J.370306

these two bands are exactly the uplink and downlink of wireless local area network (WLAN) band, endowing the antenna with qualities in overcoming interference from WLAN bands precisely. More importantly, it implemented the design as well as the fabrication within a limited space (a total size of $40 \times 32 \times 1.2\text{mm}^3$) where two distinct notching structures operating at adjacent frequency bands sustained peacefully. To highlight, the two notched bands are limited to only 1-GHz bandwidth and are capable of suppressing coupling interference efficiently. Each notched band achieved reasonable notch properties and occupied no more than 300-MHz bandwidth, which is precisely targeted and saves the frequency band resources effectively. The remainder of this paper is organized as follows. Section II gives a brief description of the antenna configuration as well as the design process. The two approaches of band-notching as well as effect analysis are also detailed in this section. Simulated and measured results are demonstrated in Section III and conclusions are drawn in Section IV.

II. METHODOLOGY

In this section, we first make an explanation for evolution principles of the plier-shaped radiated patch and then discuss design of slots and EBG loading for band-notch effects. Figure 1 illustrates the geometry of the overall UWB antenna. The front of the antenna consists of a wrench-shaped patch and feedline, on which a bent slot is etched to realize one rejected band, as can be seen in Figure 1(a). The ground is grooved and loaded with an EBG structure, as can be seen in Figure 1(c). The EBG strip is connected to the patch through a via with diameter $D_v = 0.3$ mm. We use FR-4 (e_r= 4.4) as substrate with a length L_g = 40 mm, width W_g= 32 mm, and a thickness of t = 1.2 mm. All design parameters are depicted in Figures 1(b) and (d) and are as listed in Table 1 for reference.

Table 1: Dimensions of the proposed antenna

Par.	Value (mm)	Par.	Value (mm)	Par.	Value (mm)
L_g	40	W_4	30	E_1	5.8
W_g	32	W_5	6	E_2	1.4
W_1	2.6	W_6	3.5	E_3	2.2
L_1	16.9	W_7	1.8	E_4	2.6
W_2	10	L_5	15	E_5	1
L_2	10	L_6	4	S_1	0.8
W_3	4	L_7	5	S_2	7.4
L_3	6.5	L_8	5	S_3	0.3
L_4	2	L_9	16	W_e	0.4
D_v	0.3	t	1.2	W_s	0.3

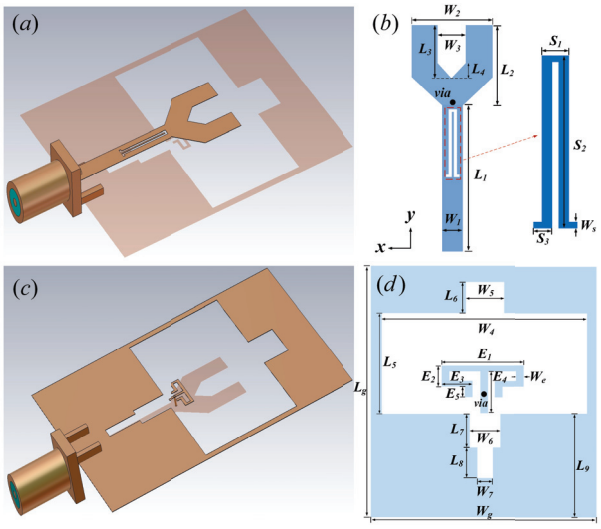

Fig. 1. Geometry of the proposed antenna. (a) Top view of the antenna 3D model. (b) Description of the patch and feedline. (c) Bottom view of the antenna 3D model. (d) Description of the ground and EBG structure.

A. Design of the patch

Figure 2 describes the optimization process of the patch and ground. The patch was initially square and the ground was also simply square grooved. A small size T-shaped slot was etched on the ground afterwards to slightly tune the resonant frequency, as shown in Ant. 2 of Figure 2. In order to realize a wider bandwidth, the patch shape was further optimized and the structure of Ant. 3 was proposed. The wrench-shaped patch succeeded in broadening the frequency band from 2.4 to 12 GHz along with the two T-shaped groove backside. It is obvious from Figure 2 that the S_{11} curve of Ant. 3 is the best among the three conditions because this configuration excited surface current more efficiently over the entire frequency band. The gains of antennas with the three different shapes are also shown in Figure 2.

B. Band-Notch techniques for upper WLAN band

Embedding varieties of slots on the feedline or patch of antenna to obtain notched band has been widely studied and applied. The slots can produce an effect equivalent to resonant circuit and conducive to the integration of the microstrip planar antenna. However, the length and width of slot as well as its position may generate distinct results.

In this work, thickness and permittivity of the substrate are taken into account during the UWB antenna design process. We calculated resonant frequency for 5.8 GHz through the following formula:

$$f_r = \frac{c}{2L\sqrt{\dfrac{2}{\varepsilon_r + 1}}}, \tag{1}$$

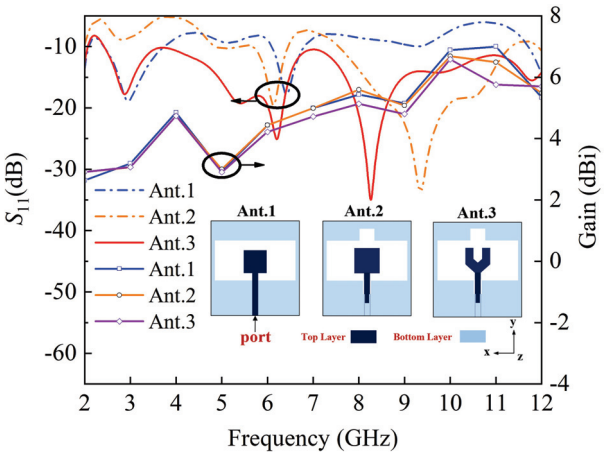

Fig. 2. S_{11} and gain of antenna vs. evolution of patch.

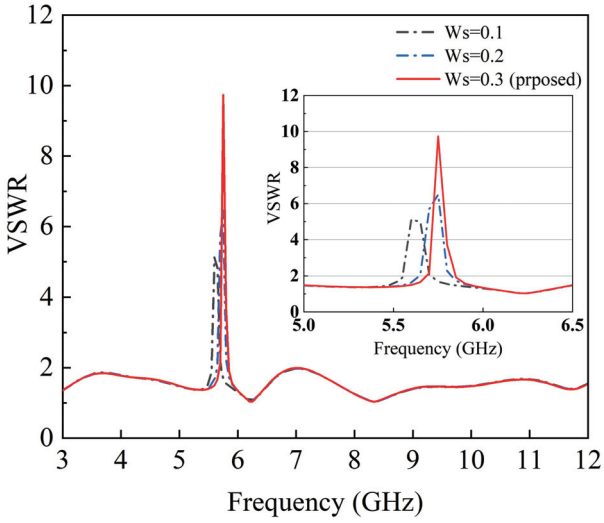

Fig. 3. VSWR of antenna for different values of W_s.

where f_r is resonant frequency for notched band, c is the speed of light in vacuum, L is the sum of the physics length, and ε_r is the dielectric constant of antenna substrate. This equation does not mention the width of the slots; however, width of the slots may produce certain influence on resonant frequencies. Based on eqn (1), preliminary parameter values can be calculated, which, however, are far from satisfying. Regarding the shape and location of the slot, as well as the manufacturing process, the parameters must be further optimized.

Based on the above analysis, a slot similar to Ω shape was proposed. Figure 3 shows the VSWR simulation results for parameter W_s varying from 0.1 to 0.3 mm when the parameter S_2 is fixed to 7.4 mm. In contrast, Figure 4 shows how the variation of parameter S_2 tuned the notched band when W_s is fixed at 0.3 mm. It is not difficult to find out that width of slot and

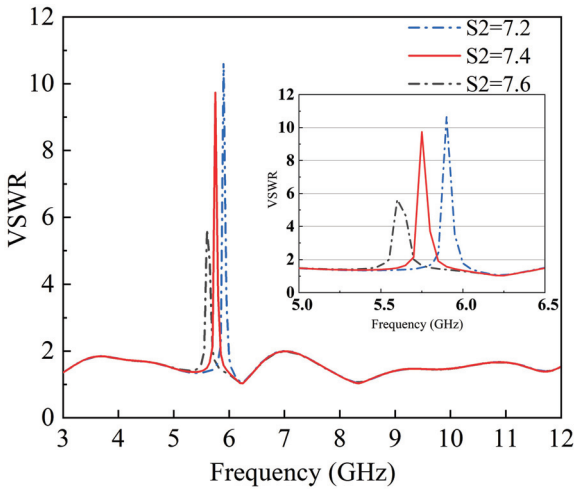

Fig. 4. VSWR of antenna for different values of S_2.

length of the slot determined the center frequency of the notched band jointly. It is determined that the center of notched band at 5.8 GHz is achieved when W_s is equal to 0.3 mm and S_2 is equal to 7.4 mm, verifying that the stop band range of upper WLAN band (5.725–5.875 GHz) is achieved.

C. Study of Band-Notch techniques for lower WLAN band

Given the design of Part B, to realize another notch effect at the lower WLAN band (5.15–5.35 GHz), it is quite necessary to reduce the effect of coupling, especially for compact antennas. In the schematic structure diagram of the traditional mushroom-shaped EBG, as shown in Figure 5(a). The metallic EBG structure is etched on the top side of antenna and connected to the ground by via, which produced LC shunt circuit. In this article, we proposed an EBG structure as shown in Figure 5(b), the EBG strips and patch are separate and connected by via, which also forms an LC shunt circuit. The proposed EBG structure possessed EBG characteristic in terms of principle. In this sense, a novel EBG structure is proposed and built on the ground plane to realize the desired band-notch feature, meanwhile suppressing the coupling as was a filter.

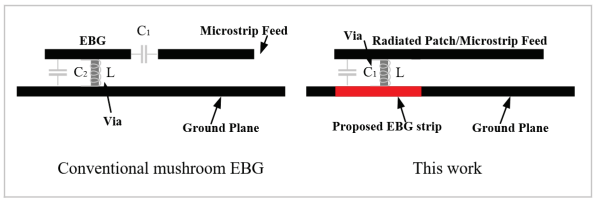

Fig. 5. Schematic view of conventional EBG structure and this work. (a) Mushroom EBG. (b) This work.

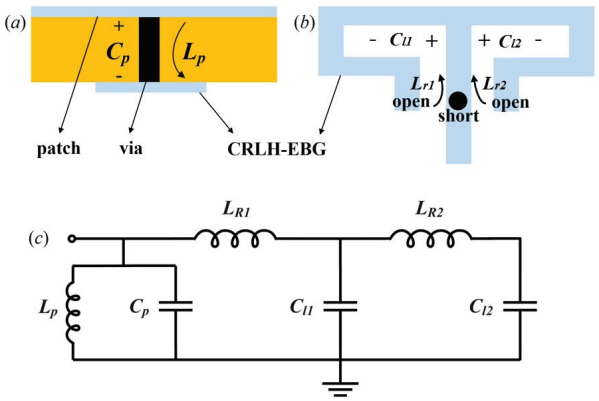

Fig. 6. Principle of EBG structure. (a) Side view. (b) Top view of the EBG strip. (c) Equivalent circuit model.

As we all know, composite right/left-handed (CRLH) transmission line has been widely used to realize novel EBG design, and we used the interdigital method to realize a CRLH-EBG structure. Figure 6(a) illustrates the side view of the EBG structure and Figure 6(b) shows the plan view of it. The relationship between the size of the structure and resonant frequency can be expressed by the following formulas:

$$l_n = n\frac{c}{4f}, \tag{2}$$

$$\theta_n = \beta_n l_n = n\frac{\pi}{2}, \tag{3}$$

where n is odd, l_n is the length of the open-loop, and f is the resonant frequency, namely, the length of the loop is a quarter of the resonant wavelength, or the electrical length is an odd multiple of $p/2$. The length of the proposed antenna is $l/4$ makes it a potential candidate for compact microstrip antenna application.

To further understand the behavior of the CRLH-EBG structure in Figures 6(a) and (b), an equivalent circuit model is constructed in Figure 6(c). The via connecting the patch and the EBG structure in Figure 6(a) brings about parasite inductance L_P and capacitance C_p and, therefore, was modeled as L_p and C_p in Figure 6(c). It can be defined as right-hand capacitance and inductance. The generated capacitances C_{l1} and C_{l2} are used to characterize the left-handed capacitance and the shorted microstrip branch is used to characterize the left-handed inductances L_{r1} and L_{r2}, as shown in Figure 6(b). It is then obvious that the above resonant circuit represented a filter model, the resonant frequency of which is calculated to be 5.25 GHz, meaning impedance mismatch at this point.

According to the above analysis and calculation, we have decided the value of E_1 to be the most significant factor and its values should be limited between 5.4 and 6. Figure 7 exhibits the optimization process of parameter E_1. The simulated results of VSWR versus E_1 demonstrate that the resonant frequency decreases as E_1 increases, and the optimal value of E_1 should be 5.8 mm.

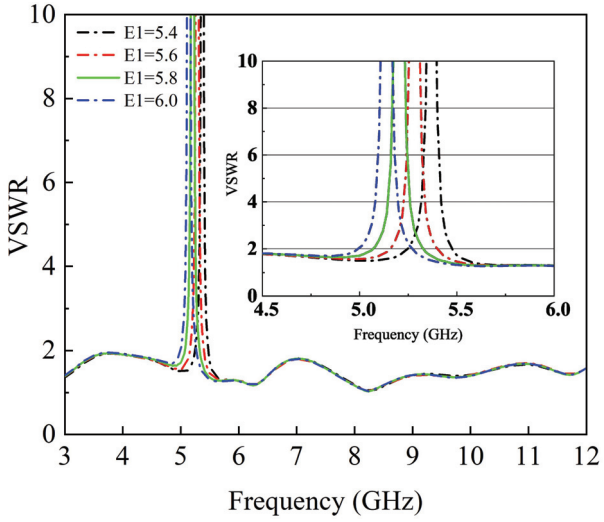

Fig. 7. VSWR of antenna for different values of E_1.

Since the proposed notching structures are aimed at two adjacent frequencies, Figures 8(a) and (b) show the surface current distribution of the antenna at resonant frequencies of 5.25 and 5.8 GHz, respectively. In Figure 8(a), the CRLH-EBG structure proposed in this paper concentrates a strong current, whereas the Omega-shaped slot etched on the feeding line produces only a weak current, which can be drawn that the CRLH-EBG structure has an effect alone at 5.25 GHz. On the contrary, the obvious strong current distribution is generated at the edge of the Omega-shaped slot in Figure 8(b), while the EBG structure on the upper side

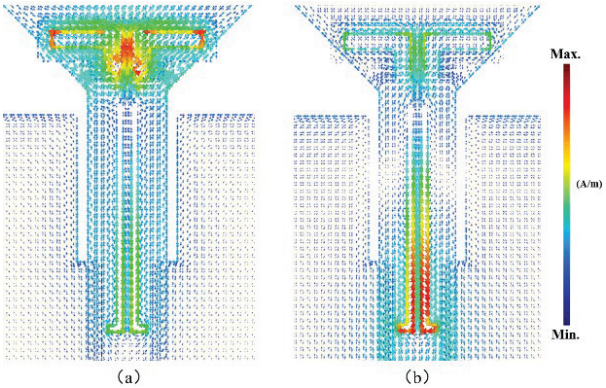

Fig. 8. Surface current distribution of the proposed antenna at (a) 5.25 and (b) 5.8 GHz.

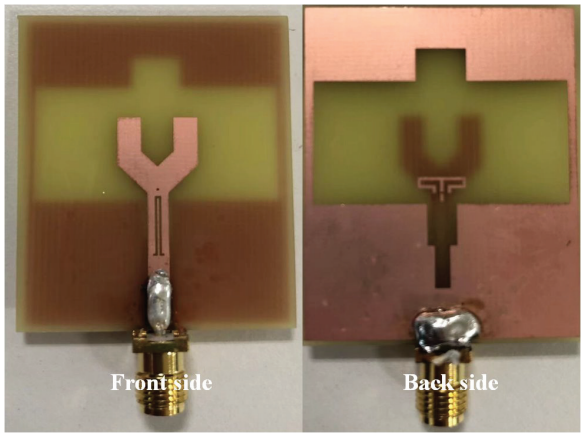

Fig. 9. Photograph of the fabricated antenna.

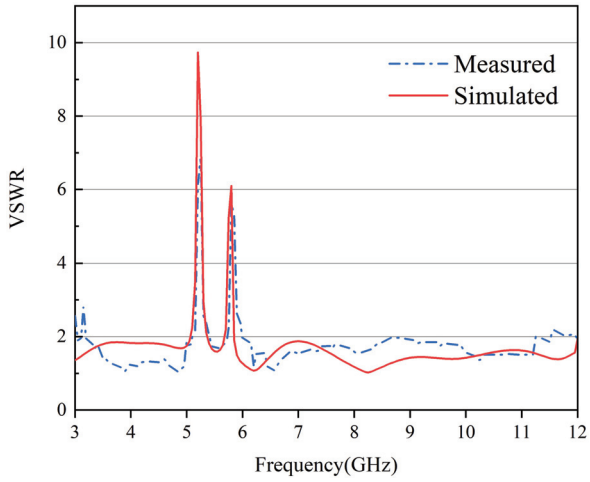

Fig. 10. Simulated and measured VSWR of the proposed antenna.

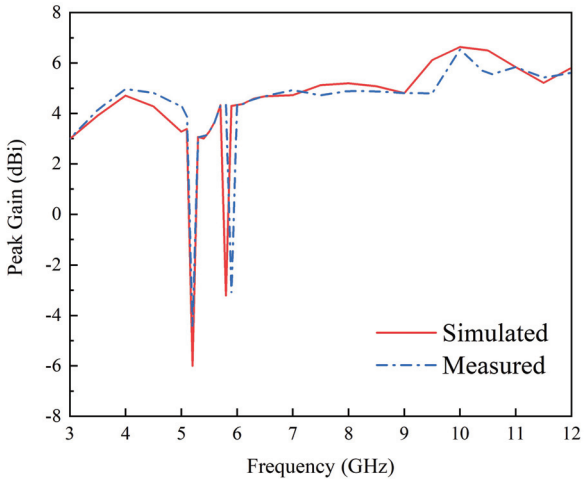

Fig. 11. Simulated and measured gains of the proposed antenna.

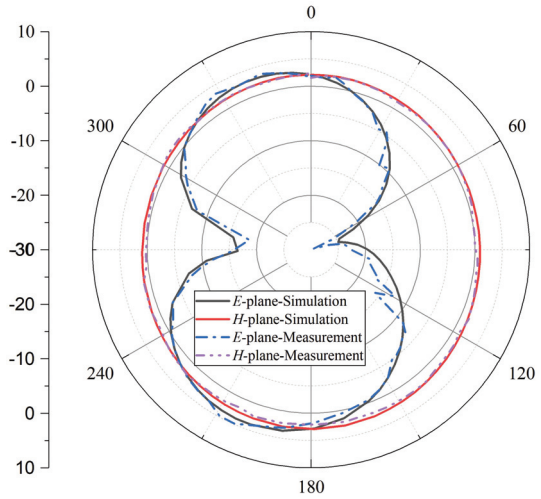

(a) 3.5 GHz

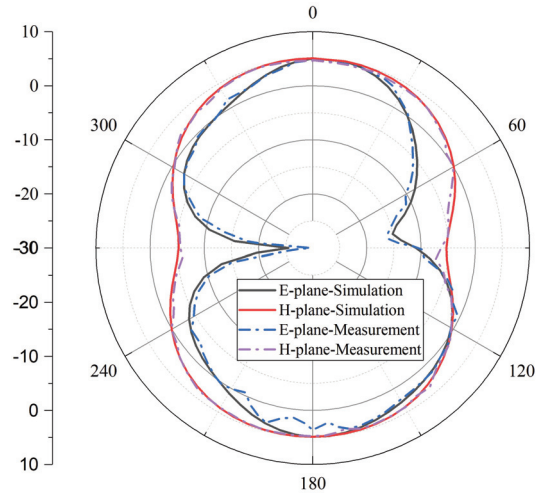

(b) 7.5 GHz

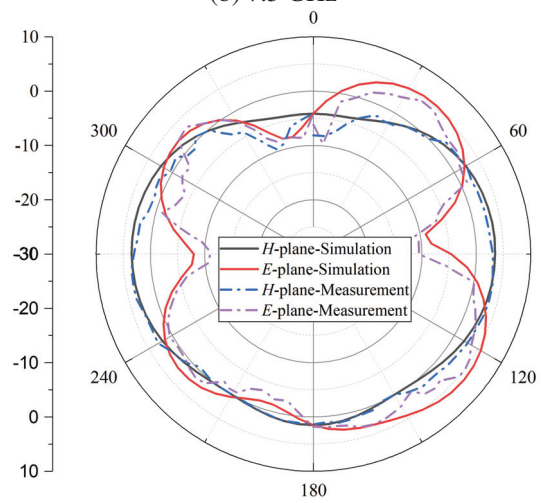

(a) 9.5 GHz

Fig. 12. Simulated and measured radiation patterns in *E*- and *H*-plane at 3.5, 7.5, and 9 GHz, respectively.

has only gathered a small current concentration. It can be concluded that the slot achieves resonance at the 5.8-GHz frequency point and produces a notch effect. Furthermore, Omega-shaped slot formed a closed-loop resonant tank, while the proposed EBG structure formed an open-loop resonant tank. And they produced two different resonances. In summary, these two structures work independently and there exists almost no interaction between them.

III. MEASUREMENT AND DISCUSSION

The antenna prototype was fabricated and shown in Figure 9. It was measured with Agilent E8362B vector network analyzer. Figure 10 presents the simulated and the measured VSWR for the proposed antenna. Measured results show that the antenna provides an impedance bandwidth (VSWR < 2) from 3.04 to 11.4 GHz except the notch band of 5.1–5.4 and 5.72–5.98 GHz.

The bandwidth requirement for UWB applications is satisfied, and the dual notched bands presented good notch characteristics for the lower (5.15–5.35 GHz) and upper (5.725–5.875 GHz) WLAN bands. Figure 11 shows the measured and simulated peak gain results. Both results are well-matched. It can be observed that the gain curve rises as the frequency increases, and the gain drops sharply at the notched frequency bands. Simulation and measurement are in good agreement.

The radiation pattern in *E*-plane (*xz*-plane) and *H*-plane (*yz*-plane) at 3.5, 7.5, and 9.5 GHz of measured and simulated results are shown in Figure 12. The proposed antenna presents an omni-directional characteristic in *H*-plane and bi-directional patterns in *E*-plane for all simulated and measured results.

IV. CONCLUSION

The proposed wrench-shaped UWB antenna has realized an impedance bandwidth of 3.04–11.4 GHz. The approaches of etching an Omega-shaped slot on the feedline and building a novel CRLH-EBG structure have achieved notched features at uplink (5.725–5.875 GHz) and downlink (5.15–5.35 GHz) of WLAN frequency bands, respectively. There is almost no interference between these two structures. Measured and simulated results of the proposed antenna are in good agreement substantially. The peak gain value of the proposed antenna is 6.53 dBi, while it sharply decreases to –4.5 dBi at notched bands.

ACKNOWLEDGMENT

This work was supported by the Educational Department of Fujian Province under Grant JAT210214 and Grant JAT190298, National Fund Cultivation Program of Jimei University under Grant ZP2020035 and Youth Top Talent Program of Jimei University under Grant ZR2019001.

REFERENCES

[1] M. S. Khan, A. Iftikhar, R. M. Shubair, A. D. Capobianco, B. D. Braaten, and D. E. Anagnostou, "Eight-element Compact UWB-MIMO/diversity Antenna with WLAN Band Rejection for 3G/4G/5G Communications," *IEEE Open J. Antennas Propag.*, vol. 1, pp. 196-206, 2020.

[2] C. C. Rong, W. Xiao, Y. H. Xu, and M. Y. Xia, "A Double Band-notched UWB Antenna for Flexible RF Electronics," *Applied Computational Electromagnetics Society (ACES) Journal*, vol. 32, no. 5, pp. 413-417, Jan. 2017.

[3] R. Gupta, M. M. Patel, S. Tanwar, N. Kumar, and S. Zeadally, "Blockchain-based Data Dissemination Scheme for 5G-enabled Softwarized UAV Networks," *IEEE Trans. Green Commun. Networking*, vol. 5, no. 4, pp. 1712-1721, Dec. 2021.

[4] X. J. Liao, H. C. Yang, N. Han and Y. Li., "UWB Antenna with Dual Narrow Band Notches for Lower and Upper WLAN Bands," *Electron. Lett.*, vol. 46, no. 24, Nov. 2010.

[5] Y. Jia, S. Jin, and P. Savi, "GNSS-R Soil Moisture Retrieval Based on a XGboost Machine Learning Aided Method: Performance and Validation," *Remote Sens.*, vol. 11, no. 14, 2019.

[6] M. K. Shereen, M. I. Khattak and J. Nebhen, "A Review of Achieving Frequency Reconfiguration through Switching in Microstrip Patch Antennas for Future 5G Applications," *Alexandria Engineering Journal*, vol. 61, no. 1, pp. 29-40, 2021.

[7] G. Gao, B. Hu and J. Zhang, "Design of a Miniaturization Printed Circular-slot UWB Antenna by the Half-cutting Method," *IEEE Antennas Wirel. Propag. Lett.*, vol. 12, pp. 567-570, 2013.

[8] G. Teni, N. Zhang and J. Qiu, "Research on a Novel Folded Monopole with Ultrawideband Bandwidth," *IEEE Antennas Wirel. Propag. Lett.*, vol. 13, pp. 802-805, 2014.

[9] C. Dikmen, S. Cimen, and G. Cakir, "Design of Double-sided Axe-shaped Ultra-wideband Antenna with Reduced Radar Cross-section," *IET Microwaves Antennas Propag.*, vol.8, pp. 571-579, 2014.

[10] H. Zhu and Q. X. Chu, "Ultra-wideband Bandpass Filter with a Notch-band Using Stub-loaded Ring Resonator," *IEEE Microwave Wirel. Compon. Lett.*, vol. 23, no. 7, pp. 341-343, July 2013.

[11] T. Sedghi, V. Rafii, and M. Moosazadeh, "UWB Monopole Antenna with Compact Polygon-shaped Patch for Portable Devices," *Applied Computational Electromagnetics Society (ACES) Journal*, vol. 29, no. 1, pp. 67-70, Jan. 2014.

[12] W. C. Weng and M. C. Chang, "Ultra-wideband Planar Log-periodic Slot Antenna with Exponential

Shapes on Slot Edges," *Applied Computational Electromagnetics Society (ACES) Journal*, vol. 34, no. 9, pp. 1280-1286, Sep. 2019.

[13] S. H. Yeung, K. F. Man and W. S. Chan, "Multiple Circular-sector Structures for Wideband Planar Monopole Antenna Designs Covering 146% fractional bandwidth," *IEEE Antennas Propag. Mag.*, vol. 54, no. 1, pp. 76-94, Feb. 2012.

[14] A. Taibi, M. Trabelsi and A. A. Saadi, "Efficient Design Approach of Triple Notched UWB Filter," *AEU – I. J. Electron. Commun.*, vol. 131, March 2021.

[15] W. Jiang and W. Che, "A novel UWB Antenna with Dual Notched Bands for WiMAX and WLAN Applications," *IEEE Antennas Wirel. Propag. Lett.*, vol. 11, pp. 293-296, 2012.

[16] R. Aldhaheri, I. Alruhaili, K. Babu and M. Sheikh, "A Compact CPW-fed UWB Antenna with Dual-band Notched Characteristics for WiMAX/WLAN Applications," *Applied Computational Electromagnetics Society (ACES) Journal*, vol. 36, no. 2, pp. 145-151, 2021.

[17] J. Y. Siddiqui, C. Saha and Y. M. M. Antar, "Compact Dual-SRR-loaded UWB Monopole Antenna with Dual Frequency and Wideband Notch Characteristics," *IEEE Antennas Wirel. Propag. Lett.*, vol. 14, pp. 100-103, 2015.

[18] M. Yazdi and N. Komjani, "Design of a Band-notched UWB Monopole Antenna by Means of an EBG Structure," *IEEE Antennas Wirel. Propag. Lett.*, vol. 10, pp. 170-173, 2011.

[19] F. Alizadeh, C. Ghobadi, J. Nourinia and H. Abdi, B. Mohammadi, "UWB Dual-notched Planar Antenna by Utilizing Compact Open Meander Slitted EBG Structure," *AEU-I. J. Electron. Commun.*, vol. 136, July. 2021.

[20] Q. Li, Y. F. Sun and H. Y. Fang, "Compact ACS-fed UWB MIMO Antenna with Dual Band Notches," *Applied Computational Electromagnetics Society (ACES) Journal*, vol. 36, no. 1, pp. 55-60, Jan. 2021.

[21] L. Y. Chen, W. S. Zhou, J. S. Hong and M. Amin, "A Compact Eight-port CPW-fed UWB MIMO Antenna with Band-notched Characteristic," *Applied Computational Electromagnetics Society (ACES) Journal*, vol. 35, no. 8, pp. 887-892, Jan. 2020.

[22] M. Ghahremani, "Miniaturised UWB Antenna with Dual-band Rejection of WLAN/WiMAX Using Slitted EBG Structure," *IET Microwaves Antennas Propag.*, vol. 13, no. 3, pp. 360-366, 2019.

[23] E. Thakur, N. Jaglan and S.D. Gupta, "Design of Compact Triple Band-notched UWB MIMO Antenna with TVC-EBG Structure," *J. Electromagn. Waves Appl.*, vol. 34, pp. 1-15, 2020.

[24] P. P. Bhavarthe, S. S. Rathod and K. T. V. Reddy, "A Compact Dual Band Gap Electromagnetic Band Gap Structure," *IEEE Trans. Antennas Propag.*, vol. 67, no. 1, pp. 596-600, Jan. 2019.

[25] B. Feng, L. Li, J. Cheng and C. Sim, "A Dual-band Dual-polarized Stacked Microstrip Antenna with High-isolation and Band-notch Characteristics for 5G Microcell Communications," *IEEE Trans. Antennas Propag.*, vol. 67, no. 7, pp. 4506-4516, July 2019.

[26] L. Peng, B. J. Wen, X. F. Li, X. Jiang and S. M. Li, "CPW Fed UWB Antenna by EBGs with Wide Rectangular Notched-band," *IEEE Access*, vol. 4, pp. 9545-9552, 2016.

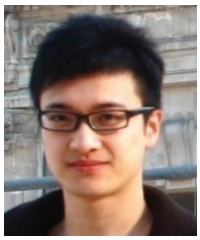

Tongyu Ding was born in Heilongjiang, China, in 1987. He received the M.S. degree from the Harbin Institute of Technology, Harbin, China, and the Ph.D. degree in electronics and communication engineering from the Politecnico di Torino, Turin, Italy, in 2011 and 2015, respectively.

He is currently an Associate Professor with the School of Ocean Information Engineering, Jimei University, Xiamen, China. His recent research interests include antennas and numerical techniques for 5G wireless communications.

Mengyu Wang was born in Anhui province, China. He received the bachelor's degree from Huainan Normal University, Anhui, China, in 2019. He is currently working toward the master's degree in information and communication engineering with Jimei University, Xiamen, China.

His research activities include antennas and millimeter wave channel modeling.

Jie Guo was born in Shaanxi province, China, in 2018. He received the bachelor's degree from the Xi'an University of Posts & Telecommunications, Shaanxi, China, in 2021. He is currently working toward the master's degree in information and communication engineering with Jimei University, Xiamen, China.

His research activities include the directional bipolarization antenna system and reconfigurable intelligent surface.

Liang Zhang received the B.S. degree in communications engineering and the M.S. and Ph.D. degrees in microelectronics and solid-state electronics from the Harbin Institute of Technology, Harbin, China, in 2004, 2007, and 2013, respectively.

After graduation, he joined Xiamen University, Xiamen, China, as a Postdoctoral Fellow. Currently, he is an Associate Professor with Jimei University, Xiamen, China. His recent research interests mainly include novel RADAR systems, smart antennas, and reconfigurable intelligent surface.

Jun Xiao received the B.S. and M.S. degrees from the Harbin Institute of Technology, Harbin, China, and the Ph.D. degree from the Beijing University of Posts and Telecommunications, Beijing, China, respectively.

In 2019, he joined the School of Ocean Information Engineering, Jimei University, Xiamen, China. His current research interests include millimeter-wave antennas and THz antennas.

Design and Development of Substrate Integrated Waveguide Based Filtenna for X Band Application

G. S. Annie Grace Vimala[1], V. R. Prakash[2], A. Akilandeswari[1], D. Sungeetha[1], and M. Saravanan[3]

[1]Department of Electronics and Communication Engineering, Saveetha School of Engineering, SIMATS, Chennai 602105, India
anniegracevimalags.sse@saveetha.com, akilandeswaria.sse@saveetha.com, sungeethad.sse@saveetha.com

[2]Department of Electronics and Communication Engineering, Hindustan Institute of Technology and Science, Chennai 603103, India
Prakashkrishna53@gmail.com

[3]Department of Electronics and Communication Engineering, Vel Tech Rangarajan Dr. Sagunthala R&D Institute of Science and Technology, Chennai 600062, India
msarawins@gmail.com

Abstract – In this paper, substrate integrated waveguide based filtenna operating at X band is proposed. The model is designed on a low-loss dielectric substrate having a thickness of 1.6 mm and comprises shorting vias along two edges of the substrate walls. To realize a bandpass filter, secondary shorting vias are placed close to primary shorting vias. The dimension and position of the vias are carefully analyzed for X band frequencies. The model is fabricated on Roger RT/duroid 5880 and the performance characteristics are measured. The proposed model achieves significant impedance characteristics with wider bandwidth in the X band. The model also achieves a maximum gain of 7.46 dBi in the operating band, thus making it suitable for X band applications.

Keywords – Antenna radiation patterns, filtenna, microstrip patch, rectangular wave guide (RWG), substrate integrate waveguide (SIW).

I. INTRODUCTION

Due to the increase in demand for multifunctional antennas in wireless communications, the size of the antenna profile is greatly reduced and also provides better feasibility in integration with high-frequency circuits. Recently, filtenna becomes popular since the RF space is occupied with much of the available spectrum, and, hence, the role of the filter along with the antenna becomes crucial. The substrate integrated waveguide (SIW) has proven to be a good choice because of its modular integration and low cost [1]. Most of the literature discusses the design of filter and antenna separately and are coupled with a 50 Ω impedance matching circuit which consumes much space in the antenna profile [2]. This can be replaced by placing a single filtenna design which reduces the overall antenna profile and also eliminates the need for an additional 50 Ω impedance matching circuit [3]. Utilization of both SIW technology along with filtenna further improves the antenna profile size and also improves the ease of fabrication and integration [4–6]. A compact SIW-based filtenna comprising the parasitic patch is proposed [7]. The model utilized a half-mode substrate integrated rectangular cavity to reduce its overall antenna size. In [8], an analysis of SIW structure for rat race couple is proposed. An SIW-based filtenna with reconfigurable nulls by means of electric and magnetic coupling structure is demonstrated [9]. Filtenna can also be designed by utilizing the synthesis of filter structures by placing vertical cavities as in [10]. Similarly, the filtenna can also be realized by placing three vertical cavities integrated with each other to achieve a wider FBW ratio. However, an increasing number of filter cavities to improve FBW results in wider profile thickness. A low-profile SIW-based filtenna is reported [11] with improved bandwidth characteristics that utilize a complementary split-ring resonator (CSRR) over the SIW structures. Most of the literature discusses filtenna operating at narrowband and also these filtenna are designed at lower operating frequencies with lossy transmission lines or with other complex geometries. Hence, there is need for designing filtenna with wide operating range and also with better miniaturization. In this paper, an SIW-based filtenna with improved bandwidth and radiation characteristics is proposed. The antenna is modeled on a low-loss roger substrate with a profile thickness of

Submitted On: August 24, 2021
Accepted On: February 8, 2022

https://doi.org/10.13052/2022.ACES.J.370307

1.6 mm which makes it feasible for the integration of other high-frequency circuits. The antenna is analyzed and fabricated to measure its performance characteristics and compared with other conventional models. Moreover, the filtenna exhibits sharp cutoff bands around the operating bands which makes it ideal for X band applications.

II. SUBSTRATE INTEGRATED WAVEGUIDE GEOMETRY

The dielectric-filled metallic waveguide can be realized by means of substrate integrated waveguide [12] which exhibits similar propagation characteristics. The design of the proposed antenna is as shown in Figure 1. The width "W" of SIW is calculated from center-to-center distance between the rows of vias. Each via has spacing "p" and has radius "r." The length of dielectric layer is "L." Let a and b denote the width and height of the rectangular waveguide, respectively. Assuming $a > b$, the propagating mode with the lowest cutoff frequency is TE10 (dominant mode). We calculate the radius of via using

$$a = \frac{C}{2f_{\text{cio}}\sqrt{\varepsilon_r}}. \tag{1}$$

The cutoff frequency of each propagating mode

$$f_{\text{cmm}} = \frac{C}{2\sqrt{\varepsilon_r}}\sqrt{\left(\frac{m}{a}\right)^2 + \left(\frac{n}{a}\right)^2} \tag{2}$$

where C is the speed of light in vacuum, m and n are mode numbers, and a and b are dimensions of the waveguide. For TE_{10} mode, the cutoff frequency is given as $f_c = \frac{c}{2a}$. For SIW, the dimension d_s is the distance between the SIW walls and is given by $d_s = a_d + \frac{d^2}{0.95p}$, where $a_d = \frac{a}{\sqrt{\varepsilon_r}}$ where d is the diameter of via and

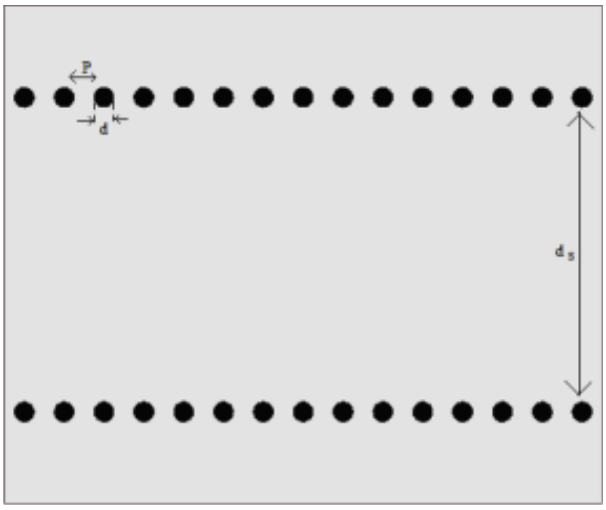

Fig. 1. SIW geometry. geometry.

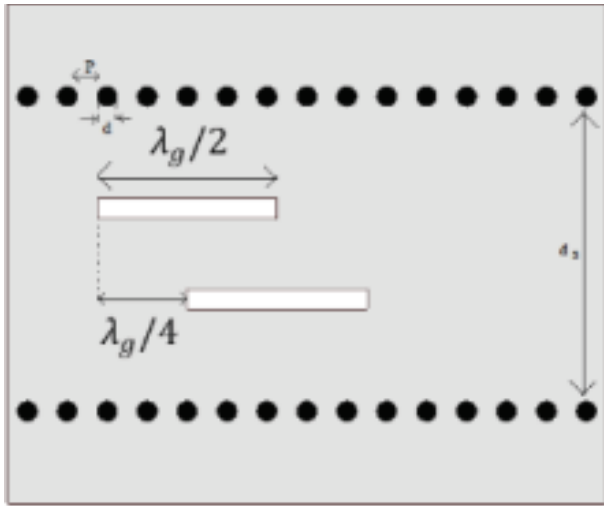

Fig. 2. Two-slot SIW.

Table 1 Geometry of SIW

Parameter	Specification
λ_g	9.25 mm
$L \times B$	25 mm × 30 mm
P	2 mm
d	1 mm
d_s	15.77 mm

p (p must satisfy $p < 2d$) is the distance between the vias. The guided wavelength is calculated from $\lambda_g = \frac{2\pi}{\sqrt{\frac{\varepsilon_r(2\pi f)^2}{c^2} - \left(\frac{\pi}{a}\right)^2}}$ and d must satisfy $d < \frac{\lambda_g}{5}$.

Based on the design equations, the geometry of the SIW along with two-slot geometry is shown in Figures 1 and 2 and its corresponding dimensions are given in Table 1 .

The surface current distribution at different instances of time "t" over the geometry is shown in Figure 3. The surface current distribution exhibits sinusoidal variation in the variations of the field on the surface of the structure and is confined within the SIW walls above its operating frequency. The antenna is modeled on roger duroid 5880tm having a relative permittivity of 2.2 and thickness of 1.6 mm. The -10 dB reflection coefficient curve corresponding to both SIW with and without slot geometry is given in Figure 4. The structure achieves -10 dB impedance characteristics over its entire operating X band which comprises 8–12 GHz with a cutoff frequency of 6.5 GHz.

SIWs have similar radiation characteristics when compared to dielectric filled metallic waveguide as shown in Figure 4 (S_{11} plot). Hence, longitudinal slots having a length of $\lambda g/2$ are incorporated in the SIW

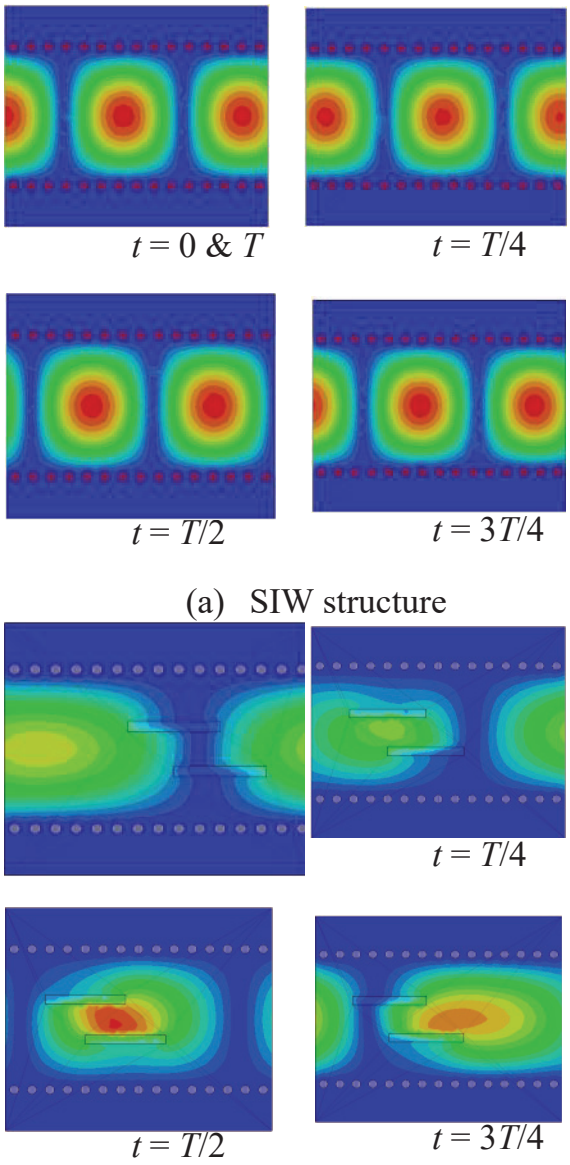

Fig. 3. Two-slot SIW.

structure which behaves like a resonant mode in the operating band. The phase constant β corresponding to the fundamental TE10 mode for given slotted SIW is given by

$$\beta=\sqrt{k_0^2\pm\left(\frac{\pi}{a}\right)^2}<k_0 \tag{3}$$

where k_0 is the wave number. Figure 5 shows the normalized phase constant $(\frac{\beta}{k_0})$ corresponding to SIW compared with slotted SIW structure. It is observed that the structure attains real phase value whose mode propagates above the cutoff frequency of 6.5 GHz.

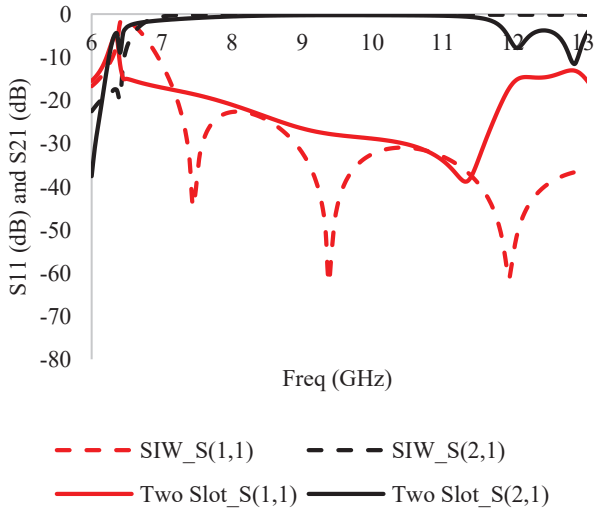

Fig. 4. Reflection and transmission coefficients (dB).

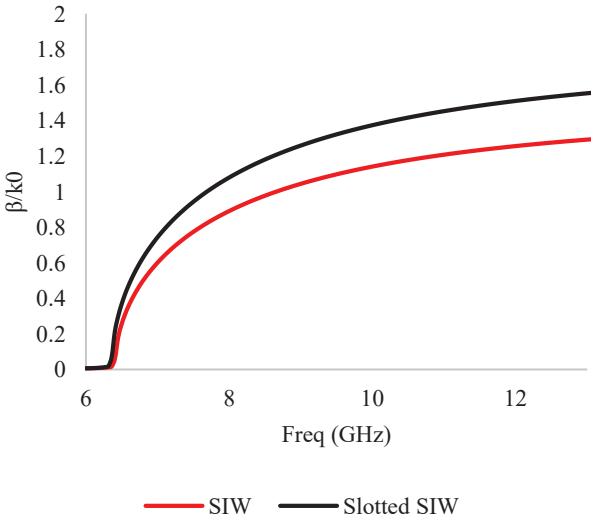

Fig. 5. Normalized phase constant $(\frac{\beta}{k_0})$.

The attenuation constant α is given by

$$\alpha=-\frac{1}{2L}\ln\left(|S_{11}|^2+|S_{21}|^2\right) \tag{4}$$

where L is the aperture length. Figure 6 shows the normalized attenuation characteristics of the SIW compared with slotted SIW structure. It is inferred that the structure attains minimum attenuation at its operating band. The dispersion characteristics of the antenna are determined from phase constant and attenuation constant of the proposed SIW structure.

III. HIGHER ORDER INDUCTIVE BASED FILTER DESIGN

A higher order inductive filter is proposed as shown in Figure 5. The filter comprises metallic vias placed to

provide inductive window having a width of W_i $(i \in 1,2)$ and length of the cavity resonators are given by $2p$ as shown in Figure 5. The coupling coefficient between the filter sections is given by K and the resonating frequency of the filter is given by

$$F_{101} = \frac{C}{2\pi\sqrt{\mu_r \varepsilon_r}} \sqrt{\left(\frac{\pi}{W_i}\right)^2 + \left(\frac{\pi}{L_i}\right)^2} \tag{5}$$

where $L_i = 2 * p$.

IV. SIW-BASED FILTENNA

The proposed antenna geometry is integrating both SIW and filtenna as shown in Figure 7. The model utilizes microstrip to SIW transition [12] connected to 50 Ω microstrip line and integrated with SIW. The feed line is tapered need the antenna feeding point for better matching the impedance of the SIW structure with the input. The width and length of the tapered section are designed and optimized for impedance matching especially at higher frequencies.

The antenna is fabricated on low-cost roger substrate having a relative permittivity of 2.2 and a thickness of 1.6 mm. The model is connected with 50 Ω SMA connector.

In order to validate the performance characteristics of the antenna model, the performances of the prototype are measured and are compared with simulated results.

The impedance characteristics of the filtenna for both simulated and measured results are shown in Figure 8. The reflection coefficient curve corresponding to filtenna geometry achieves −10 dB impedance characteristics over its entire operating X band which comprises 8–12 GHz with sharp rolloff around its operating band. The radiation characteristics of the antenna are measured by the three-antenna gain method and the gain of the proposed model is calculated by means of the Friss transmis-

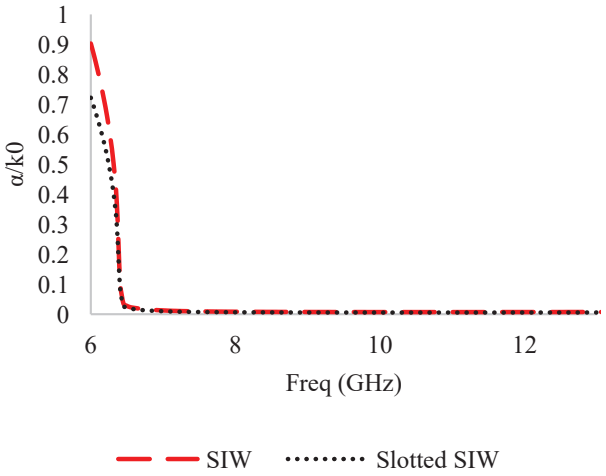

Fig. 6. Normalized attenuation constant $(\frac{\alpha}{k_0})$

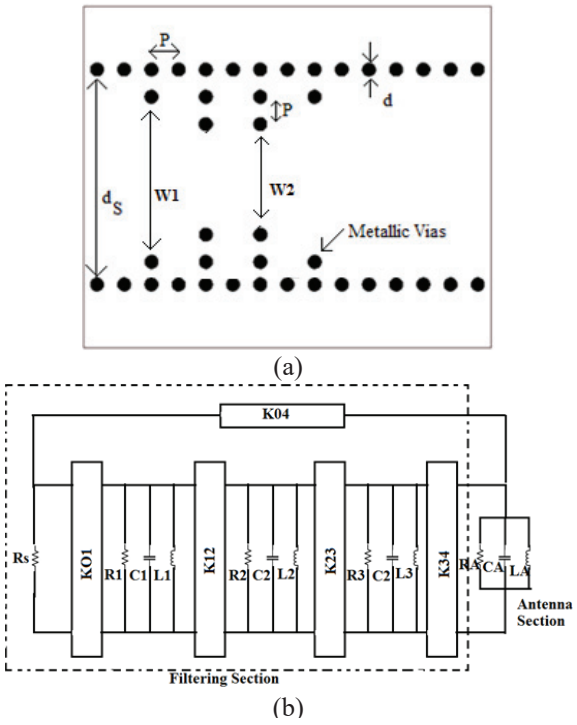

Fig. 7. Higher order inductive filter.

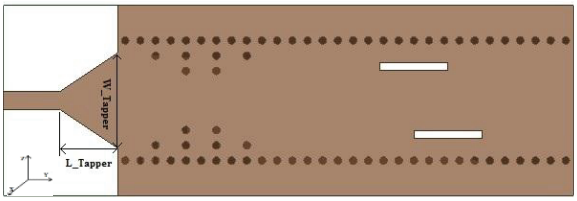

Fig. 8. Proposed SIW-based filtenna.

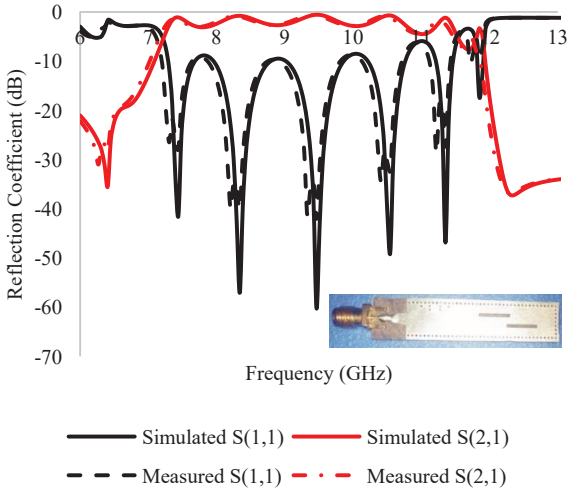

Fig. 9. Impedance characteristics of filter design.

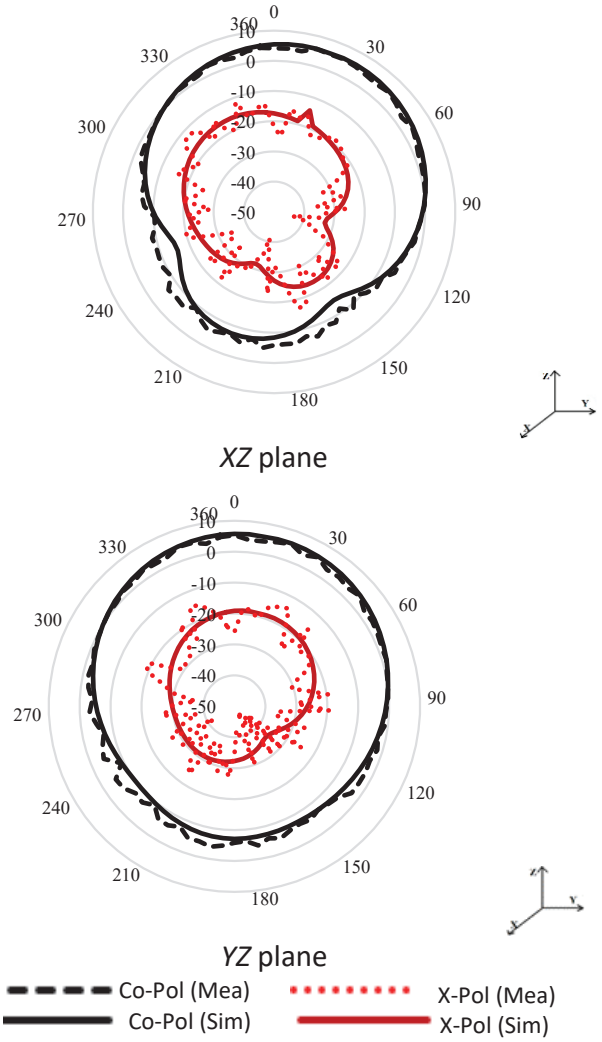

Fig. 10. Radiation characteristics.

sion equation given below

$$P_r = G_t G_r P_t \left(\frac{\lambda}{4\pi r}\right)^2. \quad (6)$$

The simulated and measured radiation characteristics of the antenna model are shown in Figure 9. The antenna radiation pattern is measured inside the anechoic chamber. The antenna achieves a symmetrical radiation pattern with a peak gain of 7.18 dBi for simulated and 6.94 dBi for measured at its 10 GHz center frequency in the operating band (8–12 GHz). Since the ground plane is limited due to its size limit, there is small amount of back radiation seen in the radiation pattern.

The proposed antenna is placed in line of sight with transmitting antenna inside the anechoic chamber. The realized gain corresponding to the proposed antenna is noted for different frequencies in the operating band and is compared with simulated gain as shown in Figure 10.

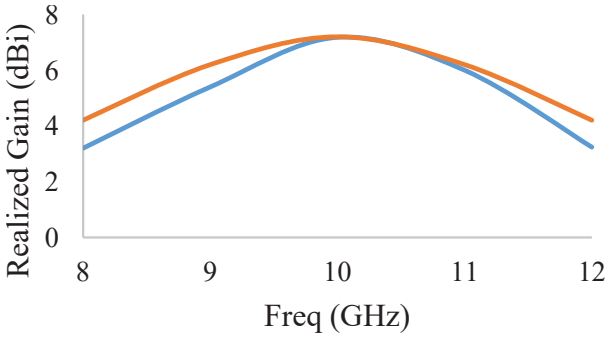

Fig. 11. Realized gain (dBi).

V. CONCLUSION

A compact SIW-based filtenna operating at X band frequencies is proposed. The model utilizes filter section integrated with SIW-based slotted section. The microstrip to taper transition is used for impedance matching and is terminated with 50 Ω transmission line. The model is analyzed for dispersion characteristics and is fabricated on low-cost substrate. The prototype attains resonates at 8–12GHz in the X band region with a peak gain of 7.18 dBi for simulated and 6.94 dBi for measured at its resonant frequency.

REFERENCES

[1] Y. Cassivi, L. Perregrini, P. Bressan, K. Wu, and G. Conciauro, "Dispersion characteristics of substrate integrated rectangular waveguide," *IEEE Microw. Compon. Lett.,* vol. 12, no. 2, pp. 333–335, Feb. 2002.

[2] K. Zhou, C.-X. Zhou, and W. Wu, "Resonance characteristics of substrate-integrated rectangular cavity and their applications to dual-band and wide-stopband bandpass filters design," *IEEE Trans. Microw. Theory Techn.,* vol. 65, no. 5, pp. 1511–1524, May 2017.

[3] M.-C. Tang, Y. Chen, and R. W. Ziolkowski, "Experimentally validated, planar, wideband, electrically small, monopole filtennas based on capacitively loaded loop resonators," *IEEE Trans. Antennas Propag.*, vol. 64, no. 8, pp. 3353–3360, Aug. 2016.

[4] K. Xu, J. Shi, X. Qing, and Z. N. Chen, "A substrate integrated cavity backed filtering slot antenna stacked with a patch for frequency selectivity enhancement," *IEEE Antennas Wireless Propag. Lett.,* vol. 17, no. 10, pp. 1910–1914, Oct. 2018.

[5] K.-Z. Hu, M.-C. Tang, M. Li, and R. W. Ziolkowski, "Compact, low-profile, bandwidth-enhanced substrate integrated waveguide filtenna," *IEEE Antennas Wireless Propag. Lett.,* vol. 17, no. 8, pp. 1552–1556, Aug. 2018.

[6] K. Dhwaj, J. M. Kovitz, H. Tian, L. J. Jiang, and T. Itoh, "Half-mode cavity based planar filtering antenna with controllable transmission zeroes," *IEEE Antennas Wireless Propag. Lett.,* vol. 17, no. 5, pp. 833–836, May 2018.

[7] K. Hu, M. Tang, D. Li, Y. Wang, and M. Li, "Design of Compact, Single-Layered Substrate Integrated Waveguide Filtenna With Parasitic Patch," *IEEE Transactions on Antennas and Propagation*, vol. 68, no. 2, pp. 1134-1139, Feb. 2020, doi: 10.1109/TAP.2019.2938574.

[8] R. Dehdasht-Heydari, K. Forooraghi, and M. Naser-Moghadasi, "Efficient and Accurate Analysis of a Substrate Integrated Waveguide (SIW) Rat-Race Coupler Excited by Four U-Shape Slot-Coupled Transitions", *Applied Computational Electromagnetics Society (ACES) Journal*, vol. 30, no. 1, pp. 42-49, Feb. 2015.

[9] C. Wang, X. Wang, H. Liu, Z. Chen, and Z. Han, "Substrate Integrated Waveguide Filtenna With Two Controllable Radiation Nulls," *IEEE Access*, vol. 8, pp. 120019-120024, 2020, doi: 10.1109/ACCESS.2020.3005948.

[10] Y. Yusuf, H. T. Cheng, and X. Gong, "A seamless integration of 3-D vertical filters with highly efficient slot antennas," *IEEE Trans. Antennas Propag.*, vol. 59, no. 11, pp. 4016–4022, Nov. 2011.

[11] K. Hu, M. Tang, M. Li, and R. W. Ziolkowski, "Compact, Low-Profile, Bandwidth-Enhanced Substrate Integrated Waveguide Filtenna," *IEEE Antennas and Wireless Propagation Letters*, vol. 17, no. 8, pp. 1552-1556, Aug. 2018, doi: 10.1109/LAWP.2018.2854898.

[12] D. Deslandes and K. Wu, "Integrated microstrip and rectangular waveguide in planar form", *IEEE Microwave Wireless Compon Lett*., vol. 11, pp. 68–70, 2001.

[13] J. E. Rayas-Sanchez and V. Gutierrez-Ayala, "A general EM-based design procedure for single-layer substrate integrated waveguide interconnects with microstrip transitions," 2008 *IEEE MTT-S International Microwave Symposium Digest*, pp. 983-986, 2008, doi: 10.1109/MWSYM.2008.4632999.

Dr. G. S. Annie Grace Vimala is currently working as a professor in the department of signal and image processing, institute of ECE, saveetha school of engineering, simats, chennai, india. she did her ph.d in B.S. Aabdur Rahman university, Chennai, India. Her area of research interest includes medical image processing, electronics and pattern recognition. she has published more than 10 papers in indexed journals and also been a reviewer for Scopus and SCI journals.

Dr. V. R. Prakash faculty in the Department of Electronics and Communication Engineering, in HITS, Chennai, India. His major research work on Video processing and Image processing He is an active IEEE member and has published paper in Scopus and Web of science.

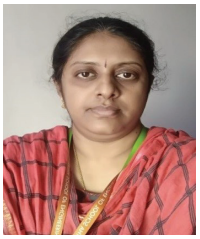

Dr. A. Akilandeswari completed her PhD in Electronics and Communication Engineering with specializing in Low Power VLSI. Her postgraduation was in Embedded systems technologies. She is presently working as an Associate Professor in Department of Electronics and communication Engineering, Saveetha school of Engineering, Chennai. Her present research areas include Low power VLSI, Imageprocessing, IOT.

Dr. D. Sungeetha faculty in the Department of Electronics and Communication Engineering, in Saveetha School of Engineering, Chennai, India. Her major research work on theory of communicating automata, formal verification using temporal logics, hybrid systems and cyber-physical systems with applications to collective robotics, distributed systems, fault tolerant computing, swarm robotics and theory of automata. She is an active IEEE member and has published paper in Scopus and Web of science.

Manavalan Saravanan was born in March 1989.He received his master of engineering degree (Communication system) from Anna University, Coimbatore, India in 2012. He did his Ph.D. degree in Electronics and Communication Engineering at the Hindustan University, India. He had two years of teaching experience in V.S.B. of college of engineering, India and more than 5 years of research experience in the field of reconfigurable antennas. Currently He is working as assistant professor at Vel tech University. His area of research includes Reconfigurable antennas, Metamaterials, and SIW based antennas.

Reduced Modeling for Electromagnetic Coupling to Randomly Wiring Automotive Cable Harness

Pei Xiao[1], Jiawei Li[1], Chao Zhang[1], Jinxin Li[2,3], and Gaosheng Li[1,*]

[1]College of Electrical and Information Engineering,
Hunan University, Changsha 410012, China
gaosheng7070@vip.163.com
*Corresponding author: Gaosheng Li

[2]College of Computer Science and Electronic Engineering,
Hunan University, Changsha 410082, China

[3]State Key Laboratory of Millimeter Waves,
Southeast University Nanjing, Jiangsu 210096, China jxli@hnu.edu.cn

Abstract – The random wiring of automotive cable harness makes electromagnetic compatibility (EMC) analysis of the whole vehicle very complicated; thus, this paper proposes a simplification modeling technique to model the electromagnetic (EM) illumination on automotive cable harness. First, the stochastic process theory is applied to determine the cable route in a randomly bundling way. Then, the inductance and capacitance parameters of the cable harness at different location are established according to multiconductor transmission lines network (MTLN) theory. On this basis, the simplification modeling technique is developed to generate the electrical and geometrical parameters of the equivalent cable model. Finally, a model of shielded nine-conductor with randomly twisted and a model of unshielded nine-conductor with stochastic wiring in the vehicle are performed to validate the proposed approach by full-wave simulation. The presented method simplifies the complexity of modeling the complete cable harness significantly with a good accuracy.

Index Terms – Random wiring, automotive cable harness, simplification modeling, EM coupling, stochastic process.

I. INTRODUCTION

The cable harness provides a main gateway for electromagnetic interference (EMI) in automotive system. The unreasonable electromagnetic compatibility (EMC) design of cable harness will produce EMI to other onboard electronic equipment, bringing great safety risks to the system [1–4]. Theoretical research and engineering practice indicate that many electromechanical systems cannot satisfy EMC standards, which can be attributed to the EMI generated by cables [5–8]. As for the electromagnetic (EM) coupling analysis in modern automotive industry, reliable and efficient generation of a full numerical model of automotive cable harness is increasingly welcomed by the EMC designers [9-12]. Therefore, a more effective method to solve the modeling problem of automotive cable harness is needed.

During the wiring process in automotive, the cable harness always has some stochastic wiring factors of "spatial bending" and "randomness" as shown in Figure 1 [13–15], which bring a great challenge to the modeling of the EM illumination. Conventional modeling and simulation methods cannot easily accommodate complicated automotive system because of the difficulties in EMC modeling for cable harness [16–18]. Numerical simulation of the whole cable harness model requires strict conditions on calculation resource and even makes it impossible. Therefore, having the purpose of simplifying the structural modeling and improving the analytic efficiency, this paper focuses on the simplification technique of automotive cable harness with stochastic wiring factors.

The equivalent cable bundle method (ECBM) is a modeling method that reduces multiconductor to no more than four conductors. The ECBM method is first presented to simplify the modeling of the EM illumination on multiconductor above the ideal conducting plane, which is used to predict the coupling common-mode (CM) current [19]. On this basis, the ECBM method is extended to model the EM radiated emission from multiconductor above an ideal conducting plane [20]. Besides, the ECBM method is applied to solve the crosstalk calculation problem of cable harness with the situation in an ideal conductive plane, an ideal cylindrical shielded cavity, and an orthogonal plane [21]. Moreover, some literatures have used the

Submitted On: August 20, 2021
Accepted On: December 28, 2021

https://doi.org/10.13052/2022.ACES.J.370308

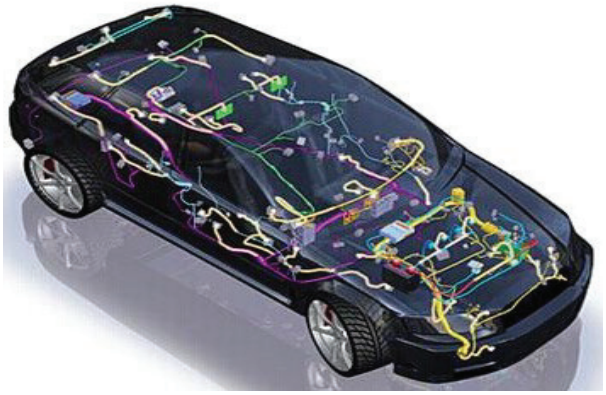

Fig. 1. Schematic diagram of automobile wiring harness distribution.

ECBM method to obtain induced current on differential cables [22].

The existing ECBM method mainly aims at simplifying the deterministic wiring cable harness; however, uncertain factors for the application cannot be ignored. The generation of cross-sectional geometry for randomly wiring cable harness is quite different from that in a deterministic wiring way reflected in the processing of random wiring parameters.

Therefore, this paper proposes a generalized ECBM method for the EM illumination on cable harness with stochastic wiring factors. First, the stochastic process theory is applied to determine the cable route in a randomly bundling way. Second, the inductance and capacitance parameters of the cable harness at different locations are established according to multiconductor transmission lines theory. In this case, the simplification modeling technique is developed to generate the electrical and geometrical parameters of the equivalent cable model. Third, the proposed method is validated by full-wave simulation. The presented method simplifies the complexity of modeling the complete cable harness significantly with a good accuracy.

II. THEORETICAL MODELING OF GENERALIZED ECBM

A. Statement of EM coupling to automotive cable harness with stochastic wiring factors

Figures 2(a) and 3(a), respectively, illustrate a typical model of braid shielded automotive cable harness in a randomly twisted bundling way and a model of unshielded cable harness with stochastic wiring factors. The corresponding schematic diagram and cross section can be seen in Figures 2(b) and 3(b). For the shielded cable harness, the geometric cross section remains the original shape along the cable length direction, while the relative position of the inner conductor changes. For the

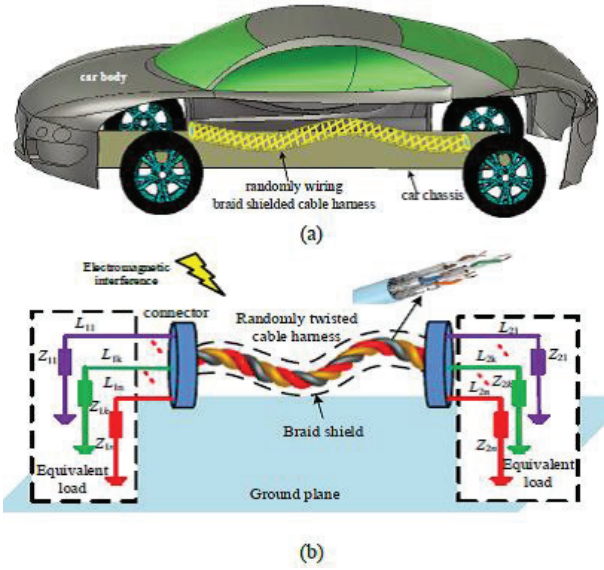

Fig. 2. Schematic diagram and cross section of braid shielded automobile cable harness in randomly twisted bundling way. (a) Cable harness in automobile. (b) Schematic diagram.

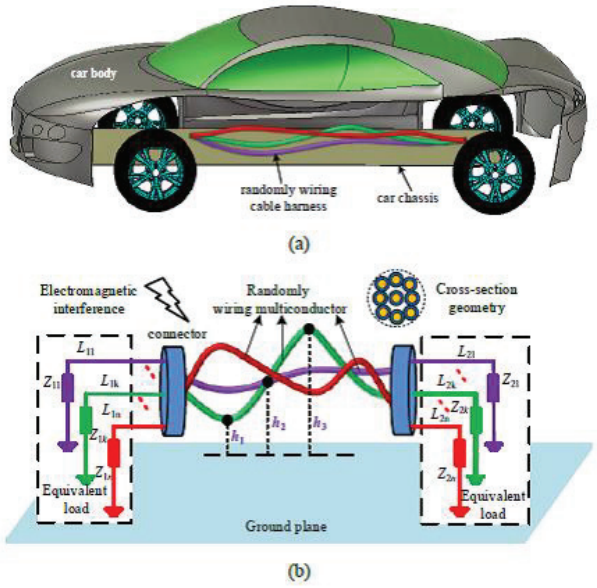

Fig. 3. Schematic diagram and cross section of unshielded automobile cable harness in randomly wiring way. (a) Cable harness in automobile. (b) Schematic diagram.

unshielded cable harness, the conductors are not exactly parallel and the position of the inner conductors is of uncertainty.

Considering the required computer resources, there is no possibility for the EM coupling problems of the

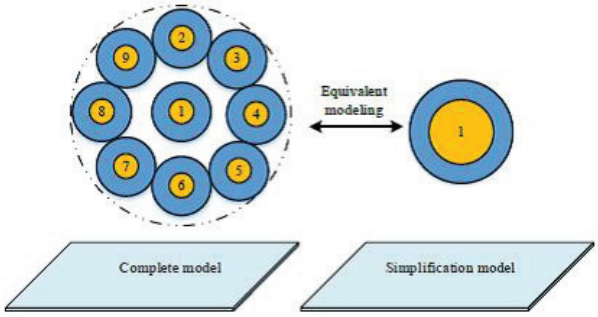

Fig. 4. Cross-sectional geometry of the complete and simplification cable harness model.

whole cable harness to be solved. However, a solution that all the conductors are wired in a determined manner was put forward by the previous ECBM method to the immunity case, but it cannot be directly applied to the case where the cable harness is in a randomly wiring way. Therefore, this paper proposes a generalized ECBM method to reduce the randomly wiring automotive harness into a single-conductor model as demonstrated in Figure 4. That is, the EM coupling to the single conductor is equivalent to describe that on a complete cable harness model.

B. Simplification modeling procedure

To simplify the cable harness with random wiring, this paper mainly discusses two stochastic wiring factors, including the relative position of the conductors within the cylindrical shielded structure and the height of the unshielded conductors to the ground.

a) Capacitance and Inductance Parameters of Equivalent Cable Harness Model

This step aims at defining the inductance l_{eq} and capacitance c_{eq} of simplification cable in multiconductor transmission lines network (MTLN) formalism [23]. The distributed parameters of capacitance matrix and inductance matrix are uncertain under the influence of the stochastic wiring factors; this phenomenon, in mathematics, can be described with expectations $E\{c\}$ and $E\{l\}$. And, the voltage and current along the conductors are defined as V_1, V_2, …, V_n and I_1, I_2, …, I_n. In the general case of N-conductor harness cable, the MTLN equations with stochastic factor can be expressed as

$$E\left\{\frac{\partial}{\partial z}[I]\right\} = -j\omega[E\{c\}][V], \tag{1}$$

$$E\left\{\frac{\partial}{\partial z}[V]\right\} = -j\omega[E\{l\}][I], \tag{2}$$

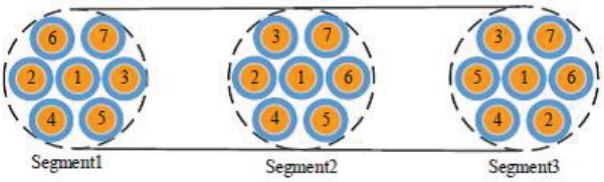

Fig. 5. Schematic diagram of transposition among conductors in a harness.

where $[I] = [I_1, I_2, \ldots, I_n]$, $[V] = [V_1, V_2, \ldots, V_n]$,

$$[E\{c\}] = \begin{bmatrix} E\{c_{11}\} & E\{c_{12}\} & \cdots & E\{c_{1n}\} \\ E\{c_{21}\} & E\{c_{22}\} & \cdots & E\{c_{2n}\} \\ \vdots & \vdots & \ddots & \vdots \\ E\{c_{n1}\} & E\{c_{n2}\} & \cdots & E\{c_{nn}\} \end{bmatrix}, \tag{3}$$

$$[E\{l\}] = \begin{bmatrix} E\{l_{11}\} & E\{l_{12}\} & \cdots & E\{l_{1n}\} \\ E\{l_{21}\} & E\{l_{22}\} & \cdots & E\{l_{2n}\} \\ \vdots & \vdots & \ddots & \vdots \\ E\{l_{n1}\} & E\{l_{n2}\} & \cdots & E\{l_{nn}\} \end{bmatrix}. \tag{4}$$

According to the MTLN theory, the per-unit-length capacitance parameters $E\{c_{\text{eq}}\}$ and $E\{l_{\text{eq}}\}$ of the simplification cable can be written as

$$E\{c_{\text{eq}}\} = \sum_{p=1}^{n}\sum_{q=1}^{n} E\{c_{pq}\} \tag{5}$$

$$E\{l_{\text{eq}}\} = \sum_{p}^{p=1}\sum_{q}^{q=1} E\{l_{pq}\} \Big/ n^2 \tag{6}$$

where the conductors are numbered p, q, and n.

b) Case 1: Shielded Cable Harness in Randomly Twisted Way

Step 1: Description of Capacitance and Inductance Parameters Matrix

Since the application of the randomly twisted way, the relative position of the inner conductor changes with the length direction of the cable. As shown in Figure 5, a schematic diagram of random transposition among conductors in a harness, the relative position of the inner conductors is uncertain, but they are limited to the connector plug-in at both ends of the cable harness where the terminals are determined. Cable harness has several adjacent segments of cable harness, and when the first segment is converted into the second segment, the positions of no. 3 conductor and no. 6 conductor are transformed. Also, with the second segment being converted into the third, the positions of no. 2 and no. 5 are transformed. Put simply, parameter matrix does not add any new element but only converts each other in element position.

Step 2: Determination of Stochastic Wiring Factors

In this step, a random spline interpolation technique is applied to solve the discontinuity problem in the con-

struction of cable harness model. At first, a number of randomly distributed coordinate points, conforming to Gaussian distribution, are generated. Then, the cable harness is divided into a series of homogeneous subsegments by the insertion of more points at other locations through spline interpolation. Finally, the piecewise polynomial form of cubic spline interpolation method is utilized to generate the cascade segments. After all these operations, a randomly twisted cable harness model can be determined.

It should be noted that the length of the subsegments should be up to one of the following two criteria: 1) Each subsegment length should be less than 1/10 of the minimum wavelength to ensure the spatial resolution of the highest frequency wave; 2) adequate subsegments (no less than 10) of the spline segment are inevitable for the continuity of the harness. Then, the smaller of the subsegments identified in the two criteria is adopted to generate the cascade subsegments through the usage of piecewise polynomial form of cubic spline interpolation technology.

Step 3: Determination of Cross-Sectional Geometry of Simplification Cable Model

In Figure 6, a model of n-conductors with a radius of r_i within a perfectly conducting cylindrical shield is displayed. The screen's radius is denoted by r_S and the distances of conductors from the shield axis are denoted by d_i, whereas the angular separations of the conductors from the shield axis are denoted by θ_{ij}. According to the study in [23], we can obtain

$$E\{l_{ii}\} = \frac{\mu}{2\pi} \ln\left(\frac{r_S^2 - E\{d_i^2\}}{r_S E\{r_i\}}\right). \tag{7}$$

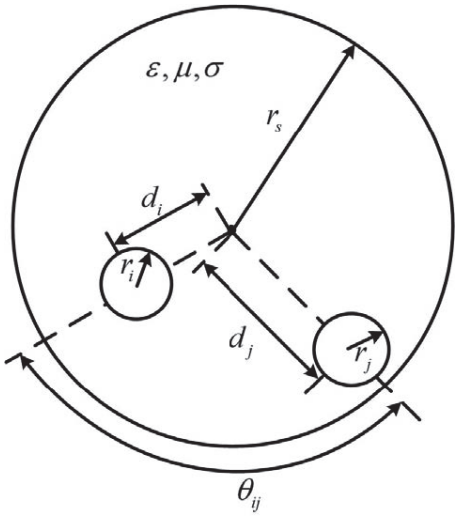

Fig. 6. n-conductors within a perfectly conducting cylindrical shield.

This step, aiming at generating the cross-sectional geometry of the equivalent cable mainly consists of two phases. The inductance and capacitance parameters are associated with the structural factors, such as the distance between the conductor and shield, and the relative distance among conductors. For this reason, the cross-sectional geometry parameters of equivalent model can be determined based on the knowledge of inductance $E\{l_{\text{eq}}\}$.

1. Phase 1: Estimate the central distance d_i between the equivalent inner conductor and the central axis of the shield. d_i of equivalent conductor corresponds to the average of the distance of all the conductors at any location in the complete cable bundle model.
2. Phase 2: Estimate the radius r_i of the equivalent cable. According to the analytical formula of self-inductance $E\{l_{ii}\}$ in eqn (7), the radius r_i of each equivalent conductor can be approximated by

$$r_i = \frac{r_s^2 - E\{d_i^2\}}{r_s \exp(\frac{2\pi E\{l_{ii}\}}{\mu})}. \tag{8}$$

c) Case 2: Unshielded Cable Harness in Randomly Wiring Way

Step 1: Description of Capacitance and Inductance Parameters

Figure 7(a) is an illustration of randomly wiring n-conductors located above an ideal conducting plane. In the figure, r_i and r_j represent the radius of any two conductors and $h(z)$ refers to the height to the ground plane at position z along the cable length direction, which satisfies Gaussian distribution as demonstrated in Figure 7(b). The corresponding probability distribution of the height to ground is illustrated in Figure 7(c), in which $S_{ij}(z)$ is the conductor's spacing and Δr_A and Δr_B stand for the insulation thickness of the conductor. According to study in [23], the calculation formula of per-unit-length inductance parameter can be written as

$$E\{l_{ij}(z)\} = \begin{bmatrix} \frac{\mu}{2\pi}\ln\left(\frac{2\chi_1}{r_i}\right) & \frac{\mu}{4\pi}\ln\left(1+\frac{4\chi_2}{\chi_3}\right) \\ \frac{\mu}{4\pi}\ln\left(1+\frac{4\chi_2}{\chi_3}\right) & \frac{\mu}{2\pi}\ln\left(\frac{2\chi_4}{r_j}\right) \end{bmatrix} \tag{9}$$

where $\chi_1 = E\{h_i(z)\}$, $\chi_2 = E\{h_i(z)\} \bullet E\{h_j(z)\}$, $\chi_3 = E\{S_{ij}(z)^2\}$, and $\chi_4 = E\{h_j(z)\}$. The diagonal element represents the self-inductance, while the off-diagonal element describes the mutual inductance. It can be seen from eqn (9) that the inductance parameters are related to the position of the conductors.

Step 2: Determination of the Cross-Sectional Geometry Parameters of Equivalent Cable

According to eqn (6) and (9), the per-unit-length capacitance parameter $E\{l_{\text{eq}}\}$ of the simplification cable model can be calculated and the geometric cross-

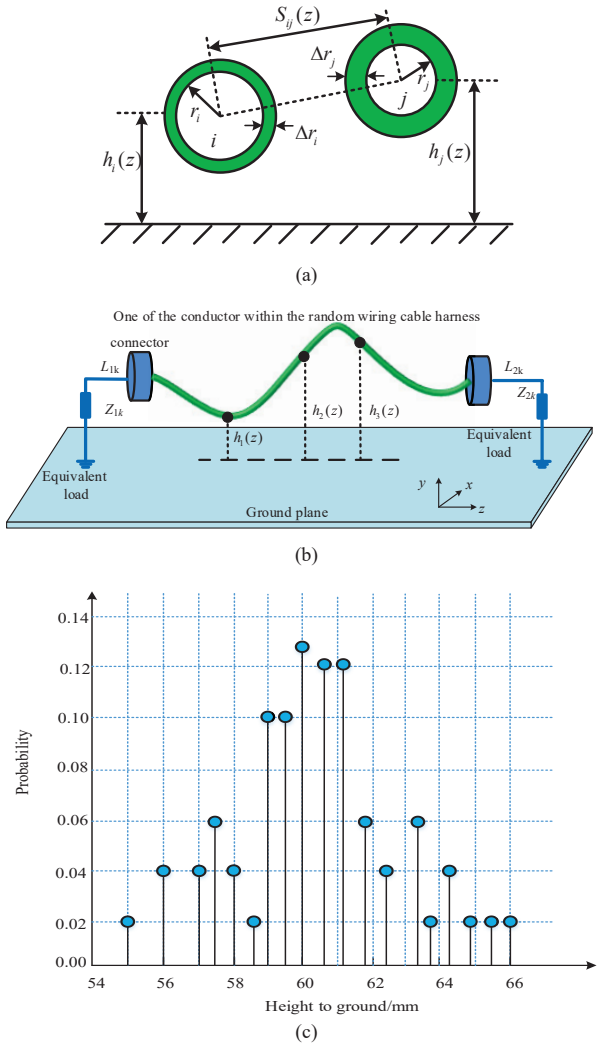

Fig. 7. Randomly wiring unshielded n-conductors. (a) Double conductors above ideal conducting ground plane. (b) Wiring diagram of one of the conductors. (c) The probability distribution of the height to ground.

sectional structure can be established with the corresponding radius r_{eq} and the ground height h_{eq}.

Calculation of r_{eq}: According to eqn (6) and (9), r_{eq} is

$$r_{\mathrm{eq}} = 2E\{h_i\} \Big/ e^{2\pi E\{l_{\mathrm{eq}}\}/\mu}. \tag{10}$$

Calculation of h_{eq} : The height of the simplified cable to the reference ground equals the average height of n-conductors to the ground at any cross section of the cable harness:

$$h_{\mathrm{eq}} = \frac{E\{h_1(z)\} + E\{h_2(z)\} + \cdots + E\{h_n(z)\}}{n}. \tag{11}$$

d) Equivalent Terminal Loads of Simplification Cable Model

This step aims at calculating the terminal loads of the equivalent model. Here, the equivalent CM loads are defined as the connection between conductor ends and the shield. The terminal load connected to the simplified cable end equals the loads at the end of all the conductors in parallel.

III. NUMERICAL VALIDATIONS

In this section, a model of braid shielded nine-conductor in randomly twisted bundling way and a model of unshielded nine-conductor with stochastic wiring in the automotive chassis are constructed for the validation of the proposed approach by CST Cable Studio with full-wave simulation. In this paper, the EM coupling value of the whole model is taken as the standard value, and the EM coupling value of the simplification model is compared.

A. Case 1: Shielded Cable Harness in Randomly Twisted Way in the Automotive

a) Description of the Validation Model

As shown in Figure 8, a nine-conductor point-point connected cable harness within a braid shielded cylindrical structure above the automotive chassis is modeled. All the conductors are bundled in a randomly twisted way. The wiring route is composed of stochastic locations and the corresponding coordinate value is listed in Table 1.

Each conductor has a radius of 0.5 mm and is surrounded by dielectric coating with a thickness $\Delta r = 1$ mm and dielectric constant of$\varepsilon_r = 2.5$ and $\mu_r = 1$. The radius

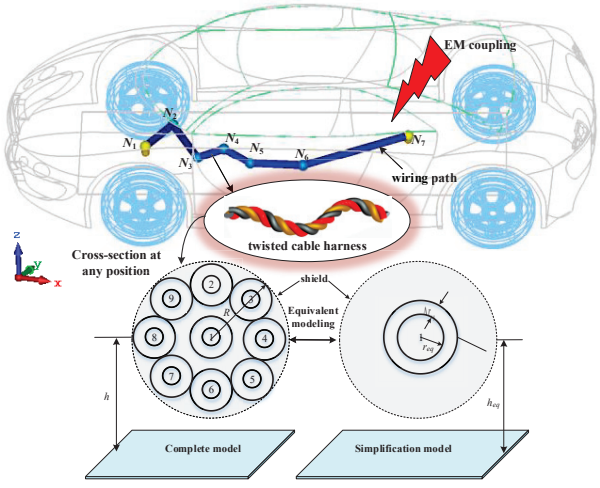

Fig. 8. The full-wave simulation model of a shielded nine-conductor cable harness model and the corresponding simplification cable model in the automotive.

Table 1: Coordinate position of arbitrarily bent cable harness (unit: mm)

Position	N_1	N_2	N_3
(x, y, z)	(0, 0, 60)	(200, 400, 10)	(400, -100, 20)
Position	N_4	N_5	N_6
(x, y, z)	(600, -100, 100)	(800, -200, 30)	(1200, -200, 10)
Position	N_7	–	–
(x, y, z)	(2000, 200, 40)	–	–

of the shield is 3 mm. The conductors with a serial number "2, 3, 4, 5, 6, 7, 8" in Figure 10 are evenly distributed on the circle with a radius of 2 mm. The terminal load connected to the ends of each conductor is 50 Ω. The plane wave incident direction is along the Y-axis and the electric field direction is along the X-axis with an amplitude of 100 V/m as shown in Figure 8. The full-wave simulation model in CST is shown in Figure 9.

The cross-sectional geometry of simplification cable model is determined through the simplification procedure of case 1 described in Section 2.2. The corresponding r_{eq} of the equivalent cable is 3.8 mm and the equivalent CM terminal loads are 5.6 Ω.

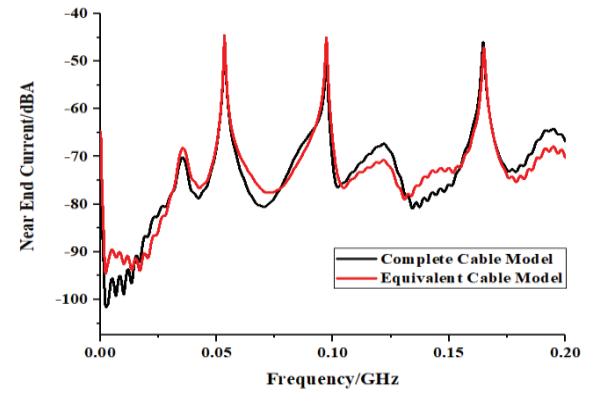

(a)

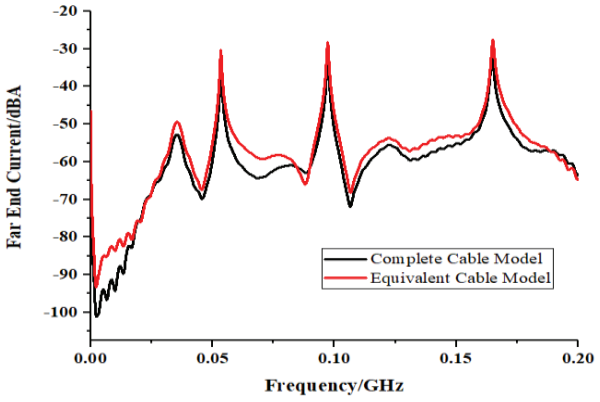

(b)

Fig. 9. Comparison of the CM current in frequency domain on complete cable harness model and equivalent cable model. (a) Near end. (b) Far end.

b) Results and Discussion

The induced CM current at the near and far ends of complete cable harness and simplification cable in frequency domain are calculated through the method of CST Cable Studio with full-wave simulation. Based on the co-simulation technique, the TLM technique and AC result solver are, respectively, adopted in the existing numerical approach to analyze the electric field around the conductors and compute the coupling to terminal loads.

In Figure 9, a comparison between the CM currents obtained at the ends of the complete cable harness model and the simplification cable model over frequency (0.200 MHz) is clearly demonstrated. The red line represents the simulation results of the complete cable model, while the black line describes that of the simplification model. The good agreement indicates a validation of the proposed method.

B. Case 2: Unshielded Cable Harness with Stochastic Wiring in the Automotive

a) Description of the Validation Model

The full-wave simulation model in CST is shown in Figure 10, and a nine-conductor point-point connected unshielded cable harness above the automotive chassis is modeled and all of the conductor is wired in a randomly bundling way. The wiring route consists of a number of random locations. Each conductor, with a radius of 0.5 mm, is surrounded by dielectric coating with a thickness Δr=1 mm and dielectric constant of $\varepsilon_r = 2.5$ and $\mu_r = 1$, and the terminal load connected to the ends of each conductor is 50Ω.The plane wave incident direction is along the Y-axis and the electric field direction is along the X-axis with an amplitude of 100 V/m.

Under the simplification procedure of case 2 described in Section 2-B, the randomly wiring route and cross-sectional geometry of simplification cable model is determined. The radius of equivalent conductor is 4 mm and the thickness of corresponding insulation layer is 1mm.

b) Results and Discussion

The comparison results of the coupling current on near end and far end of the complete cable harness model and simplification cable model over frequency (0.200 MHz) are, respectively, shown in Figures 11(a) and (b), which proves the efficacy of the proposed method. As it is seen in the figure, the red line represents the result of the complete cable model, while the black line describes that of the simplification model.

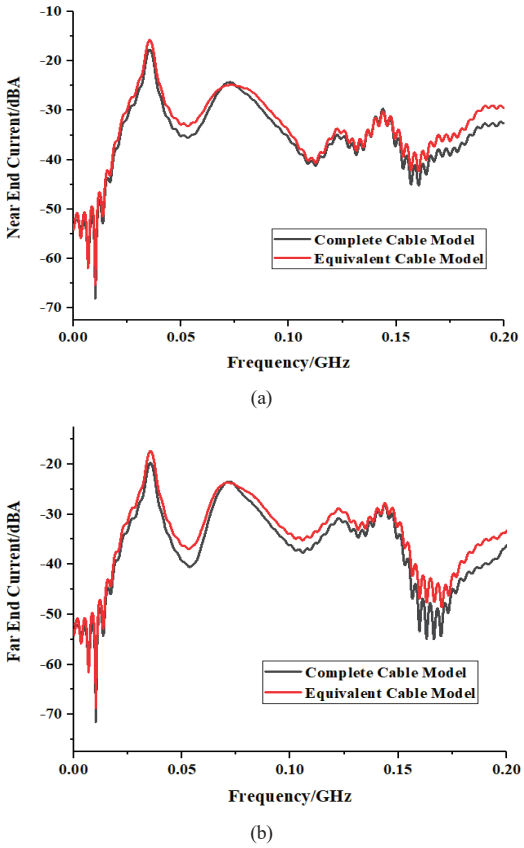

Fig. 10. Comparison of the CM current in frequency domain on complete cable harness and equivalent cable. (a) Near end. (b) Far end.

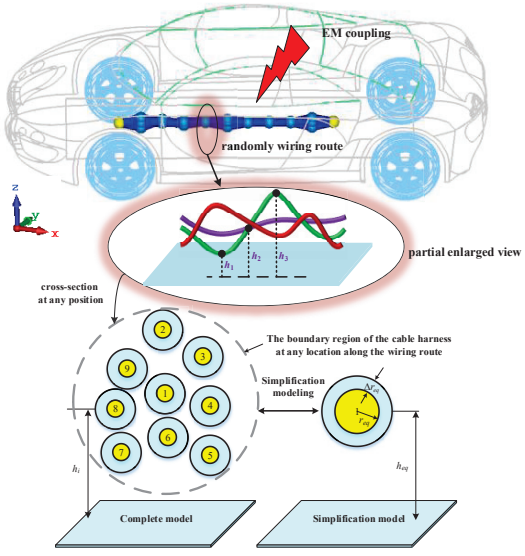

Fig. 11. The full-wave simulation model of an unshielded nine-conductor cable harness model and the corresponding simplification cable model in the automotive.

IV. CONCLUSION

This paper proposes a generalized simplification technique to model the EM illumination on automotive cable harness with stochastic wiring factors. The combination of the conductors contributes to the simplification of modeling the complete cable harness.

The randomly wiring problem in generating the cross-sectional geometrical parameters of the simplification cable model is successfully solved by the application of the Gaussian distribution and spline interpolation, which are used to determine the route of cable harness. As the position of the conductors within the harness is related to the inductance and capacitance parameters, the inductance and capacitance matrixes of the cable harness at different locations are established by the utilization of transposition relationship between the subsegments of the conductors. To this end, the generalized simplification modeling technique is developed to determine the electrical and geometrical parameters of the simplification cable. Furthermore, a model of braid shielded nine-conductor with random twisting and a model of unshielded nine-conductor with random wiring above automotive chassis are constructed to validate the proposed method by CST Cable Studio with full-wave simulation.

REFERENCES

[1] D. Ren, W. W. Ruan, P. Xiao, P. A. Du, J. H. Deng, K. M. Zhou, "An analytical method of minimizing the crosstalk of curved cable and determining the optimal wiring," *Applied Computational Electromagnetics Society (ACES) Journal*, vol. 35, no. 7, pp. 742-749, Jul. 2020.

[2] P. Xiao, W. W. Ruan, P. A. Du, "An analytic method of determining a critical cable spacing for acceptable crosstalk," *Applied Computational Electromagnetics Society (ACES) Journal*, vol. 35, no. 2, pp. 237-244, Feb. 2020.

[3] H. Chen and T. Wang, "Estimation of common-mode current coupled to the communication cable in a motor drive system," *IEEE Transactions on Electromagnetic Compatibility*, vol. 60, no. 6, pp. 1777-1785, Mar. 2018.

[4] F. Rachidi. "A review of field-to-transmission line coupling models with special emphasis to lightning-induced voltages on overhead lines," *IEEE Transactions on Electromagnetic Compatibility*, vol. 54, no. 4, pp. 898-911, Feb. 2012.

[5] Q. Jin, W. Sheng, C. Gao, and Y. Yan, "Internal and external transmission line transfer matrix and near-field radiation of braided coaxial cables," *IEEE Transactions on Electromagnetic Compatibility*, vol. 63, no. 1, pp. 206-214, Aug. 2021.

[6] Y. Hakuta, T. Watanabe, T. Takenaka, T. Ito, and A. Hirata, "Safety standard compliance of human exposure from vehicle cables using coupling

factors in the frequency range of 0.3–400 kHz," *IEEE Transactions on Electromagnetic Compatibility*, vol. 63, no. 1, pp. 313-318, Apr. 2021.

[7] J. He, Z. Guo, and X. Li, "Mechanism model and prediction method of common mode radiation for a nonisolated very-high-frequency DC–DC converter with cables," *IEEE Transactions on Power Electronics*, vol. 35, no. 10, pp. 10227-10237, Mar. 2020.

[8] Y. Zhang, S. Wang, and Y. Chu. "Investigation of radiated electromagnetic interference for an isolated high-frequency DC–DC power converter with power cables," *IEEE Transactions on Power Electronics*, vol. 34, no. 10, pp. 9632-9643, Jan. 2019.

[9] B. X. Zhang, P. Xiao, D. Ren, and P. A. Du, "An analytical method for calculating radiated emission of discontinuous penetrating cable," *Applied Computational Electromagnetics Society (ACES) Journal*, vol. 34, no. 1, pp. 25-32, Jan. 2019.

[10] Y. Cai, Y. Guan, W. Liu, and J. He, "Study of transient enclosure voltage coupling to secondary cables in a gas-insulated substation," *IEEE Transactions on Power Delivery*, vol. 33, no. 2, pp. 761-768, Mar. 2017.

[11] Y. S. Xiao, D. Ren, P. Xiao, and P. A. Du, "An equivalent modeling method for the radiated electromagnetic interference of PCB based on near-field scanning," *Applied Computational Electromagnetics Society (ACES) Journal*, vol. 34, no. 5, pp. 784-791, May 2019.

[12] D. Zhang, Y. Wen, J. Zhang, and G. Xin, "Coupling analysis for shielded cables in the train using hybrid method," *IEEE Access*, vol. 7, no. 1, pp. 76022-76029, Jun. 2019.

[13] M. Wu, D. G. Beetner, T. H. Hubing, H. Ke, and S. Sun, "Statistical prediction of "Reasonable Worst-Case" crosstalk in cable bundles," *IEEE Transactions on Electromagnetic Compatibility*, vol. 51, no. 3, pp. 842-851, Aug. 2009.

[14] M. Alibakhshi-Kenari, M. Naser-Moghadasi, R. A. Sadeghzadeh, B. S. Virdee, and E. Limiti, "Traveling-wave antenna based on metamaterial transmission line structure for use in multiple wireless communication applications," *AEU-International Journal of Electronics and Communications*, vol. 70, no. 12, pp. 1645-1650, Dec. 2016.

[15] E. Genender, H. Garbe, and F. Sabath, "Probabilistic risk analysis technique of intentional electromagnetic interference at system level," *IEEE Transactions on Electromagnetic Compatibility*, vol. 56, no. 1, pp. 200-207, Jul. 2014.

[16] G. Ala, M. C. Di Piazza, G. Tine, F. Viola, and G. Vitale, "Evaluation of radiated EMI in 42-V vehicle electrical systems by FDTD simulation," *IEEE Transactions on Vehicular Technology*, vol. 56, no. 2, pp. 1477-1484, Jul. 2007.

[17] R. G. Jobava, A. L. Gheonjian, J. Hippeli, G. Chiqovani, D. D. Karkashadze, F. G. Dogdanov, and Khvitia B. Bzhalava, "Simulation of low-frequency magnetic fields in automotive EMC problems," *IEEE Transactions on Electromagnetic Compatibility*, vol. 56, no. 6, pp. 1420-1430, Jun. 2014.

[18] N. Mora, F. Rachidi, P. Pelissou, and A. Junge, "Numerical simulation of the overall transfer impedance of shielded spacecraft harness cable assemblies," *IEEE Transactions on Electromagnetic Compatibility*, vol. 57, no. 4, pp. 894-902, Mar. 2015.

[19] G. Andrieu, L. Kone, F. Bocquet, B. Parmantier, J. P. "Multiconductor reduction technique for modeling common-mode currents on cable bundles at high frequency for automotive applications," *IEEE Transactions on Electromagnetic Compatibility*, vol. 50, no. 1, pp. 175-184, Feb. 2008.

[20] G. Andrieu, A. Reineix, M. Bunlon, J. P. Parmantier, and B. Demoulin, "Extension of the "equivalent cable bundle method" for modeling electromagnetic emissions of complex cable bundles," *IEEE Transactions on Electromagnetic Compatibility*, vol. 51, no. 1, pp. 108-118, May 2009.

[21] Z. Li, L. L. Liu, J. Yan, Z. Y. Nie, and C. Q. Gu, "An efficient simplification scheme for modeling crosstalk of complex cable bundles above an orthogonal ground plane," *IEEE Transactions on Electromagnetic Compatibility*, vol. 55, no. 5, pp. 975-978, May 2013.

[22] B. Schetelig, "Simplified modeling of EM field coupling to complex cable bundles," *Advances in Radio Science*, vol. 8, no. 13, pp. 211-217, Jan. 2010.

[23] C. R. Paul, Analysis of Multiconductor Transmission Lines, 2nd ed. Hoboken, NJ, USA: Wiley, 2007.

Pei Xiao was born in Shaoyang, Hunan province, China, in 1989. He received the bachelor's and Ph.D. degrees in mechanical engineering from the University of Electronic Science and Technology of China (UESTC), Chengdu, China, in 2013 and 2019, respectively.

He is currently a Postdoctoral Research Fellow with Hunan University. His research interests are numerical computation, theoretical electromagnetic analysis including the antennas, EMC/EMI in multiconductor transmission line, power electronic device, and electric vehicle.

Jiawei Li was born in Yueyang, Hunan province, China, in 1997. He received the bachelor's degree from the College of Physics and Information Engineering, Fuzhou University, Fuzhou, China, in 2019. He is currently working toward the postgraduate degree with the College of Electrical and Information Engineering, Hunan University.

His research interest includes EMC.

Chao Zhang was born in Huaihua, Hunan province, China, in April 1991. He received the B.S. degree in communication and information engineering from Huaihua College in 2014 and the M.S. degree in electromagnetic field and microwave technologies from Shanghai University in 2018. He is currently working toward the Ph.D. degree in electronic science and technology with Hunan University, Changsha, China.

He has authored or co-authored more than 10 research papers in international academic journals and international conferences. His current research interests include antenna technology, EMC, and plasmonic metamaterials and devices at microwave and terahertz frequencies.

Jinxin Li received the B.S. degree in electronic information science and technology in 2008 and the Ph.D. degree in electromagnetic field and microwave technology in 2017 from the University of Electronic Science and Technology of China (UESTC), Chengdu, China. From 2015 to 2016, he was a Visiting Ph.D. Student with the Department of Electrical and Computer Engineering, Duke University, Durham, NC, USA.

He has been an Assistant Professor with Hunan University since 2017. His research interests include antennas, antenna arrays, metamaterials, and passive devices and circuit.

Gaosheng Li (Senior Member, IEEE) received the B.S. degree in electromagnetic field and microwave and the M.S. and Ph.D. degrees in electronic science and technology from the National University of Defense Technology (NUDT), Changsha, China, in 2002, 2004, and 2013, respectively.

He was with NUDT as a Teaching Assistant from 2004 to 2006, a Lecturer from 2006 to 2011, and then as an Associate Professor from 2011 to 2017. He joined Hunan University as a Professor in 2018. From 2014 to 2016, he was with the Nanjing University of Aeronautics and Astronautics (NUAA) and Wuxi Huace Electronic Systems Co., Ltd., China as a Postdoctoral Research Fellow. From 2016 to 2017, he was a Visiting Scholar with the University of Liverpool (UoL), U.K., sponsored by China Scholarship Council (CSC). His research interests include antennas and propagation (AP), electromagnetic compatibility (EMC), wireless propagation, and microwave systems.

Prof. Li is the author or coauthor of 7 books and 150 papers published in journals and conference proceedings. He owns 30 Chinese patents and 10 software copyrights. He won three national scientific prizes in 2008, 2013, and 2015, respectively. He is now a Senior Member (2019) of the IEEE AP Society and EMC Society, a Member (2016) of IET, a Member (2017) of ACES, a Member (2011) of IEICE, as well as a Senior Member (2014) of the Chinese Institute of Electronics (CIE).

Low-RCS Surface Design Based on Lossy Metagratings

Kai Wang, Wei Shao, Hua Li, and Bing-Zhong Wang

School of Physics
University of Electronic Science and Technology of China, Chengdu 611731, China
wkaiuestc2016@163.com, weishao@uestc.edu.cn, lihua2006@uestc.edu.cn, bzwang@uestc.edu.cn

Abstract – A design method based on the lossy metagrating for radar cross section (RCS) reduction is proposed in this paper. According to the mechanism of the RCS reduction, the lossy metagrating with different loaded lines per supercell is studied and it is also incorporated into the metasurface to reduce RCS. The embedded metagrating provides an additional low-RCS band and it has a small effect on the original band of the metasurface. Numerical results show that the metagrating reduces RCS of the surface effectively.

Index Terms – Diffraction pattern, lossy metagrating, low-RCS, metasurface.

I. INTRODUCTION

Metasurfaces have been used for the reduction of the radar cross section (RCS) of target objects [1–4]. The fundamental mechanisms of a metasurface for RCS reduction are absorption and scattering control of electromagnetic waves [5]. The methods used for the analysis of a metasurface, such as the equivalent circuit method and transmission matrix method, take the metasurface as an impedance surface [6]. The size of the element of the metasurface and the separation distances between the elements are in the scale of subwavelength. Thus, it is costly to apply tunable and lumped elements to the metasurface.

Metagratings are proposed for the perfect anomalous reflection and then extended for controlling the diffraction pattern [7–10]. A loss-free metagrating provides an effective way to control the diffracted plane waves. The separation distance between two neighboring lines in a metagrating is bigger than half of the vacuum wavelength and the surface impedance is not available for calculation. The metagrating has the smaller number of lines than the metasurface with the same size and working frequency [7, 11]. So, the metagrating requires fewer lumped elements than the metasurface on a similar occasion.

In this paper, the lossy metagratings are designed to reduce RCS when they cover the target objects. Resistors are loaded to a loss-free metagrating, and the obtained lossy one, as far as we know, has not been studied for RCS reduction. A uniform metagrating loaded with the resistors, which consists of only one line per element, is first studied on its electromagnetic properties. The lossy metagrating provides a frequency band to absorb the incident plane wave while the loss-free metagrating cannot absorb the wave. Second, a lossy metagrating including five lines per supercell is also designed. By diffusing the diffracted plane waves, the RCS of the surface is reduced effectively. The lossy metagrating shows its lower reflection results than the loss-free one. Finally, the lossy metagrating that produces an extra absorbing band is incorporated into the low-RCS metasurface to obtain the better absorbing ability.

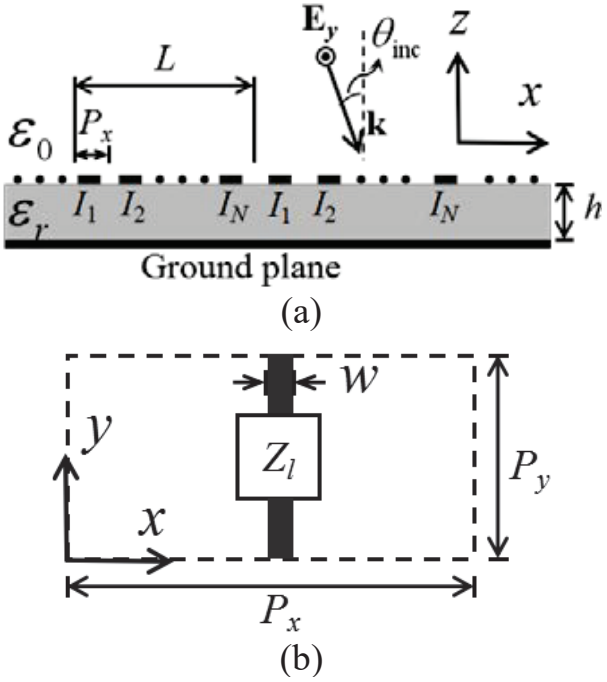

Fig. 1. Metagrating on a grounded dielectric substrate. (a) Metagrating. (b) An element in the supercell.

II. LOW-RCS METAGRATING

A two-dimensional ($\partial/\partial y = 0$) metagrating that is printed on a grounded dielectric substrate and is com-

Submitted On: July 1, 2020
Accepted On: March 10, 2022

https://doi.org/10.13052/2022.ACES.J.370309

posed of a quantity of conducting lines is shown in Figure 1. The lines are along the *y*-direction, the separation distance between two neighboring lines is P_x, and the thickness of the substrate is h. Each line is loaded by an impedance of Z_l alone the *y*-direction and it is considered as a uniform impedance line with $Z = Z_l/P_y$. The impedances are loaded with a periodicity of N; so N lines form a supercell with a length of $L = NP_x$. The metagrating is excited by a transverse electric (TE) polarized plane wave at an angle of θ_{inc}. Due to the presentation of the grounded substrate, the reflected plane wave will be also taken as the excitation.

From the Floquet-Bloch (FB) theory, the induced current on the line in the mth supercell is defined as

$$J_{y,m} = \sum_{n=1}^{N} \hat{y} I_n \delta\left(x - x_n^m, z - h\right) e^{-\mathrm{j}k_0 mL \sin\theta_{\mathrm{inc}}}, \qquad (1)$$

where δ is the Dirac function, $x_n^m = mL + (n-1)P_x$, I_n is the induced current of the nth line in a supercell, and k_0 is the vacuum wavenumber. The diffraction waves are produced by the excitation and the induced currents on the lines. The induced currents are determined by the excitation and the loaded impedance. The radiation pattern of the metagrating is available when the excitation and loaded impedance are known. After the design of the loaded impedance of the metagrating, the diffraction patterns can be controlled. The designed loaded impedances are realized with the distributed parameters and lumped resistors.

The transverse and longitudinal wavenumbers of the qth diffracted plane wave are calculated by $\xi_q = k_0 \sin(\theta_{inc}) + 2\pi q/L$ and $\beta_q = \sqrt{k_0^2 - \xi_q^2}$, respectively. When $|\xi_q| < k_0$, the qth diffracted plane wave is propagating. The diffracted wave is evanescent when $|\xi_q| > k_0$ and proper β_q is taken. The magnitudes of the electric field of the incident wave and qth reflected plane wave are denoted as A_0^{inc} and A_q^{ref}, respectively. We denote $\boldsymbol{P}$ as a set that contains all the index of the reflected propagating waves. The reflected propagating waves are controllable when the dimension of $\boldsymbol{P}$ is smaller than N.

A. Lossy metagrating with only one loaded line per supercell

The lossy component is not involved in the metagrating above. The lossy metagrating can be realized by taking Z_l as a complex number and the corresponding equations about the current and impedance still work well. We design a low-RCS metagrating working at f_0= 5GHz and there is only one loaded line in a supercell. Z_l is designed so that the normally incident plane wave is absorbed by the metagrating. The size and the loaded resistor of the supercell are calculated by Z_l. The metagrating, in this paper, is designed based on the theory where the incident wave is the TE wave.

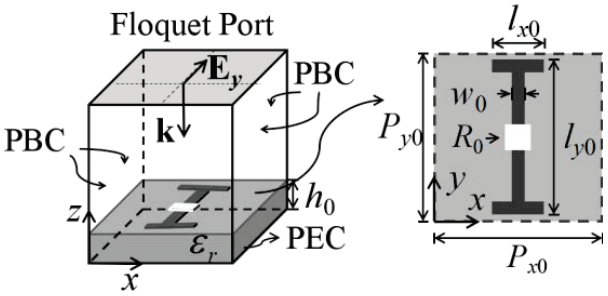

Fig. 2. Supercell of the uniform lossy metagrating, where P_{x0}= 42 mm, P_{y0}= 12 mm, h_0= 5 mm, w_0= 1 mm, l_{x0}= 1.2 mm, l_{y0}= 11 mm, and R_0= 26 Ω.

A supercell of the designed metagrating is shown in Figure 2, where the black part is the perfect electric conductor (PEC) with a thickness of 0.035 mm and the white part is the loaded lumped resistor. It is surrounded by the periodic boundary condition (PBC) and excited by a normally incident plane wave. The relative permittivity of the dielectric substrate in this paper is ε_r = 4.4(1 + 0.02j). P_{x0} is bigger than $0.5\lambda_0$, where λ_0 is the vacuum wavelength at the frequency of f_0.

The performance of the lossy metagrating is shown in Figure 3. For θ_{inc}= 0° and θ_{inc} = 45°, we get $P = \{0\}$ and $P = \{-1, 0\}$, respectively. The magnitudes of the reflected wave are shown in Figure 3(a) when θ_{inc} = 0° and θ_{inc} = 45°. The relative bandwidth with $|| < -10$ dB is about 10% when θ_{inc} = 0°. There are two diffracted propagating plane waves when θ_{inc} = 45°, $|| < -5$ dB, and $|| < -5$ dB at 5 GHz. Some power is absorbed by the lossy metagrating and the absorption rate is defined as

$$\text{Absorption } (\%) = \frac{\beta_0 |A_0^{\mathrm{inc}}|^2 - \sum_{q\in?} \beta_q |A_q^{\mathrm{ref}}|^2}{\beta_0 |A_0^{\mathrm{inc}}|^2}. \qquad (2)$$

From Figure 3(b), the incident power is mainly absorbed by the metagrating when θ_{inc}= 0° and f_0= 5 GHz. Half of the power is reflected by the metagrating when θ_{inc}= 45° and f_0= 5 GHz. The substrate also loses some of the incident power. The resistance of the loaded resistor of the metagrating is much smaller than that of a metasurface absorber. The fundamental mechanisms of the low-RCS metagrating are absorption when θ_{inc}= 0° and absorption and scattering control when θ_{inc} = 45°.

B. Lossy metagrating with five loaded lines per supercell

The metagrating with multiple loaded lines in a supercell is studied and the metagrating with five loaded lines per supercell is taken as an example. Both loss-free and lossy metagratings are studied here. The loaded reactance of the loss-free metagrating is designed so that the reflected propagating waves have an equal amplitude with a normally incident plane wave. The sizes of the

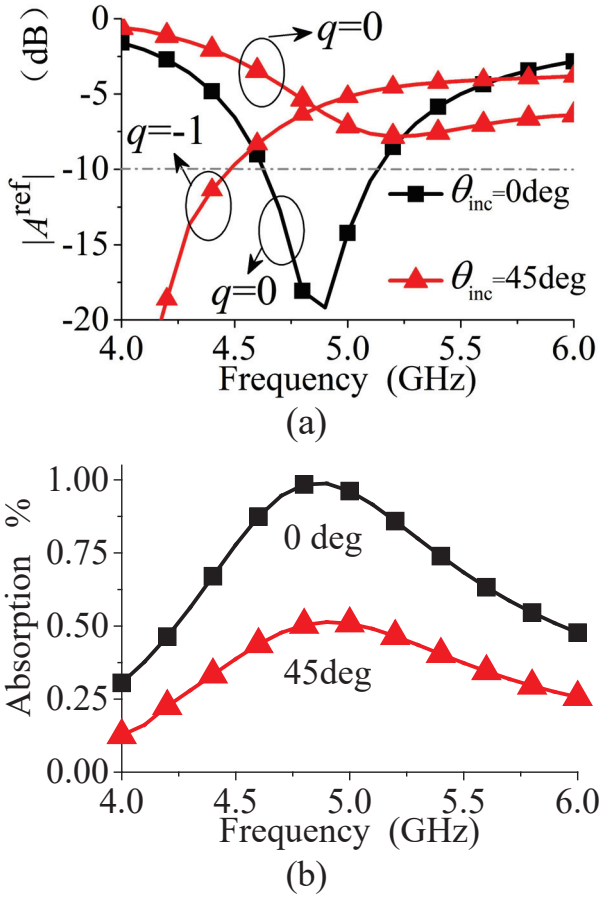

Fig. 3. Radiation performance of the uniform lossy metagrating. (a) Reflection. (b) Absorption.

elements are determined by the method proposed in [9]. The lossy metagrating takes the same geometry of the element as the loss-free one and uses the optimized lumped resistors so that all the reflected waves are suppressed. Both the loss-free and lossy metagratings are symmetrical and only three elements are needed to be designed.

The geometry of the designed metagratings is shown in Figure 4. Here, $P_{x1} = 0.5\lambda_0$ at f_0= 5 GHz and the thickness of the substrate is 5 mm. $\boldsymbol{P} = \{-2, -1, 0, 1, 2\}$ and $A_q^{\text{ref}} = A_{-q}^{\text{ref}}$ are obtained when the TE wave normally illuminates on the metagratings.

The diffracted performance of the metagratings is shown in Figure 5. We provide only the results of three plane waves due to the symmetry of the structures. The reflected waves have an equal amplitude at 5 GHz for the loss-free metagrating and there is a bandwidth of 20% with $|A_q^{\text{ref}}| < -5$ dB for $q \in \boldsymbol{P}$. With the introduction of lumped resistors, the reflected waves are suppressed effectively in Figure 5(b). The bandwidth with $|A_q^{\text{ref}}| < -10$ dB, $q \in \boldsymbol{P}$ is about 20%. The bandwidth is about the double of that of the lossy metagrating with only one element per supercell on the same dielectric substrate. The metagrating with multiple elements per supercell has a better low RCS performance than the metagrating with only one element. The absorption performance of the metagratings, calculated by eqn (1), is shown in Figure 6. The energy consumption in the loss-free metagrating results from the lossy substrate. The fundamental mechanisms of the designed low-RCS metagrating with five elements per supercell are both absorption and scattering control.

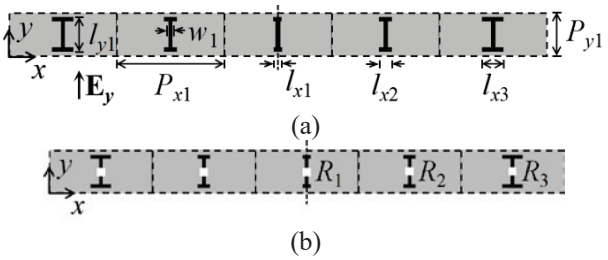

Fig. 4. Metagrating with multiple elements. (a) Loss-free metagrating. (b) Lossy metagrating. P_{x1}= 30 mm, P_{y1}= 12 mm, l_{y1}= 11 mm, w_1= 1 mm, l_{x1}= 1 mm, l_{x2}= 2.2 mm, l_{x3}= 3 mm, R_1= 15 Ω, R_2=25 Ω, and R_3= 45 Ω.

III. LOW-RCS METASURFACE EMBEDDED WITH THE METAGRATING

The low-RCS bands of the lossy metagratings designed above are narrow compared with the metasurface with the same substrate, which reduces the scope of application. In this section, we design a dual-band low-RCS metasurface embedded with a lossy metagrating. The lossy metagrating provides an extra narrow low-RCS band and has a small effect on the original low-RCS band of the metasurface.

The low-RCS metasurface is designed based on the polarization converter and scattering cancelation. The structure and performance of the element of the metasurface are shown in Figure 7. The thickness of the substrate is 2.5 mm and θ_{inc}= 0°. The bandwidth with the co-polarized reflections $|R_{xx}| = |R_{yy}| < 0.3$ is 78% (8.5-19.5 GHz) and $|R_{xx}| = |R_{yy}| = 1$ at 5 GHz. Arranging the elements as the chessboard configuration, we obtain a 78% bandwidth with low RCS. By taking the cross-polarized reflections $|R_{xy}| = |R_{yx}| = 0$ at 5 GHz, the chessboard metasurface works as a uniform isotropic metasurface at 5 GHz. The method proposed for the design of metagrating in [9] is used with the consideration of the metasurface.

The structure of the designed low-RCS metasurface embedded with the metagrating is shown in Figure 8. The separation between the loaded lines is 36 mm and it is bigger than $0.5\lambda_0$. The diffraction performance of the metasurface embedded with the metagrating under

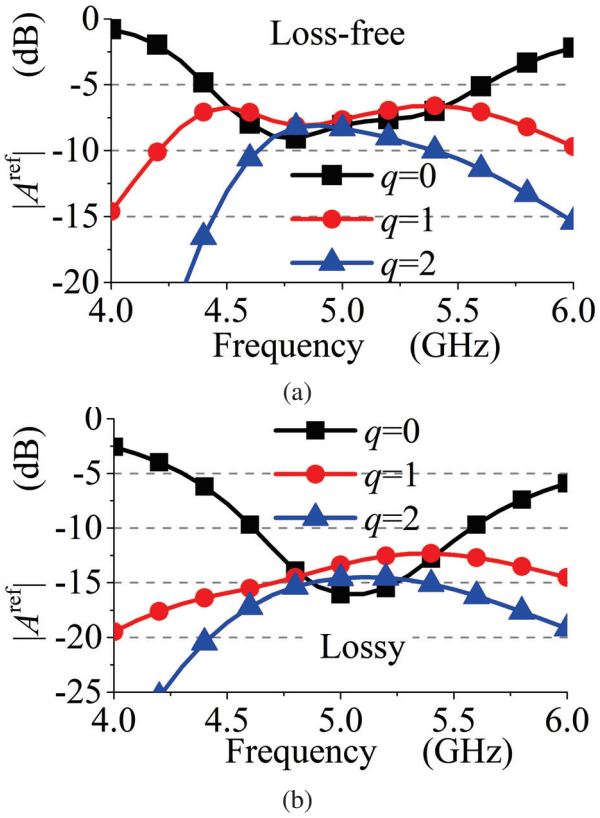

Fig. 5. Reflection performance of the metagrating with multiple elements. (a) Loss-free metagrating. (b) Lossy metagrating.

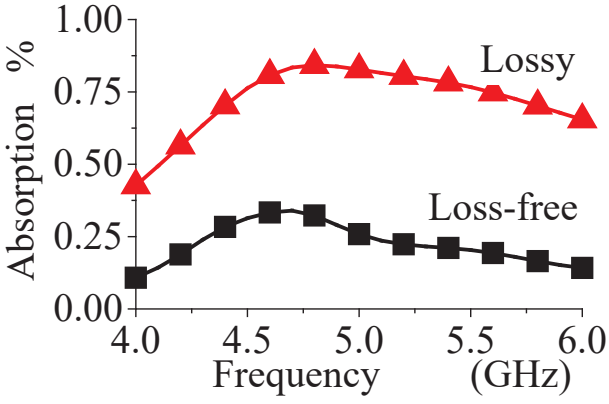

Fig. 6. Absorption performance of the metagrating with multiple elements.

the normal illumination of a *y*-polarized TE plane wave is shown in Figure 9. It also shows the RCSs of the metasurface with no metagrating and the PEC with the same size. The metasurface with no metagrating reduces the RCS effectively within 8.5-19.5 GHz. The metasurface embedded with the metagrating provides an extra low-

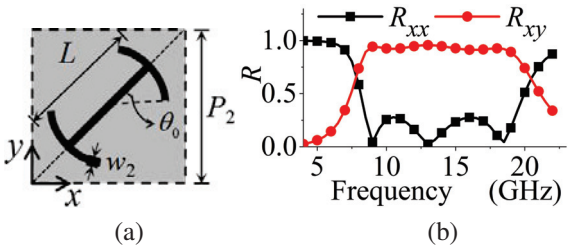

Fig. 7. Polarization converter used for the low-RCS metasurface. (a) Element of the converter. (b) Performance of the converter. L = 5 mm, w_2= 0.5 mm, θ_0= 35°, and P_2= 6 mm.

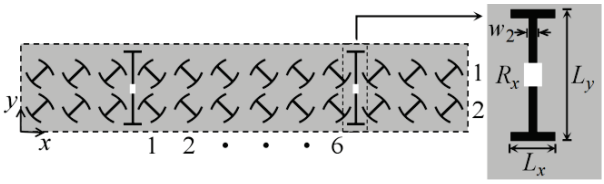

Fig. 8. Low-RCS metasurface embedded with metagrating, where L_x= 1.8 mm, L_y= 11.5 mm, and R_x= 5 Ω.

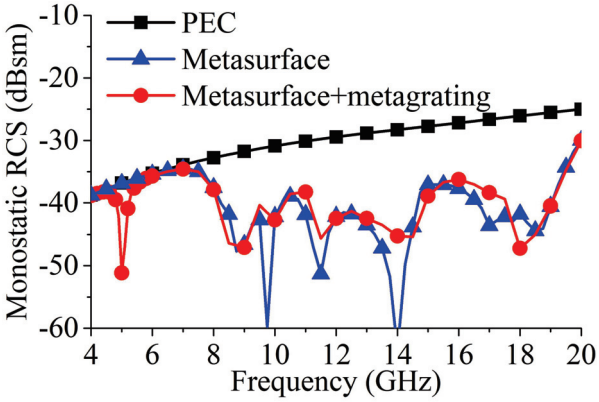

Fig. 9. RCS of PEC, the low-RCS metasurface, and the metasurface embedded with the lossy metagrating.

RCS band of 2% at 5 GHz and the original low-RCS band remains almost unchanged.

IV. CONCLUSION

The lossy metagrating is proposed to reduce RCS under the illumination of TE-polarized waves in this paper. The metagratings with both single element and multiple elements per supercell are studied. The theory based on the loss-free metagrating is used for the design of low-RCS metagrating, and numerical results show that lossy metagrating reduces the RCS effectively. The lossy metagrating is also incorporated into a wideband low-RCS metasurface to provide an extra low-RCS band and

has a negligible effect on the low-RCS band of the metasurface. The metagrating has lesser elements than the metasurface and is conveniently loaded with lumped elements for RCS reduction.

ACKNOWLEDGMENT

This work was supported by the National Natural Science Foundation of China under Grants 62171093 and 62161048.

REFERENCES

[1] F. Costa, A. Monorchio, and G. Manara, "Analysis and design of ultra thin electromagnetic absorbers comprising resistively loaded high impedance surfaces," *IEEE Trans. Antennas Propag*., vol. 58, no. 5, pp. 1551-1558, May 2010.

[2] F. Costa and A. Monorchio, "A frequency selective radome with wideband absorbing properties," *IEEE Trans. Antennas Propag.*, vol. 60, no.6, pp. 2740-2747, Jun. 2012.

[3] M. Paquay, J. C. Iriarte, I. Ederra, R. Gonzalo, and P. D. Maagt, "Thin AMC structure for radar cross-section reduction," *IEEE Trans. Antennas Propag.*, vol. 55, no. 12, pp. 3630-3638, Dec. 2007.

[4] T. Shang, J. Zhao, and J. Xu, "Convolution operations on coding metasurface for RCS reduction," *Applied Computational Electromagnetics Society (ACES) Journal*, vol. 36, no. 10, pp. 1295-1300, Oct. 2021.

[5] W. B. Pan, C. Huang, M. B. Pu, X. L. Ma, J. H. Cui, B. Zhao, and X. G. Luo, "Combining the absorptive and radiative loss in metasurfaces for multi-spectral shaping of the electromagnetic scattering," *Sci. Rep.*, vol. 19, no. 6, pp. 21462, 2016.

[6] C. L. Holloway, E. F. Kuester, J. A. Gordon, J. O'Hara, J. Booth, and D. R. Smith, "An overview of the theory and applications of metasurfaces: The two-dimensional equivalents of metamaterials," *IEEE Antennas Propag. Mag.*, vol. 54, no. 2, pp. 10-35, Apr. 2012.

[7] Y. Ra'di, D. L. Sounas, and A. Alù, "Metagratings: Beyond the limits of graded metasurfaces for wave front control," *Phys. Rev. Lett*., vol. 119, no. 6, pp. 067404, Aug. 2017.

[8] O. Rabinovich and A. Epstein, "Analytical design of printed circuit board (PCB) metagratings for perfect anomalous reflection," *IEEE Trans. Antennas Propag.*, vol. 66, no. 8, pp. 4086-4095, Aug. 2018.

[9] V. Popov, F. Boust, and S. N. Burokur, "Controlling diffraction patterns with metagratings," *Phys. Rev. Applied*, vol. 10, no. 1, pp. 011002, Jul. 2018.

[10] J. M. Liu, X. Fang, F. He, S. Q. Yin, W. Lyu, H. Geng, X. J. Deng, and X, P. Zheng, "Directional conversion of a THz propagating wave into surface waves in deformable metagraings," *Optics Express*, vol. 29, no. 14, pp. 21749-21762, Jul. 2021.

[11] Y. Ra'di and A. Alù, "Metagrating for efficient wavefront manipulation," *IEEE Photonics Journal*, vol. 14, no. 1, pp. 227513, Feb. 2022.

Kai Wang received the B.S. degree from the University of Electronic Science and Technology of China (UESTC), Chengdu, China, in 2015, where he is currently working toward the Ph.D. degree in radio physics.

His current research interests include metasurface design and computational electromagnetics.

Wei Shao received the B.E. degree in electrical engineering from the University of Electronic Science and Technology of China (UESTC) in 1998, and the M.Sc. and Ph.D. degrees in radio physics from UESTC in 2004 and 2006, respectively.

He joined the UESTC in 2007 and is currently a Professor there. From 2010 to 2011, he was a Visiting Scholar with the Electromagnetic Communication Laboratory, Pennsylvania State University, State College, PA, USA. From 2012 to 2013, he was a Visiting Scholar with the Department of Electrical and Electronic Engineering, Hong Kong University. His research interests include computational electromagnetics and antenna design.

Hua Li received the B.S. and the M.S. degrees from the Sichuan Normal University, Chengdu, China, in 1999 and 2002, respectively, and the Ph.D. degree from the University of Electronic Science and Technology of China (UESTC) in 2011.

In 2002, she joined UESTC, where she is currently an Associate Professor. From 2014 to 2015, she was a Visiting Scholar with the Department of Electrical and Computer Engineering, National University of Singapore, Singapore. Her current research interests include filtering antennas, reconfigurable antennas, implantable antennas, and metasurface antennas.

Bing-Zhong Wang received the Ph.D. degree in electrical engineering from the University of Electronic Science and Technology of China (UESTC) in 1988.

He joined the UESTC in 1984, where he is currently a Professor. He has been a Visiting Scholar with the University of Wisconsin-Milwaukee, a Research Fellow with the City University of Hong Kong, and a Visiting Professor with the Electromagnetic Communication Laboratory, Pennsylvania State University, State College, PA, USA. His current research interests are in the areas of computational electromagnetics, antenna theory and technique, and electromagnetic compatibility analysis.

A Novel Design of Microwave Absorbers Based on Multilayered Composite Materials for Reduction of Radar Cross Section

Hong Qin Zheng, Yi Tao Huang, and Mei Song Tong

Department of Electronic Science and Technology
Tongji University, Shanghai 201804, China
mstong@tongji.edu.cn

***Abstract* –** Reduction of radar cross section (RCS) for targets can be achieved by different approaches and coating absorbing materials at the surfaces of targets is one of widely used methods because of its flexibility and good effect. In the work, we put forward a novel method of reducing the RCS based on the design of multilayer composite absorbing materials. The transmission line theory and particle swarm optimization (PSO) are used to guide the design and analysis, and two kinds of designs, i.e., Type IV and Type VII, are selected finally. Simulation experiments show that the designs are insensitive to the incident angles and polarizations of incident EM wave, which is required for being coated at the surfaces of real objects. Also, the designed absorbing materials are very thin and have an ultra-wide frequency band. The bandwidth of Type-IV design can reach 14.63 GHz, ranging from 3.37 to 18.0 GHz, while Type-VII design can cover the frequency range from 2.0 to 18.0 GHz, which represents the major part of radar's frequency range. The designed absorbing materials are coated at the surface of a perfectly-electric-conducting (PEC) cylinder to validate the effectiveness of the materials, and good results have been obtained.

***Index Terms* –** Microwave absorber, absorbing media, radar cross section, transmission line theory, particle swarm optimization.

I. INTRODUCTION

Radar cross section (RCS) is a measure for the strength of electromagnetic (EM) fields scattered by targets and reducing the RCS as much as possible is the basic requirement for designing stealth targets [1]. With the significant development of radar techniques since World War II, reducing the RCS of targets has become a passive and indispensable technique for reducing the detectability of targets [2] and has been eagerly needed in military applications or even in some civilian applications [3]. Generally, there are four categories of techniques for reducing the RCS, i.e., design of geometric shape, coating of microwave absorbing material, passive cancelation, and active cancelation [4]. Each method has its advantages and disadvantages. Compared with the other three methods, coating the absorbing materials could be the most important because it is flexible, cost-effective, of good performance, and has been widely applied in the RCS reduction for the targets like airplanes, ships, missiles, etc., or even used in the interference shielding of some targets [5–7].

The reduction of RCS by covering appropriate absorbing materials is a very hot research topic and many researchers have been dedicated to working on the topic for a long time. The earliest microwave absorber can date back to the early 1940s when Winfield Salisbury invented the Salisbury screen [8]. After that, various microwave absorbers, such as the Jaumann screen, the Dallenbach layer, the frequency selective surface, etc., were proposed and have been developed for many years [9–13]. In recent years, the metamaterial as a novel absorbing material has caught up a wide attention [14]. Although the metamaterial has the property that can greatly extend the parameter space accessible with natural materials, it has some obvious drawbacks in practical applications. The metamaterial absorbers usually have a narrow bandwidth [15] although they could be insensitive to the incident angles and polarizations of incident waves which is also very desirable. He and Jiang proposed a kind of metamaterial absorber that had shown a wideband absorption, but it still cannot cover a wider frequency range which most of the radars are using [16]. Also, some metamaterial absorbers are actually sensitive to the incident angles and polarizations of incident waves, greatly reducing their applicability.

Compared with the metamaterial, some composite materials have shown a better performance, i.e., they can not only cover a much wider frequency range but also be insensitive to the incident angles and polarizations [17]. Thanks to the significant progress of material science, it has become feasible to synthesize composite materials that have much lower or higher EM

Submitted On: September 17, 2021
Accepted On: April 3, 2022

https://doi.org/10.13052/2022.ACES.J.370310

parameters which allow to extensively adjust the performance of materials [18]. Yuan *et al.* proposed an ultrathin broadband composite absorbing material which has an operating bandwidth ranging from 4.0 to 18.0 GHz [19]. Ali *et al.* presented the design of novel and lightweight microwave absorbers, which also exhibited a broad bandwidth of 3.74 GHz [20]. Ling *et al.* designed a broadband absorbing material whose effective absorption bandwidth reaches 12.6 GHz and total thickness is only 2.3 mm [21].

All designs for the microwave absorbers in the above are assumed to work on an infinitely large plate and their EM performance is also obtained under this assumption. However, real objects like airplanes have curvilinear surfaces that could include finite plates, corners, and other-shaped parts in various sizes. As a result, the absorbers are required to possess a stable performance when incident waves are of different incident angles and polarizations. Some composite materials like carbonyl iron powders (CIPs) [22] have been proven to be insensitive to the incident angles and polarizations so that they can be used as such absorbers [23]. The existing materials have the problems of narrow operation bandwidth. Meanwhile, the relative bandwidths of the absorbing materials which are suitable for the detection frequency band of the radar are small. In the operation frequency band, the existing materials also have the disadvantages of low absorptivity and angle sensitivity and the EM parameters of which are instable neither. The existing design methods often determine the final structure through the analysis of EM parameters or repeated simulation. This method costs a lot of time and may not necessarily obtain the best iterative convergence result under this condition.

In this work, we propose a novel method to design the absorbers for reducing the RCS of some objects. Since most of the radar systems are working at the frequency range from 2.0 to 20.0 GHz, we try to design the absorbers that can cover most of radar's frequency range, i.e., from 2.0 to 18.0 GHz. We apply the transmission line theory (TLT) and particle swarm optimization (PSO) to the design of multilayered absorbers which are composed of two types of CIP composite materials. We then choose two representative designs to investigate their performance on the reduction of RCS under the different incident angles and polarizations of incident waves. Based on the simulation experiments, we can find the best design of absorbers that are most insensitive to the incident angles and polarizations. Finally, the designed absorbers are coated on the surface of a perfectly-electric-conducting (PEC) cylinder and we demonstrate that the designed absorbers can perform well for real objects.

II. MICROWAVE ABSORBING MATERIALS

Microwave absorbing materials are used to coat the surface of targets in the reduction of RCS. Compered with single-layer absorbers, multilayered absorbers are more flexible and can achieve better performance, including wider bandwidth and smaller thickness [24]. As shown in Figure 1, a multilayered absorber usually consists of the matching layer and the absorbing layer [25]. The matching layer, which is on the top of the absorber, helps couple the impedance of the free space with the impedance of the absorber. On the other hand, the absorbing layer, which is on the bottom of the absorber, absorbs most of EM energies.

The used materials are essential in the design of absorbers since the performance of absorbers mainly depends upon the performance of used materials. Each layer consists of different materials so that different designs of absorber with different performances can be obtained. Usually, there are three types of material in the design of microwave absorbers, i.e., dielectric material, magnetic material, and composite material [26]. In this paper, two types of composite materials with different proportions of CIPs are used since the CIPs have exhibited a very strong absorbing capability for EM energies [22]. The composite material with 10% CIP is used to build the matching layer, and the composite material with 35% CIP is used to construct the absorbing layer. Hereinafter, we will use S_1 to represent the composite material with 10% CIP and use S_2 to indicate the composite material with 35% CIP. The complex permittivity and complex permeability of the two composite materials are frequency-dependent and their relationships are shown in Figures 2 and 3, respectively.

From the figures, we can see that the complex permittivity and complex permeability (referring to the magnitudes of their real and imaginary parts) of S_1

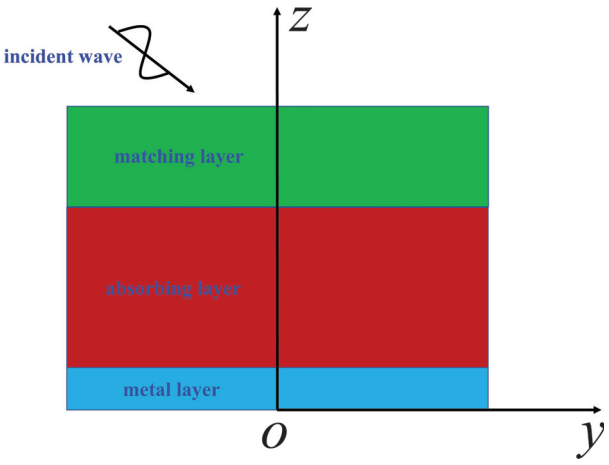

Fig. 1. Structure of a multilayered absorber.

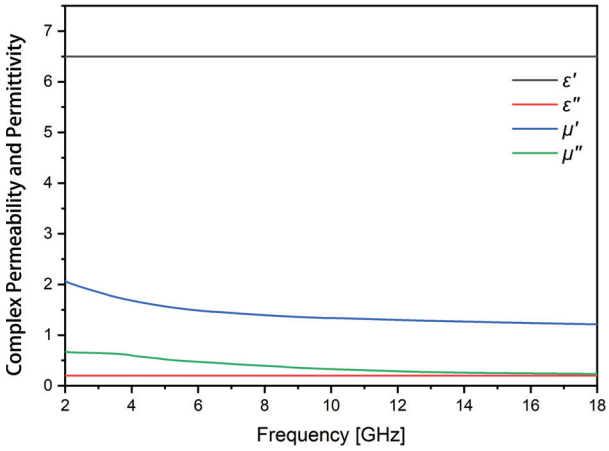

Fig. 2. Permittivity ε and permeability μ of composite material with 10% CIP. Prime denotes the real part while double prime denotes the imaginary part.

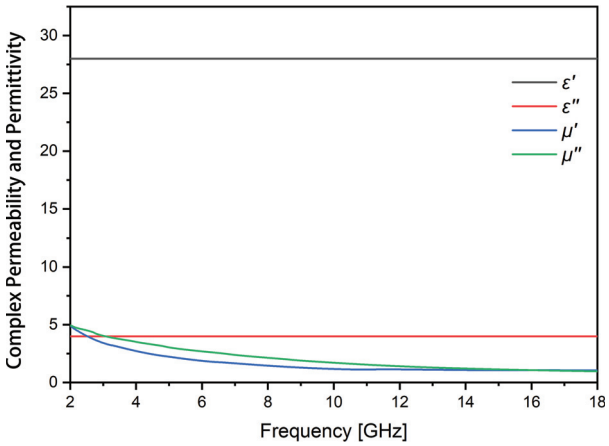

Fig. 3. Permittivity ε and permeability μ of composite material with 35% CIP. Prime denotes the real part while double prime denotes the imaginary part.

are relatively low in the frequency range from 2.0 to 18.0 GHz. Also, the complex permittivity of S_1 is almost constant in the above frequency range and the complex permeability varies with the frequency very slowly. As a result, it is possible that the impedance of a layer composed of S_1 is close to the impedance of free space in the above frequency range. Compared to S_1, the material S_2 owns a higher complex permittivity and complex permeability. Moreover, the magnitude of complex permittivity is stable and the magnitude of complex permeability decreases slightly. This feature leads to that S_2 has a good absorption and poor impedance matching while S_1 has an opposite behavior.

III. DESIGN OF MULTILAYERED ABSORBERS

The design of absorbers requires an efficient and accurate analysis or evaluation for their performance. Full-wave EM simulation is a good way to do that, but it consumes much time and resources. Compared to the former approach, the TLT can also be used to analyze but requires much less time and resources. Usually, a planar multilayered absorber can be represented by a transmission-line model so that we can apply the TLT to analyze the behavior of multilayered absorbers. In the analysis, the reflection coefficient of absorbers can be used to evaluate the performance if the input impedance is available. The input impedance can be calculated by using the TLT [27], i.e.,

$$Z_{\text{in}_j} = Z_j \frac{Z_{\text{in}_{j-1}} + Z_j \tanh\left[j(2\pi f d_j/c)\sqrt{\mu_j \varepsilon_j}\right]}{Z_j + Z_{\text{in}_{j-1}} \tanh\left[j(2\pi f d_j/c)\sqrt{\mu_j \varepsilon_j}\right]} \tag{1}$$

where

$$Z_j = Z_0 \sqrt{\mu_j/\varepsilon_j} \tag{2}$$

$$\mu_j = \mu_{r_j}\mu_0, \quad \varepsilon_j = \varepsilon_{r_j}\varepsilon_0 \tag{3}$$

$$j = 1, 2, 3, \ldots, n. \tag{4}$$

Also, d_j, f, c, ε_{r_j}, μ_{r_j}, and Z_j denote the thickness, frequency, speed of light, complex permittivity, complex permeability, and intrinsic impedance of the jth layer ($j = 1, 2, 3, \ldots, n$), respectively. In addition, ε_0 and μ_0 are the permittivity and permeability of free space, Z_{in_j} is the wave impedance of the jth layer, and n is the total number of layers. Based on the input impedance, the overall reflection coefficient of the multilayered absorber at an air-absorber interface is given by

$$\Gamma = -20\lg\left|\frac{Z_{\text{in}j} - Z_0}{Z_{\text{in}j} + Z_0}\right|. \tag{5}$$

If we choose $n = 2$, i.e., design a two-layer absorber, then the input impedance can be simplified as

$$Z_{\text{in}} = Z_2 \frac{Z_{\text{in}_1} + Z_2 \tanh\left[j(2\pi f d_2/c)\sqrt{\mu_2 \varepsilon_2}\right]}{Z_2 + Z_{\text{in}_1} \tanh\left[j(2\pi f d_2/c)\sqrt{\mu_2 \varepsilon_2}\right]} \tag{6}$$

where

$$Z_{\text{in}_1} = Z_0 \sqrt{\frac{\mu_1}{\varepsilon_1}} \tanh\left[j\frac{2\pi f d_1}{c}\sqrt{\mu_1 \varepsilon_1}\right] \tag{7}$$

and the overall reflection coefficient is

$$\Gamma = -20\lg\left|\frac{Z_{\text{in}} - Z_0}{Z_{\text{in}} + Z_0}\right|. \tag{8}$$

In the above, Z_{in_1} is the wave impedance at the surface of the first layer and Z_{in} is the wave impedance at the second layer. With the reflection coefficient, we can calculate the absorption of the incident EM wave normal to the planar multilayered absorber.

Based on the above method of evaluating the performance of absorbers, we can then design desirable multilayered absorbers. How to determine the number of layers, type of materials, and thickness of each layer is the key in the design, and optimization algorithms can be

used to efficiently select those parameters with a low cost [28]. Compared with other optimization methods, the PSO is an efficient method that can be easily used in the design of absorbers [29]. The PSO was inspired by a flying swarm of birds searching for food and we use it to seek optimal values for the thickness of each layer and the number of layers [30]. In order to obtain the optimal result, we should take the total thickness, bandwidth, and reflection peak together into consideration. Therefore, the cost function to be optimized can be set as [31, 32]

$$f = k_1 \cdot \Gamma_{\min} + k_2 \sum d_i + k_3 \cdot WB + k_4 \cdot \Gamma_{\text{ave}}$$
$$i = 1, 2, 3, \ldots, n \tag{9}$$

where $\Gamma_{\min}$ is the minimum of reflection coefficient, d_i is the thickness of ith layer, WB is the bandwidth of the absorber, Γ_{ave} is the average of reflection coefficient, and k_j $(j = 1, 2, 3, 4)$ is the weight of each term. Also, $\sum d_i$ represents the total thickness of the multilayered absorber. Selecting the appropriate weight for each term, we can get the optimal values for those parameters by minimizing the cost function.

Considering the simplest case, namely, the number of layers is chosen as $n = 2$, we can get a planar design. The two-layer absorber is composed of the matching layer and absorbing layer. The matching layer on the top of the absorber consists of the material S_1 while the absorbing layer on the bottom of the absorber consists of the material S_2. After using the PSO to minimize the above cost function, we can obtain the optimal value 2.13 mm for the matching layer and 0.87 mm for the absorbing layer, respectively, and the total thickness of the absorber is then 3.0 mm. With the optimal thickness of each layer, the reflection coefficient of the two-layer absorber can be calculated and is shown in Figure 4.

As shown in Figure 4, the absorber can cover most of the frequency range from 2.0 to 18.0 GHz. Furthermore, the bandwidth of the absorber is 14.63 GHz

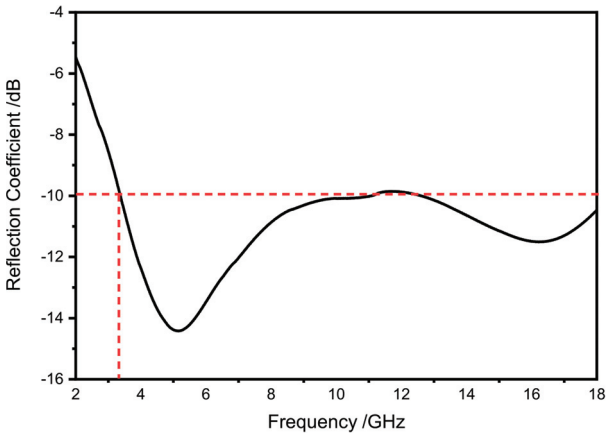

Fig. 4. Reflection coefficient of a two-layer absorber.

Table 1: Multilayered absorber design (unit: mm)

Absorber	Layer I	Layer II	Layer III	Layer IV	Layer V
Type I	S1	-	-	-	-
	3.00	-	-	-	-
Type II	S2	-	-	-	-
	3.00	-	-	-	-
Type III	S1	S2	-	-	-
	0.64	0.30	-	-	-
Type IV	S2	S1	-	-	-
	0.87	2.13	-	-	-
Type V	S2	air gap	S1	-	-
	0.01	0.87	2.20	-	-
Type VI	air gap	S2	air gap	S1	-
	0.01	1.14	1.16	1.03	-
Type VII	S2	air gap	S2	air gap	S1
	1.19	1.14	0.33	1.47	1.06

ranging from 3.37 to 18.0 GHz. The minimum return loss appears at 5.14 GHz and the value is -14.42 dB. These data demonstrate that the two-layer absorber has a good performance.

If we increase or decrease the number of layers, the behavior of the absorber could significantly change. When a multilayer absorber is designed, the performance of absorber will vary in terms of the thickness of each layer, type of materials, and number of layers. Based on the design of two-layer absorber, we change the number of layers from 1 to 5 and the thickness of each layer is different in different cases. Through the optimization by the PSO, we obtain seven multilayered designs and the final results are shown in Table 1.

As we can see from Table 1. the seven designs have different values for the number of layers, type of materials, and thickness of each layer, and their performances vary greatly in the working frequency range of $2.0 - 18.0$ GHz, as shown in Figure 5.

From Table 1 and Figure 5, we can see that the designs of Type I and Type II are both single-layer absorbers with a narrow bandwidth. The reflection peak of Type-I design cannot reach a reflection peak of -10 dB when the thickness is 3.0 mm, and Type-II design only covers a very narrow frequency band with a thickness of 3.0 mm. Thus, a single-layer absorber cannot well absorb the EM energy at most frequencies and a multilayered design is needed to increase both the reflection peak and bandwidth. Type-III design consists of the material S_1 as the absorbing layer and the material S_2 as the matching layer. As shown in the Table 1 and Figure 5, this design presents a good reflection peak with about -30 dB and covers a wider frequency band from 12.0 to 18.0 GHz. After exchanging the materials of the matching layer and the absorbing layer, Type-IV design shows a lower reflection peak with about -15.0 dB, but

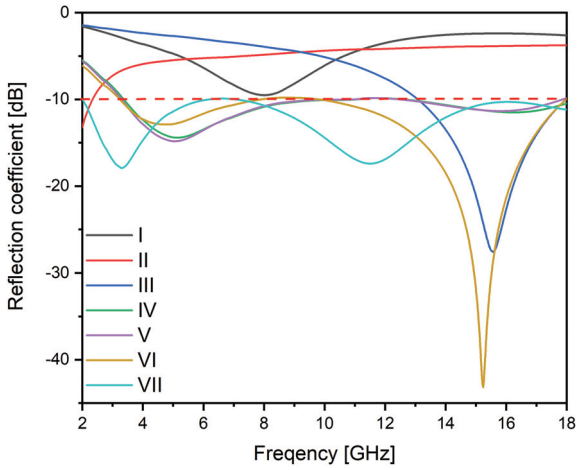

Fig. 5. Reflection coefficients of multilayered absorbers.

its bandwidth increases to nearly 15.0 GHz. After adding several air gaps to the design, we can get three different planar designs which are labeled as Type V, Type VI, and Type VII, respectively. Type-V design is a three-layer absorber composed of the material S_1, an air gap, and the material S_2. Its total thickness is 3.18 mm and bandwidth is also nearly 15.0 GHz. The total thickness of Type-VI design is 3.34 mm and its reflection peak reaches -43 dB. However, Type-VI design cannot give a good absorption performance at lower frequencies. In addition, Type-VII design is a five-layer absorber which consists of the material S_1, two air gaps, and the material S_2. Its absorption performance is improved because its absorption can cover all frequencies in the bandwidth of $2.0-18.0$ GHz. Moreover, its total thickness is 5.37 mm which is still small, and its minimum reflection peak achieves -17.0 dB. From the above results, it is clear that increasing total thickness by increasing the number of layers can significantly improve the performance of absorbers, but the thickness is still small enough when the wisely chosen composite materials are used.

IV. DESIGN OF ABSORBERS FOR COATING REAL OBJECTS

The above designs assume that the surfaces of absorbers are planar and infinitely large, but the absorbers need to cover the surfaces of arbitrarily shaped objects rather than infinitely large planar surfaces. Thus, it is required that the designed absorbers should not only have a wide bandwidth but also be insensitive to the incident angles of incident waves. We investigate how the incident angles impact the performances of absorbers by choosing Type-IV and Type-VII designs from the previous designs as examples and setting up four different incident angles from 0° to 45° with an interval of 15°. With the four different incident angles, we calculate the reflection coefficients for Type-IV and Type-VII designs and the results are shown in Figures 6 and 7, respectively. Type IV is a two-layer planar design whose thicknesses of the matching layer and absorbing layer are 2.13 and 0.87 mm, respectively. The planar design can cover the frequency range from 3.37 to 18 GHz with a bandwidth of nearly 15 GHz. The minimum reflection loss appears at 3.26 GHz with a value of -17.75 dB. Additionally, the total thickness of the design is only 3.00 mm, which is very thin. As shown in Figure 6, there are four absorption rates that are similar to each other but in different positions. The reflection coefficient becomes smaller at a certain frequency when the incident angle increases from 0° to 45°. Moreover, similar results can be seen when the incident angle is 0° and 45°, which means that the design can still give an optimal performance if the range of incident angle is not very large. Even though the incident angle increases to 45°, all the four cases have shown a good performance and their reflection coefficients are below -7.0 dB for most frequencies from 2.0 to 18.0 GHz.

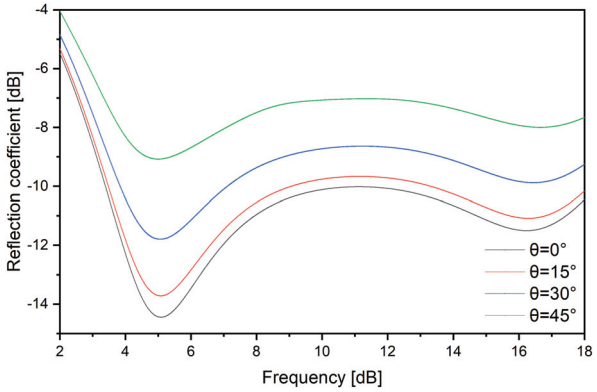

Fig. 6. Reflection coefficient of Type-IV design at four different incident angles.

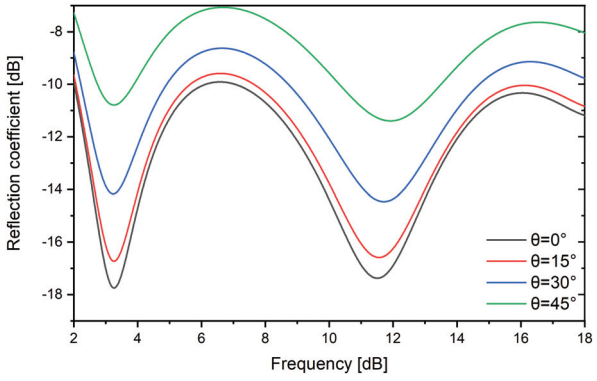

Fig. 7. Reflection coefficient of Type-VII design at four different incident angles.

Type VII is a five-layer planar design, which consists of the material S_2, an air gap, the material S_2, an air gap, and the material S_1 in the order from the bottom to the top. In addition, thicknesses of five layers from the bottom to the top are 1.19, 1.14, 0.33, 1.47, and 1.06 mm, respectively. The absorber can overcome the drawback of Type-IV design, i.e., the poor performance at lower frequencies. It can achieve a broadband from 2.0 to 18.0 GHz and a minimum reflection loss at 5.14 GHz, whose value is -14.42 dB. Obviously, Type-VII design gives a better performance as shown in Figure 7. This clearly demonstrates that the smaller the incident angle is, the lower the absorption rate of Type-VII design is. In addition, the four curves in Figure 7 resemble each other but have different Y-axis positions. Furthermore, the reflection coefficients of all the four cases are not more than -7.0 dB at the frequency range from 2.0 to 18.0 GHz.

Compared to the Type-IV design, the Type-VII design has better results for all the four cases. Type-VII design can still produce excellent results for all the four cases even at lower frequencies, and its minimum reflection loss is also smaller than that of Type-IV design. Nevertheless, both Type-IV and Type-VII designs are insensitive to the incident angles; so they can both perform well when coated at other objects with different shapes.

In order to validate the performances of designed absorbers, we coat the absorbers on the surface of a PEC cylinder and calculate the monostatic RCS for the cylinder with and without the coating. The PEC cylinder has a height of $h = 60$ mm and a cross-sectional radius of $a = 60$ mm, which is equivalent to two wavelengths at the frequency of 10 GHz. We select three incident angles to verify the absorbing capacity of two types of coating materials. When the incident wave perpendicularly incidents to the upper circular surface of the cylinder and its polarization is horizontally polarized, the results of monostatic RCS of the cylinder with Type-IV coating or Type-VII coating or without coating are shown in Figure 8.

Figure 8 shows that the performance of two kinds of coating is obviously better than that without the coating and the performance of the Type-IV coating is better than that of the Type-VII coating, especially at the lower frequencies from 2.0 to nearly 14.5 GHz. From 14.5 to 18 GHz, the performance of Type-IV is better than Type-VII. The Type-IV coating can help to reduce the RCS in minimum 2.0 dB at 2.0 GHz and in maximum 17.5 dB at 17 GHz. The Type-VII coating can help to reduce the RCS in minimum 5.0 dB at 2.0 GHz and in maximum 16.5 dB at 12.0 GHz. The RCS of the PEC cylinder without the coating increases from -10.0 to 7.0 dB as the frequency increases. In addition, for

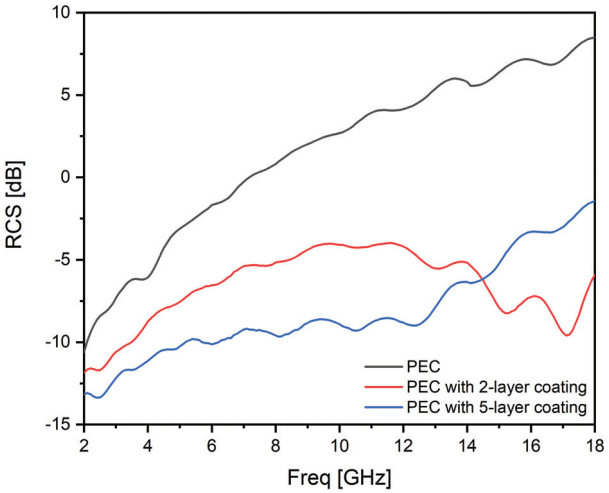

Fig. 8. Comparison of monostatic RCS solutions for the PEC cylinder without and with the coating tested by the perpendicularly incident wave.

the Type-IV coating, its RCS reduction becomes larger as the frequency increasing in most part of the operation band. While with the coating of Type-VII, its RCS reduction becomes larger from 2.0 to 9.0 GHz and then maintains a large reduction of nearly 14 dB from 9.0 to 18 GHz.

When the incident wave which is horizontally polarized incidents with an angle of 45° to the upper circular surface of the cylinder, the results of RCS of the cylinder with Type-IV coating or Type-VII coating or without coating are shown in Figure 9. The RCS of the PEC cylinder without the coating is below -20 dB at

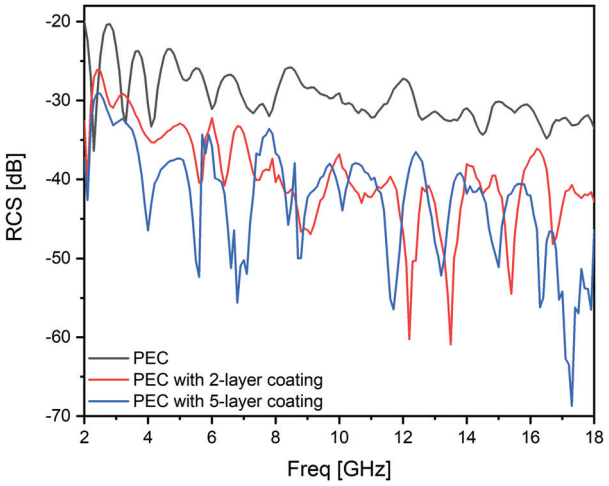

Fig. 9. Comparison of monostatic RCS solutions for the PEC cylinder without and with the coating at the incident angle of 45° to the upper circular surface of the cylinder.

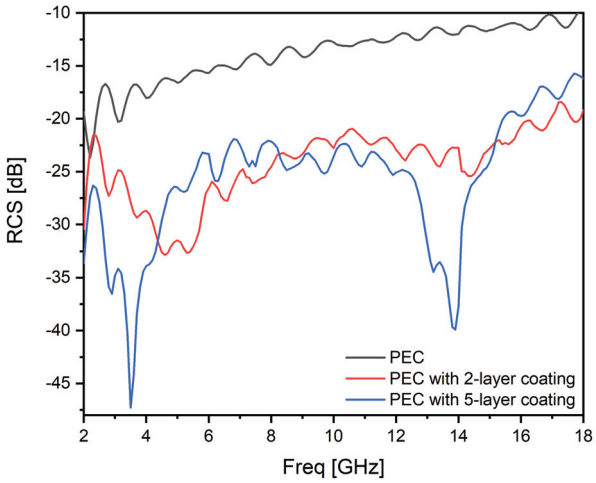

Fig. 10. Comparison of monostatic RCS solutions for the PEC cylinder without and with the coating at the incident angle of 90° to the upper circular surface of the cylinder.

low frequency and decreases to −30 dB as the frequency increases to 18 GHz. Both of the coatings have the ability to reduce the RCS more than 8.0 dB at most of the frequency band. At a huge part of the frequency band, the reduction of Type-VII coating is higher than that of Type-IV coating, especially at the lower frequencies and higher frequencies.

By further using the incident wave which is horizontally polarized incidents with an angle of 90° to the upper circular surface of the cylinder, the Poynting vector of the incident wave is parallel to the upper circular surface, and the new different consequences are obtained as shown in Figure10. From the figure, it can be seen that the coating on the cylinder generates a similar RCS reduction to that of the coating on an infinitely large plate. The performance of Type-IV coating is good at a huge part of the frequency band but cannot give a good RCS reduction at nearly 2.0 GHz. However, the Type-VII coating can reach a low RCS from 2.0 to 18 GHz and can help RCS to reduce 8.0 dB in most of the targeted frequency band. The Type-VII coating also has two absorption peaks at 3.5 and 14 GHz.

V. CONCLUSION

We develop a novel approach to reduce the RCS of targets by using multilayered composite absorbing materials. The first-layer material S_1 has a superb impedance matching capability and the second-layer S_2 has a good absorption characteristic, and their overlay constitutes the design of multilayered absorbers. In order to design more efficiently, we apply the TLT to analyze the performance of absorbers and employ the PSO to seek the optimal thicknesses of each layer, number of layers, and type of material of each layer. Seven designs with different thicknesses, materials, and numbers of layers are finally figured out and they have shown good performances. Particularly, when we change the incident angle θ of incident wave from 0° to 45°, it is found that both Type-IV and Type-VII designs among the seven designs are insensitive to the incident angles. Also, they have a small thickness and a broad frequency band. We then coat the designed absorbers on the surface of a PEC cylinder and compare the reductions of RCS between without and with the coating. It is found that the Type-VII coating can provide much more reduction of RCS than the Type-IV coating, especially at low frequencies. In addition, both designs have at least 8.0 dB reduction of RCS in the most part of the frequency band from 2.0 to 18.0 GHz. To sum up, these two material coatings have wide working bandwidths and have high relative bandwidths. They have a high absorptivity when the EM waves are incident vertically. In addition, it can be seen that these materials are angle insensitive relatively in the simulation process of the cylinder. The excellent dielectric constants also make these materials have a certain industrial application ability. The simulation results demonstrate that the designed absorbers can effectively reduce the RCS of real objects and could be good candidates for the stealth designs of targets. More importantly, this method using TLT and PSO algorithms can greatly simplify the original complex design process, save a lot of simulation time, and can be widely used in the design of many kinds of materials.

ACKNOWLEDGMENT

This work was supported by the National Natural Science Foundation of China under the Project No. 62071331 and by the International Science and Technology Collaboration Project of Shanghai Committee of Science and Technology, Shanghai, China, under the project No. 21500714400.

REFERENCES

[1] G. Ruck, *Radar Cross Section Handbook: Volume 1*, Springer, 1970.

[2] R. Grant, *The Radar Game*, Mitchell Institute Press, 2010.

[3] F. Wang, Y. Ren, and K. Li, "Broadband RCS reduction of antenna with AMC using gradually concentric ring arrangement," *International Journal of Antennas and Propagation*, 2007.

[4] H. Ucar, "Radar cross section reduction," *Journal of Naval Science and Engineering*, vol. 9, pp. 72-87, 2013.

[5] W. H. Emerson, "Electromagnetic wave absorbers and anechoic chambers through the years," *IEEE Trans. Antennas Propagat.*, vol. 21, no. 4, pp. 484-490, Apr. 1973.

[6] E. F. Knott, J. F. SChaeffer, and M. T. Tuly, *Radar Cross Section, its Prediction, Measurement and Reduction*, Artech House, Norwood, 1985.

[7] M. H. Shams, S. M. A. Salehi, and A. Ghasemi, "Electromagnetic wave absorption characteristic of Mg-Ti substituted Ba-hexaferrite," *Mater. Lett.*, vol. 62, pp. 1731-1733, 2008.

[8] B. A. Munk, *Frequency Selective Surface: Theory and Design*, John Wiley & Sons, New York, 2005.

[9] G. T. Ruck, D. E. Barrick, and W. D. Stuart, *Radar Cross Section Handbook*, Plenum press, New York, 1970.

[10] L. J. Toit, "The design of Jaumann absorbers," *IEEE Trans. Antennas Propagat.*, vol. 36, no. 6, pp. 17-25, 1994.

[11] K. Sarabandi and N. Behdad, "A frequency selective surface with miniaturized elements," *IEEE Trans. Antennas Propagat.*, vol. 55, no. 5, pp. 1239-1245, 2007.

[12] N. Landy, S. Sajuyigbe, J. J. Mock, D. R. Smith, and W. J. Padilla, "Perfect metamaterial absorber," *Physical Review Letters*, vol. 100, no. 20, pp. 207-402, 2008.

[13] F. Costa, A. Monorchio, and G. Manara, "Theory, Design and Perspectives of Electromagnetic Wave Absorbers," *IEEE Electromagnetic Compatibility Magazine*, vol. 5, no. 2, pp. 67-74, 2016.

[14] S. Kasap and P. Capper, *Springer Handbook of Electronic and Photonic Materials*, Springer, 2017.

[15] S. Chejarla, S. R. Thummaluru, S. Kalraiya, and R. K. Chaudhary, "Polarization-angle insensitive metamaterial absorber for wide incident angles," *2018 3rd International Conference on Microwave and Photonics*, pp. 1-2, 2018.

[16] Y. He and J. Jiang, "An ultra-wideband metamaterial absorber with active frequency selective surface," *2015 9th International Congress on Advanced Electromagnetic Materials in Microwaves and Optics*, pp. 100-102, 2015.

[17] R. S. Kshetrimayum, "A brief intro to metamaterials," *IEEE Potentials*, vol. 23, no. 5, pp. 44-46, Jan. 2005.

[18] N. Gill, J. Singh, S. Puthucheri, and D. Singh, "Thin and broadband two-layer microwave absorber in 4–12 GHz with developed flaky cobalt material," *Electronic Materials Letters*, vol. 14, no. 3, pp. 288-297, 2018.

[19] W. Yuan, Q. Chen, Y. Xu, H. X, S. Bie, and J. Jiang, "Broadband microwave absorption properties of ultrathin composites containing edge-split square-loop FSS embedded in magnetic sheets," *IEEE Antennas and Wireless Propagation Letters*, vol. 16, pp. 278-281, 2016.

[20] N. N. Ali, R. A. B. Al-Marieh, Y. Atassi, A. Salloum, A. Malki, and M. Jafarian, "Design of lightweight broadband microwave absorbers in the X-band based on (polyaniline/MnNiZn ferrite) nanocomposites," *Journal of Magnetism and Magnetic Materials*, vol. 453, pp. 56-61, 2018.

[21] A. Ling, G. Tan, Q. Man, Y. Lou, S. Chen, X. Gu, R. Li, J. Pan, and X. Liu, "Broadband microwave absorbing materials based on MWCNTs' electromagnetic wave filtering effect," *Composites Part B: Engineering*, vol. 171, pp. 214-221, 2019.

[22] V. A. Zhuravlev, V. Suslyaev, E. Y. Korovin, and K. V. Dorozhkin, "Electromagnetic waves absorbing characteristics of composite material containing carbonyl iron particles," *Materials Sciences and Applications*, vol. 5, no. 11, pp. 803-811, 2005.

[23] K. J. Vinoy and R. M. Jha, *Radar Absorbing Materials: From Theory to Design and Characterization*. Kluwer Academic Publishers, Boston, USA, 1996.

[24] Y. Liu, X. Liu, and X. Wang, "Double-layer microwave absorber based on CoFe2O4 ferrite and carbonyl iron composites," *Journal of Alloys and Compounds*, vol. 584, pp. 249-253, 2014.

[25] W. Meng, Y. Deng, and S. Li, "Absorption properties of carbonyl-iron/carbon black double-layer microwave absorbers," *Journal of Magnetism and Magnetic Materials*, vol. 321, no. 20, pp. 3442-3446, 2009.

[26] V. M. Petrov, and V. V. Gagulin "Microwave absorbing materials," *Inorganic Materials*, vol. 37, no. 2, pp. 93-98, 2001.

[27] M. R. Meshram, Nawal K. Agrawal, Bharoti Sinha, and P. S. Misra, "Characterization of M-type barium hexagonal ferrite-based wide band microwave absorber," *Journal of Magnetism and Magnetic Materials*, vol. 271, pp. 207-214, 2004.

[28] S. Cui and D. S. Weile, "Particle swarm optimization," *IEEE International Conference on Neural Networks*, vol. 4, pp. 1942-1948, 1995.

[29] S. Cui and D. S. Weile, "Application of a parallel particle swarm optimization scheme to the design of electromagnetic absorbers," *IEEE Trans. Antennas Propagat.*, vol. 53, no. 11, pp. 3616-3624, Nov. 2014.

[30] C. Wei, X. Shen, and F. Song, "Double-layer microwave absorber based on nanocrystalline $Zn_0.5Ni_0.5Fe_2O_4\alpha - Fe$ microfibers," *Materials and Design*, vol. 35, pp. 363-368, 2012.

[31] J. Robinson and Y. Rahmat-Samii, "Particle swarm optimization in electromagnetics," *IEEE Trans. Antennas Propagat.*, vol. 52, no. 2, pp. 397-407, Feb. 2004.

[32] J. Kennedy, "Particle swarm optimization," *Encyclopedia of Machine Learning*, pp. 760-766, 2001.

Hong Qin Zheng received the B.S. degree in Electrical Engineering from Fuzhou University, Fuzhou, China, in July 2017, and the M.S. degree in Electronic Science and Technology from Tongji University, Shanghai, China, in July 2020. She is currently working in Shanghai Kunqin Information Technology Co., Ltd. as an electronic engineer. She won the third place of the 15th "HUAWEI CUP" National Postgraduate Mathematical Contest in Modeling in 2018. Her research interest is mainly in Applied Computational Electromagnetics.

Yi Tao Huang is an undergraduate student majoring in Microelectronics Science and Engineering in Tongji University, Shanghai, China, and is expected to receive the B.S. degree in July 2023. He has won the first prize of College Students Innovation Experience Competition and the third prize of Tongji University Physics Competition and written two conference papers as the first author. His research interests include antenna design, reduction technique for radar cross section and integrated circuit design.

Mei Song Tong received the B.S. and M.S. Degrees from Huazhong University of Science and Technology, Wuhan, China, respectively, and Ph.D. degree from Arizona State University, Tempe, Arizona, USA, all in electrical engineering. He is currently the Distinguished Professor and Head of Department of Electronic Science and Technology, and Vice Dean of College of Microelectronics, Tongji University, Shanghai, China. He has also held an adjunct professorship at the University of Illinois at Urbana-Champaign, Urbana, Illinois, USA, and an honorary professorship at the University of Hong Kong, China. He has published more than 500 papers in refereed journals and conference proceedings and co-authored 6 books or book chapters. His research interests include electromagnetic field theory, antenna theory and design, simulation and design of RF/microwave circuits and devices, interconnect and packaging analysis, inverse electromagnetic scattering for imaging, and computational electromagnetics.

Prof. Tong is a Fellow of the Electromagnetics Academy, Fellow of the Japan Society for the Promotion of Science (JSPS), and Full Member (Commission B) of the USNC/URSI. He has been the chair of Shanghai Chapter since 2014 and the chair of SIGHT committee in 2018, respectively, in IEEE Antennas and Propagation Society. He has served as an associate editor or guest editor for several well-known international journals, including IEEE Antennas and Propagation Magazine, IEEE Transactions on Antennas and Propagation, IEEE Transactions on Components, Packaging and Manufacturing Technology, International Journal of Numerical Modeling: Electronic Networks, Devices and Fields, Progress in Electromagnetics Research, and Journal of Electromagnetic Waves and Applications, etc. He also frequently served as a session organizer/chair, technical program committee member/chair, and general chair for some prestigious international conferences. He was the recipient of a Visiting Professorship Award from Kyoto University, Japan, in 2012, and from University of Hong Kong, China, in 2013. He advised and coauthored 12 papers that received the Best Student Paper Award from different international conferences. He was the recipient of the Travel Fellowship Award of USNC/URSI for the 31th General Assembly and Scientific Symposium (GASS) in 2014, Advance Award of Science and Technology of Shanghai Municipal Government in 2015, Fellowship Award of JSPS in 2016, Innovation Award of Universities' Achievements of Ministry of Education of China in 2017, Innovation Achievement Award of Industry-Academia-Research Collaboration of China in 2019, "Jinqiao" Award of Technology Market Association of China in 2020, and Baosteel Education Award of Baosteel Education Foundation of China in 2021. In 2018, he was selected as the Distinguished Lecturer (DL) of IEEE Antennas and Propagation Society for 2019–2021.

Satellite Communication Effectiveness Evaluation Based on Distributed Multi-Node Receptions

Junbo Gu[1], Dongfang Zhou[1], Hailin Deng[1], Binggang Huang[2], Qiang Peng[2], Dewei Zhang[1], Dalong Lv[1] and Qing Liu[1]

[1]Academy of Information System Engineering
Information Engineering University, Zhengzhou, 450001, China.
junbogu@163.com

[2]Satellite Communication
Southwest Electronic and Telecommunication Technology Research Institute, Chengdu, 610000, China.

Abstract – Satellite-communication effectiveness evaluation is one of the key issues in the field of satellite communication links for satellite operation, maintenance, and emergency communication. However, conventional model-based calculation methods require accurate meteorological parameters, thus not applicable to practical engineering problems. In this paper, a hybrid method, combing direct calculation and equilibrium approximation, is proposed to evaluate the effectiveness of a satellite communication system, with distributed multi-node receiver stations on the earth. Especially, the proposed equilibrium approximation approach is resilient to meteorological factors. Field tests corroborate the feasibility of this new method for real-world problems.

Index Terms – Satellite communication, effectiveness evaluation, equilibrium approximation.

I. INTRODUCTION

The effectiveness evaluation of satellite communication links has attracted more and more attention in recent years, as it plays a critical role for the satellite operation/maintenance, emergency/disaster relief, counter-terrorism, and stability maintenance. When natural disasters or human-made emergencies interrupt the operators' network communication, satellite communications are more advantageous than other communication tools for rescue activities, because it has broader coverage scopes and is resilient to human attacks and weather conditions. However, the satellite communication is vulnerable to electromagnetic interference, due to various factors, such as time, path, and meteorological conditions (temperature, humidity, air pressure). Therefore, it is mandatory to evaluate the effectiveness of satellite communications.

The effectiveness of satellite communication refers to its quality and ability. Previous research on satellite performance assessment mainly focuses on the calculation of satellite links based on the attenuation model, as the effectiveness is mainly affected by various attenuations in the process of satellite signal transmission, such as free space propagation loss, rain attenuation, cloud attenuation, atmospheric gas attenuation, etc. The rain attenuation, cloud attenuation, and atmospheric gas attenuation are closely related to climatic conditions. Because of the complexity of these attenuation calculations and their important impact on satellite communications, they have attracted extensive attention. In the past few decades, many classic attenuation models have been proposed and widely used, such as (1) cloud attenuation models: the Salonen and Uppala (SU) model [1] and Dissanayake's model [2, 3]; (2) rain attenuation models: the Recommendation ITU-R P.838-3 [4], Karasawa model [5], and SAM model [6]; (3) atmospheric gases attenuation models: Liebe's models [7, 8] and the Recommendation ITU-R P.676-12 [9].

Some recent studies have focused on refining these existing models with local climate conditions. In [10], the precipitable water vapor (PWV) data, from the Global Navigation Satellite System (GNSS), is introduced into the ITU-R cloud attenuation model, which helps achieve higher temporal and spatial resolutions for the tropical region. In [11], annual and monthly CCDF (Complementary Cumulative Distribution Functions) of rainfall rate and rain attenuation are proposed by analyzing the collected data of the Guiana Space Centre (CSG) in Kourou (French Guiana). In [12], by using rainfall rate measurements collected in Howard College at University of Kwa-Zulu Natal, the rainfall attenuation time series generated by the Synthetic Storm Technique [13] are compared with other raindrop size distribution models (the Lognormal (LGN), Gamma (GM), and Weibull (WBL) distributions). In the model-based calculation

Submitted On: December 17, 2021
Accepted On: March 21, 2022

https://doi.org/10.13052/2022.ACES.J.370311

method, accurate meteorological parameters, such as rainfall height, rainfall, temperature, and cloud height, must be known. However, in the real operation, due to the limitations of geographic space, the real-time effectiveness evaluation of satellite communications often faces the following difficulties: (1) The data are generally statistical data over the years, thus poorly available [14]; (2) Because most models are sampled from several specific areas, their universality is doubtful [15]. Therefore, most model-based methods are usually limited to ideal scenarios, but not applicable to real-world engineering problems.

To resolve this problem, we propose a hybrid method, based on the direct calculation and equilibrium approximation. The innovation of this method lies in the introduction of the distributed satellite earth stations network for the effectiveness evaluation of satellite communication links. It is worth noting that the meteorological conditions in a certain area are relatively stable and consistent [16]. By building a distributed network of satellite earth stations, we use the data collected by multiple earth stations to calculate the transmission loss of the target station, so the long-term historical data is not required; instead, only short-term or real-time measurement data is needed. This hybrid method, based on the traditional model-based link calculation method, decomposes the satellite transmission loss calculation into multiple parts, and combines the theoretical direct calculation with the equilibrium approximation calculation. It is simple to use the theory to directly calculate the losses that are not related to the weather and the atmosphere. However, the direct use of the theory to calculate the losses related to the atmosphere and meteorological factors is not only complicated to calculate the model, but also difficult to obtain related meteorological parameters. Therefore, the losses related to atmospheric and meteorological factors are calculated using the equilibrium approximation method. The meteorological variables required by this method are simple, and the corresponding model is relatively simple. The combination of the two reduces the computational complexity, and makes it easier to use in practical engineering. Furthermore, we perform field experiments, corroborating that this new method can effectively eliminate the impact of uncertain meteorological factors. Therefore, this hybrid method has important application value for satellite communication effectiveness evaluation.

The novelties from this study, for the effectiveness evaluation of satellite communication links, are summarized as follows:

1. The network of distributed satellite ground stations is constructed, which enables real-time performance evaluation.
2. A new hybrid method combining direct calculation and equilibrium approximation to evaluate the effectiveness of satellite communications is proposed. This new technique has more accurate predictions and wider application scopes than conventional methods.

The remainder of this paper is structured as follows. In Section II, we analyze the satellite communication links and their influencing factors. Section III describes satellite communication effectiveness evaluation based on the topology structures. In Section IV, We explain the rain attenuation model based on multi-node reception in this method in detail. The field experiments are shown in Section VI. Finally, Section VII draws the concluding remarks.

II. ANALYSIS OF SATELLITE COMMUNICATION LINKS AND INFLUENCING FACTORS

A. Transmission characteristics of satellite communication

As shown in Figure 1, the one-way satellite communication link is composed of the uplink from the earth station to the satellite, and the downlink from the satellite to the earth station [17]. P_{TE} is the transmitting power at the output of the earth station. L_U is the total path loss of the uplink. P_{RS} is the received power of the satellite transponder. P_{TS} is the transmitting power of the satellite transponder. L_D is the total path loss of the downlink. P_{RE} is the received power at the input of the earth station. The effectiveness of satellite communication mainly depends on the signal quality received by the receiving station. So, this paper mainly focuses on the downlink transmission from the satellite to the earth station.

B. Influencing factors of satellite communication effectiveness

In the satellite downlink, the main factors affecting the receiving signal of the earth station are the

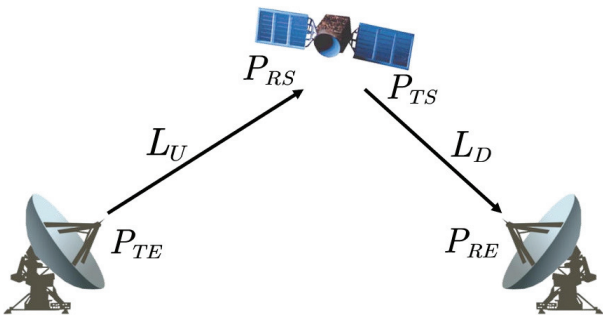

Fig. 1. The diagram of one-way satellite communication link.

transmission power of the satellite transponder and the loss from the transmission process of the satellite antenna to the ground receiving system.

When there is no interference, satellite communication executes strict power control to ensure that the transparent transponders operate in linear regions [18]. However, in practice, satellite communications may be interfered by uplink or downlink. When there is uplink interference, the transponder will change from linear state to nonlinear state or even saturated state with the increasing of the interference power, thus affecting the communication. In order to evaluate the effectiveness of satellite communications, it is necessary to measure the transmission power of the satellite transponder in real time.

In the transmission process from the satellite antenna to the ground receiving system, the signal passes through the upper atmosphere, the ionosphere, the stratosphere, and the troposphere] in turn. From the perspective of computational electromagnetics, such large-scale long-distance wave propagation can be well resolved by the total/scattered-field transmission technique [19]. It is noteworthy that [20] proposes a comprehensive computational electromagnetic algorithm, which is a remarkable tool in recent years for accurate modeling of electromagnetic wave propagation in multi-scale complex media.

The transmission loss in this process mainly includes the following two types:

1. Free space transmission loss L_{fd}: The loss is caused by energy diffusion with the increase of transmission distance in the process of radio wave propagation in free space.
2. Atmosphere and ionosphere loss L_{aid}: When the radio wave propagates through the atmosphere, it is affected by the absorption loss of the atmosphere, including the absorption of the ionosphere, and the absorption and scattering of oxygen molecules and water vapor molecules in the troposphere, clouds, fog, rain, snow, etc. These losses are closely related to the frequency of the electromagnetic wave [21], the elevation of the beam [20], and meteorological conditions.

The methods to predict the rain attenuation for a given path can be grouped into two categories, namely, physical and semi-empirical approaches. When a physical approach is used, all the input parameters are required [17]. Most prediction models resort to semi-empirical approaches. However, these semi-empirical approaches are mainly developed and evaluated using data collected in several specific areas. Therefore, they are not very effective to predict attenuation in other regions. In order to enable them to have a sufficiently preventative effect on the attenuation in other regions, an extensive meteorological database has to be used; however, these data are not usually available in most regions of the world. Therefore, in this paper, we propose a new method, combing direct calculation and equilibrium approximation to measure its effectiveness. The free space transmission loss can be directly calculated by the formula under the condition that the longitude, latitude, and altitude of the target point are known. Atmospheric and ionospheric loss is related to the real-time atmospheric and space conditions, but it is difficult to accurately measure the atmospheric and space parameters in real time, so the indirect equilibrium approximation approach is applied.

III. SATELLITE COMMUNICATION EFFECTIVENESS EVALUATION BASED ON TOPOLOGY STRUCTURE

A. System model

According to the working orbit, the satellite communication system can be divided into high orbit satellite communication system (GEO), medium orbit satellite communication system (MEO), low orbit satellite communication system (LEO). Among them, the high orbit satellite communication system is a geostationary orbit satellite communication system. At present, communication satellites are mainly concentrated in the geostationary orbit. The geostationary orbit satellite is farther from the ground than other satellites, so it has a longer propagation delay and larger link loss. This paper focuses on the effectiveness evaluation of high orbit satellite communication systems. The satellites mentioned below refer to the geostationary communication satellites.

The coverage area of the satellite communication system is very wide. The beam of one geostationary communication satellite can cover 38% of the earth's surface, so the corresponding satellite signal can be received by the earth station at any point in the satellite beam coverage area. In this paper, it is assumed that meteorological conditions within 50 km are stable and consistent. The network with certain topological structures is formed, by setting a certain number of earth stations near the target earth station. According to the stability and consistency of meteorological conditions, the relevant parameters of the target earth station are calculated, by using the signals from the nearby earth stations.

Considering the problem of satellite communication effectiveness evaluation under the condition of distributed multi-node reception, its topological structure model is shown in Figure 2. P is the target station, and Z is the satellite. Suppose that a total of n earth stations are selected for effectiveness calculation, and their set is expressed as $\mathbf{N} = \{X_1, X_2, ..., X_n\}$. Due to

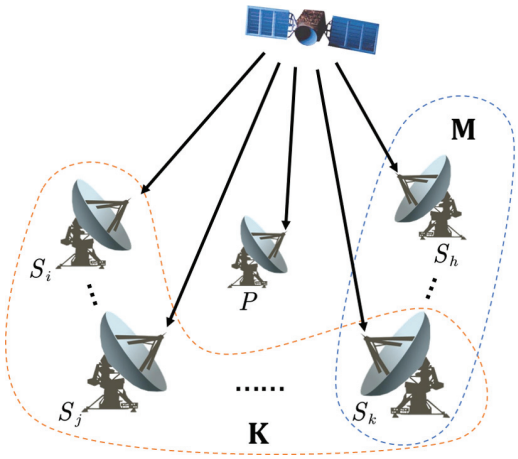

Fig. 2. The distributed multi-node reception model.

the different methods used to calculate the transmitting power of satellite transponder and the loss of atmosphere and ionosphere, these n earth stations are divided into two sets **M** and **K**. Note that **M** and **K** can have intersection. The data obtained from earth stations in **M** are used to calculate the transmitting power of the satellite transponder, and the data obtained from earth stations in **K** is used to calculate the atmospheric and ionospheric losses.

B. Transmission power of the satellite transponder

Due to the large beam area of the satellite antenna, m earth stations can be selected as **M** within the range of our observation ability, when measuring the transmitting power of the satellite transponder. The meteorological conditions of these earth stations can be directly measured, that is, L^i_{aid} is known. The longitude and latitude of the earth station and the orbital position of the satellite are known. The calculation formula of the free space transmission loss is

$$L_{fd} = \left(\frac{4\pi L}{\lambda}\right)^2, \tag{1}$$

where L is the distance from the satellite to the earth station and λ is the signal wavelength, the corresponding P^i_{RS} of the earth station X_i ($X_i \in \mathbf{M}$) can be directly measured. Then the transmission power P_{TS} of the satellite repeater can be obtained

$$\begin{aligned} \left[P^i_{TS}\right] &= \left[P^i_{RE}\right] + \left[L^i_{aid}\right] + \left[L^i_{fd}\right], \\ [P_{TS}] &= \tfrac{1}{m}\textstyle\sum_{X_i \in M}\left[P^i_{TS}\right]. \end{aligned} \tag{2}$$

Note that the square brackets imply that

$$[\cdot] = 10\,log(\cdot). \tag{3}$$

C. Losses of the atmosphere and ionosphere

The atmospheric and ionospheric losses L_{aid} are mainly composed of the ionospheric absorption loss L_{iod}, atmospheric absorption loss L_{ad}, cloud attenuation L_{cd}, fog attenuation L_{fod}, snow attenuation L_{sd}, and rain attenuation L_{rd},

$$[L_{aid}] = [L_{ad}] + [L_{iod}] + [L_{cd}] + \left[L_{fod}\right] + [L_{sd}] + [L_{rd}]. \tag{4}$$

As shown in (4), the atmospheric and ionospheric losses are mainly affected by meteorological factors, such as the atmosphere, clouds, rain, snow, and fog. Therefore, the following two situations should be considered, when we select earth stations to calculate atmospheric and ionospheric losses:

1. The distance between the earth station and the target point should be less than 50 km to ensure the similarity of meteorological and atmospheric conditions between the earth station and the target earth station (50 km is an empirical value derived from meteorological data, and reasons for choosing it will be detailed in the following content.). And the closer to the target station, the more similar the meteorological and atmospheric conditions in the transmission path of the signal received by the earth station are to those of the transmission path of the signal received by the target station.
2. Selected earth stations should be evenly distributed around the target points. When the earth stations are uniformly deployed near the target point, the information near the target point can be obtained more comprehensively, and the correlation of the data received by the earth stations can be reduced.

According to the above criteria, k earth stations within 50 km from the target point are selected as **K**. When using the data collected by these earth stations to calculate the atmospheric and ionospheric losses of the target station, we divide the atmospheric and ionospheric losses into two categories, the rain attenuation and losses other than rain attenuation. The reason for this classification is as follows.

Firstly, the ionospheric absorption, atmospheric absorption, cloud, and fog attenuation are usually small for satellite communications using C, Ku, and Ka bands. The ionospheric absorption loss is generally 0.23 dB [22, 23], and the atmospheric absorption loss, cloud attenuation, and fog attenuation are relatively small, generally 0.03 dB to 0.2 dB [24]. In particular, the weather such as snowfall is relatively rare, and the snowfall process is often relatively short-lived. So we do not consider snow attenuation in this article, i.e., $[L_{sd}] = 0$. However, the raindrop radius is about 0.025 cm to 0.3 cm. When the wave wavelength is comparable to the raindrop radius, such as Ku-band wave wavelength is about 1.5 cm to 2.5 cm, the rainfall will often cause considerable attenuation, which may be as high as 10 dB.

Then the ionosphere, atmospheric gases, cloud, and fog are often evenly distributed in a certain area, while

the rainfall is often uneven. This is determined by the formation conditions of rainfall. As the water vapor rises, the surrounding air pressure gradually decreases; its volume expands, its temperature decreases, and it gradually turns into tiny water droplets or ice crystals floating in the air to form clouds. When the cloud droplet grows to overcome the resistance of the air and the top support of the updraft, and it does not evaporate when it falls, precipitation can be formed. For example, a typical convective rain is rain formed by local heating of the air near the ground or strong cooling of the upper air, which causes convection of the upper and lower air, the lower air to rise, the water vapor cools and condenses at high altitude. Its intensity is relatively large. Strong convective rain may be accompanied by strong wind, thunder and lightning, hail or tornado, but the rain is shorter and the rain area is smaller, or distributed in discontinuous strips. Figure 3 shows a convective rain process in a region with short-duration heavy rainfall [25]. The resolution of these images is 5 km. It can be seen from the figure that even if the two points are only about 5 km apart, their rainfall intensity may differ by 16.9 mm/h and cause about 5 dB attenuation. In contrast, as shown in Table 1, the ionosphere, atmospheric gases, cloud, and fog are relatively the same in a certain area. Table 1 shows the meteorological data for parts of Qingdao, China [25]. The rainfall in the table is the cumulative rainfall for one hour. Although the difference in rainfall in some areas is large, their other meteorological conditions are not much different. By analyzing the meteorological data of previous years and considering the size of the town comprehensively, we choose 50 km as the standard, that is, in this article we consider that the ionosphere, atmosphere, cloud and fog in the area within 50 km range are similar.

To sum up, considering the fact that ionospheric absorption loss, atmospheric absorption loss, cloud attenuation, fog attenuation, and snow attenuation are small, and the ionosphere, atmosphere, cloud and fog conditions are consistent within 50 km, we assume that the ionospheric absorption loss, atmospheric absorption loss, cloud attenuation, fog attenuation, and snow attenuation of the earth station **K** are the same as those of the target station, and they are constant. Then L_{aid}^{j} of earth station X_j ($X_j \in \mathbf{K}$) can be written as

$$\left[L_{aid}^{j}\right] = \left[L_{rd}^{j}\right] + C, \tag{5}$$

where

$$\left[L_{ad}^{j}\right] + \left[L_{iod}^{j}\right] + \left[L_{cd}^{j}\right] + \left[L_{fod}^{j}\right] + \left[L_{sd}^{j}\right] = C. \tag{6}$$

When calculating the rain attenuation of the target station, it is mainly divided into two situations for discussion.

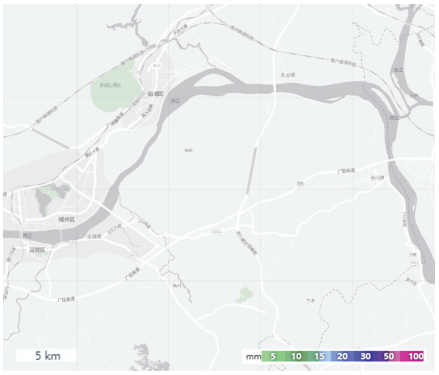

(a) 11/07/2021 19:00-20:00

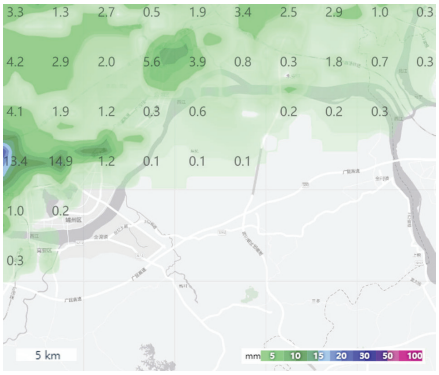

(b) 11/07/2021 20:00-21:00

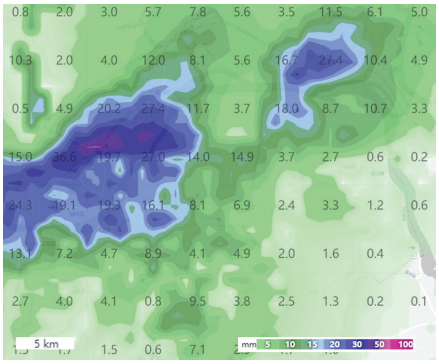

(c) 11/07/2021 21:00-22:00

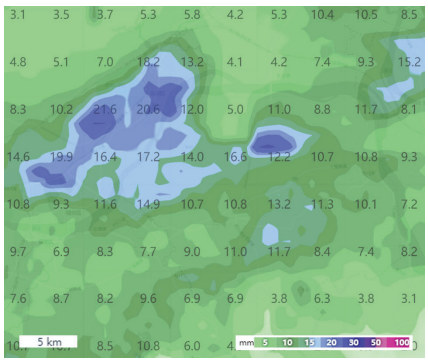

(d) 11/07/2021 22:00-23:00

Fig. 3. A convective rain process.

Table 1: Meteorological data of several areas in Qingdao

Time	Location	Ground air pressure(hPa)	Temperature (°C)	Rainfall (mm)	Relative humidity(%)	Total cloud cover
2021.07.26 03:00	Pingdu	996.66	29.04	0.00	72.03	0.71
	Chengyang	999.42	28.31	1.10	79.04	1.00
	Laoshan	997.74	27.70	0.50	81.64	0.99
	Huangdao	994.60	26.95	3.22	86.64	1.00
2021.07.26 04:00	Pingdu	996.56	29.26	0.01	69.13	0.91
	Chengyang	999.29	27.51	3.00	84.85	0.96
	Laoshan	997.40	27.28	2.13	84.54	1.00
	Huangdao	994.44	26.16	7.83	90.58	0.85
2021.07.26 05:00	Pingdu	996.21	29.81	0.47	68.51	1.00
	Chengyang	998.65	27.12	4.33	88.18	1.00
	Laoshan	996.87	27.23	2.61	86.29	1.00
	Huangdao	993.88	25.93	11.32	92.01	1.00
2021.07.26 06:00	Pingdu	995.80	29.35	1.31	73.79	0.99
	Chengyang	998.26	27.14	5.07	88.73	0.99
	Laoshan	996.54	27.47	2.06	83.42	0.99
	Huangdao	993.48	25.97	11.05	92.41	1.00
2021.07.26 07:00	Pingdu	995.43	28.65	0.00	79.53	0.99
	Chengyang	998.07	27.19	0.10	87.38	0.98
	Laoshan	996.40	27.14	0.12	87.06	0.99
	Huangdao	993.26	26.24	0.56	91.92	1.00

1. When the rainfall difference between all the earth stations in **K** and the target station is less than 2 mm/h, the sum of weighted average of X_j is taken as the atmospheric and ionospheric losses of the target station, as shown in (7).
$$\left[L^{p}_{\text{aid}}\right] = \sum_{X_j \in \mathbf{K}} \omega_j \left[L^{j}_{\text{aid}}\right], \tag{7}$$
with
$$\omega_j = \frac{1}{\left[d_j \sum_{X_j \in \mathbf{K}} \frac{1}{d_j}\right]}, \tag{8}$$
and d_j is the distance from the earth station X_j to the target station. ω_j is added, considering that the closer the earth station is to the target station, the closer their meteorological conditions are in theory; so the data from the earth station closer to the target station is of more reference value.
2. When the difference of rainfall between some earth stations in **K** and target stations is greater than 2 mm/h, we need to use earth stations' data to predict the rain attenuation of the target station. The specific method will be explained in Section IV.

IV. RAIN ATTENUATION MODEL BASED ON MULTI-NODE RECEPTION

Due to the greater impact of rain attenuation on satellite links and the complexity of its calculations, it has been a hot issue in the field of satellite communications for decades. Although more than 20 rain attenuation models have been proposed so far, there are still many related studies on rain attenuation in recent years. These models can be divided into five categories: empirical models, physical models, statistical models, gradual models, and learning-based models. Among them, statistical models are widely used due to their simple input parameters. Commonly used statistical models include M-K model, ITU-R model, MARIMA model, etc. The method in this article is also mainly improved on the basis of ITU-R model.

A. ITU-R rain attenuation model

The Recommendation ITU-R P.838-3[4] is based on the model proposed by Fedi, and its core is to adopt the concept of equivalent path length, that is, to homogenize the non-uniformity of rainfall by introducing a shortening factor with an equivalent effect. The shortened path length is multiplied by the unit path attenuation (attenuation rate) to obtain the actually measured rain attenuation. The schematic diagram of the rainfall attenuation of the ground-air path is shown in Figure 4. The calculation of the ITU-R model is equipped with the following steps:

1. Calculate the slant distance of the radio wave passing through the rain area, i.e., L_S in Figure 4.
2. Calculate the rain attenuation rate γ_R. The rain attenuation rate γ_R (dB/km) indicates the amount of rain attenuation per unit of transmission distance, which is determined by the rainfall rate $R_{0.01}$ (mm/h) and the polarization mode of the radio

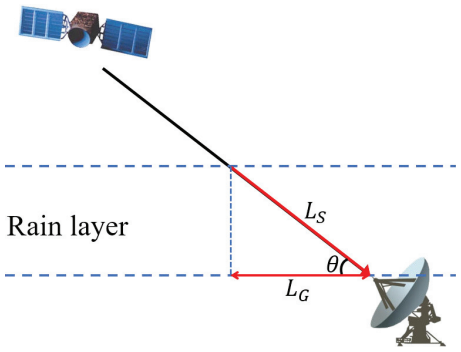

Fig. 4. Schematic diagram of rain attenuation on oblique paths.

wave. It can be calculated by (9).

$$\gamma_R = k\,(R_{0.01})^{\alpha}, \tag{9}$$

where k and α are functions related to frequency, path elevation, and polarization inclination.

3. Calculate the horizontal reduction factor $r_{0.01}$:

$$r_{0.01} = 1/\,(1+L_G/L_0)\,, \tag{10}$$

where $L_0 = 35e^{-0.015R_{0.01}}$, L_G is the horizontal projection of the slant-path as shown in Figure 4 and is given by the following expression:

$$L_G = L_S \cos\theta, \tag{11}$$

4. The total predicted path attenuation $A_{0.01}$ (dB) is obtained from:

$$A_{0.01} = \gamma_R L_E, \tag{12}$$

where $L_E = L_S r_{0.01}$ is the effective path length.

B. A robust new attenuation model

The calculation of rain attenuation rate and effective path length is very important for the ITU-R model. But k, α, and L_E are difficult to measure directly. If empirical values are used, the effect may not be ideal when the ITU-R model is applied in different climate zones. There are also many papers dedicated to solving this problem. For example, they use data from previous years in a certain area to revise k and α. The method in this paper is different from this, we use the data measured at nearby stations to calculate k, α, and L_E. Since each earth station is close enough to the target station and receives the same signal from the transmitting station, their frequency, path elevation and polarization inclination are the same. Therefore, it can be considered that k and α of each earth station and those of the target station are the same, and their equivalent rain decline paths L_E are approximately equal. The atmospheric and ionospheric losses of the earth station can be written as

$$[L_{ad}] = f\,(R,K,\alpha,C) = KR^{\alpha} + C, \tag{13}$$

where $K = kL_E$, k, α, and C are the undetermined parameters. From the signals received by earth stations, k groups of observation data $\left(R, \left[L^i_{aid}\right]\right), X_j \in K$ can be obtained. A nonlinear optimization problem is set up to obtain the parameters (K^*, α^*, C^*), where we minimize the objective function $L([L_{aid}], f\,(R,K,\alpha,C))$ for given k groups of observation data,

$$\begin{aligned}(K^*,\alpha^*,C^*) &= \arg\min_{K,\alpha,C} L([L_{aid}], f\,(R,K,\alpha,C)) \\ &= \arg\min_{K,\alpha,C} \sum_{X_j \in \mathbf{K}} \left[\left[L^j_{aid}\right] - f\,(R,K,\alpha,C)\right]^2.\end{aligned} \tag{14}$$

Then, the atmospheric and ionospheric losses of the target station can be calculated by estimating the rainfall of the target station.

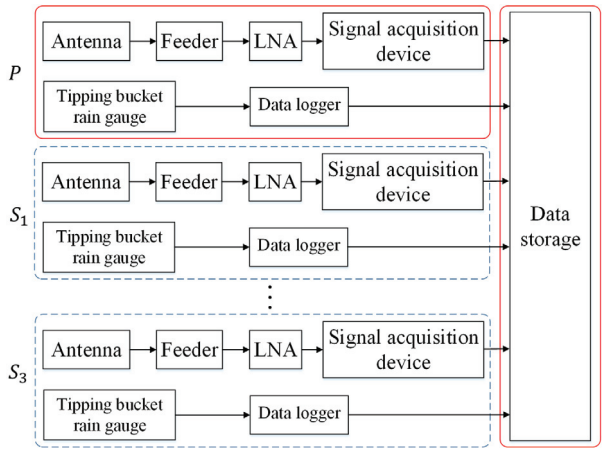

Fig. 5. Data collection systems.

V. DATA COLLECTION AND PROCESSING

In order to verify the reliability of the method in this paper, we selected a synchronous orbiting satellite in orbit 113°E and some earth stations in Qingdao, China for field measurement. The relevant parameters of the satellites and earth stations are shown in Table 2. In order to collect the required signal reception power and rainfall intensity data, we set up a data collection system between the target station P and the earth stations S_1, S_2 and S_3. The schematic diagram of the system is shown in Figure 5.

The system is divided into two parts: the data storage center set up in the target station, and the data acquisition subsystem distributed in earth stations (including the target station). Its data acquisition subsystem mainly realizes the following functions.

1. Signal acquisition. Each earth station has a Cassegrain antenna to receive satellite signals. As shown in Table 2, the antenna parameters of different sites are different. All antennas have been adjusted to point to the target satellite. The signal received by the antenna is transmitted to the

Table 2: System parameters

Class	Name	Parameter
Satellite	Orbital position	113°E
	Downlink frequency (MHz)	12334
Target station P	Antenna aperture (m)	7.5
	Antenna efficiency	0.6
	Position	36.104°N, 120.460°E
	Elevation (m)	45
Earth station S_1	Antenna aperture (m)	13
	Antenna efficiency	0.6
	Position	36.109°N, 120.444°E
	Elevation (m)	46
	Distance from target station (km)	1.6065
Earth station S_2	Antenna aperture (m)	16
	Antenna efficiency	0.6
	Position	36.446°N, 120.666°E
	Elevation (m)	84
	Distance from target station (km)	42.2625
Earth station S_3	Antenna aperture (m)	16
	Antenna efficiency	0.6
	Position	36.456°N, 120.646°E
	Elevation (m)	84
	Distance from target station (km)	42.5299

computer room via the feeder and the low-noise amplifier (LNA). Then we use signal acquisition equipment to analyze its carrier and collect its power. Finally, the collected data is transmitted to the data storage center of the target station through the network.

2. Rain intensity measurement. A tipping bucket rain gauge is installed at each station. The rain gauge can output the rainfall in the form of digital information, which is on-off value. Through the data recorder, it is sampled every one minute, and the rainfall intensity of one-minute time integration can be obtained. Then the rainfall intensity data is also transmitted to the data storage center of the target station through the network.

The data collected by this system needs to be preprocessed when applied to the calculation of the method in this paper. The collected carrier power needs to be equivalent to the antenna receiving end in order to facilitate link calculations. The signal power actually received by the earth station mentioned in the next section refers to the carrier power equivalent to the antenna receiving end. To this end, it is necessary to know the antenna gain, feeder loss and LNA gain. The receiving gain of the antenna can be calculated by (15) from the antenna diameter and antenna efficiency.

$$G = \frac{4\pi A}{\lambda^2}\eta, \tag{15}$$

where A is the area of the antenna aperture, λ is the wavelength, and η is the antenna efficiency. The sum of the feeder loss and LNA gain of the earth station is measured at the input end of the feeder and the output end of the LNA using data acquisition equipment. Therefore, the signal power actually received by the earth station mentioned in the next section P_{S_i} is obtained from

$$P_{S_i} = \hat{P}_{S_i} - [G_{S_i}] - [L_{S_i}], \tag{16}$$

where $\hat{P}_{S_i}$ is the signal power recorded by the signal acquisition equipment of the earth station S_i.

VI. EXAMPLE VERIFICATION

In order to verify the accuracy of the proposed algorithm, field measurements are carried out under different meteorological conditions, and the signal power of the target station P calculated by the proposed method is compared with the actual received power and the theoretical calculation power of ITU-R model. The ITU-R model in the calculation below comes from the latest ITU-R 2019 standard (Recommendation ITU-R P.341-7 [26], Recommendation ITU-R P.676-12 [9], Recommendation ITU-R P.838-3 [4], Recommendation ITU-R P.839-4 [27], Recommendation ITU-R P.840-8 [1]).

We measured the target station and three earth stations at four time points (T_1, T_2, T_3 and T_4) during 26/07/2021 to 30/07/2021, and calculated the theoretical value of P by using the data obtained from S_1, S_2 and S_3. The atmospheric and ionospheric losses of S_2 station are known. The meteorological conditions at T_1, T_2, T_3 and

Table 3: Weather conditions

Time	T_1	T_2	T_3	T_4
P	Cloudy	Rain (41 mm/h)	Cloudy	Sunny
S_1	Cloudy	Rain (33 mm/h)	Cloudy	Sunny
S_2	Cloudy	Cloudy	Sunny	Cloudy
S_3	Cloudy	Rain (5.8 mm/h)	Sunny	Cloudy

Table 4: The power of each station and the calculated power of P at the time of T_1, T_2, T_3 and T_4, frequency 12.334 GHz.

Power(dBW)	T_1	T_2	T_3	T_4
P_{S1} (the actual received power of S_1)	−148.79	−152.52	−148.77	−148.97
P_{S2} (the actual received power of S_2)	−149.66	−147.82	−147.82	−150.17
P_{S3} (the actual received power of S_3)	−150.76	−148.61	−148.68	−150.30
P_P (the actual received power of P)	-149.06	−154.01	−148.15	−148.49
P_{cal} (the calculated power of P)	−148.90	−154.32	−147.80	−148.85
P_{itu} (the result of ITU-R model)	−149.19	−153.27	−148.58	−149.64
$\|P_{cal} - P_P\|$(dB)	0.16	0.31	0.35	0.36
$\|P_{itu} - P_P\|$(dB)	0.13	0.74	0.43	1.15

T_4 are shown in Table 3. Tables 4 and 5 show the measured power of the four stations, the results calculated by the method in this paper, the results calculated by the ITU-R model, and their corresponding differences. In order to more intuitively show the difference between the measured data, calculated values and ITU-R model values, we draw Figures 6 and 7. In Figures 6 and 7, we compare the measured data, calculated values, and ITU-R model values for carries with center frequencies of 12.334 GHz and 12.700 GHz, respectively. Except for T_2, there was no rain at the four earth stations. So, (7) was only needed to be used for calculation at other times. At T_2, P, S_1 and S_3 have rain, and the rainfall of them is quite different. Therefore, (14) was used for calculation. As shown in the above tables and figures, at T_1, when the carrier frequency is 12.334 GHz, the calculation accuracy of the method proposed in this paper is slightly lower than that of the ITU-R model by 0.03 dB, which is very small, and the calculation errors of the two methods are very small, indicating that the two methods are relatively accurate. In addition, in other cases, the method proposed in this paper has better computational accuracy than the ITU-R model. Especially in the weather with heavy rain at T_2, it can still maintain good accuracy.

To confirm whether this method is suitable for different frequencies, we selected P, S_1 and S_2 stations and measured nine carriers on 19/10/2021. There was no

Table 5: The power of each station and the calculated power of P at the time of T_1, T_2, T_3 and T_4, frequency 12.700 GHz.

Power(dBW)	T_1	T_2	T_3	T_4
P_{S1} (the actual received power of S_1)	−160.93	−164.12	−161.19	−161.06
P_{S2} (the actual received power of S_2)	−161.39	−160.60	−160.02	−161.52
P_{S3} (the actual received power of S_3)	−162.36	−161.63	−160.60	−162.36
P_P (the actual received power of P)	−160.99	−164.82	−160.22	−160.90
P_{cal} (the calculated power of P)	−160.12	−164.71	−160.71	−160.41
P_{itu} (the result of ITU-R model)	−159.28	−165.81	−159.14	−159.72
$\|P_{cal} - P_P\|$(dB)	−0.87	−0.11	0.49	−0.49
$\|P_{itu} - P_P\|$(dB)	−1.71	0.99	−1.08	−1.18

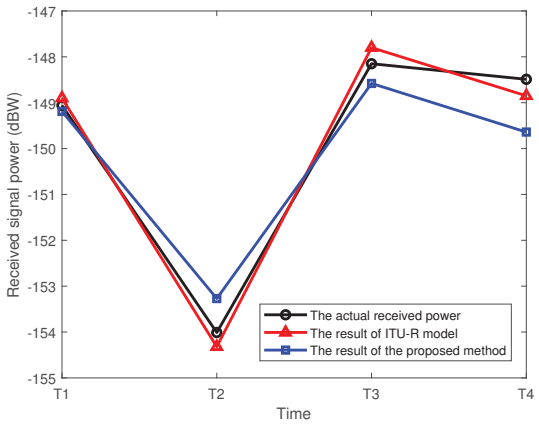

Fig. 6. The actual received signal power and calculated signal power of the target station P, frequency 12.334 GHz.

rain at each station. The measurement data of each station and calculation data are shown in Table 6. Figure 8 shows the error curve between the measured received signal power of the target station and the theoretical calculation value. As shown in Figure 8, for different frequencies, the calculation error of the method proposed in this paper is less than 1 dB. Therefore, we can conclude that the variation of frequency has little effect on the accuracy of the method.

VII. CONCLUSION

In Table 7, we refer to some attenuation calculation models newly proposed in recent years to compare with our proposed model, in terms of function, model complexity, dependent database, and university. Compared with other methods, the method proposed in this paper has the following advantages.

Table 6: The actual received signal power and measured attenuation of different carriers

Frequency (GHz)	12.334	12.347	12.417	12.498	12.514	12.59	12.602	12.676	12.700
P_P (dBW)	−140.24	−136.19	−135.29	−129.52	−140.35	−128.62	−133.23	−142.5	−139.13
P_{S_1} (dBW)	−140.11	−135.22	−134.9	−129.59	−139.97	−129.21	−133.97	−142.19	−139.55
P_{S_2} (dBW)	−141.55	−135.56	−135.7	−130.97	−142.9	−121.87	−132.72	−141.27	−138.26
Calculation Result (dBW)	−140.16	−135.24	−134.93	−129.64	−140.08	−128.94	−133.93	−142.16	−139.5
Absolute Error (dB)	0.08	0.95	0.36	0.12	0.27	0.32	0.7	0.34	0.37

Table 7: Comparison of several attenuation methods

Study	Model	Function	Model complexity	Dependent database	Universality
[1, 4, 9, 26, 27]	ITU-R Model	Total attenuations	Complex	Global historical weather data	Universal
[28]	Enhanced Synthetic Storm Technique (E-SST)	Only rain attenuation	Quite complex	The rain height and the storm velocity extracted from ECMWF (European Centre for Medium-range Weather Forecast) NWP products every hour (ERA5 database)	Universal
[29]	Rainfall Model Based on a Multilayer Medium Model	Only rain attenuation	Quite complex	None	Universal
[30]	Model of Effective Path-length Based on Rain Cell Statistics	Only rain attenuation	Complex	The Korea domestic meteorological-radar measurement data	Universal
[16]	Luini's Gas Attenuation Estimation Model	Only gas attenuation	Simple	Zenith total delay data obtained from GNSS (Global Navigation Satellite System) receivers	Universal
[10]	High Resolution ITU-R Cloud Attenuation Model	Only cloud attenuation	Quite complex	The radiosonde data and the GNSS data	Tropical Region
This work	The hybrid method combing direct calculation and equivalent approximation	Total attenuations	Simple	Short-term data collected by several ground stations	Universal

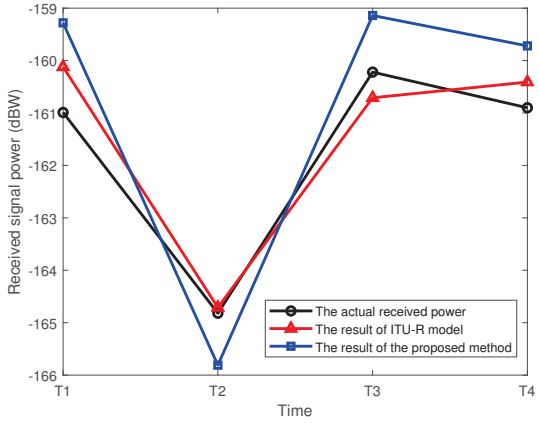

Fig. 7. The actual received signal power and calculated signal power of the target station *P*, frequency 12.700 GHz.

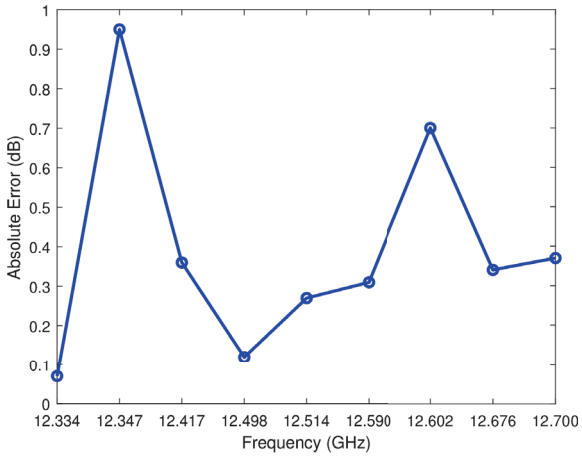

Fig. 8. The absolute errors of different carriers.

1. The computational complexity of our model is low. Moreover, the data needed in this method are only the received signal power and rainfall intensity of the earth stations, which can be obtained through ordinary signal acquisition equipment and rain gauges. In contrast, the rain height and the storm velocity required by E-SST and the precipitable water vapor (PWV) data required by the high resolution ITU-R cloud attenuation model can only be obtained through special equipment, which means the data can only be obtained from professional institutions. It increases the difficulty of data acquisition and may result in insufficient spatial accuracy of the acquired data.
2. The total attenuation of the link can be directly calculated. The models in the table can only calculate one or more attenuation except the ITU-R model. Although the ITU-R model can calculate all attenuations, its computational complexity is higher than the method in this paper.
3. The dependent database is simple. As mentioned in the first item, the data required is simple. More importantly, it only needs to collect the ground data in a short time. Except rainfall model based on a multilayer medium model, other methods require data collected over the years to ensure the accuracy of the model.
4. Our model has universal applicability. The high resolution ITU-R cloud attenuation model is mainly applicable to the tropics, because it uses the database of the tropics to modify its model. Although the ITU-R model is a universal model, current studies have shown that its adaptability in some areas (such as the tropics) is not very good. The universality of modeling of effective path-length based on rain cell statistics is also questionable, as it drives parameters of rain cell statistics from Korea domestic meteorological-radar measurement data. The method in this paper is calculated by the earth station deployed near the point of interest, so its adaptability to different regions can be guaranteed.

In conclusion, this paper presents a hybrid method combing direct calculation and equilibrium approximation to evaluate the satellite communication effectiveness. This method only needs to use short-term or real-time data to calculate the attenuation, and the corresponding link effectiveness can be accurately calculated under the condition where the transmitting power of the satellite is uncertain and the meteorological conditions of the target earth station cannot be measured. Since this method does not modify the attenuation model by using historical data, it only needs to select the station near the target point, thus insensitive to the target point. Therefore, this method is applicable to regions with different climates. Furthermore, we perform field tests on a synchronous orbiting satellite in orbit 113°E and some earth stations in Qingdao, the predicted results using our proposed model are compared. The results show that the proposed method has an improved performance than conventional ITU-R model.

REFERENCES

[1] ITU-R, "Attenuation due to Clouds and Fog," *Recommendation ITU-R P. 840-8*, Geneva, 2019.

[2] A. Dissanayake, J. Allnutt, and F. Haidara, "Cloud Attenuation Modelling for SHF and EHF Applications," *International Journal of Satellite Communications*, vol. 19, pp. 335-345, 2001.

[3] A. Dissanayake, J. Allnutt, and F. Haidara, "A Prediction Model that Combines Rain Attenuation

and other Propagation Impairments along Earth-satellite Paths," *IEEE Transactions on Antennas and Propagation*, vol. 45, no. 10, pp. 1546-1558, 2002.

[4] ITU-R, "Specific Attenuation Model for Rain for use in Prediction Methods," *Recommendation ITU-R P. 838-3*, Geneva, 2005.

[5] M. Yamada, Y. Karasawa, M. Yasunaga, and B. Arbesser-Rastburg, "An Improved Method for Rain Attenuation in Satellite Communications Operating at 10 to 20 GHz," *Radio Science*, vol. 22, no. 6, pp. 1053-1062, 1987.

[6] W., L., Stutzman, K., M., and Yon, "A Simple Rain Attenuation Model for Earth-space Radio Links Operating at 10–35 GHz," *Radio Science*, 1986.

[7] H. Liebe, "An Atmospheric Millimeter Wave Propagation Model", pp. 118, 1983.

[8] H. Liebe, "An Updated Model for Millimeter Wave Propagation in Moist Air," *Radio Science - RADIO SCI*, vol. 20, pp. 1069-1089, 1985.

[9] ITU-R, "Attenuation by Atmospheric Gases and Related Effects," *Recommendation ITU-R P. 676-12*, Geneva, 2019.

[10] F. Yuan, Y. H. Lee, Y. S. Meng, S. Manandhar, and J. Ong, "High Resolution ITU-R Cloud Attenuation Model for Satellite Communications in Tropical Region," *IEEE Transactions on Antennas and Propagation*, pp. 1-1, 2019.

[11] X. Boulanger, B. Benammar, and L. Castanet, "Propagation Experiment at Ka-Band in French Guiana: First Year of Measurements," *IEEE Antennas and Wireless Propagation Letters*, pp. 1-1, 2019.

[12] D. Sumbiri and T. Afullo, "An Overview of Rainfall Fading Prediction Models for Satellite Links in Southern Africa," *Progress In Electromagnetics Research B*, vol. 90, pp. 187-205, 2021.

[13] E. Matricciani, "Physical-mathematical Model of the Dynamics of rain Attenuation based on Rain Rate Time Series and Two Layer Vertical Structure of Precipitation," *Radio Science - RADIO SCI*, vol. 31, pp. 281-296, 1996.

[14] J. Ojo, O. Ajewole, and S. Sarkar, "Rain Rate and Rain Attenuation Prediction for Satellite Communication in Ku and Ka Bands over Nigeria," *Progress in Electromagnetics Research B*, vol. 5, pp. 207-223, 2008.

[15] S. Shrestha and D. Y. Choi, "Diurnal and Monthly Variations of Rain Rate and Rain Attenuation on ka-band Satellite Communication in South Korea," *Progress In Electromagnetics Research B*, vol. 80, pp. 151-171, 2018.

[16] L. Luini, G. Siles, J. Riera, C. Riva, and J. Nessel, "Methods to Estimate Gas Attenuation in Absence of a Radiometer to Support Satellite Propagation Experiments," *IEEE Transactions on Instrumentation and Measurement*, pp. 1-1, 2019.

[17] T. Pratt, C. Bostian, and J. Allnutt, *Satellite Communications*, 2003.

[18] D. Cimini, F. Marzano, M. Biscarini, R. Gil, P. Schluessel, F. Concaro, M. Marchetti, M. Pasian, and F. Romano, "Applicability of the Langley Method for Non-Geostationary In-Orbit Satellite Effective Isotropic Radiated Power Estimation," *IEEE Transactions on Antennas and Propagation*, pp. 1-1, 2021.

[19] Q. Zhan, Q. Ren, Q. Sun, H. Chen, and Q. H. Liu, "Isotropic Riemann Solver for a Non-conformal Discontinuous Galerkin Pseudospectral Time-domain Algorithm," *IEEE Transactions on Geoscience and Remote Sensing*, vol. 55, no. 3, pp. 1254-1261, 2017.

[20] Q. Zhan, Y. Wang, Y. Fang, Q. Ren, S. Yang, W. Y. Yin, and Q. H. Liu, "An Adaptive High-Order Transient Algorithm to Solve Large-Scale Anisotropic Maxwell's Equations," *IEEE Transactions on Antennas and Propagation*, pp. 1-11, 2021.

[21] Q. Zhan, M. Zhuang, Q. Sun, Q. Ren, Y. Ren, Y. Mao, and Q. H. Liu, "Efficient Ordinary Differential Equation-based Discontinuous Galerkin Method for Viscoelastic Wave Modeling," *IEEE Transactions on Geoscience and Remote Sensing*, vol. 55, no. 10, pp. 5577-5584, 2017.

[22] C. G. Little and H. Leinbach, "Some Measurements of High-Latitude Ionospheric Absorption Using Extraterrestrial Radio Waves," *Proceedings of the Ire*, vol. 46, no. 1, pp. 334-348, 1958.

[23] L. Zheng, Q. Zhao, and X. Xing, "Effect of Plasma on Electromagnetic Wave Propagation and THz Communications for Reentry Flight," *Applied Computational Electromagnetics Society (ACES) Journal*, vol. 30, pp. 1241-1245, 2015.

[24] T. V. Omotosho, M. L. Akinyemi, J. S. Mandeep, and M. Abdullah, "Total Atmospheric Absorption of Fixed Satellite Communication Signal due to Oxygen and Water Vapor in Nigeria," *IEEE Antennas and Propagation Magazine*, vol. 56, no. 2, pp. 108-121, 2014.

[25] National Meteorological Information Center, Republic of China, No. 46, Zhongguancun South Street, Haidian District, Beijing, http://data.cma.cn.

[26] ITU-R, "The concept of Transmission Loss for Radio Links," *Recommendation ITU-R P. 341-7*, Geneva, 2019.

[27] ITU-R, "Rain height model for Prediction Methods," *Recommendation ITU-R P. 839-4*, Geneva, 2013.
[28] L. Luini, A. Panzeri, and C. Riva, "Enhancement of the Synthetic Storm Technique for the Prediction of Rain Attenuation Time Series at EHF," *IEEE Transactions on Antennas and Propagation*, pp. 1-1, 2020.
[29] J. Tian and J. Shi, "A New Method for Analyzing the Attenuation Characteristics of Satellite Radar Altimeter Signals Due to Rainfall Based on a Multilayer Medium Model," *Radio Science*, vol. 55, 2020.
[30] W. G. Kang, T. H. Kim, S. W. Park, I. Y. Lee, and J. K. Pack, "Modeling of Effective Path-Length Based on Rain Cell Statistics for Total Attenuation Prediction in Satellite Link," *Communications Letters, IEEE*, vol. 22, no. 12, pp. 2483-2486, 2018.

Jun-Bo Gu was born in 1998. She received the B.S. degree in information engineering from the Information Engineering University, Zhengzhou, China, in 2019. She is currently pursuing the M.S. degree in the Information Engineering University, Zhengzhou, China. Her current research interests include satellite communication and satellite link calculation.

Dong-Fang Zhou was born in 1963. He received the Ph.D. degree from Zhejiang University, Hangzhou, China. He is currently working at the Information Engineering University, Zhengzhou, China. His current research interests include microwave antennas and satellite communication.

Hai-Lin Deng was born in 1992. He received the Ph.D. degree from the National Digital Switching System Engineering and Technology Research and Development Center, Zhengzhou, China, in 2019. He is currently working at the information engineering university. His current research interests include RF/microwave devices for wireless communications and radar systems and satellite communication.

Bing-Gang Huang was born in 1980. He received the Ph.D. degree from the PLA University of Science and Technology, Nanjing, China, in 2008. He is currently working at the Southwest Electronic telecommunication Technology Research Institute, Chengdu, China. His current research interests include satellite communication and signal processing.

Peng Qiang was born 1987.He received the master degree from College of Information Engineering, Zhengzhou, China. He is an engineer with Southwest Electronic telecommunication Technology Research Institute, Chengdu, China.He current research interests include Satellite communication and microwave technology, signal processing.

De-Wei Zhang was born in 1973. He received the Ph.D. degree from the Information Engineering University, Zhengzhou, China, in 2005. He is currently working at the Information Engineering University. His current research interests include RF/microwave devices for wireless communications and radar systems and satellite communication.

Da-Long Lv was born in 1981. He received the Ph.D. degree from the Information Engineering University, Zhengzhou, China, in 2013. He is currently working at the Information Engineering University. His current research interests include RF/microwave devices and satellite communication.

Qing Liu was born in 1991. He received the B.S. degree in communications engineering from Hunan University, Changsha, China, in 2014, and received the Ph.D. degree from the Information Engineering University, Zhengzhou, China, in 2020. He is currently working at the information engineering university. His current research interests include microwave filters and satellite communication.

Shape Optimization of the Momentum Ring Cross Section for Satellite Attitude Control Based on Magnetohydrodynamics

Youlin Gu[1], Qinghua Liang[1]*, Shigang Wang[1], Anlei Zhou[1], and Chaozhen Liu[2]

[1]School of Mechanical Engineering
Shanghai Jiao Tong University, Shanghai 200240, China
13007748 @163.com, *qhliang@sjtu.edu.cn

[2]Shanghai Key Laboratory of Aerospace Intelligent Control Technology
Shanghai Aerospace Control Technology Institute, Shanghai 201109, China

Abstract – Compared with the traditional actuator, the fluid momentum controller actuator based on magnetohydrodynamics (MHD) has some unique advantages and characteristics. In this paper, a method is proposed for the shape optimization of fluid momentum ring cross section. Based on the engineering situation, this article proposes a mathematical model of angular momentum that can be used for analytical calculations. Second, the two shapes obtained are unified and mathematically expressed in terms of maximum power and minimum resistance, respectively. Finally, the particle swarm algorithm is used to optimize the parameters of the proposed shape in combination with finite element method (FEM). Compared with the common rectangular section scheme, the attitude adjustment performance of fluid momentum ring can be effectively improved. Specifically, for the same area of cross section, the fluid momentum rings with the proposed shape provide the angular momentum values that exceed those of the rectangular shape by 14%-17% for the cases considered. This method avoids the huge computation of computational fluid dynamics and multidisciplinary topology optimization.

Keywords – shape optimization, cross section, magnetohydrodynamics (MHD), satellite attitude.

I. INTRODUCTION

Attitude control of satellites is an important part of performing space missions. There are several implementations of satellite attitude control, among which the fluid momentum ring possesses some unique advantages. The magnetohydrodynamics (MHD) based fluid momentum ring without bearings and moving rigid bodies has good research prospects. In 1988, NASA proposed a patent [1], explaining the concept and functioning of the fluidic momentum controller (FMC). This paper discusses the MHD-based fluid momentum ring, driven by electromagnetic forces. The related study involves the problem of coupled electromagnetic fluid multi-physical fields, and the related calculations are more complicated. There have been many studies [2–6] on fluid momentum rings based on MHD in the past decades. The fluid momentum ring adjusts the attitude of the satellite following the conservation of angular momentum, as shown in Figure 1. The fluid in the fluid cavity is subjected to an electromagnetic torque that changes the flow velocity, while the satellite body is subjected to a reaction torque. Different fractional models are estimated of unsteady MHD flow by Talha Anwar, and the solutions of velocity and energy are reached by a series of algorithms [7–11].

In the existing studies, the pipe cross section is circular or rectangular. Through analysis and comparison, the rectangular section is conducive to maximize electromagnetic force, while the circular section is conducive to minimize hydraulic resistance. In 2007 [12], MHD transient flows in rectangular cross-sectional channel is analyzed. Different cross-sectional aspect ratios of rectangular shape are discussed [13]. For satellite attitude actuators, efficiency and weight are sensitive, and the rectangular cross section is clearly not the optimal

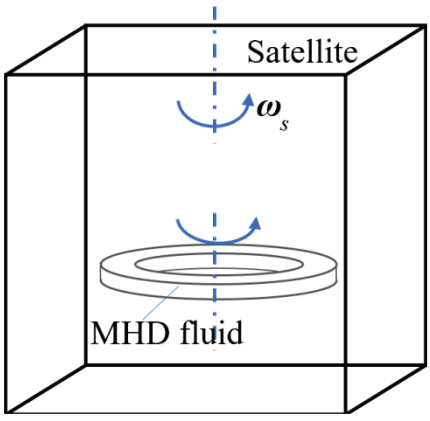

Fig. 1. Conservation of angular momentum between the fluid ring and the satellite.

Submitted On: November 15, 2021
Accepted On: April 7, 2022

https://doi.org/10.13052/2022.ACES.J.370312

solution. The shape optimization of the momentum ring cross section based MHD represents a challenging computational problem because optimization program needs to call MHD multiple physical field solutions including computational fluid dynamics (CFD) for many times, which brings a huge amount of computation. In addition, common shape optimization treatments need to deal with the problem of boundary interpolation and the transition problem of different boundary conditions.

Based on the optimization theory and the study of FMC based on MHD, this paper presents a unified equation for circles and rectangles to describe the shape of pipe interface. At the same time, a simplified MHD analytical model suitable for a fluid momentum ring is proposed. These works make the pipe section shape and the input electromagnetic field parameterized and establish a relationship with the angular momentum of a fluid momentum ring, an important satellite attitude adjustment parameter. Finally, an effective and fast framework for the shape optimization design of the fluid momentum rings is proposed. This method enables the implementation of the shape optimization of the cross section of the FMC based on MHD, allowing the actuator's attitude adjustment performance to be improved.

II. PHYSICAL MODEL

A. Satellite control principle

The attitude control principle of FMC based on MHD is the same as that of the flywheel. When the satellite is in space, it will inevitably be subjected to the torque of external disturbance T_d, which will produce an angular velocity ω_s. Suppose the angular momentum of the fluid in FMC is H_f and the angular momentum of the satellite (excluding the fluid ring) is H_s. It can be expressed as the following formulas:

$$T_d = \frac{dH_s}{dt} + \frac{dH_f}{dt} + \omega_s \times H_s, \tag{1}$$

Considering only the single-axis problem here, we have

$$\omega_s \times H_s \approx 0, \tag{2}$$

$$H_f \frac{\partial j}{\partial t} = 0, \tag{3}$$

where j is the unit vector, and $H_f = H_f j$.

If you require the satellite stable attitude, that is, after the above integral there

$$H_f = H_{f0} + \int_0^t T_d dt, \tag{4}$$

where H_{f0} is the initial angular momentum of the fluid ring. Thus, the maximum angular momentum of a fluid ring indicates its ability to absorb external torques.

According to the theory of electromagnetism, the current perpendicular to the magnetic field will be affected by the Lorenzo force, and FMC based on MHD is driven based on this basic principle. The vector product of flux density B and current density J determines the force acting on the liquid metal volume element:

$$dF_e = (J \times B)dV. \tag{5}$$

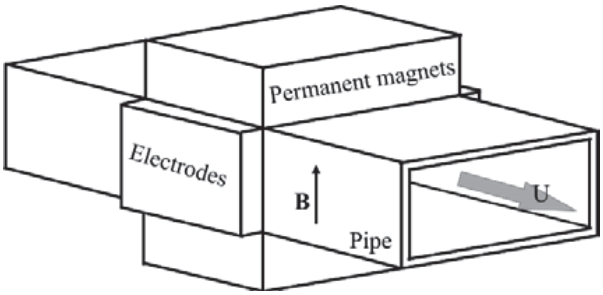

Fig. 2. Schematic diagram of electromagnetic drive.

In this work, the electromagnetic drive structure is shown in Figure 2. The magnetic field is generated by permanent magnets (PMs), the power supply is controlled by current, and the electric and magnetic fields are perpendicular to each other.

For a steady flow body, there is

$$\rho(U \cdot \nabla U) = -\nabla P + F_e + \mu \nabla^2 U, \tag{6}$$

where ρ is the density of the fluid, U is the velocity vector, F_e is the electromagnetic force, μ is the kinematic viscosity of fluid material, and P is the inner pressure. The cross section of the pipe is uniform and the shape deformation is not considered. The mechanical equations are established using the mechanical equilibrium of the fluid at steady state. The following principal assumptions are considered:

(1) The external magnetic field is a uniform static field, and the induced magnetic field is neglected.
(2) The electrodes are excellent conductors, and the single electrode is equipotential.
(3) The flow is unidirectional and one-dimensional.

According to engineering fluid dynamics, the friction loss in a continuous pipe is followed

$$F_f = h_f S, \tag{7}$$

where S is the area of the cross section of the pipe, and h_f reflects the pressure loss when flowing along a pipe with equal cross section

$$h_f = f \frac{l}{d} \frac{\rho U^2}{2}, \tag{8}$$

$$f = \frac{64}{\mathrm{Re}}. \tag{9}$$

In eqn (8), d is the hydraulic diameter of the liquid in the pipe, f is the coefficient of friction, and l is the length of the flow. Calculations confirm that the actual flow state is laminar. In eqn (9), Re is the Reynolds number. The angular momentum of FMC is a very important

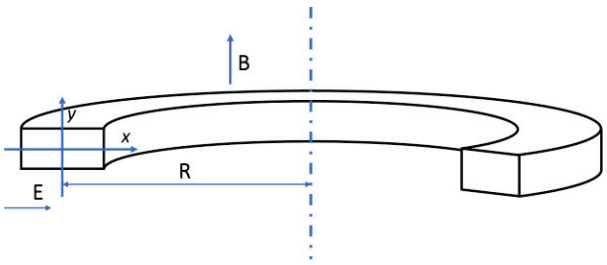

Fig. 3. FMC with rectangular cross section.

parameter, which reflects its attitude adjustment ability. It may be emphasized here that the cross section of the pipe is the same everywhere, and the whole pipe is circular with radius R, as shown in Figure 3. According to the definition of angular volume, the angular momentum in this annular pipe is as follows:

$$H_f = \iiint_V \rho(xU_y - yU_x)dV. \tag{10}$$

B. The proposed model

In order to obtain a suitable analytical model, the flow field is simplified here. This enables the electromagnetic force to be brought into the fluid momentum equation, and then the angular momentum analytical expression of the FMC can be obtained. For a closed pipe loop, when the flow is steady, the power and resistance are in balance, $F_e = F_f$. From the previous equation related to pipeline losses, it further follows that

$$F_f = 2\mu \frac{Ulp_e^2}{S}, \tag{11}$$

where p_e is the circumference of the pipe cross section. Here, the average flow velocity is used instead of the three-dimensional flow field. It should be noted that such an approximation requires $R \gg l$. Otherwise, the difference in flow velocity between the inside and outside will be difficult to ignore. Inserting these equations, the angular momentum is as follows:

$$H_f = \frac{RF_eS^2}{\mu p_e^2}. \tag{12}$$

It can be seen that the maximum angular quantity of the fluid H_f is positively correlated with F_e, $\frac{S^2}{p_e^2}$ when the confined volume ($V = 2\pi RS$) and the loop radius R are considered. According to eqn (6), the electromagnetic force F_e is proportional to the length of the current flowing through it. It is obvious that rectangle is the topological solution of the optimal problem of F_e under the constraint of pipe size. For the optimal problem of $\frac{S^2}{p_e^2}$, we can know from the basic geometry that the circle is the solution of this problem.

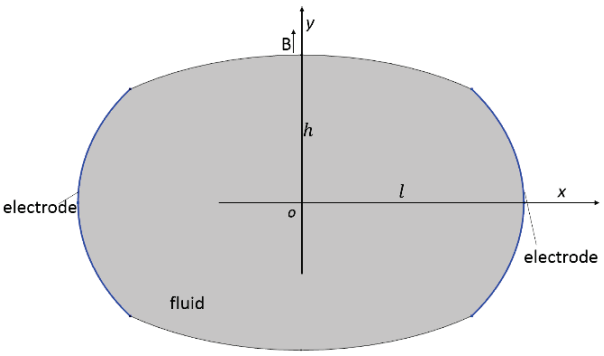

Fig. 4. The proposed shape combining circle and rectangle ($\lambda = 0.3$).

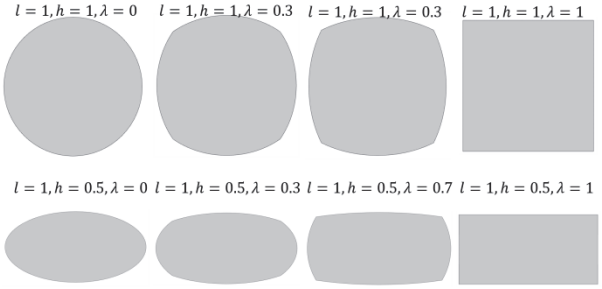

Fig. 5. The various cross-sectional shapes.

III. METHODS

A. The proposed shape scheme

According to the above study and analysis, it is known that the electromagnetic driving force depends mainly on the width of the cross section of the pipe for the same magnetic field strength and current size. Further, it is known that the driving force is maximum when the pipe shape is rectangular. From the perspective of the engineering fluid dynamics, the flow loss of the pipe depends on the hydraulic diameter of the pipe for the same flow rate and cross-sectional size. When the pipe shape is circular, the flow resistance of the pipe is the smallest. Here, the optimal problem for H is regarded as a multi-objective optimization problem of the optimal problem of with F_e and $\frac{S^2}{p_e^2}$. Thus, this paper proposes a new cross-sectional shape which is intermediate between circular and rectangular and can be regarded as a weighted combination of the two, as shown in Figure 4. The equation is as follows:

$$\begin{aligned} &(1-\tfrac{\lambda}{2})(\tfrac{x^2}{l^2}+\tfrac{y^2}{h^2}) + \tfrac{\lambda}{2}\left|\tfrac{x^2}{l^2}-\tfrac{y^2}{h^2}\right| \le 1 \\ &\lambda \in [0,1] \end{aligned}, \tag{13}$$

where l and h are the positive lengths in the x-axis and y-axis directions, respectively. λ is similar to a weighted value, as shown in Figure 5. When λ =0, the shape is elliptical, whereas when λ=1, the shape is rectangular.

Table 1 The design space and initial value

Design parameters	L(m)	h(m)	λ(m)
Lower bound	0.001	0.001	0
Initial values	0.03	0.01	0.5
Upper bound	0.05	0.05	1

Using calculus, the analytic equation for the area of the proposed shape can be obtained as follows:

$$S = \frac{\pi lh}{\sqrt{1-\lambda}} + \frac{2lh}{\sqrt{1-\lambda}}\left(\arcsin\frac{\sqrt{1-\lambda}}{\sqrt{2-\lambda}} - \arcsin\frac{1}{\sqrt{2-\lambda}}\right). \quad (14)$$

Unfortunately, similar to the ellipse, there is no analytic expression for the perimeter of the proposed shape. The value of the perimeter can be calculated numerically with the help of finite element method (FEM).

B. Optimization problems

This section illustrates the method with a case study. Here, a background magnetic field with a fixed intensity of 0.1 T and a current DC source of 10 A are used. The fluid material is liquid metal gallium. The kinematic viscosity of gallium is $3.49 \times 10^{-7}\text{m}^2/\text{s}$ at 303 K. Taking into account the size of the magnetic field area and the practical environment, the relevant design dimension parameters are shown in Table 1.

Overall, the design optimization problem can be expressed as

$$\begin{aligned} &\text{find}: l, h, \lambda \\ &\max: H_f(l,h,\lambda) = \frac{RF_eS^2}{\mu p_e^2} \\ &\text{st}: 0 \le \lambda \le 1 \\ &l \le l_c, h \le h_c, S \le S_c. \end{aligned} \quad (15)$$

The complex shape optimization problem of MHD background is simplified to the optimization problem of three-dimensional design variables, which is to be solved by the original particle swarm optimization (PSO).

The process of the shape optimization using the proposed shape equation is summarized as follows.

Algorithm: The process of the shape optimization for FMC cross section

Begin
Initial the design variables: l, h, λ **, material parameters and** ***B***, ***I***
  For ***I*** **=1:** ***n***
    CAD, mesh
    If $S \le S_c$
      Calculate H_f **by FEM**
If H_f' **<ε break end if**
    End if
    New (l, h, λ**) by PSO to find the maximum of** H_f **with all constraints**
  End for
End

Table 2 Constraints of geometric and physical parameters

Property	Value	Unit
l_c	0.05	m
h_c	0.05	m
S_c	0.005	m^2
	0.006	m^2

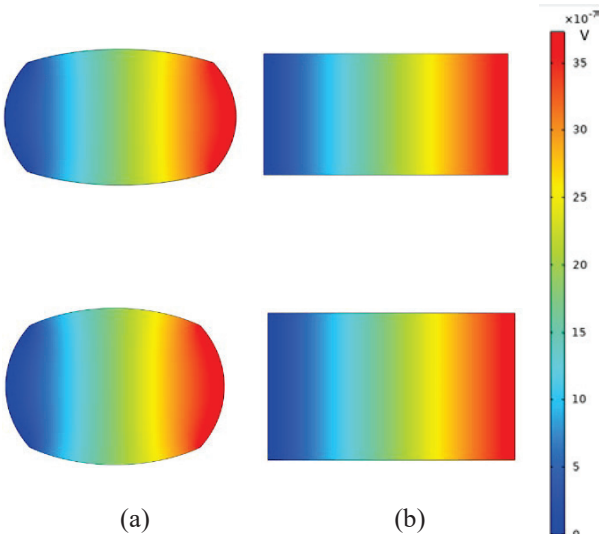

Fig. 6. Potential diagram. (a) The proposed shape. (b) The rectangular shape.

IV. RESULTS AND DISCUSSIONS

The above optimization model is solved by PSO and FEM. PSO is a population-based algorithm and is widely used in the optimization of multivariable problems. A population of particles called a swarm is moved toward a maximum of an objective function.

To demonstrate the advantages of the proposed shape scheme, rectangular section scheme is also calculated as a comparative study. The constraints of geometric and physical parameters are shown in Table 2.

In this study, the FEM analysis of electromagnetic fields is carried out using COMSOL. The PSO is programmed in MATLAB R2019b. The number of particles is 36 and the residual tolerance is set to be 10^{-5}. The optimization program was performed on a computer with a 3.6 GHz Intel 9700 CPU and 32 GB of memory.

Figure 6(a) shows the simulation results for a general rectangular cross section with the calculated angular momentum of 6.3×10^{-3}Nms, 6.68×10^{-3}Nms. Figure 6(b) shows the optimized potential with the calculated angular momentum of 5.5×10^{-3}Nms and 5.8×10^{-3}Nms.

Figure 7 shows the optimized current path and current density. As shown in the figure, the current is

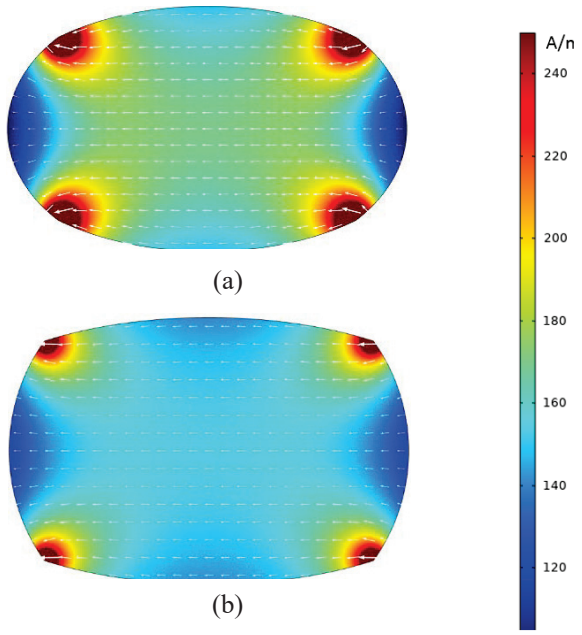

Fig. 7. Current density diagram (the direction of the arrow indicates the direction of the current, and the length of the arrow responds to the size of the current density).

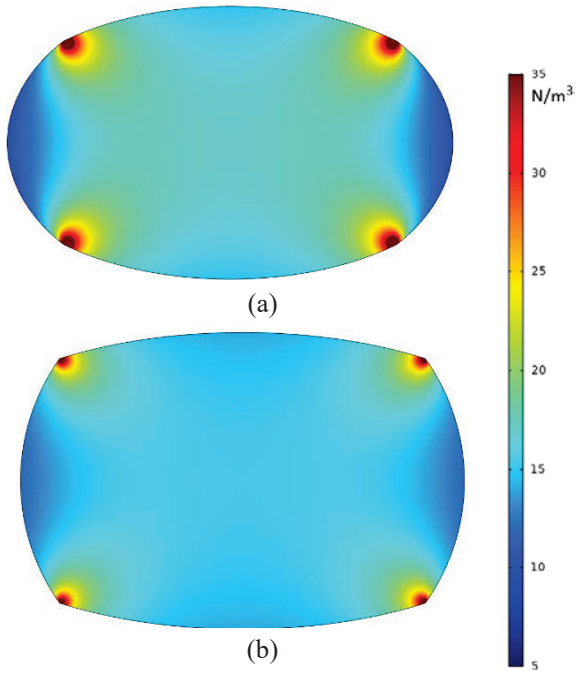

Fig. 8. Electromagnetic force density diagram.

more concentrated in the four corner regions. The closer λ is to 1, the more uniform the current distribution is. Figure 8 shows the electromagnetic force density distribution under the action of an ideal vertical magnetic field. The same concentration phenomenon exists in the four corners. Note that the electromagnetic force in the central region is greater than that near the boundary.

Table 3 The angular momentum values calculated by FEM of the proposed shape and rectangular shape

	S_c (m^2)	Size (m)	H_f (mN* m*s)	
Rec-shape	0.05	0.05,0.025	5.5	
	0.06	0.05,0.0297	5.8	
Opt-shape	0.05	0.05,0.0306, 0.204	6.3	14.5%
	0.06	0.05,0.0334, 0.525	6.8	17.2%

After this optimization method, the performance of FMC can be improved obviously. Table 3 shows comparisons between the rectangular shape and the proposed shape in the terms of angular momentum, and the enhancement is obvious.

Compared with the general shape optimization, it has lower computational cost and does not need spline interpolation.

V. CONCLUSION

In this work, we introduced a shape optimization method for the cross section of FMC, where we seek a balance between the shape for maximum electromagnetic force and the shape for minimum hydraulic resistance, such that the angular momentum is maximized. The proposed method can provide an optimized cross section for FMC quickly and efficiently. Compared with the common rectangular cross-sectional scheme, the attitude adjustment performance of FMC is obviously improved. The optimized shape is smooth and continuous and makes the follow-up design work easier.

(1) The article proposes a unified analytical equation that can both describe rectangular, elliptical, and its transition shapes simultaneously.
(2) Further, a shape optimization framework is developed. Its effectiveness is illustrated by an example, which significantly improves the attitude adjustment performance of FMC.
(3) In addition, the simplified calculation of the flow field of FMC avoids the complexity of CFD and makes the whole multidisciplinary optimization practically operable.

ACKNOWLEDGMENT

This work is supported by the National Natural Science Foundation of China under Grant 51875338.

REFERENCES

[1] R. S. Maynard, "Fluidic momentum controller: U.S. Patent 4," vol. 776, no. 541[P]. 11-10-1988.

[2] A. Kelly, C. McChesney, P. Smith, et al., "A performance test of a fluidic momentum controller in three axes." *Final Report ASE Q*, pp. 463, 2004.

[3] R. Varatharajoo, R. Kahle, and S. Fasoulas, " Approach for combining spacecraft attitude and thermal control systems." *Journal of spacecraft and rockets*, vol. 40, no. 5, pp. 657-664, 2003.

[4] R. Varatharajoo, R. Ajir, and T. Ahmad, "Hybrid spacecraft attitude control system." *The International Journal of Multiphysics*, vol. 1, no. 2, 2016.

[5] Y. Ji, X. Li, T. Wu, et al., "Quantitative Analysis Method of Error Sources in Magnetohydrodynamic Angular Rate Sensor for Structure Optimization." *IEEE Sensors Journal*, vol. 16, no. 11, pp. 4345-4353, 2016.

[6] K. D. Kumar, "Satellite attitude stabilization using fluid rings." *Acta Mechanica*, vol. 208, no. 1-2, pp. 117-131, 2009.

[7] Asifa, P. Kumam, Z. Shah, et al., "Radiative MHD unsteady Casson fluid flow with heat source/sink through a vertical channel suspended in porous medium subject to generalized boundary conditions[J]." *Physica Scripta*, vol. 96, no. 7, pp. 075213, 2021.

[8] Asifa, P. Kumam, D. At, et al., "Modeling and simulation based investigation of unsteady MHD radiative flow of rate type fluid; a comparative fractional analysis - Science Direct [J]." *Mathematics and Computers in Simulation*, 2021.

[9] T. Anwar, P. Kumam, Asifa, et al., "An exact analysis of radiative heat transfer and unsteady MHD convective flow of a second rade fluid with ramped wall motion and temperature [J]." *Heat Transfer*, 2020.

[10] T. Anwar, P. Kumam, Asifa, et al., "Generalized Unsteady MHD Natural Convective Flow of Jeffery Model with ramped wall velocity and Newtonian heating; A Caputo-Fabrizio Approach[J]." *Chinese Journal of Physics- Taipei-*, vol. 68, no. 1, pp. 849-865, 2020.

[11] T. Anwar, P. Kumam, I. Khan, et al., "Thermal analysis of MHD convective slip transport of fractional Oldroyd-B fluid over a plate [J]." *Mechanics of Time-Dependent Materials* pp. 1-32, 2021.

[12] M. Khan, C. Fetecau, T. Hayat. "MHD transient flows in a channel of rectangular cross-section with porous medium[J]." *Physics Letters A*, vol. 369, no. 1-2, pp. 44-54, 2007.

[13] X. Xiao, N. K. Chang, "Effects of the magnetic field direction and of the cross-sectional aspect ratio on the mass flow rate of MHD duct flows[J]." *Fusion Engineering and Design*, vol. 151, pp. 111373, 2020.

Youlin Gu received the bachelor's degree in mechanical engineering from Donghua University, China. He is currently working toward the Ph.D. degree with the School of Mechanical Engineering, Shanghai Jiao Tong University, China. His research focuses on optimization design of electromechanical systems, modeling and simulation of MHD, and topology optimization.

Qinghua Liang received the Ph.D. degree in mechanical engineering from Shanghai Jiao Tong University. Currently, he is an Associate Professor with the School of Mechanical Engineering, Shanghai Jiao Tong University. His research interests include intelligent machinery, complex electromechanical system innovative design, and machine vision.

Shigang Wang received the Ph.D. degree in mechanical engineering from the Huazhong University of Science and Technology. He is currently a Professor with the School of Mechanical Engineering, Shanghai Jiao Tong University, China. His research activities include complex electromechanical systems, electromagnetic drive, machine vision, pattern recognition, special robots, bionic design and intelligent control, and biologic robots.

Anlei Zhou received the master's degree in mechanical engineering from Shanghai Maritime University, China. He is currently working toward the Ph.D. degree with the School of Mechanical Engineering, Shanghai Jiao Tong University. His current research interests include CFD and other numerical methods in engineering.

Speed Interference Suppression for PD Radar Based on Adaptive Dictionary

Zhe Du[1], Lexin Yu[2], Jin Zhang[1], Mingjuan Cai[3], and Tao Jiang[2]

[1]Shanghai Electro-Mechanical Engineering Institute
Shanghai 201109, China
dudo1987@163.com, zoey0041@163.com

[2]College of Information & Communication Engineering
Harbin Engineering University, Harbin 150001, China
yulexing@hrbeu.edu.cn, jiangtao@hrbeu.edu.cn

[3]Naval Research Academy
Shanghai 200235, China
dudo1987@163.com

Abstract – Random pulse initial phase (RPIP) signal is a kind of agility waveform which is commonly used in pulse Doppler (PD) radar. Although RPIP has the merit of restraining velocity deception jamming effectively, its efficiency is restricted under the condition of strong interference. To make the RPIP signal fully play the anti-jamming performance, this paper proposed a speed interference suppression method based on adaptive dictionar that separates the target echo from the strong jamming signal with good sparsity. First, the prior knowledge of strong interference signal is obtained by the technique of peak detection which is combined with the dual channel processing. Second, the quasi-Karhunen-Loeve transform (Q-KLT) basis of interference signal is constructed based on the prior knowledge, and the approximate Q-KLT basis of target signal is constructed by the way of dictionary learning, and those signals can be obtained from the adaptive dictionary by the algorithm of base tracking (BP). Finally, the effectiveness of the proposed method is verified by numerical simulation, which proves that the method can ensure a lower Doppler sidelobe in the strong interference scene, which confirmed that it has a good anti-velocity deception performance.

Index Terms – speed deception jamming, anti-jamming, sparse decomposition, dictionary learning, KLT basis

I. INTRODUCTION

Pulse Doppler (PD) radar is one kind of radar system that adopted moving target detection (MTD) technology to detect targets in noise, clutter, and interference. It plays an important role in air reconnaissance, ground moving target recognition, and air traffic control [1, 2]. In the electronic countermeasures (ECM) scenario, PD radar often suffers from the serious threat of radar active jamming [3]. Especially, with the development of digital radio frequency memory (DRFM), active deception jamming with diversity and strong antagonism seriously reduced the performance of PD radar detection [4–6].

In recent years, to protect PD radar from the velocity deception jamming, sparse decomposition and compressed sensing have been applied to the field of radar anti-jamming. They can separate the signals of target and jamming from the echo and realize the suppression of active deception jamming. Literature [7] constructed an over-complete dictionary to match the signal and used the sparse decomposition to suppress the smeared spectrum (SMSP) jamming. For the detection and recognition of velocity false target interference, literature [8] established a combination dictionary of true targets and false targets, and then used compressed sensing to realize the recognition of target and interference. On the basis of [8], literature [9] constructed a composite dictionary and a short-time sparse recovery method to suppress translational velocity interference and micro-motion velocity jamming. It is worth noting that the method of dictionary design is adopted in literature [8, 9] to construct a dictionary. Because the dictionary constructed by this method is independent of the input signal and has no adaptability, the sparsity of the signal under this fixed dictionary is weak; so they only can recognize and suppress jamming under the weak interference intensity. In this paper, an adaptive dictionary is proposed to suppress strong speed interference.

Before constructing the adaptive dictionary of jamming signal, it is necessary to obtain the Doppler information of jamming as the prior knowledge of the

Submitted On: January 16, 2021
Accepted On: December 4, 2021

https://doi.org/10.13052/2022.ACES.J.370313

sparse domain. It can be seen from [10] and [11] that multi-channel processing technology can obtain Doppler information, but there are some problems in it, such as complex device design and low device utilization. Based on the improvement of this technology, the peak detection method proposed can estimate the pulse repetition interval (PRI) number i of jamming signal lagging radar. Then dual channels are enough to achieve the acquisition of Doppler information and it is the reason why this method is named as dual channel processing technology.

On completing the mission of obtaining the Doppler information of jamming, the method of constructing adaptive dictionary is analyzed. The basic idea is that to construct the quasi-Karhunen-Loeve transform (Q-KLT) basis of the jamming based on the prior knowledge, which enables the strong jamming signal to have good sparsity under its adaptive dictionary. Aiming at the establishment of adaptive dictionary of target signal, the approximate Q-KLT basis is constructed by the method of dictionary learning. Dictionary learning is another effective method to construct a dictionary to find the optimal set of atoms of a certain kind of signal by iteration. Here, these atoms can well reflect the characteristics of such signals and they can describe those signals most sparsely. In this paper, the orthogonal matching pursuit (OMP) algorithm is adopted to find the best sparsity atom in the pre-construction dictionary of the target signal, and the corresponding matching coefficient is calculated. Then the extracted atoms are combined into a template, and the matching coefficient is used to construct the approximate Q-KLT basis of the target signal. Finally, base tracking (BP) algorithm is used to separate the target and jamming, which can suppress the velocity deception jamming.

The main contents of the rest of this paper are as follows. In the second section, the dual channel processing is described to obtain prior knowledge which is based on the peak detection. In the third section, the adaptive Q-KLT basis is constructed to separate the target and jamming. In the fourth section, simulation result is given.

II. ACQUISITION OF PRIOR KNOWLEDGE

In our previous work, "Dictionary Learning and Waveform Design for Dense False Target Jamming Suppression" (DOI: 10.47037/2021.ACES.J.360908), the peak detection method is proposed to estimate the phase difference of adjacent pulse compression (PC) signals and realizes the detection of radar active deception jamming, which is based on wavelet transform algorithm. In this paper, the peak detection is used to estimate the PRI number i of jamming signal lagging radar signal, and the prior knowledge is obtained by combining the dual channel processing. The output results of matched filtering in the coherent processing interval (CPI) are rewritten into PC signals in the slow time domain. The signal expression is

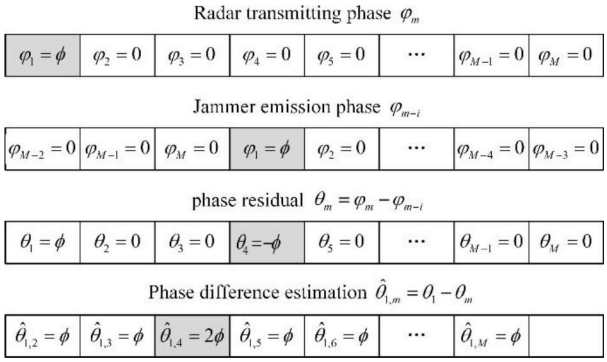

Fig. 1. Schematic diagram of estimated jamming delay i.

$$y(m)=\sum_{p=1}^{P}\tilde{\sigma}_T^p e^{j2\pi f_T^p mT_r}+e^{j\theta(m)}\cdot\sum_{q=1}^{Q}\tilde{\sigma}_J^q e^{j2\pi f_J^q mT_r}+V(m) \tag{1}$$

where T_r is the pulse repetition period, and P and Q are the number of target and interference, respectively. σ_T^p and f_T^p are the amplitude and Doppler frequency of the pth (p = 1, 2,…,P) target, respectively. σ_J^p and f_J^p are the amplitude and Doppler frequency of the qth (q = 1, 2,…,Q) target, respectively. $\theta(m)$ is the phase residual of the signal and $V(m)$ is the Gaussian white noise.

The estimation of jamming delay i based on peak detection is explained in Figure 1. The radar transmits a set of initial phase waveform of quasi-random pulse in CPI. The initial phase of the first pulse in the waveform aggregate is set to $\varphi_1=\phi$, while the initial phase of other pulse is $\varphi_m=0(m=2,\ldots,M)$. Assuming that i is 3 which is the number of PRI of the jamming, the initial phase of the fourth pulse in the random pulse initial phase (RPIP) waveform set sent by the jammer is $\varphi_4=\phi$. Then the phase residuals of the first pulse and the fourth pulse are $\theta_1=\phi$ and $\theta_4=-\phi$, respectively. Finally, the peak detection is used to estimate the phase difference between the first PC peak and the following $M-1$ PC peak. The phase difference estimated in the third detection is $\hat{\theta}_{1,3}=2\phi$, while the other phase difference is estimated to be $\hat{\theta}_{1,m}=\varphi(m\neq 3)$. Then, the number of PRI of the jamming signal sent by the jammer is determined to be 3. Based on the several kinds of quasi-random initial phase pulse set and the peak detection, the jamming delay i value can be determined, which improves the complexity of device design in multi-channel processing.

As an alternative, the Doppler information of target and jamming can be obtained by two channels, which

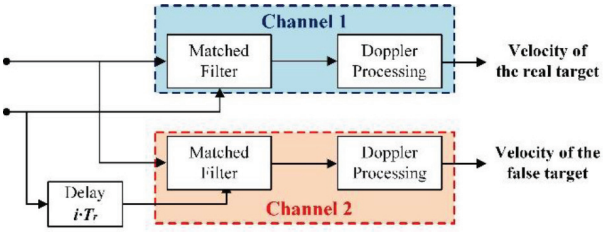

Fig. 2. Technical diagram of dual channel processing.

is called dual channel processing technology. Figure 2 shows the schematic diagram of dual channel processing technology. In channel one, the mth radar echo has the matching coefficient of $p_m^*(-t)$. The output of matched filter is described by eqn. (1), which is $y^{\text{channel 1}}(m) = y(m)$. The mth radar echo in channel two passes through the matched filter with the matching coefficient of $p_{m-i}^*(-t)$. And the output is

$$y^{\text{channel2}}(m) = e^{j\theta(m)} \sum_{p=1}^{P} \tilde{\sigma}_T^p e^{j2\pi f_T^p m T_r} + \sum_{q=1}^{Q} \tilde{\sigma}_J^q e^{j2\pi f_J^q m T_r} + V(m). \quad (2)$$

From eqn. (2), we can get that due to the influence of phase residual θ_m, and the energy of target diffuses to the whole Doppler spectrum. However, the phase cancelation of the jamming forms a peak on the Doppler spectrum; so the Doppler frequency of the peak can be obtained on channel two.

III. ADAPTIVE DICTIONARY AGAINST SPEED JAMMING

The main idea of single channel separation algorithm is to separate the mixed signals in sparse domain first and then recover the separated signals in time domain. The selection and construction of the dictionary (basis function) determines the sparsity of the signal, which is the most important step for the separation of the target and the jamming. In this section, we will introduce the method of building adaptive dictionary and the detail process.

A. Pre-construction of target signal dictionary

Usually, the target velocity is not fuzzy in the traditional sense and it can be divided into $N(N \geq M)$ parts to get the velocity resolution unit $\Delta v = \lambda / (2NT)$, where λ is the wavelength.

If the velocity of the target detected by the radar can be expressed as $v_n = (n-1)\Delta v$, $n = 1,2,\ldots,N$, then the Doppler frequency can be expressed as

$$f_n = \frac{2v_n}{\lambda} = \frac{n-1}{NT_r}. \quad (3)$$

If $v'(n) = (n-1)/N$, the target pre-constructed in the slow time domain can be expressed as

$$y_T(n,m) = \exp\left(j2\pi m v'(n)\right). \quad (4)$$

In order to simplify the expression, eqn. (4) is written as a vector $\boldsymbol{y}_{T,n}$, where $\boldsymbol{y}_{T,n}$ is a column vector of $M \times 1$.

The Doppler spectrum $\boldsymbol{y}_{T,n}$ of the target is obtained by discrete Fourier transform (DFT) of $\boldsymbol{Y}_{T,n}$ which is used as the atom $\boldsymbol{a}_{Y_T}^n = \boldsymbol{Y}_{T,n} = \text{FFT}\left[\boldsymbol{y}_{T,n}\right]$ in the pre-constructed target dictionary.

Atom $\boldsymbol{a}_{Y_T}^n$ is defined as the element of dictionary $\boldsymbol{A}_{Y_T} = \left[\boldsymbol{a}_{Y_T}^1, \boldsymbol{a}_{Y_T}^2, \ldots, \boldsymbol{a}_{Y_T}^N\right]$, and atom $\boldsymbol{g}_{Y_T}^n$ is defined as the diagonal vector of auto-correlation matrix of atom $\boldsymbol{a}_{Y_T}^n$, which has the expression as follows:

$$\boldsymbol{g}_{Y_T}^n = \text{diag}\left(\boldsymbol{a}_{Y_T}^n \left(\boldsymbol{a}_{Y_T}^n\right)^T\right), \quad n = 1,2,\ldots,N. \quad (5)$$

Atom $\boldsymbol{g}_{Y_T}^n$ is normalized to $\bar{\boldsymbol{g}}_{Y_T}^n$, and atom $\bar{\boldsymbol{g}}_{Y_T}^n$ is defined as the element of the normalized dictionary $\boldsymbol{G}_{Y_T} = \left[\bar{\boldsymbol{g}}_{Y_T}^1, \bar{\boldsymbol{g}}_{Y_T}^2, \ldots, \bar{\boldsymbol{g}}_{Y_T}^N\right]$.

B. Construction of adaptive Q-KLT basis

(a) Q-KLT basis of jamming signal

According to the prior knowledge obtained in the previous section, the jamming $y_J(m)$ in the slow time domain can be constructed, and its expression is defined as follows:

$$y_J(m) = \sum_{q=1}^{Q} \exp\left(j2\pi f_J^q m T_r + j\theta(m)\right). \quad (6)$$

In order to simplify the jamming expression, eqn. (6) is written in vector form $\boldsymbol{y}_J$, which is a column vector of $M \times 1$. Then $\boldsymbol{Y}_J$ can be gotten from $\boldsymbol{y}_J$ by DFT, and the auto-correlation $\boldsymbol{R}_{Y_J} = \text{E}\left\{\boldsymbol{Y}_J \boldsymbol{Y}_J^H\right\}$ of jamming signal in Doppler spectrum cabe calculated. Because $\boldsymbol{R}_{Y_J}$ is Hermitian matrix and a positive definite matrix, there must exist an orthogonal matrix $\boldsymbol{U}_{Y_J}$, which satisfied $\boldsymbol{U}_{Y_J} \boldsymbol{R}_{Y_J} \boldsymbol{U}_{Y_J}^H = \Lambda_{Y_J}$, where Λ_{Y_J} is a diagonal matrix with m eigenvalues of $\boldsymbol{R}_{Y_J}$.

(b) Approximation of Q-KLT basis for target signal

In the presence of velocity false target jamming, the mixed signal received can be regarded as the linear combination of target and jamming, and then the mixed Doppler spectrum signal $\tilde{\boldsymbol{Y}}$ can be obtained through the coherent processing. Suppose that $\boldsymbol{d}_{R_{\tilde{Y}}}$ is the diagonal vector of auto-correlation matrix of mixed signal $\tilde{\boldsymbol{Y}}$, which is the diagonal vector of $\boldsymbol{R}_{\tilde{Y}}$:

$$\boldsymbol{d}_{R_{\tilde{Y}}} = \text{diag}\left(\boldsymbol{R}_{\tilde{Y}}\right) = \text{diag}\left(\tilde{\boldsymbol{Y}} \tilde{\boldsymbol{Y}}^H\right). \quad (7)$$

Then, the optimal atom of the target is extracted by the OMP iterative algorithm. Among them, the OMP algorithm was originally proposed by Pati [12], which is used to calculate the sparse coefficient of signal under a certain transformation basis or an over-complete dictionary, so as to express the signal with as few atoms as

possible. The specific iterative process of the OMP algorithm in this paper is as follows:

(1) Input of signal $\boldsymbol{d}_{R_{\tilde{Y}}}$ and target dictionary $\boldsymbol{G}_{Y_T}$.
(2) Initialization of residual $\boldsymbol{r}=\boldsymbol{d}_{R_{\tilde{Y}}}$, projection vector $\gamma_I=0$, $\boldsymbol{I}=[]$, and $\boldsymbol{G}_I=[]$.
(3) Execute steps (4)–(7) when the number of iterations is not greater than N.
(4) Calculate the maximum inner product of each atom and residual in dictionary $\boldsymbol{G}_{Y_T}$, and get the corresponding atomic number $\hat{n}=\arg\max_n \left|(g^n)^T\boldsymbol{r}\right|$.
(5) Update $\boldsymbol{G}_I$ by $\boldsymbol{G}_I=[\boldsymbol{G}_I,\boldsymbol{G}_n]$.
(6) Sparse representation of computational signal $\boldsymbol{d}_{R_{\tilde{Y}}}$ in dictionary $\boldsymbol{G}_I$: $\gamma_I=\left(\boldsymbol{G}_I^T\boldsymbol{G}_I\right)^{-1}\boldsymbol{G}_I^T\boldsymbol{d}_{R_{\tilde{Y}}}$.
(7) Update $\boldsymbol{r}$ by $\boldsymbol{r}=\boldsymbol{r}-\boldsymbol{G}_I\gamma_I$.
(8) Terminate the iteration.
(9) Output subset $\boldsymbol{G}_I$ of target dictionary $\boldsymbol{G}_{Y_T}$, sparse projection vector γ_I of signal $\boldsymbol{d}_{R_{\tilde{Y}}}$ under dictionary.

In the previous section, the atoms of the target are preconstructed, the diagonal vectors of the auto-correlation matrix of several construction atoms are selected by OMP algorithm, and the corresponding matching coefficients (sparse representation) are calculated at the same time. Then the auto-correlation matrix of the selected atoms is used as the template, and the approximate auto-correlation matrix of the target is constructed by these templates and their corresponding matching coefficients. Finally, the eigen-decomposition values are calculated and the approximate Q-KLT basis of the target is obtained. The specific steps of constructing the approximate Q-KLT basis are as follows:

(1) The mixed signal $\tilde{\boldsymbol{y}}$ in slow time domain is receiv ed, and the mixed signal $\tilde{\boldsymbol{Y}}$ in Doppler domain is obtained by DFT.
(2) The auto-correlation matrix $\boldsymbol{R}_{\tilde{Y}}$ of mixed signal $\tilde{\boldsymbol{Y}}$ and the diagonal vector $\boldsymbol{d}_{R_{\tilde{Y}}}$ of $\boldsymbol{R}_{\tilde{Y}}$ are calculated.
(3) The OMP algorithm is used to iteratively calculate the signal $\boldsymbol{d}_{R_{\tilde{Y}}}$ and the target dictionary $\boldsymbol{G}_{Y_T}$. The atom $\bar{\boldsymbol{g}}_{Y_T}^{k_1},\bar{\boldsymbol{g}}_{Y_T}^{k_2},\ldots,\bar{\boldsymbol{g}}_{Y_T}^{k_j}$ matched by $\boldsymbol{d}_{R_{\tilde{Y}}}$ is selected from the target dictionary $\boldsymbol{G}_{Y_T}$, and the matching coefficient $\gamma_I=\left[\gamma_{k_1},\gamma_{k_2},\ldots,\gamma_{k_j}\right]$ is calculated.
(4) Select the atom corresponding to $\bar{\boldsymbol{g}}_{Y_T}^{k_1},\bar{\boldsymbol{g}}_{Y_T}^{k_2},\ldots,\bar{\boldsymbol{g}}_{Y_T}^{k_j}$ from dictionary $\boldsymbol{A}_{Y_T}$ and construct template $\overset{\frown}{R}_{Y_T}^{k_1},\overset{\frown}{\boldsymbol{R}}_{Y_T}^{k_2},\ldots,\overset{\frown}{\boldsymbol{R}}_{Y_T}^{k_j}$
$$\overset{\frown}{\boldsymbol{R}}_{Y_T}^{k_i}=\boldsymbol{a}_{Y_T}^{k_i}\left(\boldsymbol{a}_{Y_T}^{k_i}\right)^T,\quad i=1,2,\ldots,j. \tag{8}$$
(5) Calculating the approximate auto-correlation matrix $\boldsymbol{R}_{Y_T}=\sum_{i=1}^{j}\gamma_{k_i}\overset{\frown}{\boldsymbol{R}}_{Y_T}^{k_i}$ of $\boldsymbol{Y}_T$ according to the template and matching coefficients.
(6) Finally, $\boldsymbol{R}_{Y_T}=\boldsymbol{U}_{Y_T}^H\Lambda_{Y_T}\boldsymbol{U}_{Y_T}$ is obtained by eigen-decomposition of $\boldsymbol{R}_{Y_T}$, where $\boldsymbol{U}_{Y_T}^H$ and $\boldsymbol{U}_{Y_T}$ are orthogonal matrices, and Λ_{Y_T} is a diagonal matrix.

For convenience, we set the target signal as $\boldsymbol{Y}_T=\boldsymbol{Y}_1$ and set the jamming signal as $\boldsymbol{Y}_J=\boldsymbol{Y}_2$, then the approximate Q-KLT basis of the target is $\boldsymbol{U}_{Y_T}^H=\boldsymbol{U}_{Y_1}^H$ and the Q-KLT basis of the jamming signal is $\boldsymbol{U}_{Y_J}^H=\boldsymbol{U}_{Y_2}^H$.

Orthogonal transformation of signal $\boldsymbol{Y}_i(i=1,2)$ is defined as
$$\Theta_{Y_i}=\boldsymbol{U}_{Y_i}^H\boldsymbol{Y}_i. \tag{9}$$
Different from KLT basis, $\boldsymbol{U}_{Y_i}$ and $\boldsymbol{U}_{Y_i}^H$ are obtained by eigen-decomposition of auto-correlation matrix of signal $\boldsymbol{Y}_i$, which are only related to current signal $\boldsymbol{Y}_i$. To summarize, projection vector Θ_{Y_i} is the Q-KLT of signal $\boldsymbol{Y}_i$, and $\boldsymbol{U}_{Y_i}^H$ is the Q-KLT basis of $\boldsymbol{Y}_i$ signal.

C. Separation of target and jamming signal

In this section, BP algorithm is used to separate the mixed signals in Doppler domain. The basis of BP algorithm used l_1-norm to replace l_0-norm for convex optimization [13]. The steps of separation and reconstruction of mixed signals based on BP algorithm are given as follows:

(1) Calculating diagonal vector $\boldsymbol{d}_{R_{\tilde{Y}}}$ of auto-correlation matrix of mixed signal $\tilde{\boldsymbol{Y}}$.
(2) According to the algorithm in Section II, the Q-KLT basis $\boldsymbol{U}_{Y_2}^H$ of jamming signal $\boldsymbol{Y}_2$ is obtained, and the approximate Q-KLT basis $\boldsymbol{U}_{Y_1}^H$ of target $\boldsymbol{Y}_1$ is obtained with reference to $\boldsymbol{d}_{R_{\tilde{Y}}}$.
(3) By solving the following l_1-norm optimization problem:
$$\min f(\beta_1,\beta_2)=\min\sum_{i=1}^{2}\|\beta_i\|_1,\quad s.t.\ \tilde{\boldsymbol{Y}}=\sum_{i=1}^{2}\boldsymbol{U}_{Y_i}\beta_i, \tag{10}$$
we get the estimated Θ_{Y_i} of sparse representation of $\boldsymbol{Y}_i$ under $\boldsymbol{U}_{Y_i}$, where $\beta^{opt}=[\Theta_{Y_1},\Theta_{Y_2}]^T$ is the optimal solution of problem (10).
(4) The separated echo PC signal $\hat{\boldsymbol{Y}}_i$ is obtained by the following reconstruction:
$$\hat{\boldsymbol{Y}}_i=\boldsymbol{U}_{Y_i}\Theta_{Y_i},\quad i=1,2 \tag{11}$$

IV. SIMULATION AND MEASUREMENT RESULTS

In simulation, the radar works in X-band, the PRI is 100 US, and M = N = 128 is assumed. In this section, we verify the feasibility of dual channel processing to obtain the Doppler information of false targets; then assume that we can verify the effectiveness and superiority of the anti-strong velocity jamming in three scenarios.

First, single target corresponds to single false target (1T-1F) scene, $f_T = 0.6$ and $f_J = 0.62$. Second, single target corresponds to three false target (1T-3F) scenarios, $f_T = 0.6$ and $f_J = 0.58$, 0.62, and 0.78. Third, four targets correspond to eight false targets (4T-8F) scenarios, $f_T = 0.2$, 0.4, 0.6, and 0.8 and $f_J = 0.18$, 0.22, 0.38, 0.42, 0.58, 0.62, 0.78, and 0.82. We set signal-to-noise ratio (SNR) = 10 dB and jamming-to-signal ratio (JSR) = 20 dB.

In the 1T-1F scenario, it is assumed that the number of PRIs of jamming lagging transmission signal is 30, namely $i = 30$. It can be seen from the numerical simulation that the radian value of 30 sampling points is 1.16 (rad), which is twice the radian value of other sampling points. According to the analysis in Section II, the proposed peak detection can estimate i value as 30, as shown in Figure 3. After the i value is determined, the Doppler information of the jamming is obtained by the dual channel processing. As shown in Figure 4, due to the high jamming intensity, the target peaks of the output results of channel 1 are completely covered by the raised noise base, while the output of channel 2 have three large peaks, corresponding to the Doppler frequencies of 0.58, 0.62, and 0.78, respectively.

In the 1T-3F and 4T-8F scenarios, the effectiveness of the new method is verified. Then, in those three scenarios, peak sidelobe ratio (PSLR) after jamming suppression is used to measure the proposed anti-jamming method.

1T-3F scene: As shown in Figure 5, when there is jamming, the anti-jamming signal has the same main lobe as the target echo (no jamming) after coherent processing. Although the sidelobes of these two signals are slightly different, they do not affect the detection of single target. Therefore, the method has a good effect in suppressing strong jamming, while the traditional method of correlation processing (CP) cannot eliminate the influence of high sidelobe on target concealment. As shown in Figure 6, the projection vectors of jamming and target signals on Q-KLT basis are obtained. It can be found that the projection vector of the jamming signal in the graph has only one large amplitude, and the amplitude of other sampling points is approximately zero. From the enlarged figure, it can be seen that the projection vector of the target has only one large amplitude. It is verified that the jamming and target signal have good sparseness in the adaptive dictionary; so the effectiveness of this paper is verified in the single target and strong jamming scenarios.

4T-8F scene: Figure 7 showed that the four main lobes of the separated target are the same as the main lobes of the target echo (no jamming) after coherent processing.

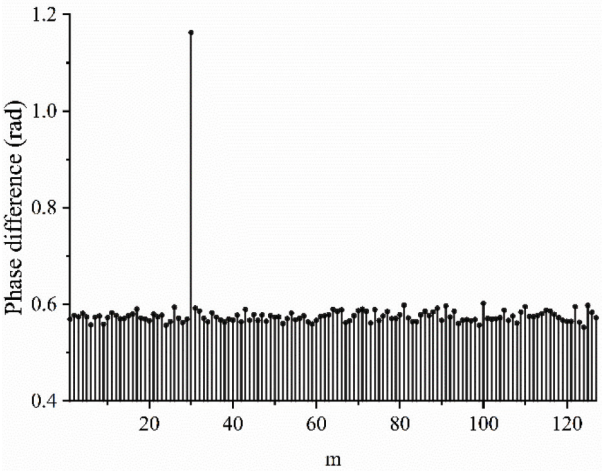

Fig. 3. Estimation of delay number i of jamming signal.

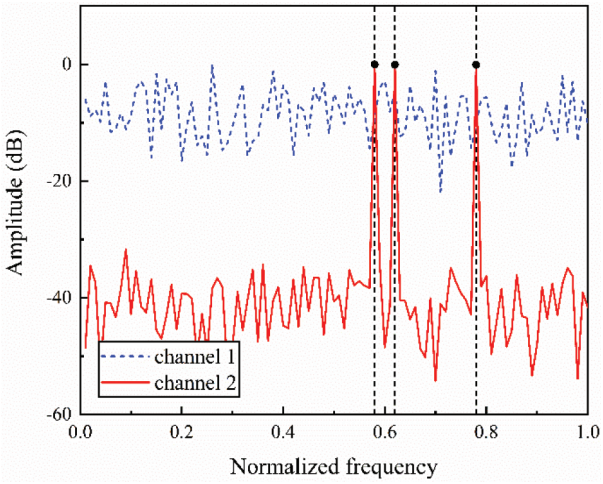

Fig. 4. Simulation of dual channel processing.

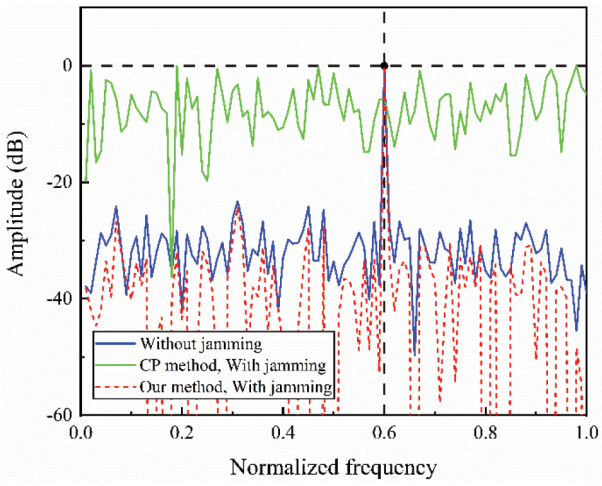

Fig. 5. Jamming suppression in 1T-3F scene.

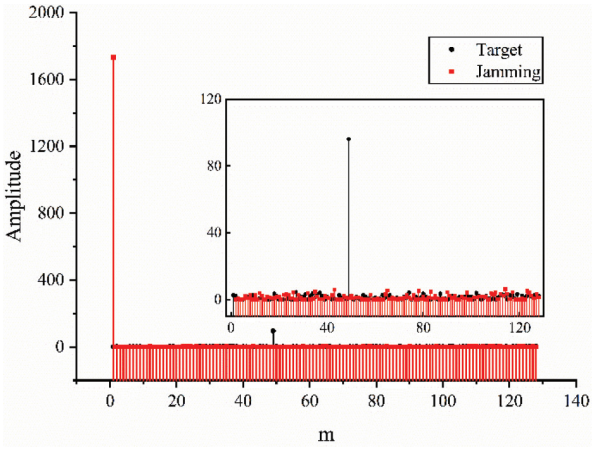

Fig. 6. Projection vector in 1T-3F scene.

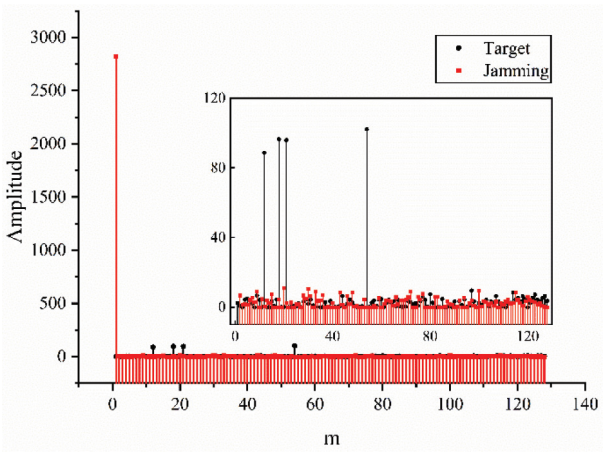

Fig. 8. Projection vector in 4T-8F scene.

It is verified that our method has good anti-jamming performance in four target scenarios, but the CP method cannot detect the target at all. As shown in Figure 8, the projection vectors of jamming and target signals on Q-KLT basis are obtained. It is found that the projection vector of jamming signal has only one large amplitude, while the projection vector of target signal has four large amplitudes. It is verified that the jamming and target signal have good sparsity in the adaptive dictionary, so that the effectiveness of method proposed in this paper is verified in the multi-target and strong jamming scenarios.

To verify the effect of different JSR and SNR on PSLR, Figure 9 showed the simulation results of 1000 independent trials for Monte Carlo simulations. In Figure 9(a), the PSLR in the three scenarios remains unchanged with the increase of JSR, and the PSLR values in 1T-1F and 1T-3F scenarios are nearly the same,

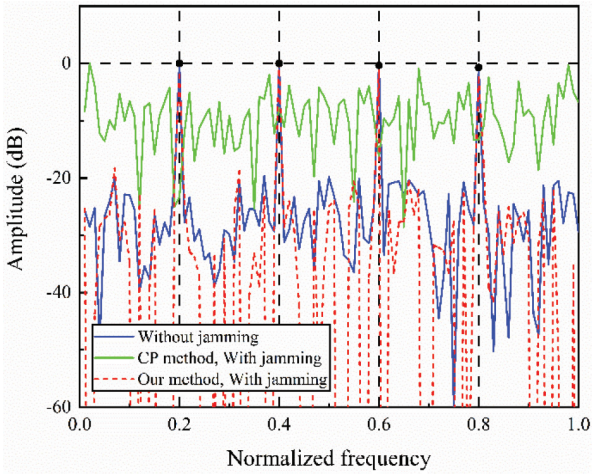

Fig. 7. Jamming suppression in 4T-8F scene.

while the PSLR values in 4T-8F scenarios are slightly less than the above two scenarios, which indicates that the change of JSR will not affect the jamming suppression performance of this method. In Figure 9(b), PSLR in the three scenarios increases with the increase of SNR, and the increase degree of PSLR in 1T-1F and 1T-3F scenarios is the identical, while the increase of PSLR in 4T-8F scenario is slower under the condition of low SNR.

Furthermore, the simulation verifies the effect of the number of N on the performance of this method. It can be seen from Table 1 that in the 1T-3F and 4T-8F scenarios, the increase of N value will reduce the PSLR value. From formula (3), it can be seen that the increase of N can improve the velocity resolution, but also increase of the number of atoms in the pre-constructed target signal dictionary, which not only improves the calculation but also reduces the jamming suppression performance. In Figure 10, for example, $N = 2M$, red and blue dashed lines show that PSLR value increases with the increase of SNR, but the increase rate slows down.

Finally, the method proposed is compared with the adaptive sequence estimation (ASE) algorithm in [14] to further verify its superiority. In [14], in a single target scenario, the noise power is $|\sigma_N|^2 = 0$ dB, the power of the jamming signal is set to $|\sigma_J|^2 = 40$ dB, and the power of the target signal $|\sigma_T|^2$ is set to 0, 10, 20, 30, and 40 dB, respectively. Under the condition of the same parameters above, 1000 independent trials for Monte Carlo simulations are carried out. Figure 11 shows the PSLR values of ASE method and this method under different target signal powers. It can be found that the PSLR value of this method is greater than ASE method under each target power, which proves that this method has better performance in suppressing velocity jamming. For the future application, the adaptive methods can also

Table 1: PSLR values corresponding to different N numbers (SNR = 10 dB)

N numbers	1T-3F scene	4T-8F scene
N= M	24.53 dB	18.27 dB
N= 2M	21.98 dB	15.20 dB
N= 3M	21.28 dB	14.60 dB
N= 4M	21.16 dB	14.36 dB

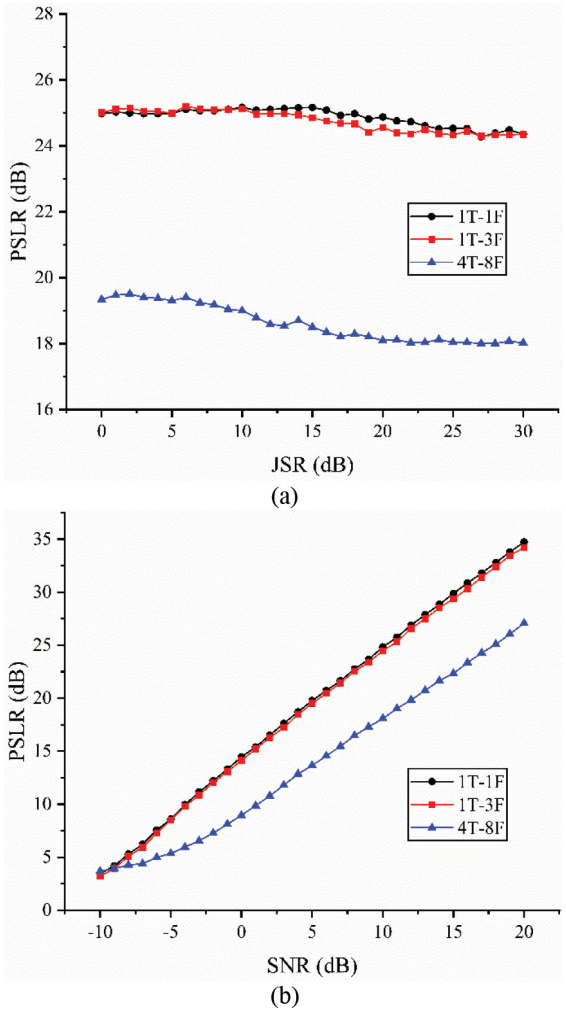

Fig. 9. PSLR after jamming suppression versus (a) JSR and (b) SNR.

be considered in the interference suppression [15–18]. In addition, the adaptive interference suppression for PD radar can be considered using adaptive filtering [19–28] and sparse arrays [29–31].

V. CONCLUSION

Because the RPIP waveform is affected by the raised noise base and cannot give full play to the efficiency of restraining the deception, the detection performance of

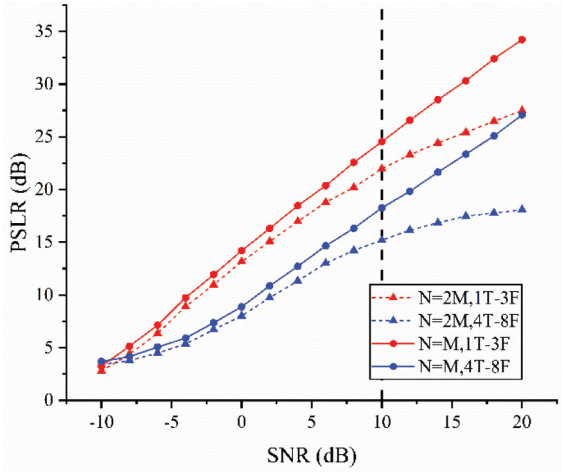

Fig. 10. Number N impact on the PSLR.

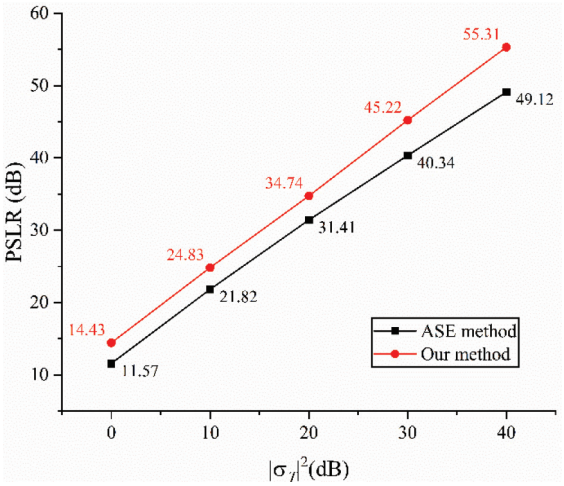

Fig. 11. PSLR performance comparison of the two methods.

PD radar is seriously damaged under the strong velocity jamming. To solve this problem, a new anti-jamming method based on adaptive dictionary is proposed by combining traditional CP technology with sparse decomposition theory. The prior knowledge is acquired by dual channel processing, and then the Q-KLT basis of jamming a target is constructed, so that the signal has good sparsity under adaptive dictionary. The superiority of the method under the condition of strong jamming is studied by numerical simulation. The results show that the change of the jamming signal strength has little influence on the algorithm performance, which means that this method can effectively suppress the jamming of strong velocity deception. In addition, this method can reduce Doppler sidelobe and has better anti-jamming performance, compared with ASE method.

ACKNOWLEDGMENT

This paper is supported by Shanghai Aerospace Science and Technology Innovation Fund under Grant SAST2019-002.

REFERENCES

[1] J. Dudczyk, "Radar emission sources identification based on hierarchical agglomerative clustering for large data sets," *J. Sens.*, vol. 2016, pp. 1-9, 2016.

[2] J. Dudczyk, "A method of feature selection in the aspect of specific identification of radar signals," *Bull. Polish Acad. Sci. Tech. Sci.*, vol. 65, pp. 113-119, 2017.

[3] N. Li and Y. Zhang, "A survey of radar ECM and ECCM," *IEEE Trans. Aerosp. Electron. Syst.*, vol. 31, no. 3, pp. 1110-1120, 1995.

[4] S. Roome, "Digital radio frequency memory," *IEE Electron. Commun. Engng J.*, vol. 2, no. 4, pp. 147-153, 1990.

[5] S.D. Berger and D.E. Meer, "An expression for the frequency spectrum of a digital radio frequency memory signal," IEEE National Aerospace Electronics Conf., Dayton, OH, pp. 90-93, May 1990.

[6] S.D. Berger, "Digital radio frequency memory linear range gate stealer spectrum," *IEEE Trans. Aerosp. Electron. Syst.*, vol. 39, no. 2, pp. 725-735, 2003.

[7] L. Ding, R. Li, Y. Wang, L. Dai, and F. Chen, "Discrimination and identification between mainlobe repeater jamming and target echo by basis pursuit," *IET Radar Sonar Navig.*, vol. 11, no. 1, pp. 11-20, 2017.

[8] J. Sui, Z. Liu, X. Wei, X. Li, B. Peng, and D. Liao, "Velocity false target identification in random pulse initial phase radar based on compressed sensing," 2015 3rd International Workshop on Compressed Sensing Theory and its Applications to Radar, Sonar and Remote Sensing (CoSeRa), Pisa, pp. 179-183, 2015.

[9] Z. Liu, J. Sui, Z. Wei, and X. Li, "A sparse-driven anti-velocity deception jamming strategy based on pulse-doppler radar with random pulse initial phases," *Sensors*, vol. 18, no. 4, 1249, 2018.

[10] J. Zhang, D. Zhu, and G. Zhang, "New antivelocity deception jamming technique using pulses with adaptive initial phases," *IEEE Trans. Aerosp. Electron. Syst.*, vol. 9, no. 2, pp. 1290-1300, 2013.

[11] J. Sui, X. Zhang, Z. Liu, X. Wei, and X. Li, "Sparse-based false target identification in pulse-doppler radar with random pulse initial phase," 2015 International Conference on Wireless Communications & Signal Processing (WCSP), Nanjing, pp. 1-5, 2015.

[12] Y. Pati, R. Rezaiifar, and P. Krishnaprasad, "Orthogonal matching pursuit: recursive function approximation with applications to wavelet decomposition," Proceedings of 27th Asilomar Conference on Signals, Systems and Computers, Pacific Grove, CA, USA, vol. 1, pp. 40-44, 1993.

[13] S. Chen, D. Donoho, and A. Saunders, "Atomic decomposition by basis pursuit," *SIAM Rev.*, vol. 43, no. 1, pp. 129–159, 2001.

[14] G. Cui, H. Ji, V. Carotenuto, S. Iommelli, and X. Yu, "An adaptive sequential estimation algorithm for velocity jamming suppression," *Signal Process.*, vol. 134, pp. 70-75, 2017.

[15] Z. Dai, L. Guo, J. Yin, Y. Li, and K. Guo, "Adaptive sparse array beamforming using correntropy induced metric constrained normalized LMS algorithm," *Applied Computational Electromagnetics Society (ACES) Journal*, vol. 35, no. 4, pp. 430-436, 2020.

[16] W. Shi and Y. Li, "A p-norm-like constraint LMS algorithm for sparse adaptive beamforming," *Applied Computational Electromagnetics Society (ACES) Journal*, vol. 34, no. 12, pp. 1797-1803, 2019.

[17] W. Shi, Y. Li, and J. Yin, "Improved constraint NLMS algorithm for sparse adaptive array beamforming control applications," *Applied Computational Electromagnetics Society (ACES) Journal*, vol. 34, no. 3, pp. 419-424, 2019.

[18] W. Li, X. Mao, Z. Zhai, and Y. Li, "A low complexity high performance robust adaptive beamforming," *Applied Computational Electromagnetics Society (ACES) Journal*, vol. 32, no. 5, pp. 441-448, 2017.

[19] Y. Li, Z. Jiang, W. Shi, X. Han, and B. Chen, "Blocked maximum correntropy criterion algorithm for cluster-sparse system identifications," *IEEE Trans. Circuits Syst. II, Express Briefs*, vol. 66, no. 11, pp. 1915-1919, Nov. 2019.

[20] W. Shi, Y. Li, and Y. Wang, "Noise-free maximum correntropy criterion algorithm in non-Gaussian environment," *IEEE Trans. Circuits Syst. II Express Briefs*, vol. 67, no. 10, pp. 2224-2228, Oct. 2020.

[21] W. Shi, Y. Li, and B. Chen, "A separable maximum correntropy adaptive algorithm," *IEEE Trans. Circuits Syst. II, Express Briefs*, vol. 67, no. 11, pp. 2797-2801, Nov. 2020.

[22] Y. Li, Y. Wang, and T. Jiang, "Norm-adaption penalized least mean square/fourth algorithm for sparse channel estimation," *Signal Processing*, vol. 128, pp. 243-251, 2016.

[23] X. Huang, Y. Li, Y. V. Zakharow, Y. Li, and B. Chen, "Affine-projection Lorentzian algorithm for vehicle hands-free echo cancellation," *IEEE Transactions on Vehicular Technology*, vol. 70, no. 3, pp. 2561-2575, 2021.

[24] T. Liang, Y. Li, W. Xue, Y. Li, and T. Jiang, "Performance and analysis of recursive constrained least Lncosh algorithm under impulsive noises," *IEEE*

Transactions on Circuits and Systems II: Express Briefs, vol. 68, no. 7, pp. 2217-2221, 2021.
[25] T. Liang, Y. Li, Y. V. Zakhrow, W. Xue, and J. Qi, "Constrained least Lncosh adaptive filtering algorithm," *Signal Processing*, vol. 183, 2021.
[26] T. Liang, Y. Li, and Y. Xia, "Recursive Constrained Adaptive Algorithm under q-R'enyi Kernel Function," *IEEE Transactions on Circuits and Systems II: Express Briefs*, vol. 68, no. 6, pp. 2227-2231, 2021.
[27] Q. Wu, Y. Li, Y. Zakharov, W. Xue, "Quantized kernel least lncosh algorithm," *Signal Processing*, vol. 189, ID:108255, 2021.
[28] Y. Li and Y. Wang, "Sparse SM-NLMS algorithm based on correntropy criterion," *Electronics Letters*, vol. 52, no. 17, pp. 1461-1463, 2016.
[29] Y. Li, C. Zhang, and S. Wang, "Low-complexity non-uniform penalized affine projection algorithm for sparse system identification," *Circuits, Systems,and Signal Processing*, vol. 35, no. 5, pp. 1611-1624, 2016.
[30] W. Shi, S. A. Vorobyov, and Y. Li, "ULA fitting for sparse array design," *IEEE Transactions on Signal Processing*, vol. 69, pp. 6431-6447, 2021.
[31] W. Shi, Y. Li, and S. A. Vorobyov, "Low mutual coupling sparse array design using ULA fitting," 2021 IEEE International Conference on Acoustics, Speech and Signal Processing (ICASSP), Toronto, ON, Canada, 13 May, 2021.

Zhe Du received the B.S. degree from Qing Dao University in 2010 and the M.S. degree from Shanghai University in 2013.

He works with Shanghai Electro-Mechanical Engineering Institute as a Senior Engineer. His research interests include electromagnetic compatibility, complex system simulation and evaluation, antenna theory, and design.

Lexin Yu received the B.S. degree from the School of Electronics and Information Engineering, Tianjin Polytechnic University in 2017 and the M.S. degree from the School of Information and Communication Engineering, Harbin Engineering University in 2021.

After studies, he worked with Huawei Company, China, as an Applications Engineer. His research interests include modeling and simulation, and anti-jamming technology.

Jin Zhang received the B.S. degree from the School of Astronautics, Northwestern Polytechnical University in 2016 and the M.S. degree from the School of Astronautics, Northwestern Polytechnical University in 2019.

She works with Shanghai Electro-Mechanical Engineering Institute as an Applications Engineer. Her research interests include electronic modeling and simulation, and guidance and control system design for flight vehicles.

Tao Jiang received the Ph.D. degree from the Harbin Engineering University, Harbin, China, in 2002.

Since 1994, he has been a Faculty Member of College of Information and Communication, Harbin Engineering University, where he is currently a Professor. He was a Postdoctoral Researcher with the Research Institute of Telecommunication, Harbin Institute of Technology, Harbin, China, from 2002 to 2003, and a Visiting Scholar with the Radar Signal Processing Laboratory, National University of Singapore, from 2003 to 2004. His current research interests include radio wave propagation, complex electromagnetic system evaluation, modeling, and simulation.

Mingjuan Cai received the Ph.D degree from National University of Defence Technology, Changsha, China, in 2006. She works with Naval Research Academy as a Senior Engineer. Her current research interests include electromagnetic simulation, electromagnetic compatibility and evaluation.

Evaluation of Pipe Cracks Based on Cloud Contour of Three-Dimensional Induced Eddy Current Field

Feng Jiang[1], Li Tao[2], Long Geng[1], and Tong Xu[1]

[1]School of Electrical and Information Engineering
Changzhou Institute of Technology, Changzhou 213032, China
jiangf@jsit.edu.cn

[2]Library and Information Center
Jiangsu Vocational College of Information Technology, Wuxi 214153, China
tao_li_@126.com

Abstract – Considering the problem of non-destructive testing and quantitative evaluation of metal materials, an electromagnetic method for visual and quantitative evaluation of surface defects on metal pipe is proposed in this paper. The dual-excitation probe with the combination of arc-shaped and rectangular coils is constructed. The eddy current magnetic field on the outer cylindrical surface of metal pipe is calculated and analyzed by COMSOL Multiphysics finite-element software, and then the influences of crack location and geometric parameters on three-dimensional magnetic field characteristics are studied. The results show that the cloud contours constructed by the magnetic induction intensity norm can accurately evaluate the information such as the location, size, depth, and orientation of the surface crack. In addition, the cloud contours constructed separately by the magnetic induction intensity in three directions can be used for auxiliary judgment to further determine the relevant important parameters of the surface crack to be tested.

Index Terms – Eddy current magnetic field, pipe, cloud contour of magnetic induction intensity.

I. INTRODUCTION

With the development of modern industrial technology, metals play an important role in various fields, and people's daily life has been inseparable from a variety of metals. Due to long-term use or aging of the equipment, the metal surface is often damaged and broken, which seriously affects the performance of the equipment, and may cause dangerous goods leakage, explosion, and other serious safety accidents [1–3]. Therefore, it is important to carry out a comprehensive inspection of metal products to ensure their integrity. Non-destructive testing (NDT) technology can obtain the surface condition of materials by processing and analyzing the changes caused by material physical characteristics. Eddy current testing (ECT) is the most popular and mature testing method in online testing [4–7]. Current research mainly focuses on theoretical model and application development [8–10]. It is used to detect defects and check the condition of samples, such as surface cracks, sub-surface cracks, and degeneration-related defects of samples. Of course, ECT itself has great limitations, such as many interference factors, large lift-off effect [11], etc. It is difficult to judge the type and shape of defects and carry out equivalent analysis of defects. In addition, eddy current technology has traditionally relied on changes in the impedance of the pickup coil. In order to detect deep defects in conductive materials, it is necessary to reduce the current frequency to obtain sufficient penetration depth. Because the sensitivity of the detection coil is proportional to the current frequency, eddy current technology is not suitable for the detection of deep buried defects. Therefore, it is advantageous to measure the magnetic field directly, rather than the change rate of the magnetic field [12, 13]. With the development of ECT technology, it is urgent to explore the response analysis of defects to magnetic field signals and extract more useful characteristic information to establish the quantitative relationship between the crack geometry and the surrounding magnetic field [14–16]. Therefore, research on magnetic field detection, analysis methods, and extraction of more characteristic quantities are the trend of improving detection accuracy for ECT development.

In order to solve the shortcomings of ECT, improve the testing ability and accuracy; the NDT of cracks in pipe surface is studied in this paper by using three-dimensional induction eddy current field measurement. COMSOL simulation software is used to obtain the magnetic induction intensity of the outer surface of the pipeline under various conditions, to build the magnetic

Submitted On: January 25, 2022
Accepted On: April 5, 2022

https://doi.org/10.13052/2022.ACES.J.370314

induction intensity cloud contour. The defect parameter information is extracted from the image to realize the visualization of the defect and improve the accurate evaluation of the pipe.

II. PRINCIPLE OF DETECTION

According to the principle of electromagnetic induction, an excitation coil with alternating current is close to the pipe, and then an induced current will be generated on the surface of the pipe, which is called induced eddy current. The magnitude of the induced eddy current is related to the excitation current parameters and is also related to the state of the pipe, such as the physical characteristics and surface quality of the pipe. In the case of a crack on the surface of the pipe, as shown in Figure 1, the originally evenly distributed current is broken by the crack, and the induced current will change the original path and choose a new path to pass through. As shown in Figure 1 (b), when the eddy current is perpendicular to the crack, the eddy current is disturbed by the defect to the maximum. However, when the eddy current is parallel to the crack, the disturbance caused by the defect to the eddy current is minimal, which can be obtained from Figure 1 (c). At the same time, the change of the direction and size of eddy current will cause the change of the space magnetic field around it, that is, the change of eddy current field. Therefore, the variation of eddy current inside the pipe can be inferred by measuring the variation of eddy current field around the pipe, and then the condition of the surface the pipe can be evaluated.

The magnetic field at any position outside the pipe is actually equal to the vector sum of the source field generated by the excitation current and the eddy current field generated by the induced current.

$$\boldsymbol{B} = \boldsymbol{B}_{\mathrm{s}}(I, f, N, \ldots) + \boldsymbol{B}_{\mathrm{e}}(L, W, D, \ldots), \tag{1}$$

where $\boldsymbol{B}_s$ and $\boldsymbol{B}_e$ denote the source field and eddy current field, respectively. $\boldsymbol{B}_s$ is related to the excitation current amplitude I, frequency f, the number of coil turns N, and other parameters. The difference is that $\boldsymbol{B}_e$ is related to the parameters of the defects in the conductor, such as the crack length L, width W, and depth D. The change of eddy current field will then lead to the change of magnetic field in space. Therefore, the defect in the pipe can be predicted to a certain extent according to the change of magnetic field around the crack. However, the selection of measurement points is arbitrary in practice. The defects in the pipe cannot be evaluated correctly if the measurement points are not selected properly. Of course, a special straight line can also be selected as the detection position, but there are still many shortcomings for the cylindrical surface like pipe. Therefore, it is particularly important to select a suitable inspection surface for accurate and comprehensive quantitative evaluation of pipe defects. As shown in Figure 1, the three-dimensional magnetic field in the grid area (the cylindrical surface coaxial with the outer surface of the pipe) can comprehensively reflect the changes caused by the defects in any direction of the pipe. If the magnetic induction intensity value can be converted into an image that can be displayed directly, it will be more convenient and direct to determine whether there is a defect in the pipe and obtain accurate information of the defect. In addition, the magnetic induction intensity contour composed of x-, y-, and z-directions in this area can also realize the visualization of defects and assist in judgment.

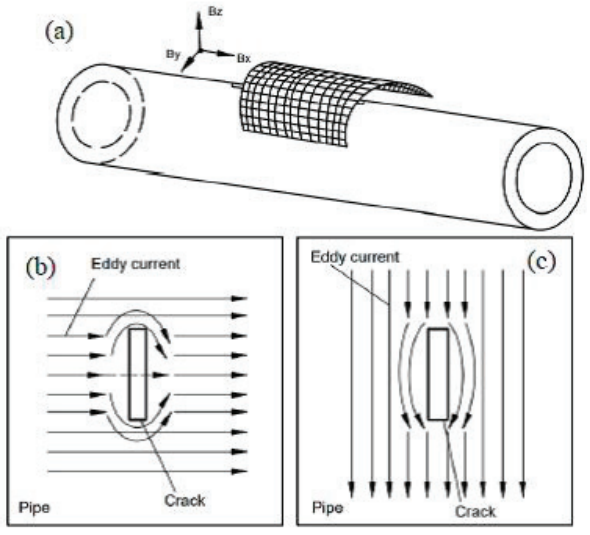

Fig. 1. Schematic diagram of pipe crack detection.

III. RESULTS AND ANALYSIS

A. Establishment of 3D model

The model which is composed of two excitation coils and pipe is established by COMSOL software, as shown in Figure 2. The outer coil is two arcs with the same center as the pipe, and the shape of the inner coil is a rectangle. The upper and lower arc radii of arc-shaped coil are 24 and 35 mm, respectively, with a width of 40 mm and a thickness of 1 mm. The rectangular coil is 38-mm long, 30-mm wide, 17-mm high, and 1-mm thick. The inner surface of the arc-shaped coil fits exactly with the outer surface of the rectangular coil. The inner and outer radii of metal pipe are 10 and 15 mm, respectively. The number of turns for the two coils is 200, and the conductivity of the coil is 6×10^7 S/m, the cross-sectional area is $1 \times 10^{-6}\,\mathrm{m}^2$, the excitation current is 10 A, and the frequency is 200 Hz. The pipe material is aluminum, with a relative permeability of 1, a relative permittivity of 1, and a conductivity of 3.774×10^7 S/m. Ampère's law automatically applies on all the domains. To ensure the accuracy of electromagnetic field in local small space,

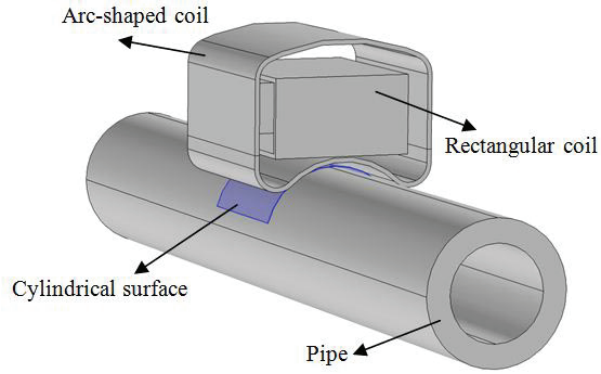

Fig. 2. 3D model.

a cube air domain with length of 400 mm is established, and appropriate boundary conditions should be applied to the solution domain. Magnetic insulation boundaries are employed to six surfaces of the air domain. The magnetic vector potential of all regions is initially set to 0. To better resolve the induced current in the pipe and the coil, use a fine mesh. The fine mesh processing is generated, and the mesh is divided into 267,440. The MUMPS direct solver is used and the relative tolerance is set to 0.001. Since the actual measurement is the magnetic field of the pipe surface, a cylindrical three-dimensional section concentric with the pipe is established above the pipe surface, and the magnetic induction intensity distribution on the three-dimensional section is calculated and analyzed.

According to the three-dimensional simulation model established above, the distribution of the induced current in the pipe is shown in Figure 3. It is the vector sum of the induced current generated under the excitation of two coils together that presents a ring shape around the pipe. Careful observation revealed that there

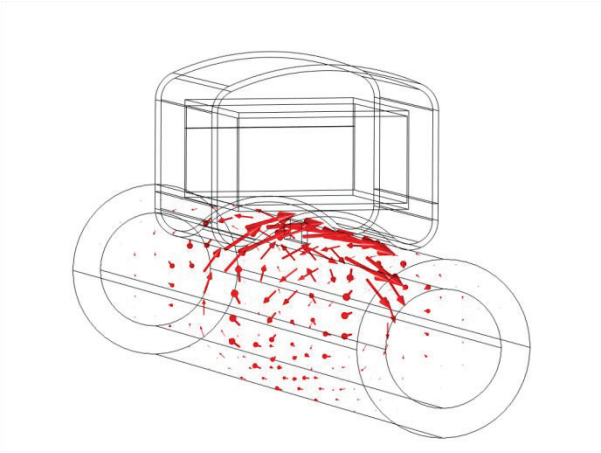

Fig. 3. Induced current in the pipe.

are slight disturbance changes in the induced current near the crack, the arrow of the induced current slightly deviated from the original track, and the eddy current distribution near the crack also changed. Although the change of induced current is not obvious, this slight change will lead to the corresponding change of the external magnetic field around the pipe. The three-dimensional magnetic field distribution of the cylindrical surface near the pipe will be studied and analyzed in detail below.

In actual measurement, the magnetic field on the surface of the pipe is collected. Therefore, a cylindrical support plate coaxial with the pipe is designed between the circular coil and the pipe, which is kept in a relatively static state with the coil. A removable slender circuit board is designed between the cylindrical support plate and the coil. The circuit board is mounted on the cylindrical support plate to provide a fixed, stable lift-off from the pipe surface. The magnetic field sensor arrays are uniformly distributed on the circuit board, and magnetic field sensors are arranged on the circuit board in an axis direction. A row of interface circuits are designed on one side of the circuit board to connect the sensor with the external circuit. During measurement, the circuit board will first scan in both directions along the circumference after the probe coil reaches an area and remains stationary. When the circumferential scanning is finished, the circuit board is moved to the next position along the axis to fill the detection area between two adjacent magnetic field sensors. The circuit board is then scanned in both directions along the circumference. Repeat the above steps until the area covered by one position of the probe is completely scanned.

B. Evaluation of pipe cracks based on cloud contour of induced eddy current field

(1) Cracks at different orientations on the surface of the pipe.

Under the double coil excitation, the magnetic induction intensity norm on the three-dimensional cylindrical surface above the pipe is calculated by COMSOL as shown in Figure 4. Figures 4 (a)-(d), respectively, represent the cloud contour formed by the magnetic induction intensity norm on the cylindrical surface with no crack, transverse crack, longitudinal crack, and 45° oblique crack on the pipe surface. The longitudinal crack size is $12 \times 1 \times 1$ mm, and the transverse crack size is 40° central angle, 1-mm width and 1-mm depth. Different colors of cloud contours represent different magnetic induction intensities. By measuring the distribution of magnetic induction intensity in this region, the cloud contours of magnetic induction intensity norm and three-dimensional component magnetic induction intensity are obtained, and the related information of pipe crack is analyzed from

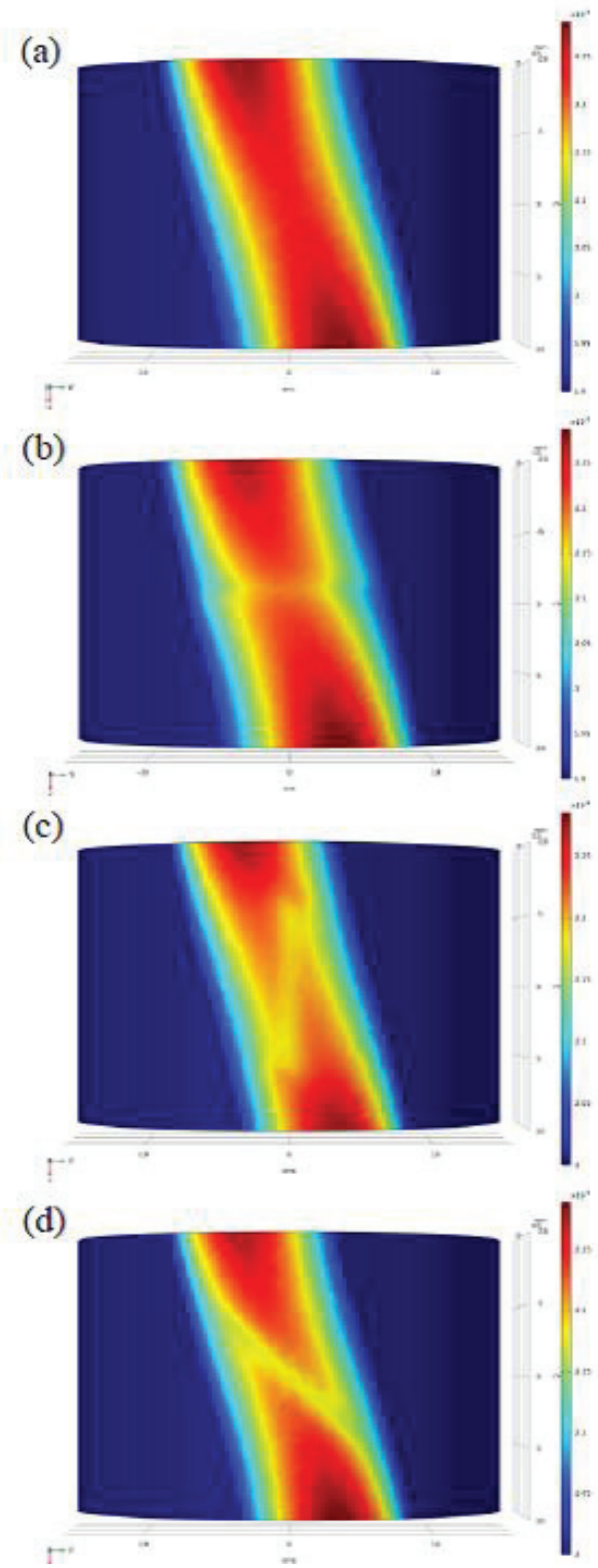

Fig. 4. The cloud contour of the magnetic induction intensity with cracks at different orientations: (a) crack-free, (b) transverse crack, (c) longitudinal crack, and (d) 45° oblique crack.

the image. In this way, the visualization of cracks are realized.

Under the action of double-coil excitation, there is no obvious "shadow" in the cloud contour of magnetic induction intensity norm in the case of no crack, as shown in Figure 4 (a). The regular magnetic field distribution of the cloud contour is broken due to the crack on the pipe. A very obvious "shadow" will be generated at the corresponding position of the crack, and the "shadow" reflected in the figure is basically consistent with the position, size, and direction of the crack, as shown in Figures 4 (b)–(d). This phenomenon proves that under the co-excitation of double coils, the existence of cracks in pipe can be judged by detecting whether there is "shadow" in the cloud contour of magnetic induction intensity above the pipe, and the crack location and orientation can also be accurately obtained. In addition, regardless of whether the crack is longitudinal or oblique, the coil can be directly placed above the pipe for measurement without rotating or moving the coil to ensure that the induced current is perpendicular to the defect. The "shadow" in the figure is an intuitive representation of the pipe crack, realizing the "visualization" of the crack.

Figures 5 (a)–(d) show the cloud contours of x-direction magnetic induction intensity caused by cracks at different orientations under double coil excitation. It can be found that the basic law of the cloud contour in x-direction under various crack conditions is similar to that shown in Figure 4, but the value of magnetic induction intensity is weakened. The "shadow" corresponding to the crack exists in the cloud contours shown in Figures 5 (b) and (d), and the degree of the "shadow" decreases compared with Figure 4, which is related to the decrease of magnetic induction intensity in the x-direction. As shown in Figure 5 (c), the cloud contour formed by longitudinal crack in the pipe cannot well show the existence and related information of cracks, and the detection effect is obviously inadequate compared with Figure 4 (c). By analyzing the magnetic induction intensity in y- and z-directions, the detection effect is similar to the magnetic induction intensity in x-direction, which some information of pipe defects can be determined according to the corresponding cloud contour. Therefore, the information provided by the cloud contour independently constructed by the magnetic induction intensity of the three axes is not complete, and the magnetic induction intensity norm with complete information is still needed to accurately analyze pipe defects.

(2) Cracks in different length on the surface of the pipe. Under the excitation of double coil, the crack length is changed and other conditions remain unchanged. The cloud diagram of magnetic induction intensity norm on the pipe surface is shown in Figure 6, in

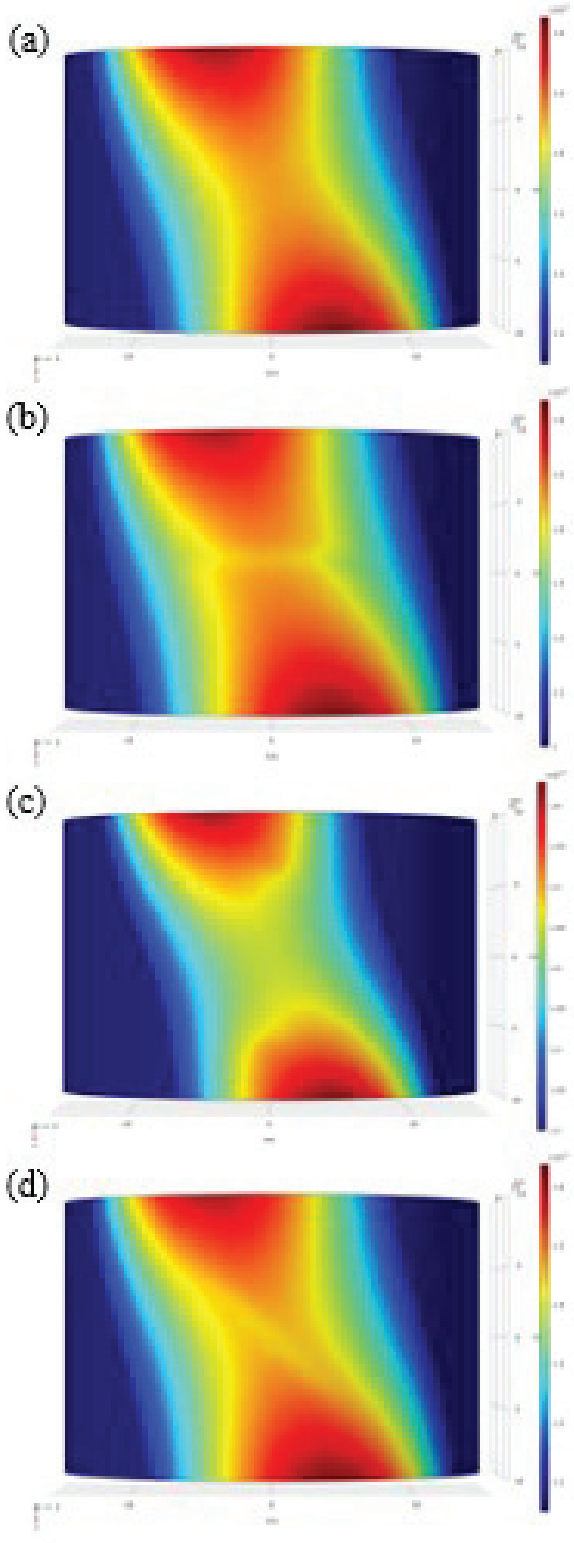

Fig. 5. The cloud contour of *x*-direction magnetic induction intensity with cracks at different orientations: (a) crack-free, (b) transverse crack, (c) longitudinal crack, and (d) 45° oblique crack.

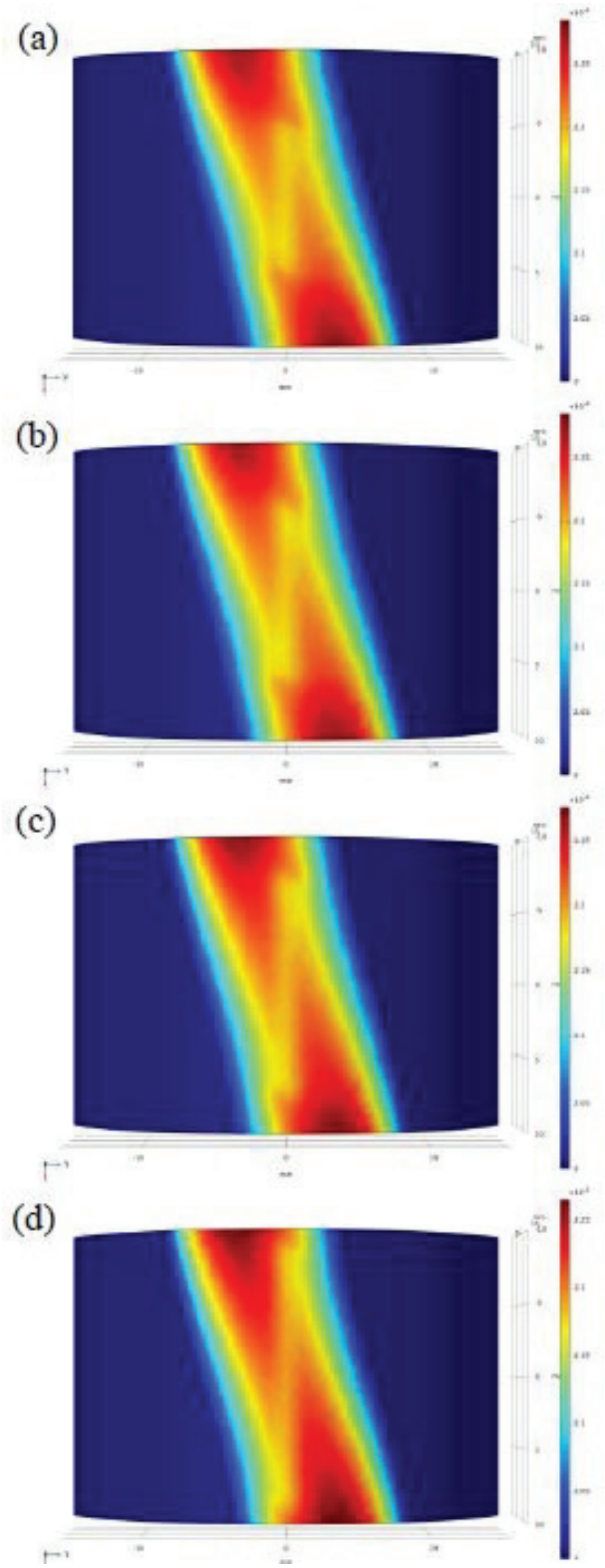

Fig. 6. Cloud contour of magnetic induction intensity norm with different crack lengths: (a) 10, (b) 12, (c) 15, and (d) 18 mm.

which Figures 6 (a)–(d) show that the longitudinal crack lengths are 10, 12, 15, and 18 mm, respectively. According to the four groups of magnetic induction intensity norm obtained, the following conclusions can be inferred. (1) The change of surface crack does not change the overall distribution of magnetic induction intensity on the cylindrical surface, and the cloud diagrams shown in Figures 6 (a)–(d) are basically consistent. (2) As the length of the crack on the pipe surface increases, the "shadow" corresponding to the crack also becomes longer, and the magnitude of the change is the same as that of the crack change. (3) Comparing the length units on the right side of the figure, it can be found that the length of the "shadow" in the cloud diagram is actually the length of the pipe crack. Therefore, the length information of the pipe crack and defect can be accurately judged according to the change of the "shadow" length in the cloud diagram. Similarly, the crack width information can also be obtained by the change of "shadow" width in the cloud diagram.

Crack depth is important information worth paying attention to. Under dual-coil excitation, other conditions remain unchanged and only the crack depth is changed. The corresponding cloud diagram of magnetic induction intensity is shown in Figure 7, where Figures 7 (a)–(d) show that the longitudinal crack depths are 1, 2, 3, and 3.5 mm, respectively.

The following conclusions can be drawn from Figure 7. (1) Different from the influence of crack length on magnetic induction intensity, the change of crack depth not only reflects the "shadow" part corresponding to the crack but also has certain influence on the magnetic induction intensity around the crack. With the increase of crack depth, the surrounding magnetic induction intensity decreases obviously. (2) The weakening of the magnetic induction intensity around the crack will bring disadvantages to the crack detection. At this time, the "shadow" appears to be fuzzy, and the boundary with the surrounding area is not obvious. (3) Although the "shadow" corresponding to the crack is not very obvious, the crack depth can still be evaluated according to the change of the "shadow." With the increase of crack depth, the size of magnetic induction intensity norm within the crack area decreases obviously. The reason why the magnetic induction intensity decreases in this region can still be explained by the principle of eddy current field. As the crack depth increases, the eddy current magnetic field around the pipe increases, resulting in the decrease of total magnetic field. As a result, the phenomena shown in Figures 7 (a)–(d) appear.

As the depth of the crack increases, the "shadow" corresponding to the crack becomes fuzzy, which is unfavorable for the actual detection; so other methods must

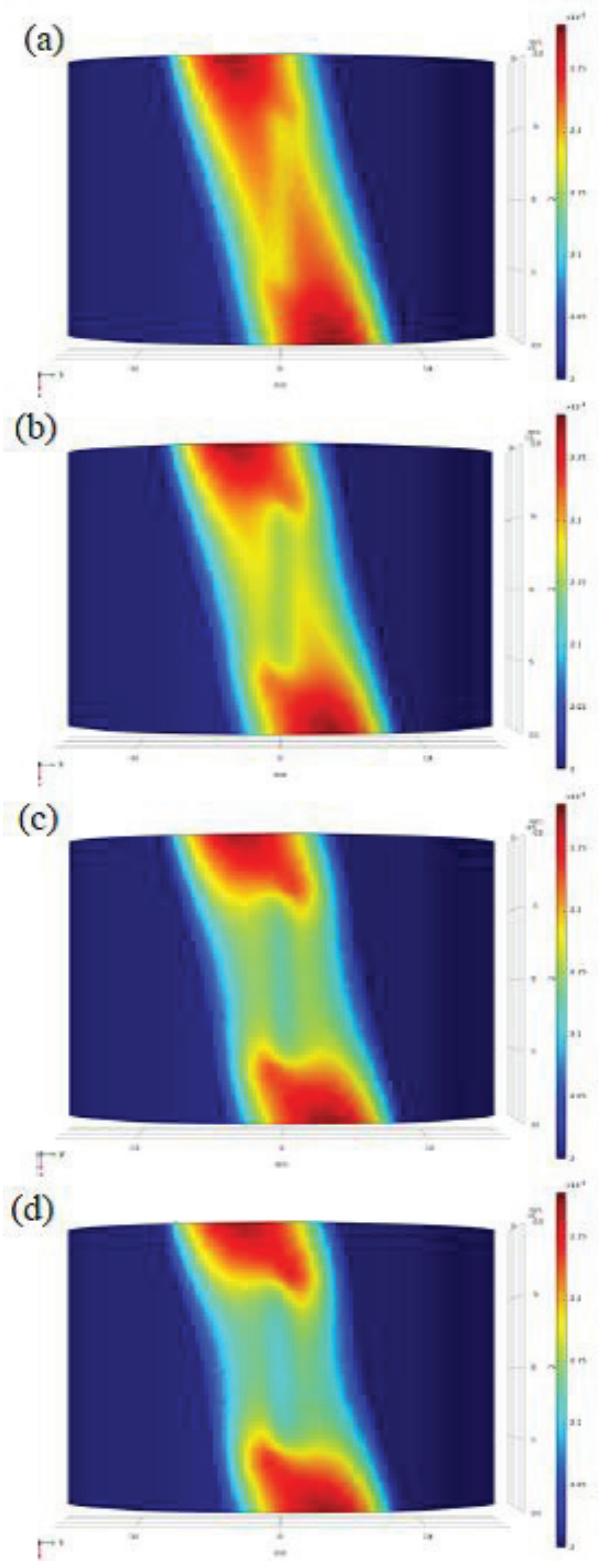

Fig. 7. Cloud contour of magnetic induction intensity norm with different crack depths: (a) 1, (b) 2, (c) 3, and (d) 3.5 mm.

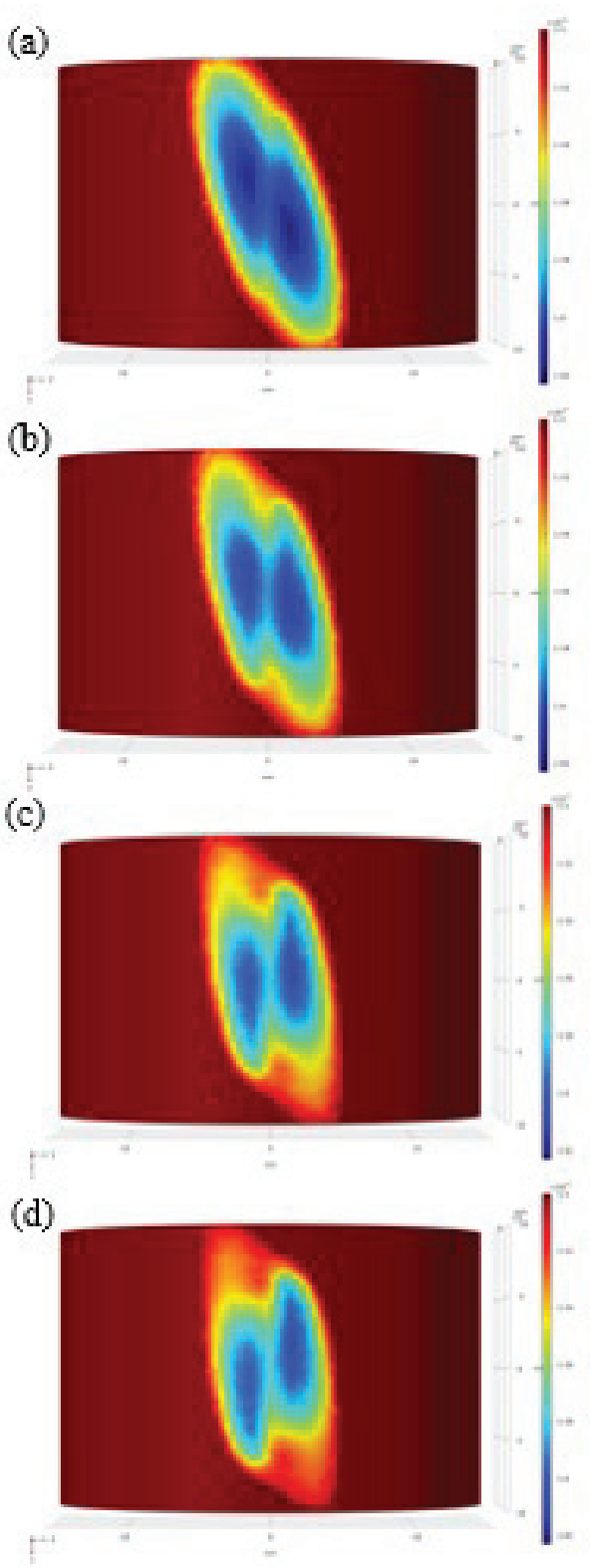

Fig. 8. Cloud contour of magnetic induction intensity in *y*-direction with different crack depths: (a) 1, (b) 2, (c) 3, and (d) 3.5 mm.

be used to assist the analysis. Figure 8 is the cloud contour of magnetic induction intensity in *y*-direction under the action of cracks with different depths. Figures 8 (a)-(d) also show that the longitudinal crack depths are 1, 2, 3, and 3.5 mm, respectively. By analyzing the cloud contour shown in Figure 8, it can be seen that the "shadow" of crack as shown in Figure 7 does not appear in the cloud contour of magnetic induction intensity in the *y*-direction; so it cannot be mainly used to evaluate cracks. However, as the crack depth increases, its image also changes regularly. The positions of the two "blue areas" in Figure 4 (a) are high on the left and low on the right. Starting from Figure 4 (b), the relative positions of the two "blue areas" change. The deeper the crack, the higher the "blue area" on the right in the cloud contour. As shown in Figure 4 (d), the two "blue areas" have appeared as low on the left and high on the right. In addition, as the crack depth increases, the transverse distance between the two "blue areas" also becomes wider. Therefore, the crack depth can be determined by means of the magnetic induction intensity norm, which can be supplemented by the magnetic induction intensity in the *y*-direction.

C. Influence of coil excitation mode on detection results

(1) Independent excitation of arc-shaped coil.

Considering that other conditions remain unchanged and only the arc-shaped coil is used, the magnetic induction intensity above the crack is studied through COMSOL calculation, and the cloud contour of magnetic induction intensity is obtained as shown in Figure 9. Figure 9 (a) shows the magnetic induction intensity distribution in the presence of longitudinal cracks on the pipe surface, and Figure 9 (b) shows the magnetic induction intensity distribution in the presence of transverse cracks on the pipe surface. The influences of different coil excitation on detection results are investigated by analyzing different cracks under the action of arc-shaped coil alone.

It can be found that there is no obvious "shadow" corresponding to the crack in the magnetic induction cloud contour under the longitudinal crack, while there is a clear "shadow" corresponding to the crack in the magnetic induction intensity cloud contour under the transverse crack. At this time, the cloud contour is divided into two symmetrical parts by the transverse crack. As can be seen from the previous introduction, the direction of eddy current generated on the surface of the pipe is the circumferential direction under the excitation of the circular coil. Therefore, it can be concluded that crack-related information can be obtained in the magnetic induction intensity norm as the winding direction of the excitation coil is consistent with the crack length.

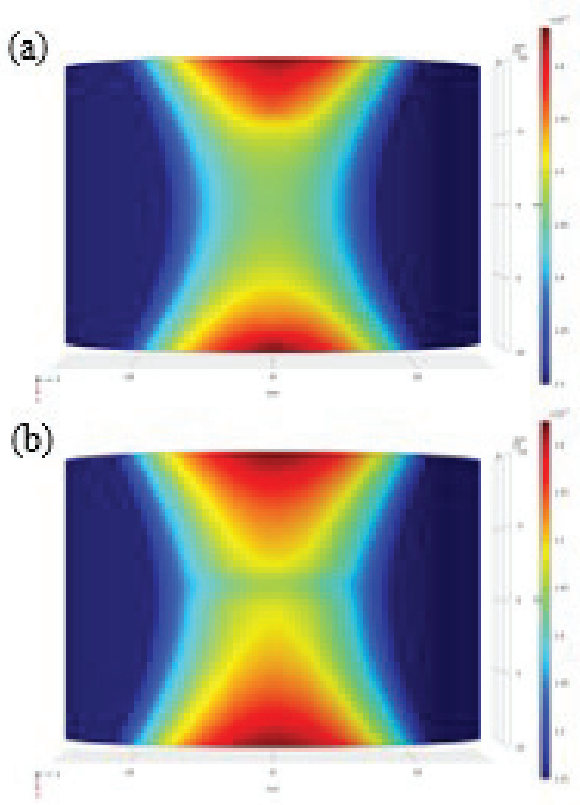

Fig. 9. Cloud contour of magnetic induction intensity excited by arc-shaped coil: (a) longitudinal crack; (b) transverse crack.

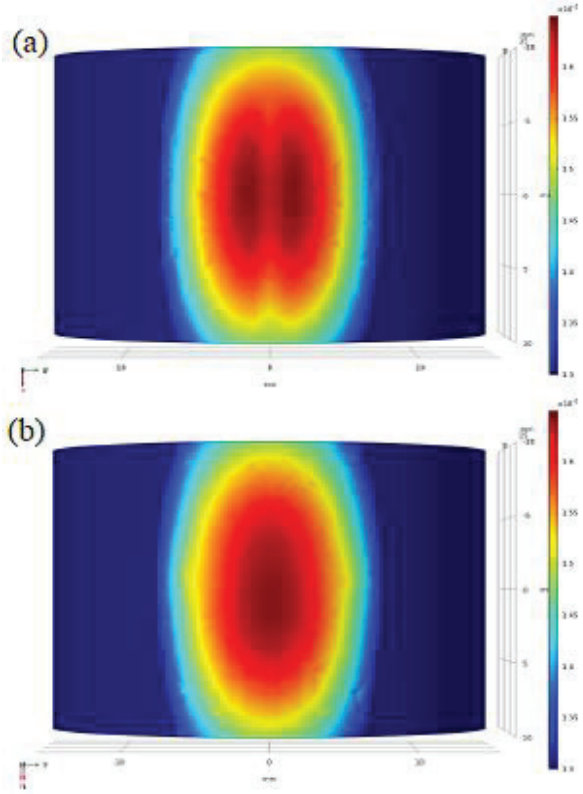

Fig. 10. Cloud contour of magnetic induction intensity norm under excitation of rectangular coil: (a) longitudinal crack; (b) transverse crack.

However, the crack cannot be determined if the direction of crack length and coil winding is perpendicular to each other.

(2) Independent excitation of rectangular coil.

Using only rectangular coil excitation, the cloud contour of magnetic induction intensity norm on the pipe surface is shown in Figure 10, where Figures 10 (a) and (b) are the magnetic induction intensity under the action of longitudinal crack and transverse crack, respectively. It can also be observed that since the rectangular coil generates longitudinal induced current inside the pipe at this time, there is an obvious "shadow" in the magnetic induction intensity cloud contour corresponding to the longitudinal crack, while there is no obvious "shadow" in the magnetic induction intensity cloud contour corresponding to the transverse crack. Combining the magnetic induction intensity generated by the above arc-shaped coil alone, it is further inferred that the information related crack can be obtained from the magnetic induction intensity cloud contour only when the coil excitation direction is consistent with the crack length direction. Therefore, under the co-excitation of the two coils, the crack can be evaluated from the cloud contour of magnetic induction intensity regardless of the direction of the crack. Whether the arc-shaped coil is excited alone or the rectangular coil is excited alone, it cannot have the ability of double coil to accurately obtain defect information.

IV. CONCLUSION

In order to obtain more obvious characteristics of defects and improve the accuracy of traditional ECT, a 3D eddy current magnetic field technology is proposed to realize the visual detection and analysis of defects on pipe surface. The results show that two coils with different excitation directions and shapes can be used to detect transverse, longitudinal, and arbitrary cracks. Different from other electromagnetic NDTs that require adjustment of the probe direction in order to obtain specific information about defects, the three-dimensional eddy current magnetic field method is more convenient in operation. By exploring the distribution of magnetic induction intensity on the cylinder near the surface of the pipe, the method can measure all the cracks at one time without adjusting the direction and position of the coil. In addition, the cloud contour of magnetic induction intensity norm collected under different cracks and

the cloud contour of three-dimensional magnetic induction intensity can realize the visualization of cracks and further quantitatively evaluate the position, length, and depth of cracks. However, other electromagnetic NDT methods, such as magnetic particle testing and magnetic flux leakage testing, are still difficult to accurately quantify defects at present. In the future, advanced image processing algorithm and image recognition technology will be adopted to realize the rapid inversion of defect depth, area, and location and truly realize the precision, automation, and intelligent NDT of pipe defects.

ACKNOWLEDGMENT

This work was supported by Major Project of Colleges and Universities Natural Science Foundation in Jiangsu Province under Grant 21KJA470003, Changzhou Institute of Technology High-level Talent Research Startup Fund Support under Grant YN21019, Jiangsu Province University Student Innovation Training Program Project under Grant 202111055033Y and Jiangsu University Philosophy and Social Science Foundation Project under Grant 2021SJA0924.

REFERENCES

[1] A. Sophian, G. Y. Tian, D. Taylor, and J. Rudlin, "Electromagnetic and eddy current NDT: a review," *Insight - Non-Destructive Testing and Condition Monitoring*, vol. 43, no. 5, pp. 302-306, May 2001.

[2] J. Tian, W. Wang, W. Yan, Z. Jianga, Y. Shanb, and K. Yang, "Cracking due to Cu and Ni segregation in a 17-4 PH stainless steel piston rod," *Engineering Failure Analysis*, vol. 65, pp. 57-64, Jul. 2016.

[3] M. Eissa, M. Naguib, and A. Badawi, "PWR control rods position monitoring," *Annals of Nuclear Energy*, vol. 81, pp. 106-116, Jul. 2015.

[4] S. Xie, Z. Chen, T. Takagi, and T. Uchimoto, "Quantitative non-destructive evaluation of wall thinning defect in double-layer pipe of nuclear power plants using pulsed ECT method," *NDT & E International*, vol. 75, pp. 87-95, Oct. 2015.

[5] B. Helifa, M. Féliachi, I. K. Lefkaier, F. Boubenider, A. Zaoui, and N. Lagraa, "Characterization of surface cracks using Eddy current NDT simulation by 3D-FEM and inversion by neural network," *Applied Computational Electromagnetics Society (ACES) Journal*, vol. 31, no. 2, pp. 187-194, Feb. 2016.

[6] J. Xin, N. Lei, L. Udpa, and S. S. Udpa, "Rotating field eddy current probe with bobbin pickup coil for steam generator tubes inspection," *NDT & E International*, vol. 54, pp. 45-55, Mar. 2013.

[7] G. Tytk and L. Dziczkowski, "Fast calculation of the filamentary coil impedance using the truncated region eigenfunction expansion method," *Applied Computational Electromagnetics Society (ACES) Journal*, vol. 32, no. 12, pp. 1461-1466, Feb. 2018.

[8] T. P. Theodoulidis and J. R. Bowler, "The truncated region eigenfunction expansion method for the solution of boundary value problems in eddy current non-destructive evaluation," *Review of Progress in Quantitative Nondestructive Evaluation*, vol. 24A, pp. 403-408, Apr. 2005.

[9] G. Tytko and L. Dziczkowski, "I-cored coil probe located above a conductive plate with a surface hole," *Measurement Science Review*, vol. 18, no. 1, pp. 7-12, Feb. 2018.

[10] Y. Yating, G. Kuanhou, L. Bowen, and L. Linfeng, "Semi-analytical method for characterization slit defects in conducting metal by eddy current non-destructive technique," *Sensors and Actuators A: Physical*, vol. 301, p. 111739, Jan. 2020.

[11] D. Rifai, A. N. Abdalla, K. Ali, and R. Razali, "Giant magnetoresistance sensors: a review on structures and non-destructive eddy current testing applications," *Sensors*, vol. 16, no. 3, pp. 1-30, Mar. 2016.

[12] J. H. Ge, W. Li, G. M. Chen, and X. Yin, "Analysis of signals for inclined crack detection through alternating current field measurement with a U-shaped probe," *Insight - Non-Destructive Testing and Condition Monitoring*, vol. 59, no. 3, pp. 121-128, Mar. 2017.

[13] F. Jiang, S. L. Liu, and S. G. Xiao, "Quantitative estimation of rectangular surface crack based on the 2-D modeling of surface magnetic field with long straight rectangular wire," *IEEE Transaction Magnetics*, vol. 54, no. 5, pp. 1-12, May 2018.

[14] T. Ozawa, S. Yabukami, J. Totsuka, S. Koyama, J. Hayasaka, N. Wako, and K. I. Arai, "Measurement of internal defects in aluminum using a nano-granular in-gap magnetic sensor," *Journal of Applied Physics*, vol. 117, no. 17, pp. 305.1-305.4, May 2015.

[15] L. Yong, Y. Bei, W. Li, H. Jinga, Z. Chen, and D. Li, "Pulse-modulation eddy current probes for imaging of external corrosion in nonmagnetic pipes," *NDT & E International*, vol. 88, pp. 51-58, Jun. 2017.

[16] N. O. Romero-Arismendi, J. A. Pérez-Benítez, and E. Ramírez-Pacheco, "Design method for a GMR-based eddy current sensor with optimal sensitivity," *Sensors and Actuators A Physical*, vol. 314, p. 112348, Oct. 2020.

Feng Jiang was born in 1981. He received the M.Sc. degree from the School of Mechanical Engineering, Jiangsu University, Zhenjiang, China, in 2006 and the Ph.D. degree from Shanghai University, Shanghai, China, in 2019.

He is currently an Associate Professor with the School of Electrical and Information Engineering, Changzhou Institute of Technology, Changzhou, China. His research interests include electromagnetic non-destructive evaluation, sensor techniques, and fault diagnosis.

Tong Xu was born in Guizhou, China. He is currently working toward the B.S. degree with the Changzhou Institute of Technology, Changzhou, China.

His research interests include electromagnetic non-destructive evaluation and multiphysics simulation.